ISBN ISBN 978-82-326-5069-9 (printed ver.)
ISBN ISBN 978-82-326-5068-2 (electronic ver.)

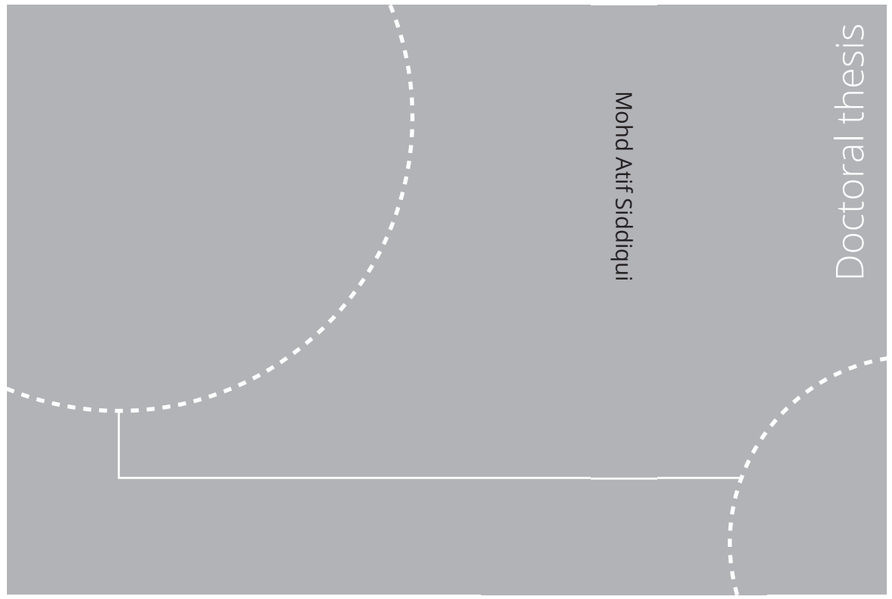

Doctoral theses at NTNU, 2020:361

Mohd Atif Siddiqui

Experimental and Numerical Hydrodynamic Analysis of a Damaged Ship Section In Waves

NTNU
Norwegian University of
Science and Technology

Doctoral theses at NTNU, 2020:361

NTNU

NTNU
Norwegian University of
Science and Technology
Thesis for the degree of
Philosophiae Doctor
Faculty of Engineering
Department of Marine Technology

NTNU
Norwegian University of
Science and Technology

Mohd Atif Siddiqui

Experimental and Numerical Hydrodynamic Analysis of a Damaged Ship Section In Waves

Thesis for the degree of Philosophiae Doctor

Trondheim, November 2020

Norwegian University of Science and Technology
Faculty of Engineering
Department of Marine Technology

NTNU
Norwegian University of
Science and Technology

NTNU
Norwegian University of Science and Technology

Thesis for the degree of Philosophiae Doctor

Faculty of Engineering
Department of Marine Technology

ISBN ISBN 978-82-326-5069-9 (printed ver.)
ISBN ISBN 978-82-326-5068-2 (electronic ver.)
ISSN 1503-8181 (printed ver.)
ISSN 2703-8084 (electronic ver.)

Doctoral theses at NTNU, 2020:361

Printed by Skipnes Kommunikasjon AS

Dedicated to Almighty God and my parents Mrs Humera Khatoon and Mr Mohd Arif Siddiqui

Abstract

In the past few decades, ships have become larger, efficient, durable but the danger of accidental events like grounding, collision etc. continues to be a major issue in ship operations. Following a damage event, a ship can either reach an equilibrium condition after initial flooding or, in the worst case, capsize. In the former case, it is important to analyze damaged ship behavior leading to formulation of protocols for safe return to port. In the latter scenario, it is important to understand the dynamic impact of flooding on the ship just after damage. This can help to implement guidelines in the design stage to mitigate effect of damage. In the present work, the main focus has been on the behavior of a damaged ship after it has achieved a static equilibrium floating condition following a flooding event. From a static point of view, buoyancy and structural strength is lost for a damaged ship. This lost buoyancy/waterplane area leads to increase in natural ship periods due to decrease in metacentric height. However, the floodwater is associated with dynamic effects; effects like vortex shedding, large inflow/outflow through the opening can be dominant in certain scenarios. The floodwater can be associated with sloshing and piston mode resonances which can lead to important phenomena, for example hydraulic-jump like behavior in shallow water conditions. In this work, the effect of these resonance phenomena on a 2D damaged ship model is analyzed experimentally, theoretically and numerically.

Dedicated experiments were performed on a midship barge-shaped section in 2D flow conditions. The experiments were conducted in three parts; a) forced heave motions of the model in intact and damaged condition, b) free-roll decay tests in intact and damaged condition and c) freely-floating model in beam-sea waves in intact and damaged condition. Various parameters such as the forcing period/incident-wave period, forcing amplitude/wave steepness, damage-opening size, airtightness in the damaged compartment etc. were varied to analyze their effect on floodwater behavior. Effect of transient flooding was also studied for an initially dry freely-floating model. Repeatability analysis was performed for a selected set of experiments. The main focus was on identification of sloshing and piston mode resonances and their effect on damaged ship loads/motions. These resonances can have serious consequence for smaller Ro-RO ferries, fishing vessels etc. and the local load effects can also be important for larger ships. Images from the experiments are used to identify occurrence of resonance and cross-check with corresponding measurements of ship-section loads/motions and wave elevation inside the damaged compartment.

The experiments were complemented with theoretical and numerical analy-

ses. Theoretical formulations are used to identify sloshing and piston mode resonance frequencies and these values are verified with images from the experiments. Linear potential flow code (WAMIT) is also employed in indirect calculation of piston mode frequencies. An open-source Navier-Stokes solver in laminar-flow conditions from the CFD platform OpenFOAM is used for dedicated numerical simulations. It is also used within a simplified strip-theory to calculate motions of the ship model in intact and damaged conditions. Snapshots from the simulations are compared with experimental images. Preliminary study of a domain-decomposition (DD) technique is performed to analyze the potential of such a strategy in maintaining accuracy and achieving efficiency. The proposed DD couples a Navier-Stokes solver from OpenFOAM with an efficient and accurate potential-flow solver based on the Harmonic Polynomial Cell (HPC) method and was applied to the case of a damaged ship section in forced-heave motion.

The experiments confirm the occurrence of sloshing and piston mode resonance in a damaged ship. Piston mode had only been described numerically in previous studies. 2D flow conditions help to visualize the sloshing/piston modes and correlate the effect of resonance on loads/motions and internal wave elevation with images. Forced heave motions show that hydrodynamic loads in the damaged condition differ significantly from the intact scenario. Sloshing modes have little effect on the hydrodynamic loads, whereas, piston modes lead to large negative added mass and large damping values. This is associated with a large influx/outflux from the damage opening. An important observation was the effect of airtightness in the compartment, which causes the damaged model to behave similarly to the intact condition. Presence of flow conditions which can lead to local loads was identified and highlighted. Free-roll decay tests also show significant effect of the damage, leading to an increase in both the natural roll period and damping, as documented in previous works. Detailed analysis shows presence of large contribution from the quadratic terms for the roll damping and quantifies its relative importance in the studied cases. In this regard, an important aspect analyzed was the roll damping due to a closed internal tank versus a tank with damage opening. Behavior of a damaged model in waves is also modified significantly as compared to an intact condition. The natural roll and heave periods are modified. Sloshing and piston modes mainly affect sway-roll coupled motions. Airightness in the damaged compartment also affects the heave motions. For a freely-floating dry model with opening lying above the waterline, flooding generally takes place near the natural roll periods. Occurrence of flooding and time to flooding depend on initial loading, incident wave period to natural roll period ratio and wave steepness. Repeatability analysis from the experiments showed acceptable results.

Numerical results document acceptable agreement with experimental data. Sloshing and piston mode frequencies calculated from theoretical formulations and WAMIT show a good match with experimental observations. Numerical simulations from OpenFOAM have a reasonable agreement with both forced heave motions and freely-floating experiments. Numerical simulations for forced heave motions confirm large influx/outflux at the opening near piston mode resonance and negligible flow near sloshing modes. Pressure sensors were not used in the experiments, however, simulations confirm the presence of local loading on the

deck. The simulations also helped analyze the difference in behavior at shallow and higher filling levels in the damaged compartment. Strip-theory results capture the general trend of freely-floating damaged model motions but over-predict the motions. Results from the domain-decomposition strategy for forced heave motions show good potential for future application in simulation of damage ship behavior.

Preface

This thesis is submitted to the the Norwegian University of Science and Technology (NTNU) for partial fulfillment of the requirements for the degree of philosophiae doctor (PhD).

This work has been carried out at the Center For Autonomous Marine Operations and Systems (NTNU AMOS), Department of Marine Technology, NTNU, Trondheim. My main supervisor has been Professor Marilena Greco with Professor Odd M. Faltinsen, Professor Claudio Lugni and Dr Giuseppina Colicchio as co-supervisors.

This work was supported by the research Council of Norway through the Centre of Excellence funding, project number 223254-NTNU AMOS. The Norwegian Research Council is acknowledged as the main sponsor of NTNU AMOS.

Acknowledgments

I have had the pleasure of working with wonderful people at the Department of Marine Technology, NTNU, Trondheim. I wish to extend my thanks to the department, in general, but I must mention some people in particular. My deepest gratitude has to be to my supervisor Professor Marilena Greco. She has tremendous knowledge and skill in this field and she always made the best efforts to impart her knowledge to me. Her patient guidance, support and encouragement helped me to cross many hurdles. She has been like a second mother to me and her guidance has been a valuable learning experience not only for my PhD study but also for my life. I would also sincerely like to thank Professor Odd M. Faltinsen, who through many discussions has taught me the value of finding a reason for everything, big or small. His unparalleled knowledge of hydrodynamics continues to astound me every time that I have a discussion with him. I would also like to thank Professor Claudio Lugni for his advice with experiments and Dr Giuseppina Colicchio for helping with numerical calculations. Their help and support has been invaluable in shaping this work. A special thanks must go to Professor Sverre Steen for his guidance and support.

I would like to thank Trond Innset, Terje Rosten and Torgeir Wahl who provided enormous help and time for proper execution of the experiments.

It has been a great experience to have worked alongside some wonderful people for the last few years. I have shared valuable discussions with my office mate Shaojun Ma who was patient enough to put up with my constant questions. Dr. Zhaolong Yu has been a great friend, giving great birthday dinners and also some great games of table tennis. I started collaborating in 2018 with Hui-li Xu and and I would like to thank her for her encouragement and the very helpful discussions on OpenFOAM. Dr. Finn-C. W. Hanssen has been an invaluable friend and has provided much valuable discussion and help with the harmonic polynomial cell method. I am always inspired by his amazing dedication. Dr. Yugao Shen provided great help and support. I must also thank Dr. M.S. Afzal, Dr Nadeem Ahmad, Woongshik Nam and Dr Bhushan Taskar for their help during my PhD. A special mention of gratitude has to be towards Laxminarayan Thorat who has been a constant source of support and like a big brother throughout my PhD work.

My deepest gratitude and thanks is to my parents. They are the most wonderful people one could have as parents. They have sacrificed greatly to provide me the best education and resources. My mother, especially, has worked extremely hard all her life to ensure that me and my brother succeed in life. My brother has been a constant source of encouragement and I owe him a great debt for his sup-

port during my depressing phases. Lastly, a special thanks to my lovely wife who put up with me during the bad phases. Her patience, understanding and help during the completion of my thesis has been tremendous.

Nomenclature

General Rules

- Only the most central symbols are listed below
- Meaning of symbols are as a minimum given when first introduced
- The same symbol may sometimes be used to describe different quantities

α	Phase fraction of fluid
η_{3a}	Forced heave motion amplitude
η_j	motion in j^{th} direction
γ	Euler's Constant
$\mathrm{B_c}$	Breadth of damaged compartment
$\mathrm{h_c}$	Height of damaged compartment
$\mathrm{I_{44}}$	Roll moment of inertia about x-axis with ballast mass
$\mathrm{L_c}$	Length of damaged compartment
$\mathrm{M_w}$	Static Floodwater mass
$\mathrm{T_d}$	Draft
∇	Divergence Operator
ω	Angular Frequency
ω_p	Natural piston mode frequency
ω_s	Natural sloshing mode frequency
ρ	Density of fluid
φ	Velocity Potential
ζ	Wave elevation
ζ_a	Wave elevation amplitude in damaged compartment
A	Wave Amplitude

A_r	Submerged area of cross-section
a_{ij}	2D Added mass coupling coefficient in the i^{th} mode due to motion in the j^{th} mode
A_{jj}	3D Added mass coefficient in j^{th} mode of motion
a_{jj}	2D Added mass coefficient in j^{th} mode of motion
B	Breadth of model
$B_{44,quad}$	Quadratic roll damping coefficient
B_{44l}	Linear roll damping coefficient
b_{ij}	2D Damping coupling coefficient in the i^{th} mode due to motion in the j^{th} mode
B_{jj}	3D Damping coefficient in j^{th} mode of motion
b_{jj}	2D Damping coefficient in j^{th} mode of motion
c_g	Group velocity of waves
C_{jj}	3D Restoring coefficient in j^{th} mode of motion
c_{jj}	2D Restoring coefficient in j^{th} mode of motion
Co	Courant Number
D	Depth of model
d	Damage opening length
Eu	Euler Number
Fn	Froude Number
g	Gravitational Constant
h	Water depth
h_d	Damage height
h_{fr}	Freeboard height
k	Wavenumber
kA	Wave Period
KC	Keulegan-Carpenter Number
L	Length of model
p_a	Atmospheric pressure
T	Wave Period
T_f	Forced motion forcing period
t_{fl}	Time to flood

2D	Two-Dimensional
3D	Three-Dimensional
ALE	Arbitrary Lagrangian-Eulerian Method
BEM	Boundary Element Method
BVP	Boundary Value Problem
CFD	Computational Fluid Dynamics
CFL	Courant-Friedrichs-Lewy number
CN	Crank-Nicolson
CoG	Center of Gravity
DD	Domain Decomposition
DM	Deforming Mesh
DoF	Degree of Freedom
FFT	Fast Fourier Transform
FL	Filling Level
FVM	Finite Volume Method
GM	Transverse Metacentric Height
ITTC	International Towing Tank Committee
KG	Vertical distance of CoG from keel
LC	Loading Condition
LS	Level-set Method
M	Dry Mass
NS	Navier-Stokes
NSLS	Navier-Stokes Level-Set
NWT	Numerical Wave Tank
OF	OpenFOAM
OG	Overset Grid
RANS	Reynolds Averaged Navier Stokes
RAO	Response Amplitude Operator
RO-PAX	Roll On/ROll Off Passenger Ferry
RO-RO	Roll On/ROll Off
URANS	Unsteady Reynolds Averaged Navier Stokes
VoF	Voulume of Fluid
WAMIT	Linear Potential flow software
WL	Waterline
WP	Wave probe

Contents

Chapter 1

Introduction

1.1 Motivation

Ships served as the main source of transportation in olden times when long voyages led to discovery of new lands. With the advent of faster and more comfortable modes of transportation such as trains and airplanes, travel by ships is reduced mostly to leisure cruises. However, ships carry almost 90% of world trade (data from Intentional Chamber of Shipping) and will continue to do so foreseeable future, remaining indispensable in the modern world. Among them, ferries/RO-RO ferries provide connection for islands with the mainland. Modern technology has made ships larger, stronger and faster. Moreover, significant improvements in hull structure, building materials and stricter safety protocols have led to a drastic decrease in maritime accidents. However, despite the advancements and newer technology, accidents can occur from time to time. Papanikolau et al. (2015) presented a systematic and detailed analysis of maritime accidents from 1990 to 2012. They concluded that the frequency of accidents increased in the last decades even with stricter safety regulations. Human error plays a big role along with rough weather, mechanical/instrument faults, etc. Marine accidents on a ship like small fires, shift of cargo, slips/fall, result in injury to crew or worse but do not threaten the structural integrity of the hull. Incidents like navigational failures, sudden turns, etc. can also lead to dangerous consequences but do not necessarily cause damage to the hull or ship structure. Events like grounding, failure of door closing mechanisms, collision with other ships and offshore structures, explosion close to the hull surface, lead to breaches in the hull and subsequent flooding in most situations. The present work focuses on situations that can lead to flooding and, in particular, their effect on ships.

Flooding in ships as a result of a damage caused by collision, grounding or violent interaction with severe sea environment can have serious consequences. A large number of ship accidents have occurred over the course of human history resulting in loss of lives, loss of cargo and/or hazardous spills. Titanic (1914) is a famous example of a maritime disaster leading to the loss of almost 1400 lives. Estonia disaster (1994) was a severe tragedy with loss of around 800 lives. The bow visor did not close properly due to a glitch in the closure mechanism. Slamming

due to waves may have caused the visor to fall off leading to flooding, water accumulation, loss of stability and eventual capsize. Following the official report from the accident investigation commission (Estonia, 1997), Karppinen and Rahka (1998) presented a detailed discussion on the sinking of Estonia (figure 1.1).

Figure 1.1: Sequence of events in the sinking of MV Estonia (image from final Accident Investigation Commission report, 1997)

Costa Concordia (2012) is another example of a ship disaster where 32 lives were lost. In this case, the ship capsized due to grounding (see the top picture of figure 1.2). The European Gateway (1982), Herald of the Free Enterprise (1987) and MV Sewol (2014; center picture of figure 1.2) are some of the other major accidents in the past decades. In the recent years, quite a few collisions between ships (for example, USS John McCain and Alnic MC) have been reported. The recent grounding of Wakashio has led to a major oil spill around Mauritius. This has threatened to compromise the local ecology severely. Dramatic accidents like these have inspired many researchers to study ship flooding and its effect on ship motions.

Flooding in ships is a complex dynamic phenomenon and difficult to analyze using engineering tools. The behavior of a flooded ship differs significantly from an intact condition. Floodwater enters through the damaged opening, leading to loss of stability, excessive heel or trim and in some cases capsizing. Roll On/Roll Off (RO-RO) ferries have become very popular on shorter sea routes and transport a large number of people and vehicles. In fact, these ships have large decks with no vertical bulkheads in car decks to be able to fit a large number of vehicles. This can cause a relevant free-surface effect due to floodwater and loss in static stability even with a relatively small amount of flooding. Therefore, they are more susceptible to capsize as compared to other vessels. Generally, ship designers calculate damage stability of a ship assuming static conditions with the requirements prescribed by the International Maritime Organization (IMO). However, it is important to understand the features of flooding dynamics and the influence of floodwater on the dynamic stability of a damaged vessel in waves. Dynamic effects are much more pronounced during flooding, large and violent motions of the floodwater inside the unobstructed decks have an important effect on the ship motions and vice versa. Ruponen (2007) mentions that usually after a damage event, flooding involves three phases:

1. Initial transient phase
2. Progressive flooding
3. Steady state behavior about a new equilibrium position

Figure 1.2: Marine accidents: The grounded Costa Concordia (top; photo by Gregorio Borgia/AP), the sinking of Sewol ferry (center; source : www.CNN.com) and the damaged hull of USS John McCain (bottom; photo by Joshua Fulton/Navy via AP)

Dynamic stability just after a damage event (Phase 1) is of greatest importance as the immediate behavior after the damage is critical for capsize occurrence. However, even after attaining a steady equilibrium condition (Phase 3), the

dynamic behavior of a damaged ship in waves is considerably different from the intact condition. Study of the dynamic behavior can help in understanding critical conditions and thus improve design and safety requirements especially for passenger vessels. Due to the complex nature of the problem, the highly nonlinear behavior of the floodwater and its coupling with ship motions, detailed investigations need to be performed. They are useful to assess reliability of simplified approaches in capturing the parameters governing the problem of a damaged ship in waves. Operational safety may be improved if the effects of flooding and damage scenarios are well understood.

1.2 Literature Review

The dynamic effects of floodwater motion inside the damaged compartments of a ship subject to the action of incident waves are very important. These are associated with the inflow and outflow of water, especially if the damage extent is large or the flooding is underway. In these cases, a large amount of water may enter or leave the compartment as the ship undergoes motions and the external incident sea waves hit the ship. During the flooding process, a ship's motion affects water flooding and sloshing in its compartment; conversely, the liquid loads acting on the compartment also influence the motion of the ship. Various authors have tried to analyze/solve for these effects both experimentally and numerically. Many simplifications have been made to the overall problem depending on the focus of the study in those works. Without pretending to be exhaustive, major works related to the aspects discussed in the present work are described here.

A lot of works are available on model tests of damaged ships. Shimizu et al. (2000) performed experiments on a RO-RO ship model with opening at the bow in head-sea waves, allowing only heave and pitch motions. They concluded that modifying heading and speed is important for survival. Vassalos and Papanikolaou (2002) presented a comprehensive and detailed discussion on the *Stockholm agreement*. Data were presented for RO-RO ships in the form of limiting significant wave height for capsize, damage metacentric height etc. from *Stockholm agreement* calculations, numerical simulations and model tests. It was concluded that the *Stockholm agreement* is too strict as compared to performance-based standards. Korkut et al. (2004) conducted an experimental study on a 6-degree of freedom (DoF) damaged RO-RO ship model. They used a freely floating model in regular waves attached to the tank walls with slack moorings and no forward speed. They varied wave periods, wave headings and wave heights to demonstrate the effect of these parameters on a damaged ship and variation with respect to an intact ship condition. They noted that the damaged vessel response is highly dependent on wave frequencies, wave headings and natural frequencies of the model. Korkut et al. (2005) presented experiments for measuring global loads on a damaged RO–RO model in regular waves and concluded that damage resulted in higher loads as compared to the intact condition. Ruponen (2007) presented extensive experiments for progressive flooding of a barge-shaped ship. The internal layout was modelled to resemble a ship-like scenario. Side and bottom damage were analyzed and results compared well with numerical simulations. Lee et al.

(2007) presented a theoretical and experimental study of a damaged RO-RO ship model experiencing flooding in regular and irregular waves. They examined three damage conditions and varied the wave height and heading, showing qualitative agreement between numerical and experimental data. Khaddaj-Mallat et al. (2012) performed experiments on a damaged ship model and identified damage opening area, damage location and air compressibility in a damaged compartment as important parameters for investigating flooding in damaged ships. Begovic et al. (2013) conducted experimental studies on a frigate hull in intact and damaged conditions. Motion responses were calculated both in intact and damaged condition. Two geosim models, at 1:100 and 1:51 scale, were tested with zero forward speed in various wave headings and wave periods. The authors investigated nonlinear behavior and calculated 2nd-order transfer function of motions, useful for validating nonlinear methods. Lee et al. (2015) performed experiments to study 6-DoF motions for a damaged ship in regular beam-sea waves with aim to build a database for Computational Fluid Dynamics (CFD) validation. Manderbacka et al. (2015b) conducted experiments on a box-shaped barge with damage on the side. They demonstrated the effect of compartment width and layout on transient flooding. Effect of initial stability on the flooding process was also examined. The authors noted that a damage event usually leads to increase in damping and natural period for the roll motion. Domeh et al. (2015) conducted experiments on a damaged ship model, examining the effect of compartment permeability and damage orifice size on the model behavior in waves. They also studied the effect of forward speed on the motion responses of a damaged ship model. They concluded that change in compartment permeability and damage size has higher effect on heave and pitch motions of a damaged model at forward speeds as compared to a stationary model. Acanfora and De Luca (2016) performed experiments on a damaged ferry hull in beam-sea waves and investigated the effect of damage location on ship motions. They also investigated the effect of compartment damage on roll period and damping. They reported that roll motions for a damaged ship can vary not only due to damage size but also due to location of damage opening and that bottom damage leads to lower natural roll period as compared to side damage. Acanfora and De Luca (2017) extended the work in Acanfora and De Luca (2016) by using a realistic modeling for the damaged compartment. They also performed experiments assuming a damaged engine compartment and focusing on the effects of obstructions for the roll motion in beam-sea waves. Begovic et al. (2017) analyzed the impact of damage conditions on the vertical and horizontal shear force and bending moment for a naval ship model and reported that the shear force/bending moment behavior can be quite different (generally higher) as compared to an intact ship. The experiments were also compared against other similar works in order to provide benchmark data to be used for validation of numerical methods. Bennett and Phillips (2017) studied experimentally the effect of floodwater on the ship motions and wave loads. They also presented transient flooding test results demonstrating the effect of sudden damage on ship motions. The authors reported that natural sloshing frequencies for higher modes (>3), although excited, do not pose significant threat as vessel motions become quite small at these frequencies. This was also observed during the present work (shown in chapter 5), and the study was limited up to the second

sloshing mode. Results from their transient flooding experiments demonstrated the time to flood of the compartment and change in RAOs from intact to flooded condition. Transient flooding tests have also been performed in the present work (see section 5.1.4), although with a different setup, and showed similar behavior as documented by Bennett and Phillips (2017). More recently, Gu et al. (2018) presented experiments on a combatant vessel and analyzed the effect of floodwater on the vessel stability. They discussed damaged ship motion RAOs and wave-induced loads on the damaged ship model from the experiments, and also demonstrated the impact of damage on hull girder loads. The authors reported that damage increases the roll damping and natural period.

Forced motion tests to calculate hydrodynamic coefficients of damaged ship models have also been performed in some works. Cichowicz et al. (2011) performed forced roll experiments on a body with a flooded compartment. The model was a cylindrical midship section of a RO-RO Passenger ferry (RO-PAX) and had an internal gyroscopic mechanism designed to produce periodic roll moment. Tests were conducted both in intact and damaged condition. The authors presented added mass and damping in roll for a flooded ship model and reported negative added mass at low frequencies. They argued that this might be caused by slightly underestimated restoring coefficient. Hashimoto et al. (2017) also presented experimental results for a damaged ship model undergoing forced roll motions. They performed numerical simulations for flooding in damaged ships and validated them against experimental data for forced roll motions and flooding test of a Pure Car and Truck Carrier model. A hybrid model was used combining a potential-flow solver for the intact region of the ship and a Moving Particle Simulation for the damaged region. Smith et al. (2009) also performed a series of forced experiments in heave on a damaged ship model. The damage location was at the keel and extended along the length of the keel. The experimental setup was similar to Vugts (1968) and the hydrodynamic loads were expressed per unit length and made non-dimensional as 2D loads so that the experimental results can be interpreted as 2D results. Added mass and damping in heave for a flooded ship model section were presented. They show a clear change in behavior and, in particular, the values for damaged condition are much higher for both added mass and damping coefficients in the region of low frequencies. Effect of air compressibility in the damaged compartment was also demonstrated.

Air compressibility in a damaged compartment can have important consequences on the flooding behavior. Palazzi and de Kat (2004) performed model tests on a damaged ship model taking into account the effect of air compressibility in an airtight damaged compartment. They compared the test with numerical results and showed good agreement. The authors modeled the airflow using gas laws and flow through an orifice. They noted that air compressibility may cause extra roll damping and concluded that airflow effects must be taken into account in the simulations. Air compressibility effects on motions of a damaged ship were also examined by Ruponen et al. (2013) and Khaddaj-Mallat et al. (2012). The latter identified damage opening area, damage location and air compressibility in damaged compartment, as important factors for flooding. Ypma (2010) presented experiments for a damaged scenario in vacuum conditions. This helped to avoid scaling issues that occur due to presence of air-cushion in the damaged compart-

ment. They concluded that air compressibility affects the flooding process and provided data to be used for numerical models.

The floodwater in a damaged compartment of a ship can experience resonance behavior. Sloshing and piston mode resonance can be of particular significance. Sloshing is an internal flow problem associated with resonance of a liquid in a closed tank. Faltinsen and Timokha (2009) studied theoretically sloshing in a tank with various structures and configurations. Piston mode resonance is a coupled external/internal flow problem associated with an opening and appears as a pumping in-and-out flow. It has been studied extensively for harbor resonance (Miles and Munk, 1961) and moonpools (Molin, 2001; Faltinsen et al., 2007). Kristiansen and Faltinsen (2010) analyzed experimentally and numerically the effect of piston mode resonance on ship motions when the ship section is close to a terminal wall and resonance occurs in the gap between them and reported important effects near resonance. Fredriksen et al. (2014) studied wave response of a 2D body with moonpools using experiments and numerical schemes. They concluded that the piston mode frequency strongly affects the heave motions. Kong and Faltinsen (2010) numerically analyzed the effect of sloshing and piston mode resonance in a damaged ship by a linear potential flow method. They demonstrated good agreement with ITTC benchmark experiments, capturing the peaks in roll motions quite well. de Kat (2000) studied numerically and experimentally the motions of a ship with a partially filled tank and presented the effect of filling ratios on first natural mode of sloshing in a flooded compartment. Acanfora and De Luca (2017) also demonstrated sloshing mode for a damage case without an opening and showed that the presence of the engines causes excitation of the second sloshing mode. Excitation of resonance can be critical for the motions as shown in some mentioned experimental studies and also demonstrated in our work (see section 5.1.3). Resonance behavior in a damaged compartment can also lead to important global and local loads. Begovic et al. (2017); Gu et al. (2018) analyzed global loads but resonant behavior in the damage compartment can also cause local loads like roof impact, hydraulic jump like condition etc. without necessarily causing large ship motions. Kong and Faltinsen (2010); Kong (2009) also showed very large free surface amplitude near first natural piston mode frequency causing large dynamic pressures on the deck, which may lead to local structural failures.

In addition to those already examined, other works documented dedicated numerical investigations with various methods proposed/implemented to study the behavior of damaged ship sections. Spouge (1986) presented one of the earliest works for the simulation of a damaged ship. He simulated the capsize of the RO-RO vessel 'European Gateway'. He used a hydraulic orifice flow model to calculate the flow of liquid through a small orifice between two fluid chambers, and empirical equations to determine the center of gravity (CoG) of the floodwater. Vredeveldt and Journée (1991) also used a hydraulic flow model coupled with the roll motion of the ship to study the motions of the damaged ship in calm water due to inflow of water. They used the Bernoulli's equation to compute flow rates through the opening along with a pressure loss coefficient (King and Brater, 1963). Turan and Vassalos (1993) proposed a numerical method which coupled the motions of the ship and the floodwater to assess the survivability

of a damaged ferry. A large-amplitude nonlinear motion simulation of a damaged ship in time domain was performed, where the coupled equations of motion for sway-heave-roll were employed. The motion equations take account of the amount of water entering and leaving a damaged compartment, and also of variations in the ship's mass. In this study, no comparison between theoretical and experimental results was made. Although large-amplitude motions had been investigated in these studies, the equations of motion were solved in a linear sense, where Euler angles are implicitly assumed to be small. de Kat (1990) also used a coupled system for 6-DoF to calculate extreme motions of a damaged ship in waves. He solved the nonlinear equations of motion for ship capsize events. The author considered both potential hydrodynamic forces and empirical viscous forces. Papanikolaou et al. (2000), Spanos and Papanikolaou (2001) and Spanos et al. (2002) used a lumped mass method to simulate floodwater dynamics. The flooded ship is modelled as a two-mass system: the intact ship, having six degrees of freedom, and the floodwater, considered as a lumped mass. The lumped mass model assumes that the floodwater is located at its CoG and moves over a predefined surface or path. This approach gives reasonable results when sloshing effect is not dominant. Manderbacka et al. (2015a) also used a lumped mass method with a moving free surface and presented time-domain simulations of damaged ship motions with validation against experiments. Jasionowski (2001) used a strip theory formulation to study damaged ship motions. He used a hydraulic flow model to account for inflow/outflow of floodwater and a free mass model instead of a rigid lumped mass model. The free mass model means that the floodwater is decomposed into small masses over the entire flooded compartment. Ruponen (2007) presented an iterative time-domain solver for the simulation of flooding in ships and validated it against experiments on a damaged barge model. Santos and Guedes Soares (2008) used shallow-water equations to solve the problem of flooded water on decks with the assumption that the water height on flooded deck must be small compared to the deck dimensions. More recently, fast simulation methods have also been employed, for example Acanfora and Cirillo (2017) presented a method to examine the transient stage of flooding. They used a lumped mass method, considering the free surface of floodwater to be always normal to the gravity vector. An improvement of this method was presented in Acanfora et al. (2019). They demonstrated reasonable comparison with experimental data. The 23^{rd} ITTC specialists committee on extreme motion and capsizing in waves, Papanikolaou (2001), conducted an international benchmark study where the accuracy of existing computational models was examined by comparing them against experimental motions of a damaged ship. There were five independent participants in this study. The benchmark study demonstrated disagreement among the results from the numerical simulations of the same ship. The presented models can predict well the behavior at non-resonant wave periods but have limitations in capturing roll resonance period and magnitude accurately depending on the simplifications used in the respective numerical technique, differences in roll viscous damping models, floodwater-handling method and wave-body interaction calculations. The 24^{th} ITTC benchmark study, Papanikolaou and Spanos (2004), presented a detailed analysis for the roll-decay data in intact and damaged conditions for a RO-RO ship model (PRR01), comparing experimen-

tal data with five participant numerical studies. The benchmark data showed that all numerical methods captured natural period and damping well for the intact condition. For the damaged scenario, all studies showed deviation as compared to the experimental values. The authors concluded that this can be due to modelling of roll-damping terms and simplification in modeling of floodwater-dynamics. It must be emphasized that both these important benchmark studies were performed almost 20 years ago. They provided significant insights in the understanding of damaged ship behavior and highlighted limitations on the numerical side. Papanikolaou and Spanos (2008) presented a benchamark study on numerical codes for assessing damaged ship stability in waves. They concluded that the results from the different examined solvers were divergent and especially sensitive to incident-wave period. Recently, a benchmark study was presented by Parunov et al. (2020) on the numerical prediction of motions and wave loads on a damaged ship using strip theory and 3D BEM codes. They demonstrated good agreement for vertical motions but larger scatter for the horizontal and vertical wave bending moment among the codes. They also suggested to include sloshing effects for improvement of the results.

The modern availability of large computational power has driven the surge in usage of CFD in hydrodynamic studies. Numerical wave tanks (NWT) incorporating viscous solvers have been successfully implemented for studying various hydrodynamic problems. Jacobsen et al. (2012) presented a wave generation and absorption system using OpenFOAM (OF). They used two benchmark test cases, to demonstrate the ability of wave propagation. Windt et al. (2019) analyzed various methods available for development of NWTs in OF. For seakeeping applications, CFD methods have been used for estimating added mass and damping coefficients in recent studies as shown by Bonfiglio et al. (2011) for two-dimensional (2D) ship shaped sections, Chen and Christensen (2016) for cylinders and Thilleul et al. (2013) for 2D ship sections and cylinders. Added mass and damping coefficients for angular motions (roll/pitch) are the hardest to estimate accurately. In beam-sea waves, roll motion is significant and for its estimation, we need to calculate roll damping precisely. Some recent studies have tried to understand and highlight the best practices to calculate roll damping using CFD for intact ships, see e.g., Jaouen et al. (2011); Mancini et al. (2018). The former referred work used forced roll motions whereas the latter employed URANS (Unsteady Reynolds averaged Navier Stokes) simulation of roll decay for a ship model in 3/6 DoF motion using overset grid technique. Conclusions were presented to identify best practices for roll decay simulations and on error uncertainty.

These solvers have also become quite attractive to study damaged ship behavior. Gao and Vassalos (2012) employed a commercial RANS (Reynolds averaged Navier Stokes) solver to study forced roll motions of a damaged ship. They analyzed the damping effect of floodwater in a damaged ship as compared to intact condition. Begovic et al. (2015) presented CFD results for roll decay of intact and damaged ship models. They analyzed the effect of grid size and time step on numerical simulations and presented reasonable agreement with experimental data. Sadat-Hosseini et al. (2016) performed CFD simulations for a damaged passenger ship in calm water and in beam-sea waves. They compared results with experiments and demonstrated better agreement than potential-flow solvers but with

significant computational cost.

Hybrid (or domain decomposition (DD)) methods have become popular in recent years to improve efficiency of computationally-expensive solvers. Gao et al. (2013) used a hybrid method coupling a potential-flow solver for intact region and Navier-Stokes solver for the damaged region, to study the behavior of a damaged ship in waves. Hashimoto et al. (2017) presented numerical simulations and experiments for forced roll motions and flooding test of a damaged Pure Car and Truck Carrier model. They also used a hybrid model as Gao et al. (2013) combining a potential-flow solver with a Moving Particle Simulation. CFD has emerged as an important complementary tool in the study of damaged ships. Nevertheless, full-scale time domain simulation is still complex and extremely time-consuming.

1.3 Present work

1.3.1 Objectives

Many of the experimental studies mentioned in section 1.2 focus on the transient flooding cases, survivability in damaged conditions and time to flood measurements. Some studies discuss free-roll decay tests and effect of various parameters on roll damping behavior of a damaged ship. Studies like Korkut et al. (2004), Begovic et al. (2013, 2017), Acanfora and De Luca (2016, 2017) and Gu et al. (2018) focus on the dynamic behavior of a freely-floating stationary damaged ship in waves at its equilibrium position after flooding has taken place. In fact, though the most important phase is the initial transient flooding, it is also important to study the behavior of a floating damaged ship in waves. The former phase usually governs whether or not capsizing takes place, the latter will help in decision implementation on evacuation or in guiding the ship safely to the nearest port. Therefore, the present work analyzes behavior of a damaged ship in wave as compared to the intact condition with specific focus on effect of sloshing and piston mode resonance in damaged condition. To the knowledge of the author, no experimental studies available in literature focus specifically on sloshing and piston mode resonance frequencies for a damaged ship and the effect of sloshing and piston modes occurrence on damaged ship motions in waves. This is one of the main goals for the present work, taking the numerical work by Kong and Faltinsen (2010) as inspiration and extending in more detail the sloshing studies performed by de Kat (2000), Acanfora and De Luca (2016, 2017).

Study of transient flooding cases, where the model experiences sudden abrupt flooding, has also been targeted in the present study. This is important to analyze how transient flooding occurs in waves as almost all available literature provides data on transient flooding in calm water. Bennett and Phillips (2017) performed transient flooding tests and showed the effect of abrupt flooding on ship motions in waves. In this case, a mechanism where damage openings are initially sealed and can be opened suddenly to simulate transient flooding, was employed. In the present case, due to a larger opening and due to restrictions in the wave flume, such a mechanism could not be simulated. Instead, a scenario where the model is initially dry, and flooding takes place due to the ship motions was examined. Soon after the model opening gets exposed to external water, flooding occurs. This was

likely the case with Estonia (1994). Transient flooding is, however, associated with scale effects. Katayama et al. (2005) concluded that transient flooding stage does not follow Froude-scaling. They also reported that time to reach the maximum heel angle depends on model scale. Model scale has to be varied to analyze the scale effect. This is out of scope for the present work. The focus of the present transient flooding experiments is to qualitatively assess the effect of loading, wave steepness and wave periods on flooding behavior.

Finally, the present work aimed to perform a synergistic research strategy, complementing the data from aforementioned experiments with theoretical and numerical results. In this regard, simplified theoretical formulations, potential flow solvers and CFD solvers have been identified to cross check the model tests and contribute in the physical investigations. The primary focus was on open-source CFD solvers, OF, in this case. These solvers are particularly advantageous due to the availability of large number and type of utilities for pre-processing, solution and post-processing of CFD problems. In addition, easy implementation of user-defined routines makes them very valuable for developers and researchers. Also the use of a hybrid scheme, coupling a potential-flow solver with a viscous solver, was attempted.

1.3.2 Main Contributions

The main contributions from the present work involve experimental and theoretical/numerical analysis and are outlined below. Main findings for each examined scenario are documented in detail in chapters 3-5 and summarized in chapter 6.

Experimental Work

A detailed series of experiments were performed on a ship section (designed as a midship section of simple shape) in intact and damaged conditions with predominantly 2D flow conditions. The tests were designed and executed by the author over a period of 8-10 weeks and examined the effect of many parameters. This helped to identify the critical aspects governing flooding behavior/phenomenon. More in detail:

- Forced heave motion experiments were performed for the model in intact and damaged condition. Two waterlines and three filling levels were tested for the intact and damaged scenario, respectively. For the damaged condition, airtightness in the damaged compartment and effect of change in damage-opening size were also examined; the results demonstrate the effect of sloshing and piston mode resonance on the hydrodynamic added mass and damping coefficients. As an example, a selected case is shown in figure 1.3 to highlight importance of some of the the physical parameters analyzed. More in detail, figure 1.3 presents forced-heave motion results for the ship section in intact, damaged ventilated and damaged airtight conditions. The results refer to a waterline/filling level of 14 cm at a forcing frequency of 2.4 rad/s and forcing amplitude of 5 mm. The dynamic force shows a significant difference between the intact section and the section with ventilated damaged compartment. The forcing frequency is close to the calculated values of piston mode resonance. Therefore, the difference is mostly due to the

effect of piston mode resonance which is associated with a large water flux in/out of the damaged compartment. This is confirmed by the oscillations of the free-surface elevation inside the damaged compartment, given in the right plot of figure 1.3. The oscillations amplitudes are substantially reduced in the case of the airtight compartment, also documented in the plot. This explains why the damaged airtight compartment gives almost equal force as the intact section (see left plot of figure 1.3).

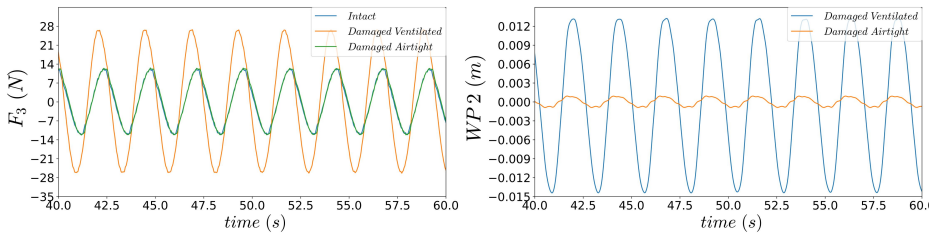

Figure 1.3: Forced heave motion experiment results: Dynamic heave force (left) and free-surface elevation in damaged compartment (right) for intact and damaged section in ventilated and airtight conditions

- Free-roll decay tests in intact and damaged conditions were performed. For these tests, the loading condition, damage-opening size and airtightness in the damaged compartment were varied. Damage condition leads to increase in damping and natural roll period.
- Tests were conducted with freely-floating model in beam-sea waves for the intact and damaged model. The damage opening always faced the weather side, i.e. it faced the incoming waves from the wavemaker. Effect of change in loading condition, damaged-compartment size, airtightness in the damaged compartment and damage-opening size was studied. Roll motion is highly modified due to presence of damaged as compared to heave and sway motions. This effect is studied in detail and related to the occurrence of piston and sloshing mode resonances.
- Transient flooding tests were also performed with an initially dry model in beam-sea waves. Although it was limited in scope due to the simplified body shape and 2D conditions, few studies have been performed in such an analysis. Therefore, this can serve as an important basis for future studies. A simple approach, used to predict occurrence of flooding, provided reasonable agreement with experiments.
- Error analysis and repeatability tests (for selected cases) were performed.
- These tests can serve as an important database for validation purposes due to the simplified model design and setup.

Theoretical/Numerical Work

A variety of tools have been used: theoretical formulations; the linear potential flow BEM code, WAMIT; a NS solver implemented using OpenFOAM and a Do-

main Decomposition strategy. These tools served to verify and complement experimental results so to understand better the physical phenomena. More in detail:

- Theoretical formulations have been used to calculate sloshing and piston mode resonance frequencies. Theoretical formulations from Newman et al. (1984) for a submerged body in forced heave motion were modified to analyze a 2D damaged section. The effect of piston mode resonance was confirmed using this method and reasonable agreement was documented with the experimental results.
- WAMIT was used to model the 3D damaged experimental model and its results, in terms of the natural sloshing and piston mode frequencies were successfully compared against the experimental and theoretical values.
- CFD simulations using OpenFOAM were performed to cross-check and complement the experimental studies. A Numerical Wave Tank was setup and validated through comparison against simple diffraction experiments. Then, it was used to perform diffraction and radiation simulations within a simplified strip-theory formulation of the freely-floating damaged section. Overall, the agreement of results obtained from OpenFOAM for forced heave motion, free-roll decay and freely-floating body in waves, was reasonable when compared to the experiments.
- A 2D potential-flow nonlinear Harmonic Polynomial Cell (HPC) method was implemented and was coupled with a NS solver from OpenFOAM within a DD strategy. The DD is presented as an initial study to analyze the potential of a DD scheme in achieving computational savings while maintaining accuracy. Results for forced heave motion of a damaged ship section were compared against the experimental results and documented a reasonable accuracy.

Table 1.1 summarizes the contributions of the present work and important aspects are highlighted in bold font.

Topic	**Contributions / Increments to existing studies**
Experimental Work Forced heave motions	2D Model- **Effect of filling level, damage-opening size**. Detailed analysis for hydrodynamic loads with respect to **occurrence of sloshing and piston mode resonances. Effect of airtight compartment** and damage-opening size studied
Free-roll decay tests	3 DoF model- Detailed analysis of damping for damaged condition with ventilated and **airtight compartment, effect of change in loading conditions** and damage-opening size studied. **Damping for a closed internal tank versus a tank**

	with a damage opening was studied to highlight the effect of damage opening
Freely-floating model in waves	Assessment of 3 DoF motions in damage condition focusing on **effect of sloshing and piston mode resonance. Effect of loading and airtight compartment analyzed in detail**. Also studied, effect of asymmetric damage and damage-opening size
Transient flooding tests	3 DoF model with half-compartment damage (asymmetric damage) condition in beam-sea waves. The damage lies above the floating waterline. **Effect of loading, wave height and wave period** on flooding behavior presented
Numerical Work Theoretical formulations	Calculated **piston mode frequencies and loads** for a 2D damaged section in forced heave motion by **extending formulation from Newman et al. (1984)** demonstrating good agreement with the experiments
WAMIT	3D Model, mainly used for verification of sloshing and piston mode resonance frequencies
CFD	Verification of OF as a reasonable solver for complex studies. **Simplified Strip theory using a NS solver to simulate damaged ship** motions in waves
DD	**Preliminary study of a DD scheme** for a simple forced heave motion case **using newly proposed HPC and the OF solver**

Table 1.1: Summary of main contributions from the present work

1.3.3 Outline of the thesis

The thesis comprises of seven chapters and is structured as following:

Chapter 1 introduces the background and objective for the present work. A literature study is provided along with the main contributions from the present work.

Chapter 2 documents the experimental setup and conditions used in the present work. Description of the model, wave flume, test parameters, is given. Data acquisition and analysis techniques during and after the experiments, respectively, are examined. Detailed discussion is provided for possible error sources in the experiments.

Chapter 3 describes the theoretical and numerical tools used to study physical phenomena observed in the experiments. Calculation of the sloshing and piston

mode natural resonance frequencies is discussed. A brief background and setup of tools used in the present work (WAMIT and OpenFOAM) is provided. Validation and verification studies are discussed for OpenFOAM (OF) solver used in this work. Implementation of a simplified strip theory using radiation and diffraction loads from OpenFOAM solver is discussed.

Chapter 4 presents experimental results for the forced heave motions of a damaged section in calm water. Parameters such as filling level, damage-opening size and air-tightness in the damage compartment are examined. Effect of sloshing and piston mode resonance on the hydrodynamic coefficients is examined and compared to the intact condition. Theoretical and numerical results are presented to complement the experimental data.

Chapter 5 presents experimental results for the freely-floating damaged section in beam-sea waves. The chapter also documents the free-roll decay tests for both intact and damaged conditions. Effect of sloshing and piston mode resonance on damaged ship motions is examined in detail. Effect of damage-opening size, compartment size, air-tightness in damage compartment, loading condition, are examined. Scenarios of transient flooding in waves are also examined experimentally. Numerical results are documented to complement experimental data.

Chapter 6 provides the summary of the present work, as well as suggestions for future research on this topic. Additionally, a preliminary analysis of a domain-decomposition technique coupling a potential-flow solver with a viscous-flow solver is presented.

1.3.4 List of Publications

The following publications have been produced as a part of this doctoral study:

Conference Papers

- Siddiqui, M.A., Greco, M., Colicchio, G., and Faltinsen, O.M., (2018). Validation of damaged ship hydrodynamics by a Domain Decomposition Approach using the Harmonic Polynomial Cell method and OpenFOAM. Proceedings of the 33rd International Workshop on Water Waves and Floating Bodies.
- Siddiqui, M.A., Xu, H-L., Greco, M. and Colicchio, G., (2020). Analysis of Open-Source CFD tools for simulating complex hydrodynamics problems. Proceedings of the ASME 2020, 39th International Conference on Ocean, Offshore and Arctic Engineering.

Journal Papers

- Siddiqui, M.A., Greco, M., Lugni, C., and Faltinsen, O.M., (2020). Experimental studies of a damaged ship section in beam sea waves. Applied Ocean Research Volume 97.
- Siddiqui, M.A., Greco, M., Lugni, C., and Faltinsen, O.M., (2019). Experimental studies of a damaged ship section in forced heave motion. Applied Ocean Research, Volume 88, 254-274.

The following co-authored paper, where work on quad-tree refinement and effect of rectangular cells for the HPC method was developed as part of present work, is considered as additional background:

- Ma, S., Hanssen, F-C. W., Siddiqui, M.A., Greco, M., and Faltinsen, O.M., (2018). Local and Global Properties of the Harmonic Polynomial Cell Method: In-depth Analysis in Two Dimensions. International Journal for Numerical Methods in Engineering, Volume 113.(4), 681-718.

Chapter 2

Model Experiments

A series of experiments were performed in three sets on a prismatic hull form in a small wave flume between May-June 2017, September 2017 and September 2018. The main aim of the experiments was to examine the behavior in damaged condition, with emphasis on resonance phenomena of the floodwater in the damaged compartment, and also to provide data from clean test scenarios for numerical validation. The hull form was designed as a midship section of a Roll On/Roll Off (RO-RO) ship with rectangular damage opening on the starboard side and an intended scale ratio of 1:40. Each set of experiments was carried out with the same model in the same flume and focused on different experimental conditions. Firstly, forced oscillatory heave motion tests in intact and damaged conditions were performed to analyze the influence of the floodwater on the radiation loads. Secondly, free-roll decay tests were performed in intact and damaged conditions to understand the effect of floodwater on natural period and corresponding damping for roll motions of the model. For these tests, an additional damaged condition with the opening sealed after flooding (i.e. intact model with a partially-filled tank) was also studied. Lastly, a freely-floating model in intact and damaged condition was tested in regular beam-sea waves. The tests in waves focused on the flooded model after it reached an equilibrium condition. In addition, transient flooding tests were also performed. For this scenario, the model is initially dry with the damage opening above the waterline and subsequent flooding takes place due to model motions. Repetition tests for forced heave motion, free-roll decay and beam-sea waves were also performed. Video recordings, measurements of wave elevation inside and outside the damaged compartment, were carried out in all experiments. In the present chapter, the model, the flume, test conditions/parameters and experimental setup are described in detail. Additionally, experimental data and uncertainty analysis along with possible error sources are also discussed.

2.1 The Model

The model is designed as part of a midship section and location of the damage is chosen to be at the side. A midship side damage is generally considered critical, as

also stated in the *Stockholm Agreement*. It requires that if the worst damage (according to Safety-of-Life-at-Sea (SOLAS) 90 rules) lies outside ± 10% of the midship region, an additional model test with midship damage must be carried out. Chang (1999) has also demonstrated that the damage in the midship section is more critical in beam-sea waves as compared with aft part of a RO-RO vessel. A schematic view of the actual and Computer-Aided-Design (CAD) models with Cartesian coordinate system Oxyz and origin at the center of gravity (CoG) is defined in figure 2.1. Typically ships have a small cross-sectional gradient in the midship region. This allows for a two-dimensional study in the cross-sectional plane, with a consequent simplified experimental set-up of the problem. The model size along the width of the flume was kept slightly smaller than the flume breadth to achieve two-dimensional behavior in the experiments. In the damage scenario, the large clean compartment bottom can be assumed to be a simplified midship deck of a RO-RO ship (scale of 1:40) and is ,hereafter, referred to as compartment deck. In actual scenarios, compartments are not empty and contain machinery/cargo etc. which can locally modify the flow features. Permeability of Ro-Ro space is assumed to be 0.90 by SOLAS regulations. However, flow features (for example sloshing resonance) are associated with a scale equal to the compartment breadth. Thus, it is assumed that small cargo/permeability will not modify the flow behavior remarkably. Unless explicitly specified, in the examined cases the opening bottom was at the level of the compartment deck. This damage scenario is not compliant with the *Stockholm Agreement* which states that the damage should be of unlimited vertical extent. However, to achieve 2D behavior in the experiments, especially for resonance scenarios, and due to limitations in model construction, the damage was kept at deck level. The model is constructed using aluminum plates (all external plating), divinicell i.e. compressed foam (ballast region in the bottom), wood (overall structure) and plexiglass on the front side (compartment and model) for visualizing the floodwater. Main dimensions of the model and of the internal compartment are given in table 2.1. To achieve intact condition, a thin wooden plate was placed over the damaged opening and sealed watertight (using sealant).

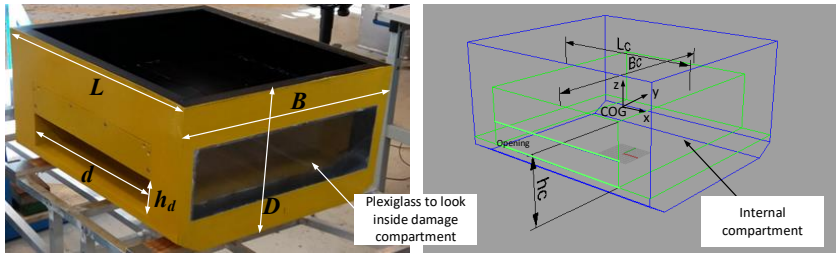

Figure 2.1: Model section (left) and damage compartment (right) with symbols

Swing tests in air were performed to estimate the roll moment of inertia about the x-axis and location of CoG for the intact model. This helped in distributing weight (solid ballast) to achieve the required moment of inertia and vertical distance of CoG from the keel (KG) of the model. They were distributed so to guar-

Description	Variable	Value
Length [m]	L	0.57
Breadth [m]	B	0.5
Depth [m]	D	0.3
Side damage length [m]	d	0.4
Side damage height [m]	h_d	0.08
Length of compartment [m]	$\mathrm{L_c}$	0.4
Breadth of compartment [m]	$\mathrm{B_c}$	0.5
Height of compartment [m]	$\mathrm{h_c}$	0.15
Height from keel to opening bottom [m]	h_o	0.05
Intended Scale	Λ	1:40

Table 2.1: Dimensions of the model and damaged compartment

antee an even keel condition for the floating model. The KG of the intact model is kept relatively low, in order to attain a relatively sufficient restoring moment even in the damaged condition. Inertia properties and hydrostatic parameters for the model in intact and corresponding damaged condition are provided for the two examined drafts (loading conditions) in table 2.2. The lost buoyancy method, as described by Biran and Pulido (2013), is used to calculate the parameters for the model in damaged condition. This is described in detail in appendix A. To assess the influence of the opening size in various experimental conditions, four different opening sizes have been studied as described in table 2.3. Two thin rectangular appendages were glued and sealed (using plastic sealant), one on each side of the opening (Figure 2.2). This reduces the horizontal width of the opening while the height of the opening was the same in all cases.

	Symbol	Intact Condition		Damaged Condition	
Loading condition		LC 1	LC 2	LC 1	LC 2
Draft [cm]	T_d	7	8.5	11	15.5
Dry mass [kg]	M	15.2	15.2	15.2	15.2
Solid Ballast mass [kg]	M_B	4	8	4	8
Vertical distance of CoG from keel [m]	KG	0.105	0.125	0.105	0.125
Roll moment of inertia about x-axis with ballast mass [kg m^2]	I_{44}	0.545	0.545	0.545	0.545
Transverse metacentric height [m]	GM	0.175	0.2	0.048	0.03
Static Floodwater mass [kg]	M_w	-	-	12	21

Table 2.2: Inertia and hydrostatic parameters of the model in intact and damaged condition

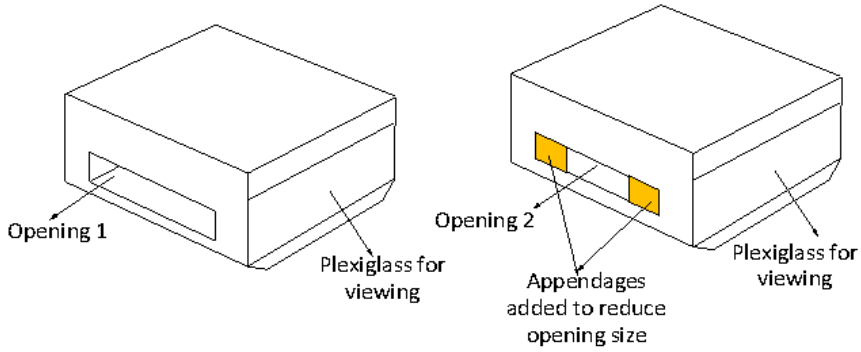

Figure 2.2: Sketch illustrating the change in damage opening sizes

Opening Name	Symbol	Width of opening [m]	Height of Opening [m]
Opening 1	O1	0.4	0.08
Opening 2	O2	0.3	0.08
Opening 3	O3	0.2	0.08
Opening 4	O4	0.28	0.08

Table 2.3: Damage openings used in the experiments

2.2 The Flume

The experiments were performed in the student wave flume, also called Lader Tank, at the Department of Marine Technology, NTNU, Trondheim. The flume is 15 m long, 0.58 m wide and 1.6 m high. This flume can be used to generate regular waves and perform model tests in two-dimensional (2D) flow conditions. The water depth can be varied in the flume. In the present experiments, we used water depth between 0.95-1 m. The exact depth for each test condition is described later in the text. The wave flume has plexiglass walls, which allows recording of waves/water interactions with the floating body. To study incident waves-body interactions, the flume is equipped with a flap wave maker on one end and a parabolic beach at the opposite end to absorb transmitted/radiated waves. For forced-oscillatory heave motion tests in calm water, the wave maker is kept fixed and a parabolic beach is added on its side.

2.3 Experimental Parameters

An intended scale ratio of 1:40 has been used for geometrical scaling. The velocities are scaled as the square-root, i.e. Froude scaling is followed. In case of airtight scenarios, another important parameter that has to be considered is the Euler number (see discussion in chapter 4). However, proper Euler scaling would require depressurized conditions and, even so, it is not straightforward to prop-

erly account for this (see e.g. Lugni et al. (2010b,a)). Depressurized conditions were not considered in the present study.

2.3.1 Forced Heave Motion Tests

Forced oscillatory heave motions were studied for the model in intact and damaged conditions. For the intact condition, two drafts were studied, whereas in the damaged condition, three drafts corresponding to three flooding levels inside the damaged compartment were investigated (see figure 2.3). Table 2.4 gives the details of the drafts in intact and damaged conditions. For the latter, the depth and mass of floodwater at equilibrium are also reported. Three forced-oscillation amplitudes and ten to fifteen forcing periods have been used for the model with different draft values. The examined forcing periods cover a wide range and are distributed non-uniformly with more periods studied in regions of resonant behavior of the floodwater in the damaged compartment, as identified in chapter 3. The experimental test matrix is given in table 2.5. For two filling levels (FL 2-3), effect of air compressibility in the damaged compartment was studied by using an airtight compartment. Lastly, the effect of changing the size of damage opening was examined. For these experiments, two opening sizes, O1 and O4, were used for the damaged condition.

Figure 2.3: Damaged section in forced heave motion at three filling levels

	Condition	Draft T_d [cm]	Flooding depth $(T_d - h_o)$ [cm]	Opening Condition	Equilibrium floodwater mass (M_w) [kg]
Waterline 1 (WL 1)	Intact	8	-	-	-
Waterline 2 (WL 2)	Intact	14	-	-	-
Filling Level 1 (FL 1)	Damaged	8	3	Partially submerged	6
Filling Level 2 (FL 2)	Damaged	14	9	Fully Submerged	18
Filling Level 3 (FL 3)	Damaged	16	11	Fully Submerged	22

Table 2.4: Drafts examined in the model tests with depth and mass of flooded water at equilibrium in the damaged conditions

Draft [cm]	Forcing Amplitudes (η_{3a}) [mm]	Forcing period (T_f) [s]	Condition
8	5	0.5 – 2.4	Intact
14	5	0.5 – 2.4	Intact
8	3,5,7	0.5 – 2.4	Damaged
14	3,5,7	0.5 – 2.4	Damaged
16	3,5,7	0.5 – 2.4	Damaged
14 (airtight)	5	0.5 – 2.4	Damaged
16 (airtight)	5	0.5 – 2.4	Damaged

Table 2.5: Test matrix for forced heave motions

2.3.2 Free-roll Decay Tests

Free-roll decay tests were performed to determine the natural roll period and corresponding roll damping of the model in both intact and damaged conditions. Table 2.6 shows the various conditions and parameters used in the free-roll decay tests. The initial non-zero roll angle varied for different conditions of the model. Exact values of initial angles were measured after image analysis. In general, at least two different initial angles for each condition were tested. Additionally, the initial heel angle used for the damaged condition were larger as compared to the intact condition. This ensured a suitable minimum number of roll cycles before the motion died out as roll damping is much higher in damaged condition. For these tests, a damage case with no opening, i.e. internal tank with no hull breach, was also investigated.

Loading Condition	Intact Condition	Damaged condition	Flooded tank with opening closed	Airtight compartment
LC 1	Yes	Yes	Yes	No
LC 2	Yes	Yes	Yes	Yes

Table 2.6: Test matrix for free-roll decay experiments

2.3.3 Freely-floating Model in Beam-Sea Regular Wave Tests

Tests in regular beam-sea waves were carried out on the freely-floating model section at zero speed in intact and damaged conditions. In the latter scenario, the ship section was allowed to attain a stable equilibrium in flooded condition before interacting with incident waves. Two regular wave steepnesses were used and wave periods were selected non-uniformly between T = 0.5 s - 2.5 s (at model scale), corresponding to 4-18 seconds in full scale (assuming a scale factor 1:40). The spacing between examined wave periods was selected to capture resonance phenomena of the floodwater in the damaged compartment, as for the forced heave motions. Here, the incident wave steepness is defined as kA, where $k = 2\pi/\lambda$ is the wave number, λ is the wavelength and A is the wave amplitude. Relatively low values of the wave steepness were examined because of limitations in the flume. More in detail, for the damaged condition, higher wave periods have to be tested as natural periods for a damaged ship section shift to higher values. Combining them with larger wave steepnesses would involve wave amplitudes

beyond the wavemaker limits. Also, larger wave steepnesses could lead to large motions and even capsizing of the model, with complications for the tests. This danger was identified for T =1.8 s and kA =0.1, when the model motions caused contact with tank walls. The freely-floating model in intact and damaged scenarios was examined for two selected loading conditions. Details for the two drafts are documented in table 2.2. Selected tests were also performed with the damaged compartment halved through placing a watertight plate at the centerplane of the damage compartment. This is referred to as half compartment damage and helps in analyzing the effect of asymmetrical flooding. In this scenario, draft at the opening side (h_1, as defined in right plot of figure 2.4), is used as relevant draft in the text. Table 2.7 shows the draft (h_1) for half compartment damage at the two examined loading conditions. Effect of change in size of the damage opening was examined for both full and half damaged compartment cases. The opening sizes and corresponding case names are given in table 2.3. Effect of air compressibility in the damaged compartment was examined by sealing all openings above the floodwater level inside the compartment. The examined conditions in beam-sea waves are summarised in table 2.8.

The transient stage of flooding was investigated for half compartment damage (side damage) in regular beam-sea waves. This is the most crucial phase in flooding and most capsizes generally occur during such a phase. Half compartment damage was used because it leads to larger roll motions with smaller amounts of floodwater. It also helped to avoid capsize and subsequent complication for the model tests. In these experiments, the model was initially freely floating and dry with freeboard of the damage opening above the draft waterline. In this case, the height of the damage opening (h_o , see table 2.1) was increased, using a small wooden plate, to 10 cm. This allows for sufficient initial freeboard (h_{fr}), so that flooding does not occur for all investigated parameters and their individual effect can be highlighted. In addition to the conditions defined earlier, two additional loading conditions, LC 3 and LC 4, were used for transient flooding tests (see table 2.9). Solid ballast weights were redistributed/added to attain required draft and GM. In addition to loading conditions (defined in terms of KG/GM), the effect of wave period and wave steepness was also examined. Loading LC 1 was used as basis to investigate the influence of incident wave steepness, ranging between 0.033 and 0.1, and incident-wave periods, ranging between 0.7 and 1.5 s. Following this, effect of the loading conditions was studied for kA = 0.066 and incident-wave periods 0.8-1 s.

Loading Condition	Full compartment damage draft [cm]	Half compartment damage draft (h_1) [cm]
LC 1	11	12.5
LC 2	15.5	16.5

Table 2.7: Draft for half compartment damage conditions

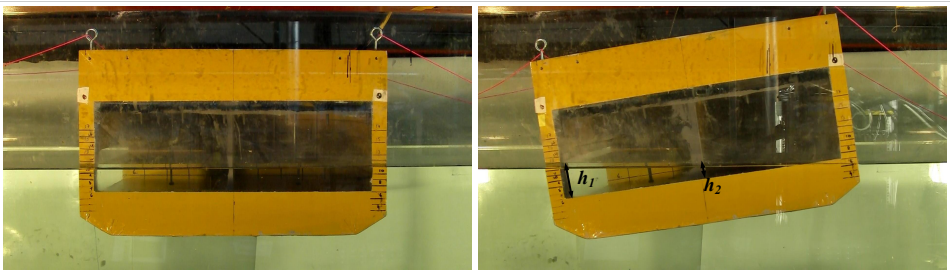

Figure 2.4: Freely-floating model at equilibrium in damaged condition for loading LC 1 with full compartment damage (left) and half compartment damage (right). (Here h_1 and h_2 are defined perpendicular to the bottom of the compartment)

Test	Wave period T [s]	Wave steepness (kA)	Condition	Compartment damage	Repetitions
Freely floating in waves (two drafts)	0.5 – 2.2	0.033	Intact	-	-
Freely floating in waves (two drafts)	0.5 - 2.5	0.033,0.066	Damaged	Full, half	5
Freely floating in waves in airtight condition	0.5 – 2.5	0.033	Damaged	Full	-
Freely floating in waves (three openings O1, O2, O3)	0.5 – 2.5	0.033	Damaged	Full, half	-

Table 2.8: Text matrix for the freely-floating model in beam-sea waves

Loading Name	Ballast (kg)	Draft [cm]	GM before flooding [m]	Freeboard h_{fr} [cm]	Wave Period [s]	Wave Steepness (kA)
LC 1	4	7	0.175	3	0.7-1.2, 1.5	0.033, 0.066, 0.1
LC 3	4	7	0.18	3	0.8-1	0.066
LC 4	6	7.8	0.2	2.2	0.8-1	0.066

Table 2.9: Loading conditions and associated parameters used for transient flooding tests

2.4 Experimental Setup

The setup and instrumentation in the flume varied slightly in each set of experiments. Common instrumentation and setup are described here, whereas specific features of each set are described in detail in the corresponding dedicated sections.

Instrumentation: A semi-automatic digital camera with a frame rate of 60 fps was used. Although the frame quality may have varied for some videos, the image quality was always at least 640x480 pixels. The height of the tripod stand used for the camera was calibrated and adjusted according to individual test programs. A trigger mechanism was designed and realized so to synchronise the measured signals with the video recording. Twin wire wave probes (WPs) were used to measure the wave elevation inside and outside the damaged model. The wire diam-

eter for the wave probes is around 1 mm. Two wave probes (WP 1 and WP 2) were placed, respectively, at 0.25 B and 0.75 B from the opening inside the damaged compartment. The wave probes extend from the compartment roof up to a distance of 5 mm above the compartment deck. In general , the measured wave elevation for these probes is water level relative to the initial water depth inside the flooded compartment. However, for transient flooding tests, the measured wave elevation is the water level above (relative to) the compartment deck. For the external field two/four WPs were used, the location of these WPs was modified depending on the test conditions, as shown later in this section. For these probes, the measured wave elevation is relative to the external mean waterline. Three accelerometers (Acc 1-3) were placed on the model to verify/complement the motion measurements from the videos. Figure 2.5 shows a top view of the model with location of wave probes and accelerometers. Estimation of accuracy for these instruments is provided in table 2.11.

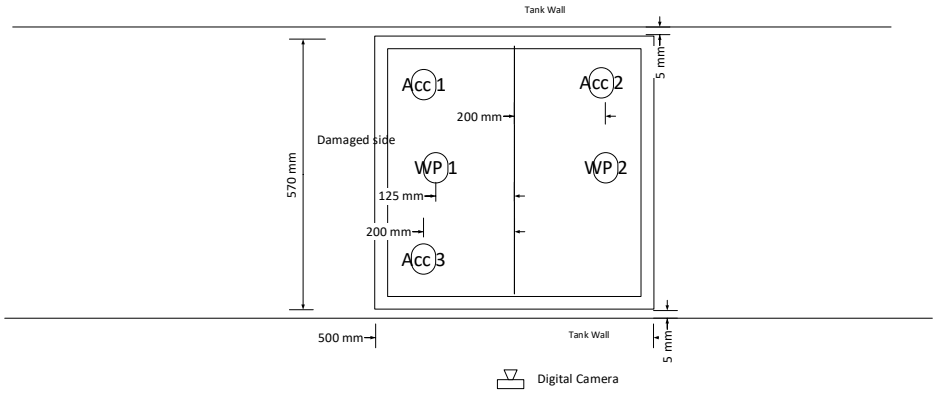

Figure 2.5: Sketch of the damaged section (top view) with location of wave probes and accelerometers (not to scale)

Parabolic Beach: A parabolic beach was used to absorb waves travelling to the end of the flume by inducing wave breaking similar to a real beach. As the waves approach the beach, the change in water depth causes the wave height to increase as compared to the wavelength. The waves become steeper until wave breaking limit is reached. This wave breaking leads to dissipation of wave energy. The beach is placed such that the highest point is $\sim$ 3-5 mm below the water surface. The horizontal and vertical extent of the beach are about 1.5 m and 0.9 m, respectively.

2.4.1 Forced Heave Motion Tests

Figure 2.6 provides a simplified sketch of the experimental setup for forced heave motions in the (y,z) cross-sectional plane. In this case, parabolic beaches were placed at both ends of the flume to absorb radiated waves. These tests were performed in calm water conditions with a water depth of 1 m and the model section rigged to a linear oscillator connected through a supporting frame. The sup-

port consists of two rigid aluminium beams bolted to a wooden plate which is screwed to the top frame of the model. This setup helped to achieve pure heave motions avoiding undesired roll/pitch moments. The linear oscillator is designed such that it generates steady-state oscillatory linear motions, with a ramp function at start-up and shut-down of each test. This is necessary to avoid damage of the oscillator and sudden jerk in the experiments. The exact ramp formulation is encoded directly in the oscillator operating software and, therefore, is not provided here. However, since the time-series for the heave motion of the oscillator is available, the time evolution of the ramp is known. The heave motion in steady-state conditions is assumed to be of the form, $\eta_3 = \eta_{3a}\sin(\omega_f t)$, where t is the time variable, $\omega_f = \frac{2\pi}{T_f}$ is the angular frequency of oscillation and η_{3a} is the heave amplitude.
Load cells were mounted on the oscillator to measure the force components in the y and z directions. The measurement set-up was the same as shown in figure 2.5, accelerometers (Acc 1-3) measured heave acceleration and were used to verify the actual heave motion with respect to the prescribed forced motion. WP 1 and WP 2 measured the free surface elevation inside the compartment while the general behaviour of floodwater was recorded using the camera described above.

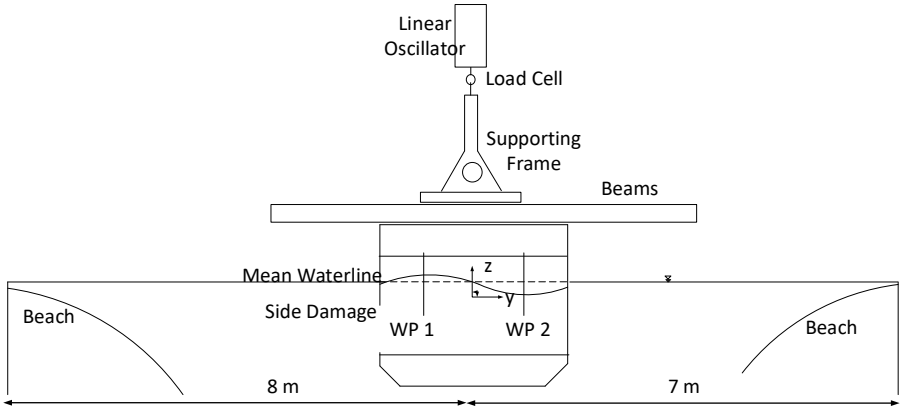

Figure 2.6: Sketch of the experimental setup (front view) for forced heave motion (not to scale)

2.4.2 Free-roll Decay Tests

The wave tank set-up for the free-roll decay tests was exactly same as for the forced heave motions (see figure 2.7) except that the model was free to oscillate after an initial non-zero roll angle and was not mounted to the linear oscillator. The model was allowed to drift freely without any moorings/restraints. This allows the model to be coupled with sway for the intact condition and with sway and heave for the damaged condition. However, the drift was limited since for almost all cases, the model remained inside the viewing range of the camera. The water depth was equal to 1 m. The instrumentation in the flume was the same

as shown in figure 2.5. For these tests, two wave probes were also placed in the external field: WP 3, 3 m upstream of the model and WP 4, 2.7 m downstream of the model (see figure 2.7).

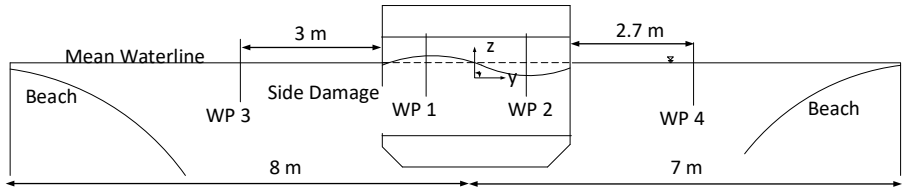

Figure 2.7: Sketch of the experimental setup (front view) for free-roll decay tests (not to scale)

2.4.3 Freely-floating Model in Beam-Sea Wave Tests

The setup in the flume for the model tests in beam-sea waves is shown in figure 2.8. The center of the model was at a distance of 8 m from the wavemaker. The damage opening faced the incoming waves in beam-sea condition. Two slack horizontal moorings were used to control drift in sway direction and also helped to restrict yaw motion, therefore, the model had three degrees of freedom in sway, heave and roll. It was ensured that the moorings had negligible effect on the natural roll and heave periods of the model. This setup allows the model to drift freely to a certain extent and, therefore, the sway and roll motion coupling can be captured. It also helps to keep the model in the viewing window of the camera. The drift velocity was analyzed and observed to be small enough to not affect the roll motion strongly.

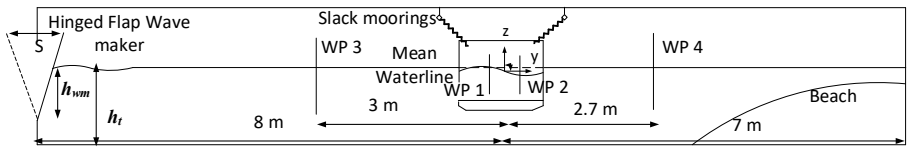

Figure 2.8: Sketch of the experimental setup (front view) for freely-floating model in beam-sea waves (not to scale)

Wave Generation in the Flume

Incident waves were generated by a flap wavemaker hinged at $h_t - h_{wm}$= 0.1 m from the bottom with a dry backside in water depth, h_t. Input signals for the flap motion were provided to a dedicated computer terminal. The motions of the flap are calculated using linear wavemaker theory which is described in detail in Dean and Dalrymple (1984) and briefly discussed here. For a wave period T and desired wave height H, Dean and Dalrymple (1984) provide a transfer function

for the required flap motion in terms of stroke S of the flap. The transfer function for a hinged flap wavemaker is defined in eq. (2.1).

$$\frac{H}{S} = \frac{4\sinh(kh_t)}{\sinh(2kh_t) + 2kh_t}\left(\sinh(kh_t) + \frac{\cosh k(h_t - h_{wm}) - \cosh(kh_t)}{kh_{wm}}\right) \tag{2.1}$$

Here, k is the wavenumber and the other variables are defined in figure 2.8. A linear ramp up function as described below is used during the first five periods ($5T$) of the flap motion S_f. Therefore, the latter is defined as

$$S_f(t) = \begin{cases} \frac{S}{2}\frac{t}{5T}\sin\left(\frac{2\pi}{T}t\right) & : t \leq 5T \\ \frac{S}{2}\sin\left(\frac{2\pi}{T}t\right) & : t > 5T \end{cases} \tag{2.2}$$

Preliminary Wave Calibration and Diffraction Tests

Prior to testing of the freely-floating model in beam-sea waves, calibration tests were performed to check the wave generation capability of the wavemaker and the wave propagation in the flume. The tests were conducted without the model, using four wave probes and a beach at the far end. In addition, diffraction tests were performed with the model rigged to the oscillator and locked in all degrees of freedom. The load cell on the oscillator measured the heave force on the fixed model in beam-sea waves. The distance of the model from the wavemaker was modified slightly for these tests. This is because the mounting frame was shifted to this location for other experiments in the flume and the same frame was used for rigging model to the oscillator. This is expected to have influence on the transient phase of the wave-body interactions, not the steady-state behavior that is examined in this study. The water depth (h_t) was also slightly lower, that is 0.95 m. However, this small change in water-depth is expected to have limited effects in the wave-body interactions. The setup is shown in figure 2.9. In addition to the wave calibration, the wave propagation and diffraction tests are important for numerical-validation purposes because the relatively simple setup helps to minimize experimental error sources.

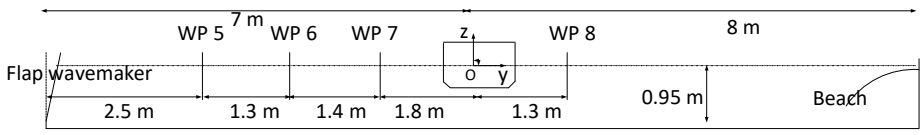

Figure 2.9: Sketch of the experimental setup (front view) for wave calibration and diffraction cases (not to scale)

The input signal to the wavemaker was verified by measuring the horizontal flap motion at a height of 1.6 from the tank bottom. An example is shown in figure 2.10 for wave condition, kA =0.033 and T =0.9 s. For this wave period at a water

depth of 1 m, the wavenumber is k= 4.97, leading to a wave amplitude A =0.066 m. Figure 2.11 shows the wave elevation at WP 5-8 in wave calibration tests.

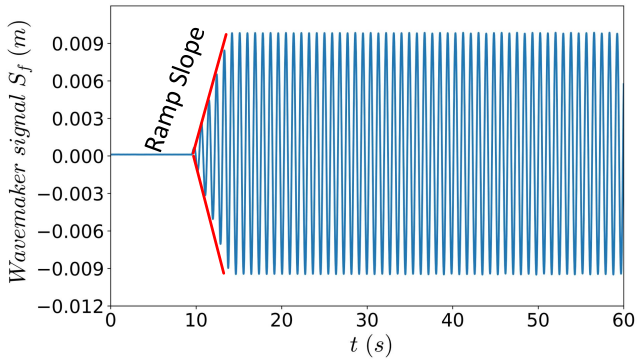

Figure 2.10: Flap motion measured at a height of 1.6 m from the tank bottom for T=0.9 s

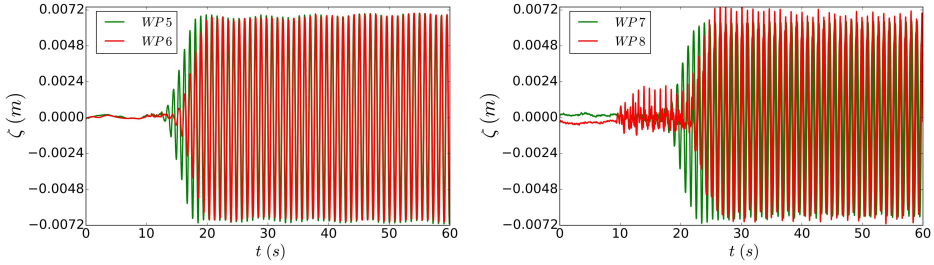

Figure 2.11: Wave elevation ζ in the flume for T= 0.9 s. The probe positions are defined in figure 2.9

Figure 2.12 shows the wave elevation amplitudes at the wave probes following a Fast Fourier Transform (FFT) analysis of the time series shown in figure 2.11. A peak value of $\sim$ 0.066 m (equal to the required steady-state amplitude) was measured for WP 5-6 at the main wave frequency, i.e. $\omega = 1/T = 1/0.9$=1.11 Hz. A very minor 3^{rd}-order frequency component was observed for these two wave probes. This third order component could be related to the wavemaker mechanism. A slightly lower peak value ($\sim$ 0.061 m) corresponding to wave frequency ω was observed for WP 7 and WP 8. A lower value was observed for these probes, probably, because of the larger energy distribution at higher order frequency components ($2\omega, 3\omega$,..). The higher frequency components have larger values for WP 8 as compared to WP 7. This is also visible from the right plot of figure 2.11. Similarly, wave calibration was performed for other wave periods.

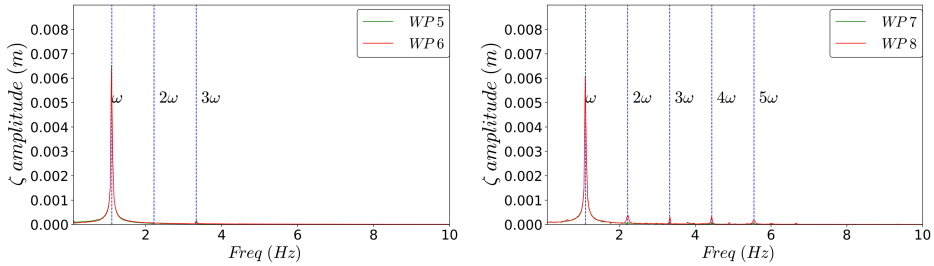

Figure 2.12: Wave elevation amplitudes for wave probes WP 5-6 (left) and WP 7-8 (right) following a FFT analysis of the time series shown in 2.11. Here, T= 0.9 s and $\omega = 1/0.9$=1.11 Hz

2.5 Data Analysis

Raw time histories of measurements are dominated by the main frequency, i.e. the incident wave frequency/forcing frequency, but also contain some high-frequency content of relatively smaller magnitude. This is mostly associated with noise from the instruments but can also be due to other effects such as excitation of super-harmonics (Faltinsen and Timokha, 2009). Therefore, the raw signals were low-pass filtered to remove frequencies above 10 Hz to remove high-frequency content above the third natural sloshing mode (inside the damaged compartment). The butterworth filter is employed and does not cause any significant phase shift or reduction in amplitude of the signal. The heave force amplitude and wave amplitudes at the wave probes inside and outside the compartment are measured by performing FFT analysis of the filtered time series data. The measurements used in the FFT analysis refer to the time interval after steady state is reached and before the effect of reflected waves from the beach becomes significant. Usually this corresponds to the time window from 30 to 60s, i.e. to a time interval of at least 10 periods for the highest forcing period examined. Figure 2.13 demonstrates a set of time series data recorded during the experiments with forced heave amplitude $\eta_{3a} = 5$ mm and forcing period $T_f = 1$ s. The data for heave force and wave probe WP2 in raw and filtered form (top and middle plots) and power density spectra of the raw and filtered data (bottom plots) are shown. It is observed that the signal for both measurements is centered at the input frequency, i.e. 1 Hz in this case. The raw heave force time series contains noise which is confirmed in the power spectrum showing energy content at higher frequencies. The heave force amplitude at the forcing frequency, however, is almost equal for the raw and filtered data. Therefore, it is demonstrated that filtering should not cause significant amplitude reduction for the frequency range examined in the experiments (0.4-1.66 Hz). The wave probe data (raw and filtered) do not contain much noise as seen from the time series and corresponding power spectra. The effect of reflections from the beaches is not strong for this case. For higher forcing periods, this may not be valid.

In case of free-roll decay tests and freely-floating model in waves, the motions of the model were calculated from analysis of the video recordings of the tests.

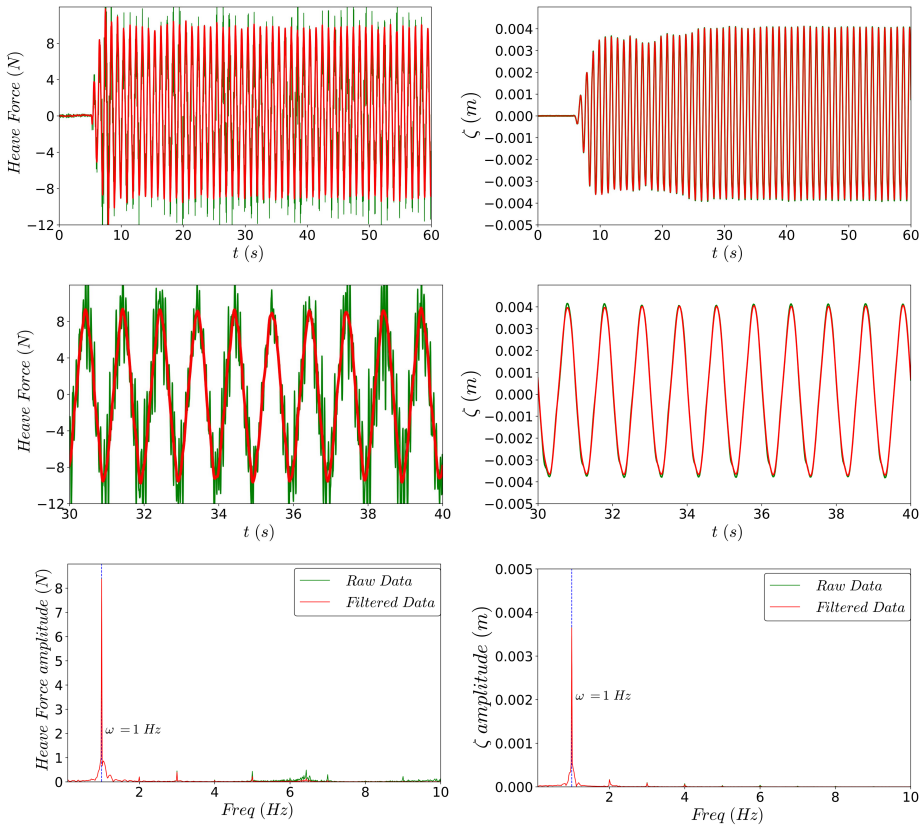

Figure 2.13: Time series for heave force (top left) and WP 2 elevation (top right) with enlarged view (middle plots) and power spectrum of heave force (bottom left) and WP 2 (bottom right) amplitudes, respectively, during forced heave motion test in damaged condition (FL 2), $\eta_{3a} = 5$ mm and $T_f = 1$ s

Two circular markers were placed at known locations (one on the port and one on the starboard side) on the front plexiglass side plate (yz plane) of the model facing the camera. Videos were processed to get a time series for sway, heave and roll motions using image-processing toolbox in MATLAB. Preliminary check was done for the camera setup and it was found that the error related to lens deformation was small. The correlation factor for pixel to mm was calculated to be 2.54 in y direction and 2.47 in z direction. For each incident wave period T, the steady-state amplitude of motions (sway, heave and roll) was obtained by taking mean of the absolute values of maxima and minima, for 5-10 T from the motion time series. Figure 2.14 shows an example of identification of marker points using image analysis at two time instants for the freely-floating damaged section in incident wave period of T =0.9 s, $kA = 0.033$ and loading condition LC 2. During the analysis, the wave probe data is first checked manually to exclude effect of wave reflection, especially from the wavemaker. The amplitudes of the wave probe elevations are

calculated using FFT as described above in this section.

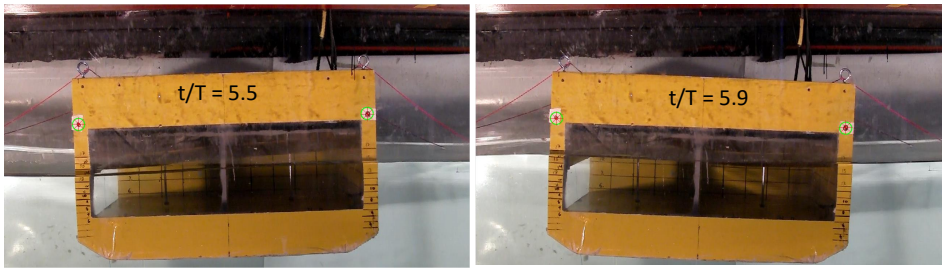

Figure 2.14: Example of motion calculation using marker identification. (Red markers represent identified marker locations at each time instant and green circles are filtered locations)

2.6 Error Sources and Analysis

Possible error sources in the present experiments are discussed here. This helps to control major errors and to ensure reliability of experimental data. Some error sources are hard to control but their effect on the experiments must be understood preferably quantitatively and at the very least qualitatively. Main error sources are divided into physical and instrumental error sources and discussed in following sections.

2.6.1 Physical Sources

Initial condition for the model and the flume has to be the same for each test. All tests were conducted with a calm water condition and the model completely at rest. Therefore, a waiting time of 4-10 minutes in between each individual test was allowed for all cases depending on the incident wave period.

Model loading (ballasting), especially in the damaged condition, has to be realized very carefully. In the damaged scenario, the model becomes very sensitive to even a small displacement of the solid ballasts. This can cause the model to have an initial heel or trim. It was ensured that the floating model was in even keel condition after every new loading setup by checking draft marks on all the four sides manually and with images. However, when large model motions occur, there is chance of displacement of ballast. This was minimised by checking regularly the draft marks and by repetition analysis. Model loading is also related to the error for the evaluation of the CoG and moment of inertia.

Seiching refers to the excitation of longitudinal sloshing in the wave flume with wavelength equal to twice the flume length. This is typically a shallow water wave associated with a small amplitude and is almost always excited after tests with long wave periods. It can take 3-6 minutes to damp out these oscillations after shutting off the flap motion. The natural seiching period ($\sim$10 s) is much higher

that the examined wave periods/heave oscillation periods. This large time-scale combined with allowing sufficient time interval between successive tests makes the effect of seiching minimal.

Transverse sloshing in the flume can be a possible error source. Standing waves can also be excited along the breadth of the flume at certain wave periods. The flume breadth is 0.58 m and at a water depth of 1 m, the first three natural sloshing periods are 0.87, 0.62, 0.504 s, respectively. We observed the second harmonic being excited at a wave period of 0.6 s, which is close to the second resonant period 0.62 s. At this period, the transverse sloshing can cause 3D behavior in the flume. For higher periods, transverse sloshing is not excited and, therefore, had minimal effect on the wave behavior in the flume.

Wave reflection inside the flume both from the beach/beaches and the flap wavemaker is a source of error. Using a simple group velocity estimation, we find that reflection can occur as soon as after 5 cycles for smaller frequencies. Quantitative analysis of wave reflection has not been performed. Ouelett and Datta (1986) have shown that a reflection of 10% is present even for well designed beaches and mentioned that for wavelengths larger than 0.75 the length of wave beach, it is nearly impossible to attain a reflection less than 10% from the beach. The latter corresponds to wave periods greater than 1.8 s for these tests. The wave absorption by the beach is generally less effective for longer incident wave periods. Reflection from the flap wavemaker is a potential error source and difficult to avoid because the installed automatic absorption system did not work as expected. Data with clear evidence of wavemaker reflection were disregarded.

Three-dimensional (3D) sloshing is observed inside the damaged compartment at smaller frequencies because the longitudinal mode (along x) is excited. In the external field, 3D effects can be present due to the small gap between glass flume walls and the model. These gaps are also associated with small viscous shear effects. In most cases, these forces are much smaller compared to hydrodynamic forces on the model.

Human error is an error source which is hard to specify and quantify. It is usually related with small errors and can be minimized by repetition tests. One possible example is measurement of the wave probes and model locations along the length of the tank. It is done manually with a metre scale and is always associated with some error ($\sim$1 cm).

Table 2.10 provides a summary of the physical error sources.

Error Source	Condition	Quantification
Model loading	After setup of new loading condition/ large model motion	Small if controlled
Seiching	Prominent after long wave/forced oscillation periods	Negligible
Transverse sloshing	Usually at resonant wave periods	Negligible except at T =0.6 s
Wave reflection	Prominent at larger wave periods but present in all cases	Negligible for T<1.3 s, non-negligible for T>1.5 s
3D effects	Always present	Negligible

Table 2.10: Summary of physical error sources with possible effects and conditions

2.6.2 Instrumental Sources

Calibration of instruments can lead to small errors. All instruments were calibrated by measuring standard physical quantities. A best-fit linear curve was plotted through these measured data to convert voltage measurements to physical quantities. However, there can be some nonlinearity associated with these calibrations factors. Also, prior to each test, the instruments were set to their respective "zero points". All instruments do not necessarily give measurements with a natural zero mean value. Therefore, mean value of real-time data being measured from the instruments (generally over a time window of 10 s) was calculated before the start of a test. This mean value is referred to as "zero point" and the measurements are then automatically recorded relative to this "zero point". This should ideally be performed before each test and at least every few hours because in some cases a drift occurs in this mean value due to voltage leakage. Also, a check was performed for the calibration factor every 2-3 days. It was also ensured that the output amplifier was adjusted so that the variation of physical quantities was in the middle of the output amplifier voltage. This was usually checked before the start of each test program.

Meniscus effect, caused due to surface tension, leads to "rise up" of water on the steel wires of the probes at the intersection of the probe wire and free surface. Faltinsen and Timokha (2009) mention a bias error less than or comparable to the steel-wire diameter (1 mm in our case). For test cases causing small free-surface disturbance inside the compartment, e.g. forced heave motion with 3 mm oscillation amplitude, the wave elevation may be too small and within the error range.

Heave actuator is also an error source in the forced motion tests. In some cases, especially at higher frequencies, it only attains 90-95% of the prescribed heave amplitude. The exact cause for this was not known. Also, it is strictly not an error source because we used the measured steady-state amplitude in the analysis and the forced heave motion reached steady state easily for each experimental test.

A summary of the uncertainty errors associated with instruments is provided in table 2.11.

Instrument	Error/uncertainty
Dynamometer [N]	0.75-1
Wave Probes [m]	0.001-0.002
Accelerometers [$\mathrm{m/s^2}$]	0.05-0.1

Table 2.11: Uncertainty in measurement for the instruments

2.6.3 Repeatability

Specific cases of forced heave oscillation tests, free-roll decay tests and model in regular beam-sea waves were repeated up to 3-5 times to assess test repeatability. This can help minimize/understand possible random errors (for example human errors). If a certain variable of interest is defined as x , the mean value ($\bar{x}$) and absolute deviation ($\Delta\bar{x}$) of x are estimated as

$$\bar{x} = \frac{\sum\limits_{N} x_i}{N} \quad , \Delta\bar{x} = \frac{\sum\limits_{N} |x_i - \bar{x}|}{N} \tag{2.3}$$

where x_i is the measurement for ith repetition and N is the total number of repetitions. An example of repetition test for forced heave motion in damaged condition at FL 2, forcing amplitude $\eta_{3a} = 5$ mm and forcing period $T_f = 1$ s is shown in figure 2.15 in terms of heave force and WP 2 elevation time histories.

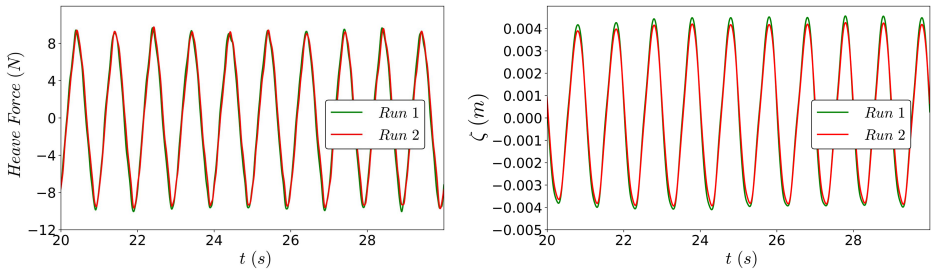

Figure 2.15: Heave Force and wave probe elevation (WP 2) for two repetition cases of forced heave motion in damaged condition, FL 2, $\eta_{3a} = 5$ mm and $T_f = 1$ s

The two runs were performed 3 days apart. We observe a very good agreement for the force and wave probe time series with a slight difference (<5%) in the maxima. The repeatability analysis of the experiments and related errors are discussed in detail for each test program in the corresponding chapters.

This chapter provides a detailed description of the setup and parameters employed for the experimental studies. Data analysis performed on the measurements from experiments is presented. In addition, a discussion of possible error sources and the related error values are discussed. Results from the experiments and associated discussions are provided in following chapters 3-5.

Chapter 3

Theoretical and Numerical Research Tools

This chapter describes the theoretical and numerical tools used in chapters 4, 5 and 6 to complement the model tests.

The first part of the chapter presents theoretical estimates for the resonance phenomena of the floodwater inside a damaged compartment. The experiments do not provide directly the values of natural frequencies for such phenomena. Therefore, a theoretical estimate of them and the knowledge on the resonance scenarios will help interpreting the experimental findings in terms of occurrence and relevance of resonance phenomena. A damaged ship is associated with two flow regions, the interior floodwater and the external sea environment connected through the damage opening. The focus is on the resonance in the internal floodwater domain. Resonance modes occur at specific (natural) oscillation frequencies of the internal floodwater motion induced by external, incident waves interacting with the vessel and/or by the ship motions. In the general scenario of a freely-floating ship in waves, the ship motions and the internal-liquid motion are coupled. Firstly, the resonance phenomena are examined in a general context and then in detail for the damaged-ship scenario. Theoretical linearized approaches to estimate the natural frequencies are outlined and applied to the case studies documented in chapter 2. The theoretical calculation of resonance frequencies for a damaged ship is complex and has been achieved using simplifications in the models. Effect of reducing the damaged compartment size and of air compressibility in the damaged compartment on the resonance phenomena is discussed. The effect of excitation of these resonance frequencies on loads/motions of the damaged section are discussed in later chapters 4, 5 and 6.

The second part of this chapter describes the numerical tools used in chapters 4, 5 and 6 to confirm the experimental findings and to help in the physical investigation of damaged-ship behavior. Firstly, linear potential flow theory (using WAMIT) is applied to estimate natural resonance frequencies for the damaged section. On the other hand, a damaged section involves non-negligible viscous and vortex-shedding effects especially at the damage opening. Therefore, a Computational Fluid dynamics (CFD) viscous solver implemented in the open-

source platform OpenFOAM (OF) has been selected to investigate the behavior of the damaged ship section and for cross-check of measurements and observations from the physical tests. A numerical wave tank (NWT) has been setup in OF for this purpose. Here, the numerical convergence of the results, the choice of grid types, mesh-motion techniques used for moving boundaries in OF and the effect of temporal evolution schemes on the results are examined for selected diffraction cases of the intact section in regular waves described in section 2.4. OF results are validated against the model tests. A nonlinear potential flow Boundary Element method (BEM) and a Navier Stokes level-set (NSLS) solver have also been used to simulate some of the diffraction cases for verification of the OF results and to complement the physical analysis.

In the last section of the present chapter, a strip theory formulation implemented in OpenFOAM is presented. It is used for estimation of motions for the freely floating damaged section in waves. These are compared against experimental results in chapter 5, showing reasonable agreement, and used as complementary research tool.

3.1 Theoretical Floodwater Problem Formulation

The internal domain (floodwater inside the damaged compartment) is associated with natural frequencies which can be excited due to the aforementioned factors, leading to floodwater resonance. The natural eigen-frequencies and eigenmodes are associated to nontrivial solutions for zero external excitation. The latter, assuming 2D potential flow of incompressible fluid, can be formulated as a boundary value problem (BVP) with corresponding velocity potential φ. In linear steady-state conditions with oscillation frequency ω, φ satisfies the Laplace equation up to the mean internal free surface, where

$$-\omega^2\varphi + g\frac{\partial\varphi}{\partial z} = 0 \tag{3.1}$$

applies as linearized combined free-surface boundary condition (FSC). Along the compartment deck and the non-damaged wall, the normal derivative of φ , i.e. $\partial\varphi/\partial n$, is known, and equal to zero due to the impermeability conditions (see figure 3.1). Here, ω represents the natural circular frequency of the floodwater and the vertical z- axis is positive upwards. The boundary condition at the opening determines the resonance scenarios, which can be categorized as sloshing and piston mode resonances. A wall condition ($\frac{\partial\varphi}{\partial n} = 0$) at the opening transforms the problem into the BVP for the *sloshing* modes of a partially-filled closed tank. Whereas, a zero-Dirichlet condition ($\varphi = 0$) corresponds to non-zero flux through the opening and leads to the BVP for the *piston* modes. As mentioned in chapter 1, Kong and Faltinsen (2010) numerically analyzed the importance of sloshing and piston mode resonance for a damaged ship. Their work has been used as inspiration and extended in detail here.

Sloshing is an internal resonant flow phenomenon associated with fluid motion inside partially filled closed tanks. It is relevant in various engineering disciplines such as aerospace (fuel tanks), civil (tuned liquid dampers for buildings),

transportation (tanker trucks) etc. Faltinsen and Timokha (2009) have provided a detailed theoretical background for several practical applications. In the field of marine technology, the main focus is on the effect of sloshing in partially filled tanks on vessel motions and vice-versa, and on the design of passive/active anti-roll tanks.

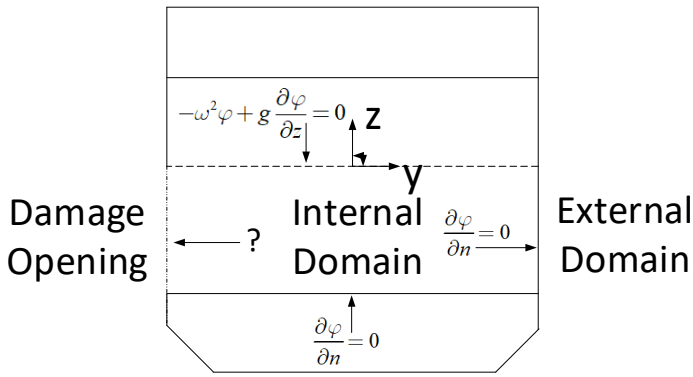

Figure 3.1: Internal flow problem in a 2D damaged ship section with homogeneous boundary conditions, assuming linear potential-flow theory and steady-state conditions

Piston mode resonance is generally associated with pumping modes in a domain with inflow/outflow through an opening. Two fluid domains (interior and exterior) are coupled through the opening. The pumping mode causes large free surface oscillations connected with large mass flow through the opening. This phenomenon is well known in harbor resonance, see for example Miles and Munk (1961). This has also been studied extensively for ocean vessels with moonpool operations, for example by Molin (2001), Faltinsen et al. (2007) and Fredriksen et al. (2014).

3.1.1 Sloshing Resonance Frequencies

Rognebakke and Faltinsen (2003) and de Kat (2000) studied the effect of sloshing on motions of a ship with a partially flooded closed tank (no opening) both numerically and experimentally. Many experimental studies mentioned in chapter 1 have considered the effect of sloshing on damaged ship motions. Most authors take into account the highest natural sloshing period in the damaged compartment, disregarding the others. This is adequate in general, but at shallower filling depths higher-order modes of sloshing can have significant effects as demonstrated in chapter 4.

Here, for the damaged compartment, the sloshing frequencies are calculated assuming negligible flow through the damage opening and then transforming the problem into a closed rectangular tank. It is demonstrated in later chapters that this assumption holds true by employing numerical simulations. Moreover,

sloshing along the breadth (y axis) is considered as the dominant sloshing direction. Therefore, a 2D clean rectangular damaged compartment with mean depth (filling level) h and length $\mathrm{B_c}$ is examined, as shown in the left of figure 3.2. A clean tank implies that the damaged/closed tank has no structures, for example baffles, fixed structures etc., and is consistent with the present experiments. The natural frequency of the $j-th$ sloshing mode is given by

$$\omega_{sj} = \sqrt{g\frac{\pi j}{\mathrm{B_c}}\tanh(\frac{\pi j}{\mathrm{B_c}}h)} \tag{3.2}$$

This equation is obtained by solving the linear, homogeneous boundary value problem shown in the right of figure 3.2 and finding the corresponding eigenfrequencies through enforcing non-trivial solutions of the resulting homogeneous equation system.

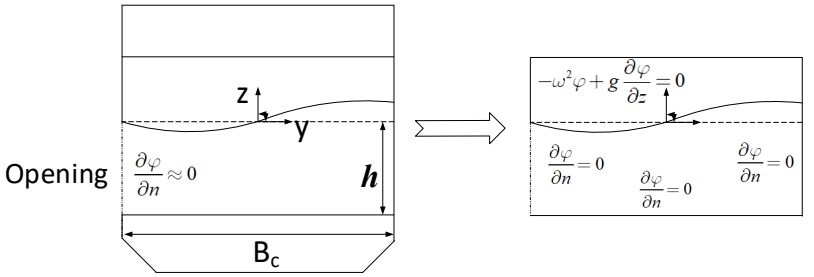

Figure 3.2: Damaged compartment with nearly zero flux at the opening and first natural sloshing mode (left) and corresponding linearized, homogeneous boundary-value sloshing problem (right)

The natural sloshing frequencies for the cases studied experimentally and defined in chapter 2 are documented in Tables 3.1 and 3.2. In particular, table 3.1 shows the non-dimensional sloshing frequencies for the first, second and third 2D sloshing modes, i.e. j =1, 2 and 3, for a full compartment damage condition in forced heave motion tests at different filling levels. In this table, and in the other of this chapter, the values in bold are those within the examined range in the various test conditions. One should note that, in general, for a closed partially-filled tank/compartment, the lateral motions (sway or roll) can excite sloshing resonance, while according to linear theory (Faltinsen and Timokha, 2009), the vertical motions (heave) cannot excite resonant sloshing. Therefore, the fact that forced heave motions excite similar resonance behavior may not a priori be expected. However, in the case of a damaged ship, as examined in this research study, the damage opening connects the interior and exterior water domains. The resulting pressure field at the opening (due to vertical motion of the body) behaves as a *nonlinear* external forcing and can excite resonant water motion in the compartment near the sloshing natural frequencies. Table 3.2 documents the non-dimensional sloshing frequencies for a freely floating model in waves with full compartment damage and loading conditions LC 1 and LC 2. In the case of incident beam-sea waves, both the induced ship motions and flow through the opening contribute

to the excitation of sloshing near natural frequencies. It must be noted that sloshing resonance occurs close to but not exactly at the calculated natural frequencies since the calculations are done for idealized flow conditions and assuming negligible flow through the damage opening.

Tests with half compartment damage of the freely-floating model were also studied. This condition causes the floating model section to have an initial heel angle. Therefore, sloshing resonance frequencies are modified due to change of tank breadth and due to inclination. They are calculated as described in Faltinsen and Timokha (2009) for an inclined closed tank with respect to the vertical direction. Figure 3.3 defines the parameters related to the half compartment damage section with an initial heel angle. Figure 4.17 in Faltinsen and Timokha (2009) describes the effect of inclination on natural sloshing frequencies in a tank using the ratios $(h - h_2)/h$ and h/l. Table 3.3 provides the non-dimensional sloshing frequencies for the first and second sloshing modes for inclined half compartment, along with the parameter values. It is concluded that the effect of inclination on first natural sloshing frequency is quite small. In fact, it is 98% of the natural frequency for a vertical tank with the same dimensions.Therefore, eq. (3.2) is sufficiently reasonable for the inclined-tank cases examined in the present experiments. It is to be noted that in the half-compartment case the tank breadth is $\mathrm{B}_c/2$.

Condition	h [m]	$\omega_{s1}\sqrt{\frac{B}{2g}}$	$\omega_{s2}\sqrt{\frac{B}{2g}}$	$\omega_{s3}\sqrt{\frac{B}{2g}}$
FL 1	0.03	**0.54**	**1.06**	**1.55**
FL 2	0.09	**0.89**	**1.6**	2.09
FL 3	0.11	**0.97**	**1.66**	2.14

Table 3.1: Non-dimensional sloshing resonance frequencies for the full damaged compartment in forced heave motion tests at all filling levels defined in table 2.4

Loading	h [m]	$\omega_{s1}\sqrt{\frac{B}{2g}}$	$\omega_{s2}\sqrt{\frac{B}{2g}}$	$\omega_{s3}\sqrt{\frac{B}{2g}}$
LC 1	0.06	**0.78**	**1.45**	1.99
LC 2	0.105	**0.95**	**1.65**	2.13

Table 3.2: Non-dimensional sloshing resonance frequencies for the examined freely-floating model with full compartment damage at two loading conditions defined in table 2.2

Loading	h_1 [m]	h_2 [m]	h [m]	h/l	$(h - h_2)/h$	$\omega_{s1}\sqrt{\frac{B}{2g}}$	$\omega_{s2}\sqrt{\frac{B}{2g}}$
LC 1	0.075	0.05	0.0626	0.25	0.2	**1.43**	2.39
LC 2	0.115	0.0782	0.0966	0.386	0.19	**1.62**	2.48

Table 3.3: Non-dimensional sloshing resonance frequencies for the examined freely-floating model with half compartment damage at two loading conditions defined in table 2.2, see figure 3.3 for definition of h_1, h_2, h and l

For a shallow filling depth ($h/\mathrm{B_c} < 0.1$), a phenomenon called *secondary* resonance can occur leading to excitation of *superharmonics*. Faltinsen and Timokha

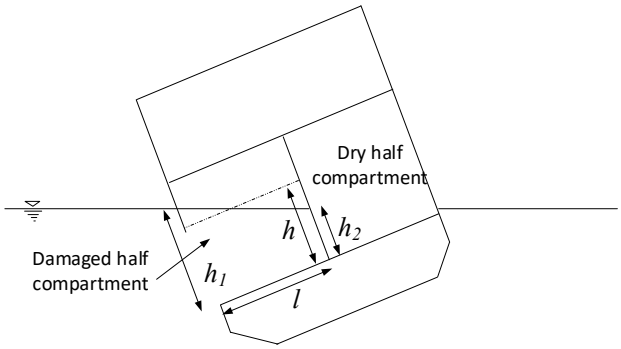

Figure 3.3: Model with initial heel angle due to half compartment damage along with parameters used for resonance frequency estimation

(2009) have described this in detail. Such resonance occurs when the higher harmonics are a multiple of the first natural sloshing mode frequency. For small $h/\mathrm{B_c}$, $\tanh(\pi j h/\mathrm{B_c}) \approx \pi j h/\mathrm{B_c}$, therefore, eq. (3.2) can be simplified as

$$\begin{aligned} \omega_{sj} &= \frac{\pi j}{\mathrm{B_c}}\sqrt{gh} \\ \omega_{sm} &= m\omega_{s1}\ , m = 2, 3, .. \end{aligned} \tag{3.3}$$

It implies that excitation near the lowest sloshing frequency can excite higher modes. This phenomenon is of a nonlinear nature and is the reason why at shallow filling depths, a large set of modes is needed to describe resonant sloshing at the lowest frequency (Faltinsen and Timokha, 2009). For filling level FL 1, $h/\mathrm{B_c} = 0.06$, and higher harmonics can be excited in the vicinity of the lowest sloshing frequency. This was observed for forced heave motion tests at FL 1 and will be demonstrated in chapter 4.

As mentioned above, in the present analysis the breadth along the y axis is considered the dominant sloshing direction. For completion, however, sloshing along the length of the compartment (x axis) must also be considered. In addition, three-dimensional (3D) sloshing can also be excited, i.e. modes along both length and breadth of the tank. To calculate the resonance frequencies for 3D sloshing, formulation for a 3D rectangular tank by Faltinsen and Timokha (2009) is used

$$\begin{aligned} \omega_{_{j,i}} &= \sqrt{g k_{j,i} \tanh(k_{j,i} h)}\ ; \\ k_{j,i} &= \pi\sqrt{\left(\frac{j}{\mathrm{B_c}}\right)^2 + \left(\frac{i}{\mathrm{L_c}}\right)^2}\ , i + j \neq 0 \end{aligned} \tag{3.4}$$

Here, j and i are the modes in y and x directions, respectively. 2D sloshing along the x direction implies j=0 and i=1,2,3.. These values are shown in table 3.4 for filling height corresponding to loading LC 1. The table also shows values of 3D

sloshing resonance frequencies with different modes along x and y directions for damaged compartment at loading LC 1.

h [m]	j^{th} mode	i^{th} mode	$k_{j,i}$	$\omega_{sj,i}\sqrt{\frac{B}{2g}}$
0.06	0	1	7.853982	**0.929111**
0.06	0	2	15.70796	**1.701359**
0.06	0	3	23.56194	2.288612
0.06	1	1	10.058	**1.165337**
0.06	1	2	16.91799	1.80304
0.06	2	1	14.81886	**1.623764**
0.06	2	2	20.11601	2.051184

Table 3.4: Non-dimensional 3D sloshing resonance frequencies at the filling depth of the damaged compartment with loading LC 1 defined in table 2.2

This loading condition is taken as an example because it corresponds to the lowest filling depth in the intermediate depth range for both forced heave motion and freely-floating tests in waves examined in the present experiments. At higher filling depths, resonance frequencies are much higher than the oscillation frequencies examined in the present tests. 2D second sloshing mode along x direction was observed in forced heave motion tests at filling level FL 2. Also, 3D sloshing was not observed for mode j, i =1,1 but the mode j, i =2,1 occurred at an oscillation frequency near the corresponding calculated natural frequency.

3.1.2 Piston Mode Resonance Frequencies

Kong and Faltinsen (2010) calculated lowest piston mode resonance frequency for a damaged ship using the formulation for a harbor presented by Miles and Munk (1961). One of the underlying assumptions is that $kC << 1$, where k is the wavenumber associated with natural frequency for a harbor with opening size C. This is not satisfied for the damaged section examined in the present experiments ($kC \approx 1.26$) and, therefore, cannot be employed here.

In this case, the damaged ship problem is simplified by using the analysis from Newman et al. (1984) who studied an external 2D flow problem for forced heave motion of a submerged rectangle close to the free surface. The sketch of the problem and the definition of the main parameters are given in the right of figure 3.4. They used matched-asymptotic expansions for the solution of the problem that coupled the flow above a semi-infinite rectangle, $d_T \rightarrow \infty$, with the flow in the outer region. The problem solved by Newman et al. (1984) implies a wall like condition at $y = 0$ and allows mass flux at the opening ($y = -b$). This means that there is an analogy between this problem and the case of damaged compartment with filling level FL 1 (left plot of figure 3.4). This can be seen by modeling the effect of the compartment side wall with a mirroring so that there is zero normal velocity at the wall position (see center plot of figure 3.4). Therefore, the solution of the submerged rectangle by Newman et al. (1984) can be used as basis to estimate the natural piston-mode frequencies at FL 1, and is discussed further. The details of

the derivation can be found in Newman et al. (1984), only the expressions needed for calculations and analysis in this case are presented here.

The edges of the submerged top of the rectangle have coordinates $z = -h$ and $y = \pm b$. On top of the rectangle the velocity potential is

$$\varphi = \frac{v_0}{K} + A\cos(k_0 y) \tag{3.5}$$

where $K = k_0 \tanh(k_0 h) = \frac{\omega^2}{g}$, v_0 is the amplitude of heave oscillation velocity, k_0 is the wavenumber, and h is the submergence depth. A time dependence $e^{i\omega t}$ is assumed in the analysis with i as the complex unit. After using matching conditions Newman et al. (1984) derived

$$A = -(\frac{v_0}{K})\,\{\cos(k_0 b) + (2/\pi)\,(k_0 h)\sin(k_0 b)\,[\ln(4Kh/\pi) + \gamma - 1 + \pi i]\}^{-1} \tag{3.6}$$

Here, $\gamma = 0.57721..$, is the Euler's constant. The undamped resonance frequencies are hereafter, referred to as the piston mode frequencies because of they are associated with large inflow/outflow and can be obtained by solving

$$\{\cos(k_0 b) + (2/\pi)\,(k_0 h)\sin(k_0 b)\,[\ln(4Kh/\pi) + \gamma - 1]\} = 0 \tag{3.7}$$

This equation follows by considering the real part of the expression in eq. (3.6) and calculating when its RHS goes to infinity with real v_0. Eq. (3.7) is an implicit equation and $k_0 b$ is solved for, which can then be used to compute the natural piston mode frequencies. It mus be noted that in the present case, $b = \mathrm{B_c}$.

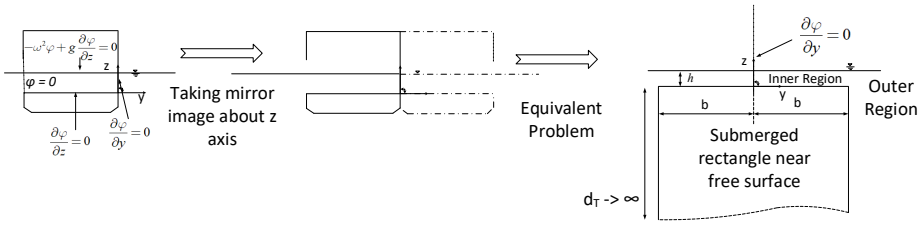

Figure 3.4: Equivalence of the damaged section case in the left (corresponding to filling level FL 1) with the problem of a submerged rectangle near the free surface in the right, through the mirroring process applied in the center

For filling levels FL 2 and 3, the inner and outer water surface are not directly connected to each other but are vertically separated by the left side wall plate of the ship model (see center and right plots of figure 2.3). The piston-mode condition at the opening can be approximated as $\varphi = 0$ (see left plot of figure 3.5), which corresponds to zero vertical velocity, i.e. it allows only horizontal flux through the opening. The effect of the opening and of the above plate can be modeled by mirroring the compartment about the opening side (see right plot of figure 3.5). This means that the natural piston-mode frequencies for the damaged compartment at these filling depths can be estimated examining a closed tank with double size of

the damaged tank and with a vertical baffle at the center as studied by Faltinsen and Timokha (2009). Piston modeshapes calculated from Newman et al. (1984), and reported in figure 3.6, demonstrate that at the opening $\varphi = 0$ is a valid approximation. A nodal line, implying zero vertical velocity, does not exist exactly at, but close to, the opening. Following the solution from Faltinsen and Timokha (2009), the effect of the baffle on the natural eigenvalues of the compartment plus its mirror image is given by

$$\frac{\omega_n^{'2}}{\omega_n^2} = 1 - \frac{\pi g \frac{\partial \varphi_n}{\partial x}^2 l_b^2}{2\omega_n^2 \int\limits_{\Sigma_0 + \Sigma_{0M}} {\varphi_n}^2 ds} \tag{3.8}$$

where $\omega_n^{'}$ is the modified natural frequency due to presence of vertical baffle, ω_n is the natural frequency calculated from eq. (3.7), φ_n is the velocity potential for the tank plus its image, Σ_0 and Σ_{0M} are the mean free surface in the tank and its mirror image, respectively, and l_b is the submerged length of the baffle. The modes with zero velocity potential at the centerplane of the fictitious tank are only considered because these correspond to piston mode resonance. The resonance frequencies for piston mode at all filling levels in the forced heave motion tests defined in chapter 2 are shown in table 3.5. It is observed that the effect of a baffle on the natural frequencies is small and is limited to a difference of 2 %. It must be emphasized that Newman et al. (1984) assumed an infinite depth condition for the outer region. In the experimental cases studied here, this may be valid for higher frequencies but at smaller frequencies finite depth effects are non-negligible. Therefore, the resonance frequencies calculated in table 3.5 should be taken as a close approximation for the present problem.

Condition	h [m]	l_b [m]	$\omega_{p1}\sqrt{\frac{B}{2g}}$	$\omega_{p1}{}'\sqrt{\frac{B}{2g}}$	$\omega_{p2}\sqrt{\frac{B}{2g}}$	$\omega_{p2}{}'\sqrt{\frac{B}{2g}}$	$\omega_{p3}\sqrt{\frac{B}{2g}}$	$\omega_{p3}{}'\sqrt{\frac{B}{2g}}$
FL 1	0.03	0	0.27	0.27	**0.73**	**0.73**	**1.23**	**1.23**
FL 2	0.09	0.01	0.3424	0.3418	**1.1809**	**1.1784**	1.874	1.8688
FL 3	0.11	0.03	0.3611	0.3564	**1.282**	**1.2605**	1.9768	1.9276

Table 3.5: Non-dimensional piston mode frequencies for the full damaged compartment in forced heave motion tests at all examined filling levels defined in table 2.4

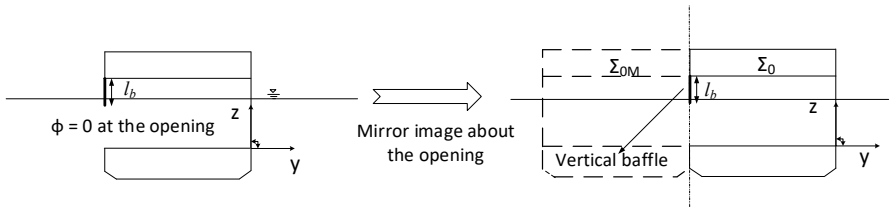

Figure 3.5: Equivalence of the damaged section case in the left (corresponding to filling levels FL 2 and 3) with the problem of a closed tank with a vertical baffle in the right, through a mirroring process

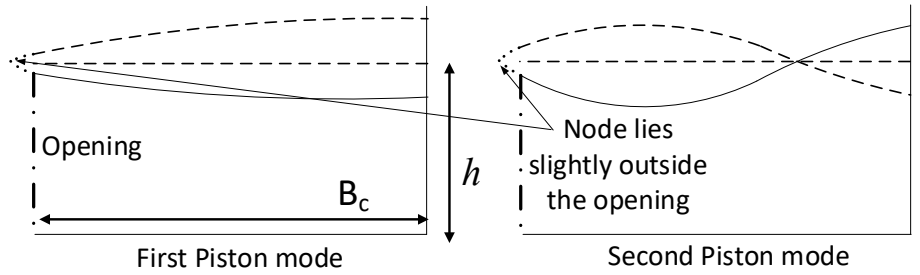

Figure 3.6: First (left) and second piston mode (right) calculated from Newman et al. (1984)

The aforementioned analysis can also be applied to calculate piston mode resonance frequencies for the freely-floating model condition in waves. The results for the cases studied experimentally are documented in table 3.6 and 3.7. Table 3.6 shows the non-dimensional piston mode frequencies for the first, second and third piston modes for a fully damaged compartment. Using a similar argument as that for sloshing in a half-compartment damage case, the effect of inclination on the natural frequencies is neglected. Table 3.7 shows the non-dimensional piston mode frequencies for the first and second piston modes for half compartment damage.

Loading	h [m]	$\omega_{p1}\sqrt{\frac{B}{2g}}$	$\omega_{p1}{}'\sqrt{\frac{B}{2g}}$	$\omega_{p2}\sqrt{\frac{B}{2g}}$	$\omega_{p2}{}'\sqrt{\frac{B}{2g}}$	$\omega_{p3}\sqrt{\frac{B}{2g}}$	$\omega_{p3}{}'\sqrt{\frac{B}{2g}}$
LC 1	0.06	0.3	0.3	**1.02**	**1.02**	**1.68**	**1.68**
LC 2	0.105	0.364	0.359	**1.257**	**1.24**	1.953	1.92

Table 3.6: Non-dimensional piston mode frequencies (with effect of baffle) for the examined freely-floating model with full compartment damage at two loading conditions defined in table 2.2

Loading	h [m]	$\omega_{p1}\sqrt{\frac{B}{2g}}$	$\omega_{p1}{}'\sqrt{\frac{B}{2g}}$	$\omega_{p2}\sqrt{\frac{B}{2g}}$	$\omega_{p2}{}'\sqrt{\frac{B}{2g}}$
LC 1	0.0626	**0.59**	**0.59**	2.06	2.06
LC 2	0.0966	**0.65**	**0.64**	2.215	2.2

Table 3.7: Relevant non-dimensional piston mode frequencies (with effect of baffle) for the examined freely-floating model with half compartment damage at two loading conditions defined in table 2.2

3.1.3 Resonance in Airtight Compartment

When the air exits above the floodwater level in the damaged compartment are sealed, an air cushion occurs above the floodwater (see sketch in figure 3.7). This air cushion can cause significant changes in behavior of inflow/outflow through the opening and thus affect the excitation of resonance in the floodwater. More-

over, it can undergo resonant conditions. It is considered that the pressure is uniform in the dynamic air cushion and the latter can be modeled as a mass-spring system where the air compressibility causes the spring effect and the mass comes from the generalized added mass associated with water oscillations generated by the air cushion oscillations (Faltinsen and Timokha, 2009). Assuming that the air cushion acts as a piston, Faltinsen and Timokha (2009) give a simplified formula for calculating its natural frequency as

$$\sigma_{nc} = \frac{2\pi}{T_{nc}} = \sqrt{\frac{4\kappa p_0}{\pi a^*_{33c} \rho \Omega_0}} \tag{3.9}$$

Here, p_0 is the static (i.e. with internal free surface at rest) pressure in the air cushion, ρ is water density, Ω_0 is the air cushion volume at rest, k is the ratio of specific heats. Finally, $a^*_{33c} = \frac{a_{33c}}{\rho\pi(\mathrm{B_c}^2/4)}$ is the non-dimensional added mass, with a_{33c} the added mass associated with water oscillations generated by the air cushion oscillations with a high frequency condition at the free surface outside the opening. If the undamaged wall on the right is considered as a symmetry plane for the flow and rest (deck and external body) of the structure is neglected, a^*_{33c} can be assumed as 1. This simplification is geometrically explained in center plot of figure 3.7. This leads to a natural period of air cushion oscillations at filling levels FL 2 and 3 in the model scale as $T_{nc} \simeq 0.05$ s and $T_{nc} \simeq 0.06$ s, respectively. It is expected that accounting for the complete structure (see right plot of figure 3.7) will lead to larger added mass values. For instance, as a rough estimate, assuming that the compartment floor has infinite extent gives $a^*_{33c} = 3.63$ and $a^*_{33c} = 2.93$ for FL 2 and 3, respectively. This leads to the upper limits of the air-cushion natural periods for filling levels FL 2 and 3 as $T_{nc} \simeq 0.095$ s and $T_{nc} \simeq 0.1$ s, respectively. The values for the freely-floating model at loading LC 2 are almost similar to those for filling FL 3. The examined forced-oscillation/incident wave periods are considerably higher than these natural periods, therefore, in the experiments the air-cushion acted as a stiff spring.

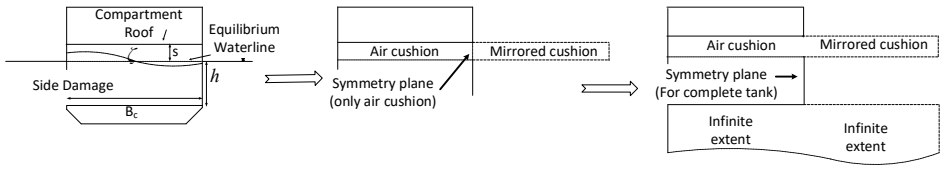

Figure 3.7: Simplification of an airtight flooded compartment for calculation of air cushion natural periods

The effect of this stiff spring is in the change in pressure (over-pressure) inside the damaged airtight compartment. This over-pressure leads to a modification in the internal FSC (eq. 3.1). The new condition can be derived similarly as Malenica and Zalar (2000) did by using Bernoulli's equation, continuity of pressure and assuming only vertical velocity at the internal free surface. It is assumed that $p_0 = p_a$, where p_a is atmospheric pressure at the time of air exits closure. It follows from continuity of air mass in the air cushion and using an adiabatic pressure-density

relation that the pressure in the air cushion is

$$p_{gas}\left(t\right) = p_0 \left[\frac{\Omega_0}{\Omega\left(t\right)}\right]^{\kappa} \tag{3.10}$$

when the instantaneous air cushion volume is $\Omega(t)$. Considering small air cushion volume change $\Delta\Omega = \mathrm{L_c}\int_{S_{FI}} \zeta dy$ with respect to the initial value Ω_0. Here, $\mathrm{L_c}$ is the length of the air cushion in the transverse model tank direction and the integral is along the internal free surface S_{FI} in the cross-sectional ship section plane. It means that 2D conditions in this plane are assumed. Furthermore, ζ is the internal vertical free-surface elevation relative to the mean filling depth. Using Taylor expansion about the configuration at rest, it follows that the dynamic change in the air cushion pressure $\Delta p = p_{gas} - p_0$, can be expressed as

$$\Delta p = -p_0 \kappa \mathrm{L_c} \frac{\int_{S_{FI}} \zeta dy}{\Omega_0} \tag{3.11}$$

The change in the pressure condition leads to a modified combined boundary condition for the internal free-surface as

$$\frac{\partial^2 \varphi}{\partial t^2} + g\frac{\partial \varphi}{\partial z} - \frac{\kappa p_0 \mathrm{L_c}}{\rho \Omega_0} \frac{\partial \int_{S_{FI}} \zeta dy}{\partial t} = 0 \tag{3.12}$$

Here, φ is the velocity potential describing the water flow in the damaged airtight compartment.

In the present experiments, the over-pressure (spring constant) for the air-cushion is very high. The consequence of the large over-pressure is that the integral $\int_{S_{FI}} \zeta dy$ in eq. (3.12) has to be very small. This is consistent with the occurrence of a pure sloshing mode, because for a sloshing mode $\int_{S_{FI}} \zeta dy = 0$. The last term in the LHS of eq. (3.12) becomes zero resulting in the combined linearized free-surface condition given by eq. (3.1). Therefore, sloshing mode can occur and its natural frequencies are not affected by the presence of air cushion in the compartment. For piston mode resonance, $\int_{S_{FI}} \zeta dy \neq 0$ and a significant change in volume occurs in the water inside the compartment. The high over-pressure does not allow for such a large volume change and thus piston mode resonance cannot be excited for the airtight case. These conclusions have been confirmed by the experiments with the compartment in airtight conditions, as documented in chapter 4.

3.2 Numerical Tools

Theoretical formulations used in WAMIT and OpenFOAM are well established in literature. Therefore, only the necessary details required for implementation of the software/method in the present study are described in this section. The description of the OF solver will also serve as a basis for the Domain Decomposition technique proposed in chapter 6 and appendix C.

3.2.1 WAMIT

WAMIT is a well established 3D panel method used to estimate motions/loads and corresponding natural resonance periods for ship/offshore structure with zero forward speed, for example as shown in Newman and Sclavounos (1988), Newman (2018). It has been validated extensively for engineering calculations over the past decades. For the present study, first-order WAMIT module, which assumes linear potential flow theory, is employed. Linear free-surface and body boundary conditions along with far-field radiation condition are enforced to solve the BVP for velocity potential through use of the Green function, see e.g. Lee and Newman (2004). A harmonic time-dependence is used and, therefore, a frequency domain solution is obtained with the numerical boundary element method (BEM). Linear potential flow theory implies that the seakeeping problem is divided into radiation and diffraction problems, i.e. the total velocity potential is sum of the radiation (φ_R) and diffraction (φ_D) fields. The diffraction component is composed of incident wave potential (φ_I) and the scattered disturbance (φ_S) of incident field from the fixed body. Following this, WAMIT returns hydrostatic data, eg. submerged volume, longitudinal and transverse metacentric heights, etc., and hydrodynamic parameters, eg. added mass/damping coefficients, Response Amplitude Operators (RAOs), free-surface elevation, etc., as output. A detailed description of the theoretical framework can be found in Lee (1995). WAMIT does not include viscous damping and effects like vortex shedding, which are very crucial for the present study of a damaged ship section. Therefore, the use of this tool is limited to the estimate of the natural resonance frequencies in the floodwater. This provides a cross-check of the values obtained from simplified theoretical models documented in the previous section.

One of the inputs required by WAMIT is the geometrical description and discretization of the body in ".gdf" format. Linear free-surface boundary conditions are implemented, therefore, only the portion of the body below the mean waterline is discretized. For a damaged ship section, the geometry has to be specified carefully because a floodwater free-surface exists inside the body. To tackle this issue, Kong and Faltinsen (2010) introduced a method where the external hull surface and the flooded compartment were defined separately using the "Hull-Reshaped Method" (HRM). The details can be found in Kong and Faltinsen (2010) for a full scale ship with small side damage opening. In the present study, the model shape is simpler and, therefore, some approximations can be employed. Section 3.1.2 showed that the effect of the wall above the opening (baffle) is small, therefore, the baffle has been excluded in WAMIT simulations (see left plot of figure 3.8). This helps in simplifying the geometry description and avoids using the HRM method. The non-damaged compartment wall separates the internal (compartment) and external (hull) surfaces through a small thickness. In order to avoid numerical issues, the thickness used in the simulations is larger than in the physical ship-section model (see right plot of figure 3.8) and, in particular, set to $0.02B$. It will be demonstrated in this section that reasonable results can be obtained even after applying these approximations to the actual geometry.

WAMIT can handle two different discretization approaches, low-order and higher-order panel method. In the present case, the low-order method is em-

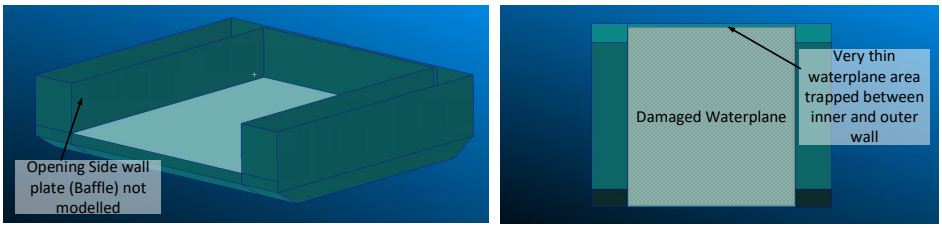

Figure 3.8: 3D perspective view (left) and top view (right) of geometric model used as approximation for the damaged ship section

ployed. In this case, the body surface is discretized with quadrilateral planar elements. The velocity potential over each panel is an unknown quantity (which has to be solved) and assumed to be constant over the panel. Therefore, the panel size on the body surface must be sufficiently small to achieve convergence depending on the examined frequency. Additionally, in order to ensure converged and reliable results, the following conditions must be satisfied:

1. Added mass and damping tensors with generic components A_{kj}, B_{kj}, respectively, where $j, k = 1, 2, 3..$ are the modes of motion, are symmetric without body forward speed, i.e. $A_{kj} = A_{jk}, B_{kj} = B_{jk}$
2. Damping coefficients $B_{kk} > 0$
3. External wave forces/moments calculated from scattering velocity potential must be equal to those calculated using Haskind relation (Newman, 1977)

Taking these aspects into account, three body discretizations are defined referred to as Coarse (708 panels), Medium (872 panels) and Fine (1072 panels) and the numerical convergence was examined for the damaged ship section with filling level FL 1. Left plot of figure 3.9 demonstrates "Medium" discretization for this filling level. One should note that, for a given discretization ($\delta x; \delta y; \delta z$), number of panels vary with filling levels due to change of the body wetted surface. As an example, right plot of figure 3.9, the "Medium" discretization for filling level FL 2.

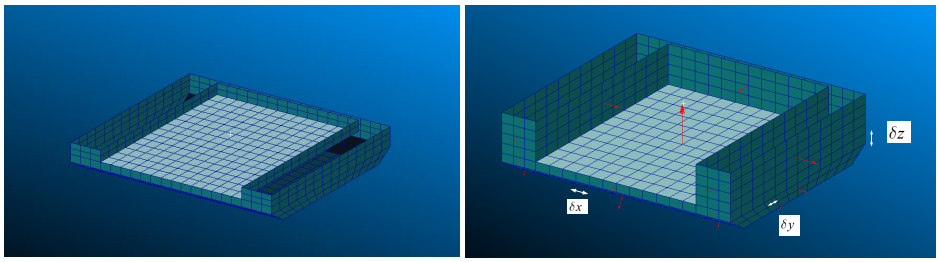

Figure 3.9: Panel model used for computation in WAMIT for FL 1 (left) and FL 2 with definition of body normal vectors pointing into the fluid (right)

Property 2 is satisfied for all discretizations. Property 1 is not satisfied perfectly by any of them, cases, whereas, property 3 is satisfied within a range of 5-10

% difference between the direct calculation of the scattering force and the value of the force from Haskind relation for the "Medium" and "Fine" discretizations. Figure 3.10 shows the heave damping coefficient for filling level FL 1 for the three panel sizes. The difference in the heave damping coefficient corresponding to the first piston mode frequency for "Medium" and "Fine" solutions is small ($\sim$ 10 %), whereas between the "Fine" and the "Coarse" solutions, a large difference ($\sim$ 20 %) is observed. Estimating the convergence ratio as $R_i = (B_{33,peak,Med} - B_{33,peak,fine})/(B_{33,peak,Coar} - B_{33,peak,Med})$, gives R_i=-0.65. This indicates oscillatory convergence (Roache, 1998) and needs more than three grid sizes to estimate order of accuracy. The main focus in these simulations is to obtain location and not exact values of peaks. Therefore, as a compromise between accuracy and CPU cost, the "Medium" panel size is used for all examined damage scenarios (i.e. various filling levels and freely-floating drafts).

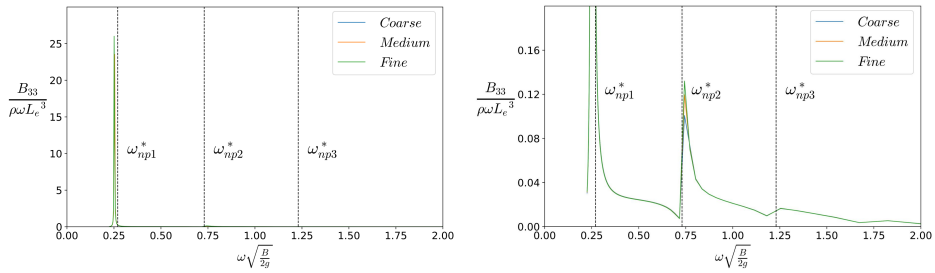

Figure 3.10: Left: Non-Dimensional heave damping coefficient as a function of non-dimensional frequency calculated by WAMIT with three panel sizes at filling level FL 1. Dashed lines indicate piston mode frequencies calculated in table 3.5. Right: Enlarged view

Figure 3.10 demonstrates that the frequency corresponding to the large peak in heave damping (left plot) is very close to the theoretically calculated frequency for the first piston mode (see in table 3.5). The enlarged view (right plot of figure 3.10) also demonstrates the occurrence of smaller peaks near the second and third piston mode frequencies. The difference between the frequencies estimated from WAMIT (frequencies corresponding to peak values) and the theoretical values in table 3.5 is less than 10 % for all the modes. Therefore, the theoretical values of piston mode frequencies are confirmed by WAMIT. The reason for the differences may be because the width of the damaged compartment is slightly smaller in WAMIT (98 % B), due to the larger thickness needed at the non-damaged wall. For higher filling levels, as mentioned above, the baffle (opening side wall) is not modelled in WAMIT simulations and will lead to some differences in the frequency values when compared with theoretical results.

It is to be noted here that the heave damping coefficient from WAMIT does not show any peak or relevant change near sloshing resonance frequencies. This is because, as mentioned before, under linear potential flow theory assumption pure forced heave motion cannot excite sloshing. The effect of sloshing may be observed on other modes of motion and will be discussed in detail in chapters 4 and 5. Another important aspect to be examined is how WAMIT can model

the hydrodynamic effect of the side walls in the physical tank. This can be done substituting the walls with ship-section images. Theoretically, an infinite number of images is needed to recover the effect of the two side walls. Numerically, at least 12-20 image bodies should be used. This means a very large number of panels (to discretize the ship section and its images) implying high memory space and computing costs requirements. Another technique is to model thin-walled bodies to replicate physical tank walls up to the mean free surface and depth equal to the tank depth in experiments. They are assumed fixed in all degrees of motion (see figure 3.11). It means that the physical problem is solved as an equivalent problem with a free surface inside the damaged compartment, between the ship-section and the thin-walled bodies and outside the thin-walled bodies. Therefore, walls are modelled with a small thickness and discretized into panels (both inner and outer surfaces). In this way, the hydrodynamic effect of the tank side walls on the damaged ship section can be captured with much less number of panels, and therefore, less computational effort than using image bodies. Figure 3.12 shows the damping coefficient in heave with the thin-walled model of the side walls for filling level FL 1; the results without side-wall effect are also provided for comparison. A difference in the value of damping is observed but the difference in the value of the first three natural piston mode frequencies is less than 5% for the damaged section with and without modeling the tank walls. Therefore, it can be safely assumed that the natural frequencies can be estimated with almost the same accuracy without modelling the tank walls.

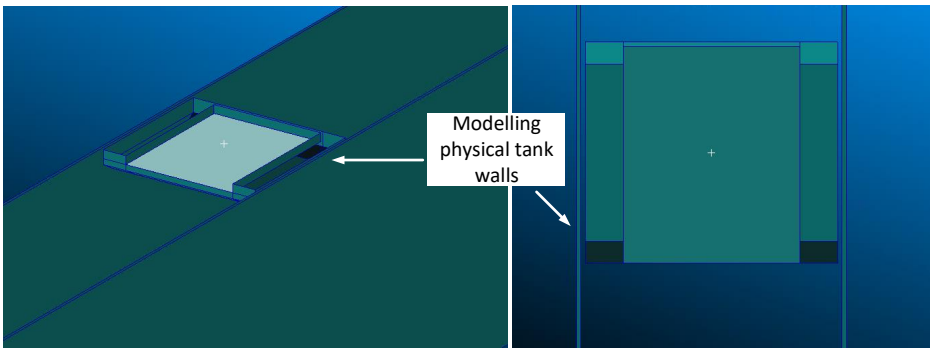

Figure 3.11: 3D perspective view (left) and top view (right) of geometric model along with tank walls

3.2.2 NS Solver using OpenFOAM

OpenFOAM is a widely used open-source environment for simulating complex fluid dynamic problems, developed initially by H. Weller, H. Jasak (Jasak, 1996). Numerous solvers and numerical schemes have been added by various authors in the recent years. The numerical discretization is based on the Finite Volume Method (FVM) and implemented in C++ templates. Some of the advantages are that the source-code is freely available, relatively easy to modify and well parallelized. However, in-depth knowledge and experience are required to setup

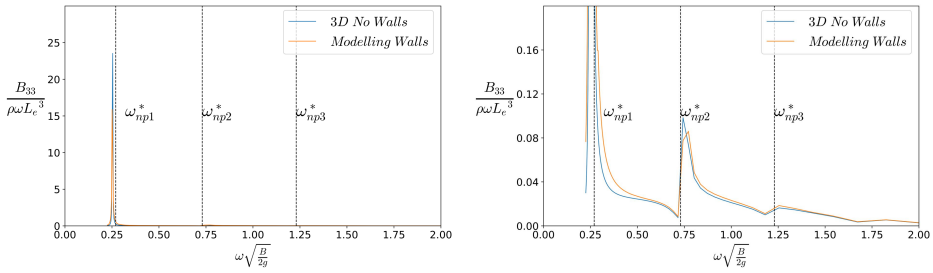

Figure 3.12: Left: Non-Dimensional heave damping coefficient as a function of non-dimensional frequency calculated by WAMIT with and without modelling physical tank walls. Dashed lines indicate piston mode frequencies calculated in table 3.5. Right: Enlarged view

solvers for specific problems due to limited literature. Detailed discussion on the formulation of Navier-Stokes (NS) equations,

$$\begin{aligned} \nabla \cdot \mathbf{u} &= 0 \\ \frac{\partial(\rho \mathbf{u})}{\partial t} + \nabla \cdot (\rho \mathbf{u}\mathbf{u}) &= -\nabla p + \nabla \cdot \tau + \mathbf{F}, \end{aligned} \tag{3.13}$$

on numerical discretization schemes and their solution techniques can be found in Versteeg and Malalasekera (2007) and Ferziger and Peric (2010). In eq. (3.13), $\mathbf{u}$ and p are the fluid velocity and pressure at the cell centers, τ is the stress tensor , $\mathbf{F}$ is the external force (including gravity) and ρ is the fluid density. To handle air-water interface evolution, an improved version of the original Volume-of-Fluid (VoF) technique (Hirt and Nichols, 1981), the Piecewise-Linear Interface Calculation (PLIC) scheme is implemented in OpenFOAM. This is handled by solving for an additional scalar quantity, the volume fraction α, which is governed by the phase equation,

$$\frac{\partial \alpha}{\partial t} + \nabla \cdot (\mathbf{u}\alpha) + \nabla \cdot (\mathbf{u}_r \alpha(1-\alpha)) = 0 \tag{3.14}$$

In eq. 3.14, $\mathbf{u}_r$ is called the compressive velocity field and is defined as $\mathbf{u}_r = \min\left[C_\gamma \frac{|\phi|}{|\boldsymbol{S}|}, \left(\frac{|\phi|}{|\boldsymbol{S}|}\right)_{\max}\right].\boldsymbol{n}$,where S is cell boundary face normal vector, ϕ is the volume flux across the cell face and C_γ is a coefficient for interface compression. This is an artificial convective term used to achieve a sharper interface between the fluids and, therefore, the compressive term, $\mathbf{u}_r(\alpha(1-\alpha))$, behaves such that it is non-zero only in cells containing both phases. Values of $C_\gamma > 0$ help to get a sharp interface but very high values can lead to reduction in accuracy. In the VoF method, eq. (3.14) must be solved along with eq. (3.13) and the constraint $\sum_{m=1}^{n} \alpha_m = 1$, where n is the number of phases. In the cases examined here, n=2; which means that water and air are treated as phases of a single fluid with properties (density, viscosity, etc.) varying across the air-water interface. Therefore, the

momentum equations are solved for a single fluid throughout the domain and the air-water interface conditions are automatically fulfilled.

In-depth details for implementation of Eqs. (3.13),(3.14), related quantities and solution procedures in OF can be found in OpenFOAM (2019).

NWT Setup and Settings

A viscous two-phase NWT is implemented in OF versions 1806/1812 to complement the experimental data and investigate other relevant phenomena. OF applies a FVM discretization on a hybrid collocated/staggered grid in the fluid domain. A second-order discretization in space is used for the fluid domain. The pressure-velocity coupled equations (eq. 3.13) are solved using the PIMPLE solver, which is a combination of SIMPLE (Semi-Implicit Method for Pressure-Linked Equations) and PISO (Pressure Implicit with Splitting of Operator) techniques. The last two schemes involve the solution of a Poisson equation for the pressure and are used within an iterative approach for an accurate solution of the Navier-Stokes equations. The inner iterations for the pressure correction from SIMPLE and the outer iterations for the pressure correction from PISO iterations are set to 2 for all simulations in the present case as they give converged results. The transport equation (eq. 3.14) for the phase fraction (α) is solved using the MULES (Multidimensional Universal Limiter with Explicit Solution) solver. For the time evolution of the discretized equations, three numerical schemes were investigated, namely first-order implicit Euler scheme, unbounded second-order backward scheme and second-order Crank-Nicholson scheme. An adaptive time-step is employed to ensure stability by enforcing the maximum Courant number (Co) to be 1 and the interface Courant number (Co_{pf}) to be 0.5. The Courant number is associated to the "Courant-Friedrich-Lewy" condition, which is a numerical constraint on the maximum allowed time step for particular flow-conditions and grid size. In the simulations, the time step usually varies and can reach values as small as 1e-05 s in the beginning of the simulations but gradually achieves constant values of around 0.0005-0.005 s depending on grid size and simulation parameters. These settings are used to ensure stability in the simulations and to avoid nonphysical behavior during the initial phase of simulations. All simulations are performed using laminar flow settings since the studied problem involves a section with nearly sharp edges and using turbulence models will not cause a large difference in the results. Additionally, all simulations are run on NTNU supercomputer VILJE (Intel Xeon E5-2670), using 2 nodes (32 cores) per simulation. Initial and boundary conditions used to model a specific physical scenario are described in the sections where OF results are used.

Mesh Generation and Motion

Both structured and unstructured meshes can be generated with OpenFOAM utilities. For simple body shapes and for general background meshes, a Cartesian structured hexahedral (hex) mesh can be generated using *blockMesh* utility. This is quite simple to use and requires definition of corners forming the hexahedral block along with the number of divisions in each of the three dimensions. *snappy-*

HexMesh is used for generating unstructured meshes, for complex body shapes, where the body surface intersects the background mesh arbitrarily. This utility first requires the generation of a computational domain larger than the body size in all directions. This domain (or background mesh) is usually generated using *blockMesh*. The body geometry is input in the form of a stereolithography format. The *snappyHexMesh* utility "snaps" the body surface onto the background mesh. "Snap" means that any background cell inside the body surface is removed and the cells near the body surface are aligned perpendicularly to the local surface normal vector and merged with this surface. Generally, this process involves refinement of cells near the body surface and cannot be performed with hexahedral blocks alone due to arbitrary shapes/curvatures. Therefore, prism/ tetrahedral (tet) shapes are also required and this results in unstructured meshes. The number of refinement zones, size of unstructured cells relative to the background mesh, number of prismatic layers near the body surface and overall quality of the mesh (e.g. maximum boundary face skewness, maximum concaveness allowed) are some of the important parameters controlled by the user in order to obtain a good mesh. There is no quantitative measurement of a "good" mesh, but the mesh quality is generally assessed by metrics such as skewness, non-orthogonality, aspect ratio etc. These quantities can be checked using the *checkMesh* utility after mesh generation.

A structured block hex mesh and a square unstructured mesh for the 2D intact ship section are shown in figure 3.13. A structured grid must be generated manually using available software (ICEM©) or the *blockmesh* utility whereas unstructured grids are generated automatically without much user intervention using *snappyHexMesh*, with the geometry of the body and relevant mesh parameters, required as input. However, structured grids provide better control in mesh generation, e.g. refinement only in regions where large flow gradients are expected. If a body shape can be generated using a structured mesh, they generally provide a more efficient computation as compared to an unstructured grid due to higher number of cells (because of automatic refinement near body surface) and poorer mesh quality (non-orthogonal and skewed cells) in an unstructured grid. A summary of the advantages and disadvantages for the two grid types is given in table 3.8. Additionally, an H-type (structured or unstructured) grid may not be suitable for all types of simulations. For example, a structured/unstructured O-type grid (see figure 3.14) may be better suited for forced roll motion and free-roll decay simulations. Therefore, mesh generation and mesh-type selection must be chosen depending on individual scenarios to ensure an accurate and efficient simulation. For individual simulations, the type of grid, i.e. H/O and structured/unstructured, along with the discretization parameters will be defined in relevant sections of chapters 4 and 5.

Features	Structured mesh	Unstructured mesh
User control	High	Low
Computation time	Generally low	Generally higher than structured grids
Generation Strategy	Manual, so challenging	With automatic algorithms, so easy
Applicability	Simple geometries	Any geometry

Table 3.8: Summary of structured *versus* unstructured grids

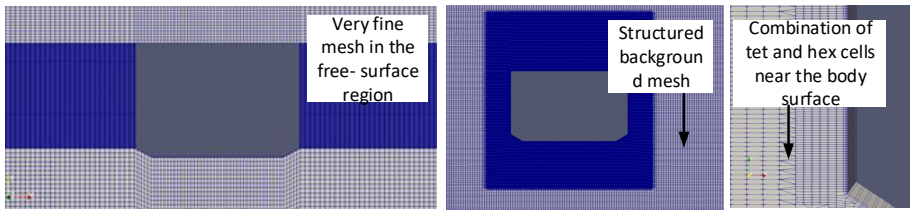

Figure 3.13: Structured mesh (left) and unstructured mesh showing details near the boundary surface (right) for the 2D intact section

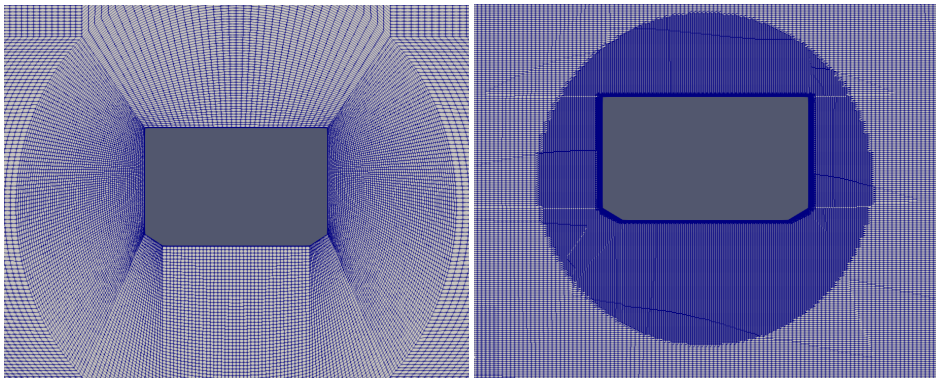

Figure 3.14: O-type structured (left) and unstructured (right) meshes for the 2D intact section

In the present study, moving rigid bodies have to be examined. OF employs various strategies under the Arbitrary Lagrangian Eulerian (ALE) formulation to allow for mesh motion and deformation (moving rigid bodies). The strategies, in general, can be applied to any CFD solver and fall into two categories: deforming mesh and rigid body motion techniques. Both strategies preserve the topology of the mesh, i.e., the number of cells and their connections (through planes/neighbour faces) is not modified. In the deforming mesh (DM) method, the mesh deforms to allow for body motions. In the rigid mesh motion strategy, the mesh moves with the body. This is applied in the "sliding interface" method and the overset grid (OG) technique.

Detailed analysis of various deforming mesh techniques and their implementation in OF is given by Jasak and Tukovic (2006) while the main features relevant for the present numerical analysis, are outlined here. In the present study, the *laplacianDisplacement* solver is chosen for implementing the deforming mesh method. The mesh motion for the entire domain is handled by solving the Laplacian equation for the mesh displacement, i.e. $\nabla \cdot (k_d \nabla \vec{d}) = 0$. Here, k_d is a diffusivity coefficient and $\vec{d}$ is the motion displacement vector for each cell. A quadratic distance-based diffusivity coefficient ($k_d = 1/r^2$) is employed, with r the minimum cell-center distance from the specified moving boundary. This implies that deformation decreases when moving further away from the boundary. However,

when the moving boundary undergoes large motions, large mesh distortion can occur (see left plot of figure 3.15) affecting accuracy and stability.

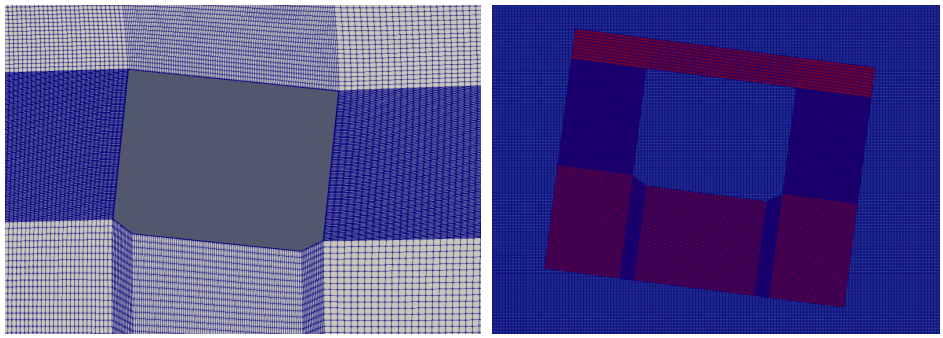

Figure 3.15: An example of deforming mesh technique (left) and overset and background mesh setup (right) for the 2D intact section

To avoid severe mesh deformation for simulation of large body motions, overset grid technique can be used (right plot of figure 3.15). Here, two grids are considered, a background mesh (generally structured) spanning the computational domain and a smaller body-fitted overset mesh. Only the overset mesh moves, undergoing rigid mesh motion, i.e. the whole inner mesh moves with no distortion. Fluid equations are solved on both grids and interpolation techniques are used for information exchange between the grids. The information is exchanged at two single celled layers, one for the background mesh at the border with the body (see grey layer in left plot of figure 3.16) and the other at the outermost layer of the overset mesh (see in right plot of figure 3.16). The former layer provides information from the overset to the background mesh and the latter layer provides information from the background mesh to overset region. Additionally, for proper exchange of information between the two grids, cell sizes in the exchange layers must be relatively similar, i.e. a size ratio between background and overset cells more than 2 should be avoided when possible. For the overset mesh, the region occupied by the body is empty, i.e. this mesh is boundary fitted, but cells exist in the background mesh inside the area occupied by the body. No fluid equations have to be solved here and they are denoted as ”hole” cells. Figure 3.16 shows an example of the body covered (hole) background mesh in red.
At each time step in the computation, the hole and interpolation layers are updated, as shown in figure 3.17. This additional process leads to a considerable computational overhead for the overset mesh as compared to the DM method. In the present study, presence of the water-air interface must be considered as the ship section is surface piercing. In the OF framework this means performing two-phase flow simulations with use of the VoF technique. In this context, one should note that the two-phase overset solvers implemented in OF have a first-order scheme for data interpolation between the grids and only first-order Euler scheme available for the time evolution. This represents an issue in terms of numerical accuracy and requires sufficiently fine meshes and small time steps. For the damaged scenario free-roll decay simulation and transient flooding cases,

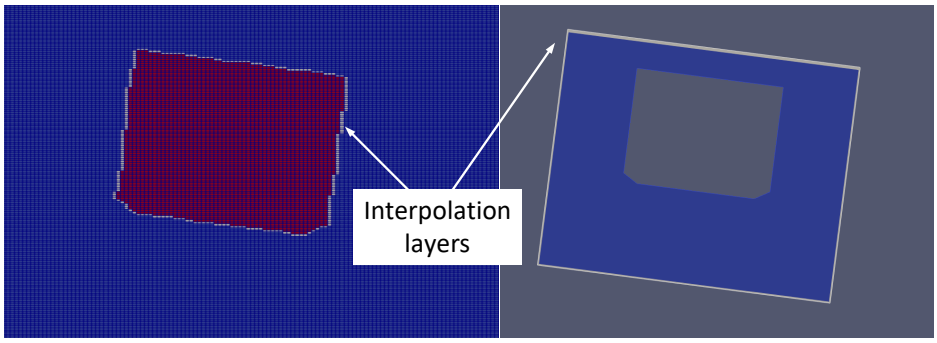

Figure 3.16: Interpolation layers with hole region for the background mesh (left) and interpolation layer for overset grid (right) of 2D intact section

2D simulations cannot be employed and, therefore, a 3D structured overset mesh (shown in figure 3.18) with a structured background mesh is used. The structured mesh in the overset region is generated using ICEM©. Additional mathematical details on the implementation of overset grids in OF can be found in e.g., Ma et al. (2018b).

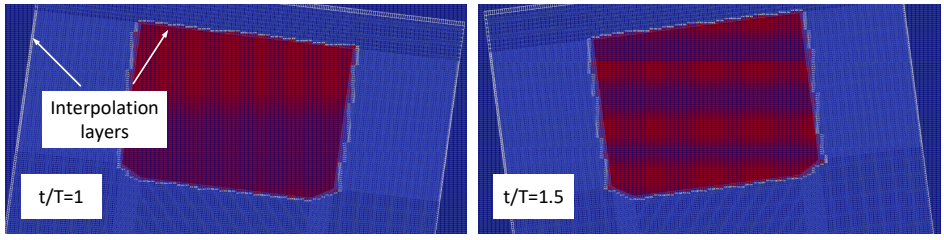

Figure 3.17: Position of hole (background mesh) and interpolation regions (both background and overset mesh) at two time instants for prescribed roll motion at forcing period $T_f = 1$s

Validation and Verification Studies

The selected OF solver is applied to selected diffraction cases for the intact and the damaged ship section described in section 2.4.3 to examine numerical convergence and accuracy of the results. The latter are compared against the experiments, as well as against those from another available NS solver with different features and against those from a nonlinear potential-flow solver. This allows to examine the influence of numerical choices on the results and to examine relevance of nonlinear and viscous effects in the studied wave-body interaction scenarios.

The fully nonlinear NSLS solver used for comparison is the one described in Colicchio et al. (2005). It employs a second order finite difference representation of the NS equations and a second order predictor-corrector scheme for the time integration. An adaptive time-step is used such that the Courant number

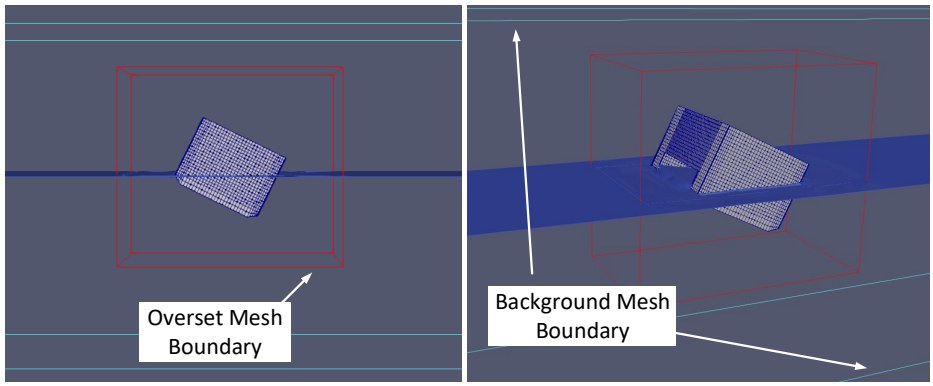

Figure 3.18: Front view (left) and damage opening view (right) of the 3D structured overset mesh (only outline marked) for the damaged section (figure 2.1) used in the present study

is less than 0.3. A single Earth-fixed Cartesian boundary-immersed grid is used and both moving body surface and deforming free-surface are represented with two level set functions that define the minimum signed distance of each computational point from those surfaces. A local grid refinement is applied close to the wavemaker region, the free-surface region and the ship section.

The fully nonlinear potential-flow solver is described in Greco et al. (2005). It simulates a NWT with a flap wavemaker at one end and a numerical beach at the other end. A BVP is solved for the velocity potential, φ, at any time instant with a BEM using linear shape functions. The free-surface boundary conditions, with Lagrangian formulation, are stepped in time with a fourth-order Runge-Kutta scheme. To estimate wave-induced loads, the body pressure is obtained from the Bernoulli equation. The latter involves the time derivative of φ for which a similar BVP as for the potential is solved. The diffraction-problem simulations are performed with a time step equal to $0.01T$, with T the incident wave period, and with spatial discretization such as to ensure converged results. The BEM helps to compare the importance of nonlinear and viscous-flow effects for the examined case.

A set of diffraction experiments for the intact and damaged ship section as described in section 2.4.3 are examined. The simplicity in the setup of the experiments helps to minimize errors and provides suitable cases for validation of the NWT in OF. The length and depth of NWT used for validation purpose are the same as in the diffraction experiments (figure 2.9). Figure 3.19 provides the boundary conditions for the diffraction problem along with the contour plot of the volume fraction, with red shading indicating water ($\alpha = 1$) and blue shading indicating air ($\alpha = 0$). For 2D computations, the direction in the plane of the paper is one cell thick, i.e. the flow is not solved in x direction. For comparison with experimental time series, the diffraction problem is simulated using a wavemaker at the left end for generating waves and a beach at the far end on the right side. The beam to draft (T_d) ratio for the intact-section experiments and simulations

is B/T_d=5.88. For the damaged section cases, the damage opening faces the incoming waves. A forced angular motion (moving boundary condition) about the hinge is given as input on the left end of the NWT. Here, the prescribed motion is the same as that of the experimental wavemaker. To implement a beach at the opposite end, waves are absorbed using the shallow-water absorption condition. This absorption method is shown to be quite effective and details of this method for OF are presented by Higuera et al. (2013). A no-slip boundary condition is set at the bottom of the flume. At the top boundary (atmosphere), a fixed-value pressure condition is applied, i.e. total pressure, considered here relative to the atmospheric pressure, is set to zero (constant). For the diffraction simulations, the DM technique is employed due to the fixed ship section and small motion required for the wavemaker. Also, a structured block hexahedral (BH) grid is generated using *blockMesh* due to the relatively simple 2D cross-sectional shape for both intact and damaged sections. The mesh is generated such that it is highly refined near the free-surface and where the waves interact with the fixed body (left plot of figure 3.13). This "free-surface" region extends from $z = -0.55\mathrm{T}_d$ to $z = 3.75\mathrm{T}_d$. The size of cells in z direction for this region is so to obtain 6-16 cells per wave height depending on mesh discretization. Windt et al. (2019) has shown that OF gives a good degree of accuracy for wave-propagation cases with cells per wave height $>$10 in the free-surface region.

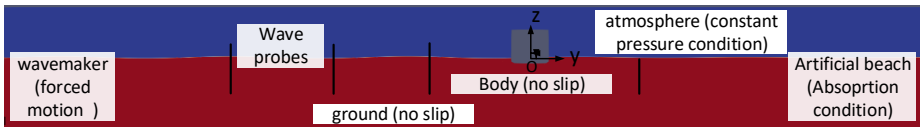

Figure 3.19: Computational OF domain for the 2D intact and damaged ship section diffraction problems, with enforced boundary conditions

Before comparing and validating against experimental data, it must be ensured that the results have converged. The case of waves with period T =1 s and steepness kA = 0.033 is used for this investigation. As mentioned before, an adaptive time-step is implemented to satisfy the CFL condition. Therefore, the time step is automatically set by the solver, the maximum value being set to 0.0025 s. However, the effect of time evolution schemes must be analyzed because it is one of the most important factors controlling numerical diffusion in a NWT with propagating waves. The effect of implemented time-evolution scheme is analyzed in terms of local variables, i.e. the wave elevations at WP 5 and WP 8 (see definition in figure 2.9), and of a global quantity, i.e. the vertical force. The wave probe elevation times series using the first-order Euler method and the second-order Crank-Nicolson (CN) method with under-relaxation values of 0.7 and 0.9, indicated hereafter as CN 0.7 and CN 0.9 schemes, for WP 5 and WP 8 are shown in figures 3.20 and 3.21, respectively. To make a quantitative comparison between the numerical schemes, mean values of the maxima and minima in the steady-state region for at least $5T$ are considered. From the results, the Euler scheme is observed to be very diffusive, with a difference of more than 50% for the wave elevation when compared with CN 0.9 scheme. The CN 0.7 scheme also shows a difference

up to 10%. After a transient phase, steady-state is achieved and after about $10T$ the effect of reflection from the wavemaker becomes evident. This is discussed in detail later. Figure 3.22 shows the heave force per unit length $F_3 = f_3/L$, where f_3 is the total 3D heave force and L is the length perpendicular to the cross-section, for the three time schemes. A similar behavior as for the wave probes is observed, i.e. after a transient phase, the force reaches steady-state conditions (right plot of figure 3.22). Also, as for the wave elevation, a large difference between Euler and CN schemes (>50%) is observed. It should be noted that the time intervals of the steady-state region for the force and for the two wave probes differ, as expected, due to difference in the physical locations of the wave probes and ship section in the tank. The results from the CN 0.9 scheme are closest to the experiments (not shown in the figure), therefore this scheme is chosen as the base scheme for all studied ship-section cases using the DM strategy.

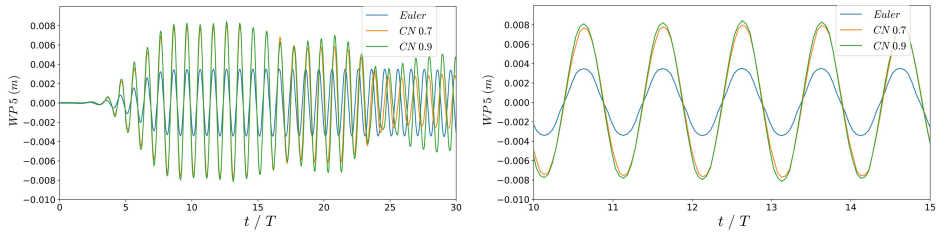

Figure 3.20: Intact section, diffraction: Wave elevation time series for WP 5 from OF (left) and corresponding steady-state region (right) for different time schemes; incident waves with period T =1 s and steepness kA =0.033

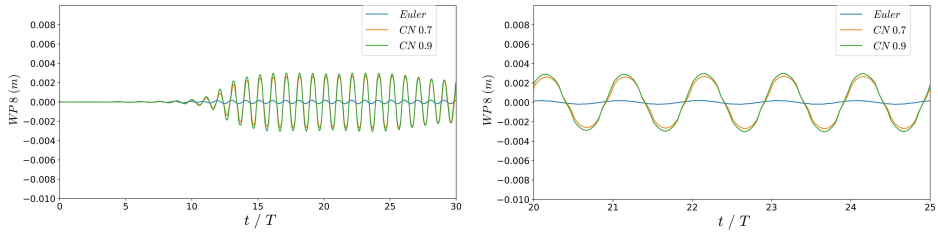

Figure 3.21: Intact section, diffraction: Wave elevation time series for WP 8 from OF (left) and corresponding steady-state region (right) for different time schemes; incident waves with period T =1 s and steepness kA =0.033

As described earlier, Euler scheme is very diffusive when wave propagation is involved. In order to obtain reasonable results with Euler time-stepping, a very small time-step has to be employed leading to a higher computational time. Reasonable results with Euler scheme can be obtained with a value of dt=0.0005 s (removing the adaptive time-step). Figures 3.23 and 3.24 show the wave probe elevations and force on the intact section for waves with period T =1 s and steepness kA = 0.033. The comparison with the CN 0.9 scheme is reasonable for this case. Smaller time steps can result in almost similar results as the CN 0.9 method.

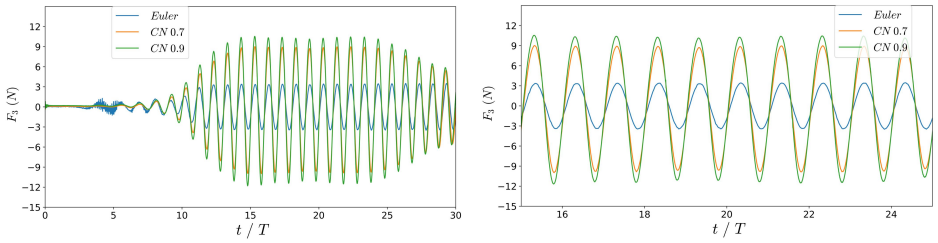

Figure 3.22: Intact section, diffraction: Heave force time series from OF (left) and corresponding steady-state region (right) for different time schemes; incident waves with period T =1 s and steepness kA =0.033

This demonstrates that Euler scheme can be used with much smaller times steps to get reasonable results in cases involving wave propagation. This is important because only Euler scheme is available in OpenFOAM for an overset mesh with a multiphase solver.

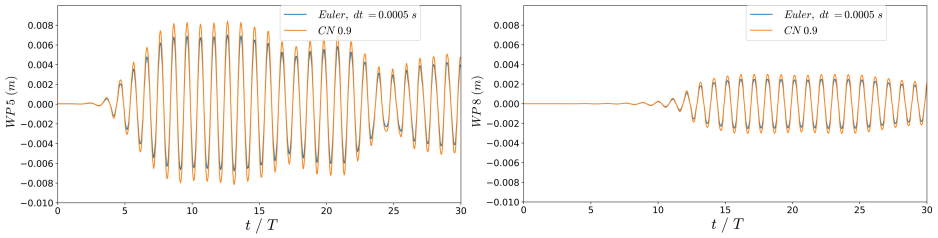

Figure 3.23: Intact section, diffraction: Wave elevation time series for WP 5 from OF (left) and WP 8 (right) for Euler scheme with sufficiently small dt compared with CN 0.9 scheme; incident waves with period T =1 s and steepness kA =0.033

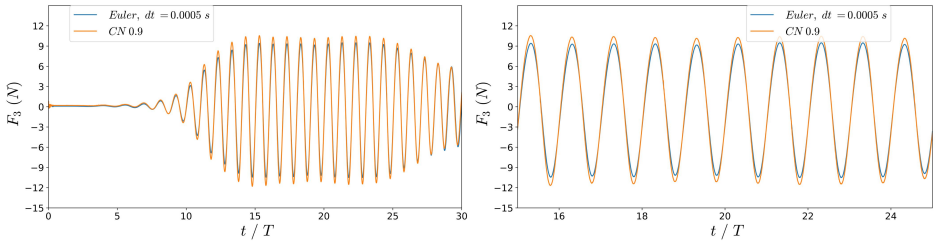

Figure 3.24: Intact section, diffraction: Heave force time series from OF (left) and corresponding steady-state region (right) for for Euler scheme with sufficiently small dt compared with CN 0.9 scheme; incident waves with period T =1 s and steepness kA =0.033

Convergence analysis in spatial domain has been performed to ensure accuracy while limiting the computational costs. Here, the focus is on the simple hex grid and the grid is systematically refined as defined in table 3.9. For the three

studied grid sizes, the wave elevation time series for WP 5, 8 and the heave-force results are shown in figures 3.25, 3.26 and 3.27, respectively, using the CN 0.9 scheme. Overall, the three mesh sizes show good agreement for the wave elevations and the force. The difference in mean values of maxima/minima for the wave elevation in the steady-state region between "Coarse" and "Fine" mesh is around 8%, whereas it is less than 5% between the "Medium" and "Fine" mesh size. The difference in the force values is almost negligible for the three mesh sizes. It must be noted that the mean buoyancy calculated from OF is subtracted from the total heave force and that, in general, the numerical mean buoyancy varies with grid discretization. The results indicate very small differences for the mean buoyancy, the largest value being for "Coarse" grid. This is visible in the beginning of the simulations where non-zero values of force (small oscillations) are observed. It can be concluded that using the "Fine" mesh as a base mesh is appropriate to achieve converged values.

	$B/\Delta y$	$B/\Delta z$	$B/\Delta z$ (near free-surface)	Number of cells
Coarse	50	50	128	312980
Medium	50	50	160	347820
Fine	50	50	200	393380

Table 3.9: Intact section, diffraction: Mesh details used for convergence studies

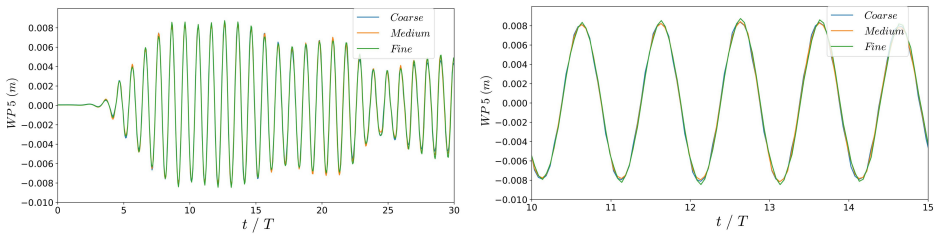

Figure 3.25: Intact section, diffraction: Wave elevation time series for WP 5 from OF (left) and corresponding steady-state region (right) for different sizes of block hex grid; incident waves with period T =1 s and steepness kA =0.033

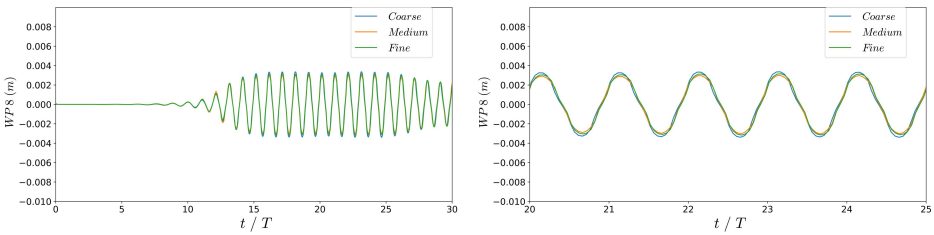

Figure 3.26: Intact section, diffraction: Wave elevation time series for WP 8 from OF (left) and corresponding steady-state region (right) for different sizes of block hex grid; incident waves with period T =1 s and steepness kA =0.033

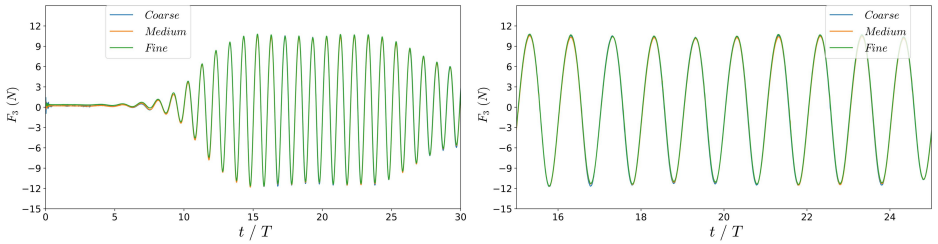

Figure 3.27: Intact section, diffraction: Heave force time series from OF (left) and corresponding steady-state region (right) for different sizes of block hex grid; incident waves with period T =1 s and steepness kA =0.033

Comparison for the heave force is also demonstrated for structured and unstructured grid types shown in figure 3.13. The mesh discretization used for the structured grid and for the background mesh of the snappy unstructured grid is the ”Fine” mesh. The unstructured grid near the body has two levels of refinement. The time-scheme is CN 0.9 for both grid types. The grid for the unstructured case is modified only close to the body and, therefore, only the comparison for heave force is shown here. The results from figure 3.28 show small differences for the mean values of force peaks in the steady-state region using the two grids. Therefore, the block hex (BH) grid can be employed for the diffraction case. However, in scenarios with complex body shapes or moving bodies, snappy mesh may provide improved results.

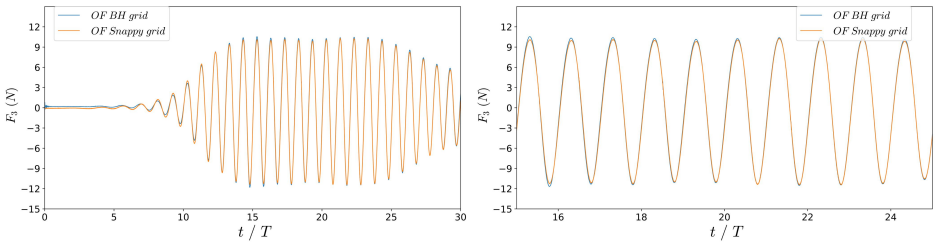

Figure 3.28: Intact section, diffraction: Heave force time series from OF (left) with steady-state region (right) for two grid types and incident waves with period T =1 s and steepness kA =0.033

Computational time is an important parameter to be taken into account for CFD solvers. A balance must be maintained between accuracy and efficiency as Supercomputer hours require intensive resources. Table 3.10 gives the computational time taken (Clock Time) for various grid types, mesh sizes and temporal schemes. It is observed that the *snappy* mesh takes more than twice the time as compared to the ”Fine” grid using the same temporal scheme while offering negligible change in the results. The difference in computational time needed for the ”Fine” grid with different temporal schemes is very small but the results vary significantly especially for the Euler scheme. The ”Coarse” grid with CN 0.9 scheme takes the least time with reasonable results. However, it is wise to use a finer grid,

which may be needed for cases with smaller wave heights or complex flow features. Therefore, as mentioned earlier, it is observed that mesh type/size selection is important both for accuracy and efficiency.

Time Scheme	Mesh Type/Size	Computational Time (s)
CN 0.9	BH (Fine)	9727
CN 0.7	BH (Fine)	9560
Euler	BH (Fine)	9132
CN 0.9	BH (Coarse)	6233
CN 0.9	Snappy (Fine)	21575

Table 3.10: Computational time for different mesh type, size and time-schemes

After establishing convergence criteria, the OF results are validated against the experiments and compared against the BEM and NSLS results. As shown earlier for spatial and temporal convergence, the comparison is done both in terms of the local wave elevation in the tank (WP 5 and WP 8) and the heave force. This is important to analyze the effectiveness of the NWT implemented in OF for the wave propagation and the wave induced loads on the body. The local wave elevation at WP 5 and WP 8 is analyzed in figures 3.29 and 3.30, respectively. The behavior of experiments and the numerical solvers is in good agreement within a time interval of 15 T, i.e. before the effect of wave reflections become visible. WP 5 is closer to the wavemaker, thus, the steady state region occurs earlier (between 8-18 oscillations) as compared to WP 8. The numerical solvers display a behavior similar to the experiments, more consistent for WP 8. The ramp-up time of the wavemaker, i.e. $5T$, is also visible in the wave elevation time series.

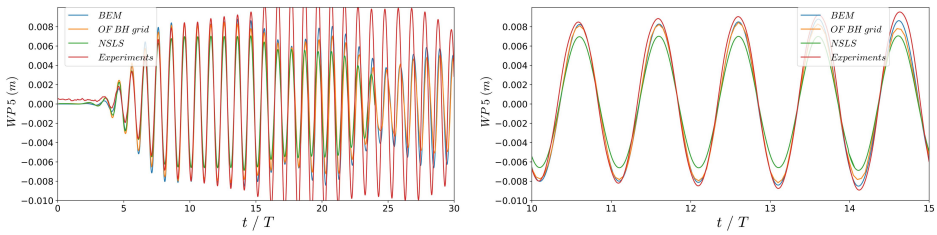

Figure 3.29: Intact section, diffraction: Wave elevation time series for WP 5 from BEM, OF, NSLS and experiments (left) and corresponding steady-state region (right) for incident waves with period T =1 s and steepness kA =0.033

Roughly, the occurrence of wave reflection from the fixed body and wavemaker can be estimated using the group velocity $c_g = \frac{gT}{4\pi}$ for deep water waves (Faltinsen and Timokha, 2009). Deep water waves imply that $h_t > \lambda/2$ (Faltinsen and Timokha, 2009), h_t is water depth and λ is wavelength. In the present case with incident waves of period T =1 s and h_t =0.95 m , λ =1.56 m; therefore, the deep water condition is satisfied. It is assumed that waves originate from the wavemaker and are reflected from the fixed body. Following this, they approach the wavemaker and are reflected by it to reach WP 5. The effect of these two reflections (one from the fixed body and one from the wavemaker) is visible in the

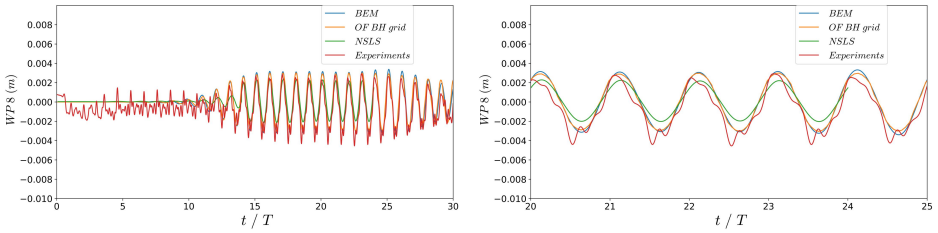

Figure 3.30: Intact section, diffraction: Wave elevation time series for WP 8 from BEM, OF, NSLS and experiments (left) and corresponding steady-state region (right) for incident waves with period T =1 s and steepness kA =0.033

time series for WP 5 at $\sim$ 15 and 20 s. The double distance between the wavemaker and the fixed body is 13.5 m and the distance between wavemaker and the WP 5 is 2.5 m. Therefore, the time taken for effect of reflections from the body to reach WP 5 is $t = (13.5 - 2.5)/c_g = 14.1$s and from the wavemaker to WP 5 is $t = (13.5 + 2.5)/c_g = 20.13$ s. These estimated values are close to the values observed from the experimental time series. The right plots of figures 3.29 and 3.30 show steady-state conditions within a time interval of $5T$. The agreement between all numerical solvers and experiments is quite reasonable with the difference between OF and experiments less than 10% for mean values of maxima and minima.

Figure 3.31 shows the heave force per unit length (F_3) on the fixed intact section from the OF, with CN 0.9 scheme and the "Fine" mesh, the experiments, the BEM and NSLS solvers. The effect of reflections is evident after a steady-state region (right plot of figure 3.31). The general agreement for all solvers with experiments in this steady state region is reasonable both for amplitude and phase of the heave force. The amplitude after 30 oscillations follows a similar behavior as the experiments but the phase difference between the numerical solvers and experiments increases significantly. A difference of 20% is observed between OF and experiments for average maximum values but the difference for minima is smaller, $\sim$5%. The phase difference is negligible. The nonlinear potential-flow BEM solver gives similar mean values as compared to OF. This would suggest that viscous effects are not are not large for this case. At least flow separation is expected to be limited. In fact, Faltinsen (1990) describes that a blunt object without sharp corners in oscillatory flow will not have flow separation at small Keulegan-Carpenter number, $KC = \frac{UT}{D_c}$. Here, U are the oscillatory flow velocity and D_c the characteristic body length. For the present case, $KC = \frac{H\pi}{B}$, where H is the wave height. Therefore, KC =0.1, implying negligible flow separation. However, the NSLS-solver results appear closer to the experiments with larger mean peak values ($\sim$ 15%) as compared to OF and BEM results. This might suggest that some viscous-flow effects are not properly captured by the OF simulation. The resolution of the free-surface zone in the NSLS simulation is higher than that in the OF solution and is evident from the results. The grid near the body is also much more refined for the NSLS. The difference in grid size is more pronounced near the inclined edges. This is one of the reasons for better accuracy of the NSLS solver as compared to OF. The time taken by NSLS solver is much higher ($\sim$ 5 times OF) because version

of the code used in this work is sequential and not optimized. Overall, OF results can be considered satisfactory considering efficiency and accuracy.

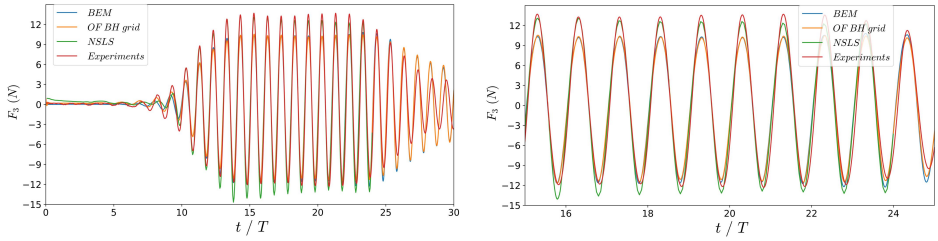

Figure 3.31: Intact section, diffraction: Heave force time series from BEM, OF, NSLS and experiments (left) and corresponding steady-state region (right) for incident waves with period T =1 s and steepness kA =0.033

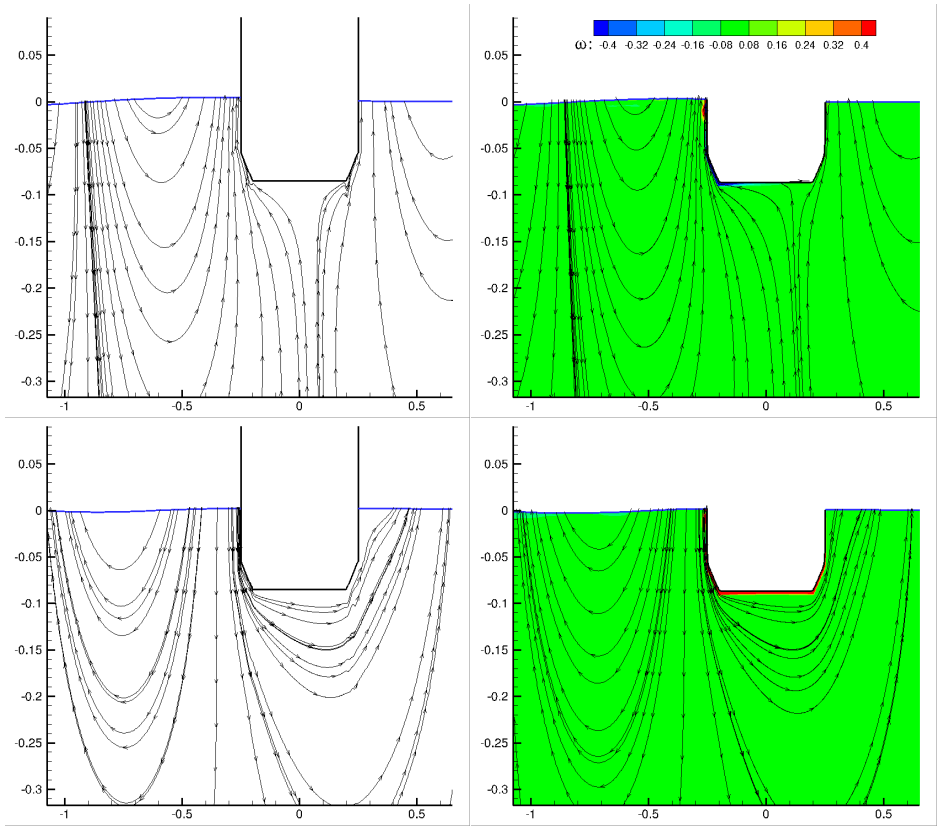

Figure 3.32: Intact section, diffraction: Streamlines from OF BH grid (left) and NSLS (right) at t/T=10.2 (top) and t/T=10.5 (bottom). For NSLS the vorticity (s^{-1}) field is also given

In order to investigate the difference in the OF and NSLS solvers in detail, fig-

ure 3.32 shows snapshots with streamlines from both solvers at two time instants. The results document no vortical structures near the body, confirming limited viscous-flow effects in this diffraction study. Moreover, the NSLS vorticity field indicates negligible values in the water domain (see right plots of the figure 3.32). The NSLS solver uses a LS function to define the body surface and, therefore, a smooth distribution of streamlines near the body is observed. For the OF case, a hex grid is used and the discretization near the body is fine close to the free surface but coarser towards the submerged part of the body. Thus, minor differences in the streamlines are mostly observed near the body bottom. This, however, does not affect the integrated loads greatly with a fixed body and limited viscous-flow effects. In other parts of the liquid and near the free-surface, the behavior is quite similar. This study suggests that the body modeling in OF requires greater grid refinement especially near the free-surface. Attention should be paid when viscous effects and vortex shedding are involved.

Figure 3.33 shows the comparison between OF and experiments for $F_{3a,int} = \sum_{n=1}^{5} \frac{(|F_{3\,\max}|+|F_{3\,\min}|)/2}{5}$, i.e. the mean heave force amplitude per unit length for 5 oscillations in the steady-state region. Linear BEM results from WAMIT and the error uncertainty for the experiments are also shown. This includes the instrumental error and standard deviation in measurement from the five oscillations. The mean values of the force amplitude from the BEM and NSLS solver are also provided for T=1s. The OF numerical results show a satisfactory agreement with the experiments. OF follows the general trend of experiments but underestimates the heave force with an average difference of 25%. One possible reason is that the grid near the body, especially near the inclined edges, needs to be refined even further. Results from WAMIT simulations are in good agreement with OF except for T =0.9 and 1 s and both are close to the experiments at the lowest examined incident-wave period. Excluding the case with T =1.2 s, for which the experiments indicate a larger error, the experimental measurements have larger values for intermediate T, indicating that some phenomena in the physical tests are not fully modelled/handled by the examined numerical methods. The in-depth analysis performed for T =1 s suggests that, in this case, nonlinear potential-flow effects play an important role.

Finally, the diffraction problem for a damaged 2D section is examined with OF. Simulation parameters are similar as for the intact section, but now the fluid domain (block hex grid) is also present inside the damaged compartment (see figure 3.34). Therefore, the number of cells increases slightly for this case. In the internal compartment, open to water, the discretization in y and z directions is set to be the same as that near the free surface of the close external flow and the time scheme used is CN 0.9. The examined incident wave periods vary between 0.8-2.3 s and the draft for the fixed body is 15.5 cm (B/T_d=3.22), corresponding to freely-floating draft in damaged scenario for loading LC 1. In this case, the time series cannot be compared directly to the experimental results. It must be considered that the experimental 3D body has a damaged and an intact part (see figure 2.1). Therefore, numerically the diffraction force has also been calculated for a 2D intact section at the same draft. Then, assuming valid a linear strip theory, 2D forces can

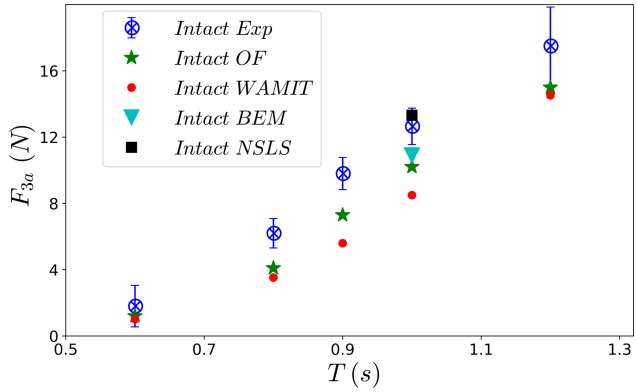

Figure 3.33: 2D Intact section, diffraction: Heave force amplitude from OF, WAMIT, BEM, NSLS and experiments

be translated to 3D numerical results using steady-state amplitude values (F_{3a}) as in eq. (3.15)

$$F_{3a,dam,3D} = F_{3a,dam,2D}d + F_{3a,int,2D}(L - d) \tag{3.15}$$

with L and d defined in figure 2.1. This numerical 3D force is compared with the experimental values in figure 3.35. Error bars for the experiments include uncertainty in the measurement and standard deviation for five oscillations. OF captures the general trend and is in the range of experimental error for most periods. It underestimates the heave force with an average difference of ∼25% against the experiments. The exact reason for this behavior could not be located. The 3D force from the simulations is a linear sum of the 2D intact and damaged section contributions. An underestimation of the heave force from OF has been documented in figure 3.33 for the intact section. Thus, there is a possible error contribution from the intact section in the 3D force. Another reason for difference may be the change in cross-section from damaged to intact, leading to relevant local 3D effects and rendering questionable the assumption of linear strip theory.

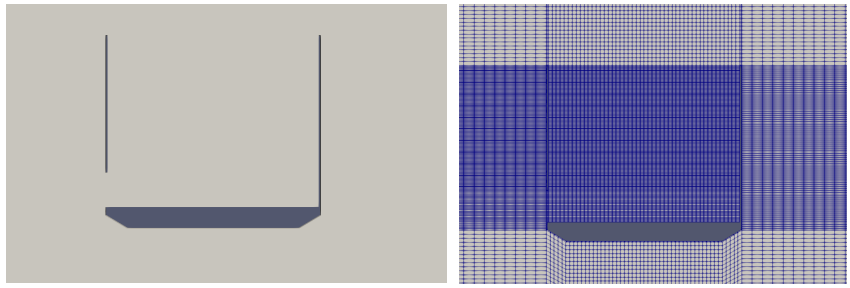

Figure 3.34: 2D damaged section model (left) and block hex mesh for the damaged section (right)

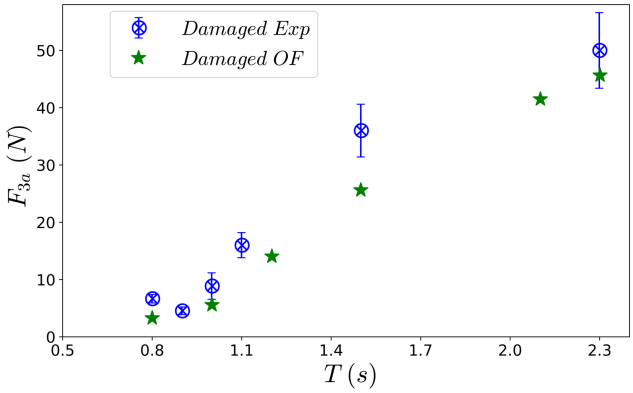

Figure 3.35: 3D damaged section, diffraction: Heave force amplitude from OF and experiments

Numerical diffraction results demonstrate that the NWT implemented in OF is a satisfactory tool for studying wave propagation and wave-structure interaction within the examined body and wave parameters. The numerical diffraction studies were aimed to show the ability of the OF method to complement the physical investigations from the experiments. This fact has been demonstrated satisfactorily in the meaning that the OF results are able to capture the general trend of the experiments in both intact and damaged condition though with differences (<25% for most periods) when compared to the experiments. The diffraction studies also helped in deciding optimum solver schemes/ settings. The CN 0.9 scheme provides good wave propagation capabilities without additional computational overhead and this scheme is used for all cases demonstrated further in this work. The structured grid with "Fine" discretization provides best results with slight increase in computational time. The type of grid (structured or unstructured) has to be chosen according to simulation scenarios because it involves significant increase in computational resources. Therefore, grid selection and discretization have to be done carefully for all specific cases.

3.2.3 Strip Theory using OpenFOAM

Assuming negligible 3D effects in the wave flume, a linearized strip-theory numerical method was implemented for calculating intact and damaged ship section motions, incorporating a nonlinear roll viscous damping term based on OF numerical calculations for the damaged scenario. Consistently with strip theory (Salvesen et al., 1970; Faltinsen, 2005), the body is divided into strips along its elongation direction. In each strip, the loads are found as 2D in the cross-section plane and multiplied by the strip length to obtain corresponding 3D-load contributions. Summing the contributions from all strips provides the total 3D loads acting on the body. In this case, for the intact ship section only one 2D problem has to be solved to estimate the 2D hydrodynamic loads at a given incident-wave frequency and then one needs to multiply the 2D loads by L. For the damaged ship

section, the 3D ship model has intact and damaged strips and one needs to examine 2D problems for both the damaged and intact strips and then multiply the corresponding 2D hydrodynamic loads with the corresponding strip lengths to get the total 3D loads (see figure 3.36 and eq. 3.15). Consistently with linear theory, the 2D cross-section loads are found by splitting the seakeeping problem in radiation and diffraction problems. Their solutions provide, respectively, the added-mass, damping and restoring coefficients, and the wave excitation loads. Generally, for strip-theory seakeeping methods, potential flow solvers with additional nonlinear roll viscous damping terms are employed to solve these problems. Here, a viscous solver with laminar flow assumption is implemented in OpenFOAM. An error source is that the free vorticity flow is likely to be turbulent. Flow separation occurs from sharp corners, thus, boundary layer plays a secondary role. Intact condition and full compartment damage were examined. The latter assumes that the damaged compartment is fully ventilated. The total loads are estimated from the steady-state solution of the radiation and diffraction problems and then extracting the wave-frequency contribution.

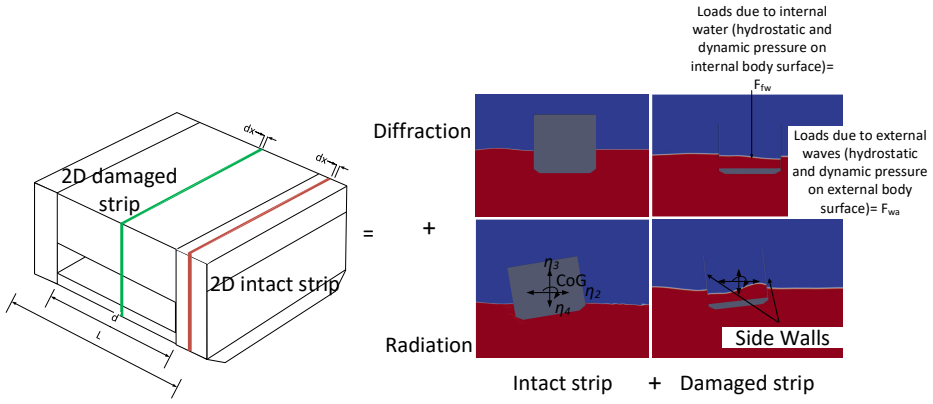

Figure 3.36: Strip theory illustration for a damaged section (decomposition into radiation and diffraction problems)

The setup for the radiation/diffraction problem is shown in section 3.2.2. For the radiation problem, a beach is placed at both ends of the NWT. Loads on the body are calculated using pressure integration along the internal and external wetted parts of the damaged ship section. The no-penetration body boundary condition is applied at the instantaneous position of the body surface for the radiation problem. Since, the radiation problem solves for the pressure on the instantaneous body surface, the added mass terms contain the dynamic effect of the hydrostatic pressure. The radiation moments are evaluated about the CoG. The radiation problem is amplitude dependent and two amplitudes, 8 and 14 degrees for forced roll motion and 0.005 m and 0.01 m for forced sway and heave motions of CoG, are used to check for nonlinear behavior. Nonlinear behavior in terms of mean and higher harmonic force components are small, but nonlinear viscous damping must be included especially for roll motions at resonance. This cannot be properly handled within the described linearized seakeeping approach and is

included for the damaged section as an additional quadratic damping term based on OpenFOAM forced roll calculations and discussed later in this section.

The diffraction problem is solved considering the same setup as in the experiments with the body fixed at the initial floating location of the body. In this case, wavemaker faces the damage opening and a beach is placed downstream of the 2D body. No-penetration condition is applied at the mean fixed position of the body surface. Loads on the body are calculated as for the radiation problem. The diffraction forces at any incident wave period are calculated by taking the average of the steady-state amplitudes over 3-5 time periods (depending on the incident wave period).

Assuming a complex time dependence $e^{i\omega t}$, where i is the complex unit and ω is the circular incident wave frequency. η_2, η_3 are defined as the sway and heave motion of the CoG and η_4 is the angular roll motion about CoG. The linear equations of motion in the frequency domain can be expressed as

$$\left\{ -\omega^2 \begin{bmatrix} A_{22}+M+M_b & A_{23} & A_{24} \\ A_{32} & A_{33}+M+M_b & A_{34} \\ A_{42} & A_{43} & I_{44}+A_{44} \end{bmatrix} + i\omega \begin{bmatrix} B_{22} & B_{23} & B_{24} \\ B_{32} & B_{33} & B_{34} \\ B_{42} & B_{43} & B_{44} \end{bmatrix} + \begin{bmatrix} 0 & 0 & 0 \\ 0 & C_{33} & 0 \\ 0 & 0 & C_{44} \end{bmatrix} \right\} \begin{bmatrix} \eta_2 \\ \eta_3 \\ \eta_4 \end{bmatrix} = \begin{bmatrix} F_2 \\ F_3 \\ F_4 \end{bmatrix} e^{i\omega t} \tag{3.16}$$

Here, A_{jk}, B_{jk}, C_{jk}, (j, k=2,3,4) are the added mass, damping and restoring terms, $F_k e^{i\omega t}$, is the wave excitation load in sway ($k = 2$), heave ($k = 3$) and roll ($k = 4$), respectively, M is the dry mass of the model and M_b is the solid ballast mass. One should note that heave is uncoupled from sway and roll only in the intact numerical case, but not in general for the damaged scenario. Moreover, as explained above, the solution of the radiation problem does not provide the added-mass and restoring coefficients separately but their combination, i.e., $-\omega^2 A_{jk} + C_{jk}$. It means that A_{jk} and C_{jk} are not uniquely defined. C_{jk} is estimated by a quasi-steady linear hydrostatic analysis as it is done for intact ships. The 2D restoring coefficients in heave and roll for an intact cross-section (i.e. with unitary length perpendicularly to the cross-section) are $c_{33} = \rho g B$ and $c_{44} = \rho g \nabla GM$, where ρ is the mass density of water, ∇ is the displaced cross-sectional area and GM is the metacentric height for the cross-section. For the damaged section, the quasi-steady hydrostatic effect of the floodwater in the compartment is considered. For a fully ventilated damaged cross-section (i.e. with unitary length perpendicularly to the cross-section), restoring effects could only come from the side walls of the compartment (indicated in the bottom-right panel of figure 3.36). However, their thickness is only $0.01B$, and their restoring effect can be neglected, therefore, $c_{33} = 0, c_{44} = 0$ are assumed. Once the restoring coefficients are calculated, the sectional added mass coefficients, as well as the damping coefficients can be estimated from the time series following the approach in Vugts (1968). This procedure is shown as an example for the heave hydrodynamic coefficients in chapter 4 and also documented for sway and roll in appendix B.

Influence of nonlinear roll damping on the roll motion, especially near roll resonance, becomes important. This can be quantified by incorporating the viscous drag term $B_{44,quad}\dot{\eta}_4 |\dot{\eta}_4|$, where $B_{44,quad}$ is quadratic roll damping, in the roll equation. This is accomplished by using the equivalent linearized roll damping (Faltinsen, 1990) in the motion equations (3.16) as

$$B_{44,tot} = B_{44l} + \frac{8\omega}{3\pi} B_{44,quad}\eta_{4a} \tag{3.17}$$

Here, B_{44l} is the linear roll damping coefficient, $B_{44,quad}$ is the quadratic roll damping coefficient ω is the incident wave frequency and η_{4a} is the roll amplitude in radians. B_{44l} and $B_{44,quad}$ are calculated with OpenFOAM by simulating two radiation problems in roll at oscillation frequency ω and with two different forced-roll amplitudes. In particular, they can be estimated using a linear fitting curve of the roll-damping results from the two simulations. $B_{44,tot}$ depends on the roll amplitude, so the equations of motion (eq. 3.16) must be solved iteratively until the roll amplitude used for estimating the damping in eq. (3.17) gives the same roll amplitude for the next iteration. The obtained damping values show good agreement with the damping from the free roll decay tests (see in section 5.1.1).

In this chapter, the potential of OF as complementary research tool has been demonstrated. The main focus of the numerical simulations in the present work is to capture the behavior from the experiments and to provide additional information/insights on the mechanisms and flow features associated with resonance phenomena inside the damaged section. Simplified diffraction experiments are presented in the present chapter to verify the accuracy of the NWT. OF simulations provide satisfactory results within a certain margin of error ($< 25\%$) for most of the diffraction cases. The convergence for temporal and spatial discretization schemes used for simulations in the present work have also been established. The solver can be improved in future studies to achieve better accuracy. In the following chapters 4-6, this solver is used to complement experimental studies, after proper check of numerical convergence for the analyzed quantities. The boundary conditions and grid types must be selected based on the examined problem and will be documented in chapters 4, 5 and 6.

Chapter 4

Damaged section in Forced Heave Motion

This chapter presents analysis and discussion for the damaged model section undergoing forced heave motions. Forced oscillatory heave tests were carried out in calm water in a range of model-motion parameters, both in intact and damaged conditions. The experimental conditions and setup are described in detail in chapter 2. The results are documented in terms of heave added mass and damping coefficients. The effect of damage opening in the model on hydrodynamic loads is examined by comparing with an intact section. To demonstrate the physical behavior of the floodwater inside the damaged compartment, wave probe elevations and images from the experiments are presented. The experimental results are compared with results from the theoretical and numerical analysis described in chapter 3. The analysis demonstrates occurrence of sloshing and piston mode resonances in the tests and their influence on the hydrodynamics loads of a damaged ship. Detailed physical investigations are presented at these resonance frequencies for the damaged section. Effect of filling level in the damage compartment, damage-opening length and air compressibility in the airtight compartment is examined. Nonlinear effects are documented and appear dominant, especially for lowest filling level for which shallow-water depth conditions occur in the damaged compartment.

4.1 Calculation of Hydrodynamic Coefficients

Hydrodynamic heave force amplitudes obtained from FFT analysis described in chapter 2 can be better analyzed in terms of heave added mass and damping coefficients. A brief description is presented below for the calculation of 2D/3D added mass and damping coefficients for the intact and damaged ship section. Theoretical estimates of heave added mass and damping for a 2D damaged section are presented using analysis from Newman et al. (1984).

4.1.1 Experimental Analysis

During the forced heave tests, the heave force, oscillator signal and wave elevation time histories inside the damaged compartment are measured. As mentioned earlier in section 2.5, the raw data are filtered and FFTs are performed on the filtered time histories of all measured quantities. The amplitude and phase of heave force/wave elevation are calculated for the signal component at the forcing frequency. In the following analysis, axes and symbol definitions documented in chapters 2 and 3 are used.

For forced heave motions of intact section, in steady state conditions, the force part F, oscillating at the forcing frequency and measured by the load cells in the z direction, according to linear theory can be decomposed as

$$F = (m + {A_{33}}^{Intact})\ddot{\eta}_3 + {B_{33}}^{Intact}\dot{\eta}_3 + {C_{33}}^{Intact}\eta_3 \tag{4.1}$$

Here, m is the total mass of the oscillating system (see discussion below), ${A_{33}}^{Intact}$ and ${B_{33}}^{Intact}$ are, respectively, the 3D linear frequency-dependent hydrodynamic added-mass and wave radiation-damping coefficients in heave and ${C_{33}}^{Intact}$ is the restoring coefficient in heave. In the intact condition, ${C_{33}}^{Intact} = \rho g A_{wp}$, where $A_{wp} = LB$ is the intact waterplane area. From this decomposition, in general F can be written as, $F = F_a \sin(\omega t + \varepsilon)$, where ε is the phase relative to the forced heave motion, i.e. $\eta_3 = \eta_{3a}\sin(\omega t)$. Substituting η_3 and F in eq. (4.1), gives

$$\begin{aligned} {A_{33}}^{Intact} &= \frac{{C_{33}}^{Intact} - \frac{F_a}{\eta_{3a}}\cos(\varepsilon)}{\omega^2} - m \\ {B_{33}}^{Intact} &= \frac{F_a sin(\varepsilon)}{\eta_{3a}\omega} \end{aligned} \tag{4.2}$$

Assuming that strip theory is valid, for the intact section, the 2D added mass and damping are calculated as ${a_{33}}^{Intact} = \frac{{A_{33}}^{Intact}}{L}$, ${b_{33}}^{Intact} = \frac{{B_{33}}^{Intact}}{L}$, respectively.

For the damaged section, with intact parts on the ends (see figure 4.1), the force F can be decomposed into intact force from the end regions and force due to the damage region in the middle, i.e.

$$\begin{aligned} F = \left[(m^{Intact} + {A_{33}}^{Intact})\ddot{\eta}_3 + {B_{33}}^{Intact}\dot{\eta}_3 + C_{33}\eta_3\right] + \left[(m^{damaged}\right. \\ \left. + {A_{33}}^{damaged})\ddot{\eta}_3 + {B_{33}}^{damaged}\dot{\eta}_3\right] \end{aligned} \tag{4.3}$$

Here, $C_{33} = \rho g A_{wpd}$, where $A_{wpd} = A_{wp} - B_c L_c$ is the end intact sections waterplane area. Eq. (4.3) can be further re-written as

$$\begin{aligned} F = m\ddot{\eta}_3 + \left[{A_{33}}^{Intact}\ddot{\eta}_3 + {B_{33}}^{Intact}\dot{\eta}_3 + C_{33}\eta_3\right] + \left[{A_{33}}^{damaged}\ddot{\eta}_3\right. \\ \left. + {B_{33}}^{damaged}\dot{\eta}_3\right] \end{aligned} \tag{4.4}$$

$m = m^{Intact} + m^{damaged}$. Following Smith et al. (2009), m includes the dry mass of model and the equilibrium weight of floodwater inside the damaged compartment. The added mass and damping for the damaged section with intact ends can

be calculated as done above for an intact model in eq. (4.2), i.e.,

$$\begin{aligned} A_{33}{}^{measured} &= \frac{C_{33} - \frac{F_a}{\eta_{3a}}\cos(\varepsilon)}{\omega^2} - m \\ B_{33}{}^{measured} &= \frac{F_a sin(\varepsilon)}{\eta_{3a}\omega} \end{aligned} \tag{4.5}$$

Here,

$$A_{33}^{measured} = A_{33}^{Intact} + A_{33}^{damaged}, B_{33}^{measured} = B_{33}^{Intact} + B_{33}^{damaged} \tag{4.6}$$

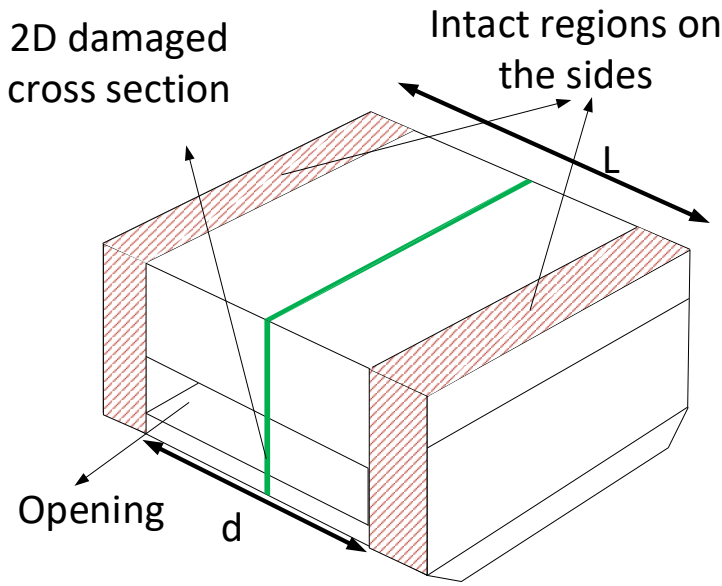

Figure 4.1: Illustration useful for the calculation of added mass and damping coefficients of a 2D fully damaged cross-section

Assuming that strip theory is valid along the intact and damaged parts of the model (see sketch in figure 4.1 for the definitions of them and of their lengths), then eq. (4.6) can be re-written as

$$A_{33}^{measured} = a_{33}^{intact}(L-d)+a_{33}^{damaged}d, B_{33}^{measured} = b_{33}^{intact}(L-d)+b_{33}^{damaged}d \tag{4.7}$$

Here, the 2D hydrodynamic coefficients for an intact cross-section are known from the experiments with the intact model. Therefore, the 2D added-mass and damping coefficients for a damaged section (see the green cross-section in figure 4.1),

can be estimated as

$$\begin{aligned} {a_{33}}^{damaged} &= \frac{A_{33}^{measured} - {a_{33}}^{Intact}(L-d)}{d} \\ {b_{33}}^{damaged} &= \frac{B_{33}^{measured} - {b_{33}}^{Intact}(L-d)}{d} \end{aligned} \tag{4.8}$$

Model tests for the intact section were performed for fewer frequencies as compared to the damaged section. The values for the intact section to be used in eq. (4.8) are interpolated for the missing frequencies from the experimental data for the model with drafts corresponding to filling level FL 1 and 2. Unfortunately, intact tests were not performed with a draft of the model corresponding to FL 3 and, therefore, experimental values of 2D added mass and damping coefficients were interpolated from Vugts's experimental data. Vugts (1968) performed tests for an intact section similar to the section used in the present experiments with beam-to-drafts ratios, B/T_d, of 2, 4 and 8. For FL 3 with B/T_d =3.125, the values are estimated from linear interpolation for B/T_d =2 and 4 documented by Vugts (1968). The 2D hydrodynamic coefficients from eq. (4.8) are examined in detail in section 4.2 for the cases studied in the present experiments. Resonance conditions will be discussed with reference to the sloshing and piston mode natural frequencies provided in chapter 3.

For an airtight damaged compartment, the heave restoring coefficient used for the section needs to be given special attention. The heave restoring coefficients are associated with change in mean buoyancy force due to the influence of heave motion. When the air-cushion is examined, the pressure can be considered spatially constant and equal to the pressure at the air-water interface. This implies that due to the high air stiffness (see section 3.1.3), the floodwater almost acts as a solid mass oscillating with the damaged section. The consequence is a resulting restoring coefficient as if the section was intact and, therefore, for a damaged airtight section $C_{33}^{damaged,airtight} = C_{33}^{Intact}$.

4.1.2 Theoretical Analysis

The vertical force acting at the top of an infinite submerged rectangle (see figure 3.4) can be estimated as in Newman et al. (1984) giving the 2D non-dimensional added mass and damping as

$$\begin{aligned} (b_{33} + ia_{33})_{d_T \to \infty} = \frac{-2i}{\pi K b}(1 - Kh) + \frac{2i\sin(k_0 b)}{\pi K k_0 b^2}\{\cos(k_0 b) + (2/\pi) \\ (k_0 h)\sin(k_0 b)\left[\ln(4Kh/\pi) + \gamma - 1 + \pi i\right]\}^{-1} \end{aligned} \tag{4.9}$$

Newman et al. (1984) introduced a correction for calculating added mass and damping of submerged rectangles with finite draft. In particular, for a draft $d_T = 2b$, they found non-dimensional hydrodynamic coefficients as

$$(b_{33} + ia_{33})_{d_T = 2b} = (b_{33} + ia_{33})_{d_T \to \infty} + (b_{33} + ia_{33})_{SP} \tag{4.10}$$

Here $(b_{33} + ia_{33})_{SP}$ involves the added mass and damping for a surface-piercing rectangle having draft d_T as $\frac{d_T}{2b} = 1 + \frac{h}{2b}$, where h is the submergence depth of the

rectangle (see figure 3.4). If d_T is chosen equal to $2b$ as in the present experiments, this leads to

$$\begin{aligned} {a_{33}}^{damaged,semi-Infinite} &= a_{33}^{damaged} - {a_{33}}^{Intact} \\ {b_{33}}^{damaged,semi-Infinite} &= b_{33}^{damaged} - {b_{33}}^{Intact} \end{aligned} \tag{4.11}$$

In section 4.2, eq. (4.11) will be used to cross-check qualitatively the force measurements from the tests. In particular, the 2D non-dimensional hydrodynamic coefficients for a semi-infinite submerged rectangle calculated from eq. (4.9) are compared with $a_{33}^{damaged,semi-Infinite}$, $b_{33}^{damaged,semi-Infinite}$ calculated from experimental values of the hydrodynamic coefficients in the right-hand side, as described in section 4.1.1.

4.2 Results and discussion

In this section, results for forced heave motions of the intact and damaged model section are presented. The experimental results are documented in terms of wave elevation amplitude inside the damaged compartment, added mass and damping coefficients in heave described in section 4.1.1. The influence of filling depth inside the damaged compartment, of the opening size, and of the airtightness in the damaged compartment is examined. The force measured in the horizontal direction is small and, therefore, the main focus is on vertical hydrodynamic loads in the discussed results. Sloshing and piston mode resonance scenarios are presented using images from the tests with the green bold lines representing the 2D free surface inside the compartment. For the plots presented in this section, the vertical dashed lines correspond to the non-dimensional linear natural frequencies for sloshing and piston modes reported in tables 3.1 and 3.5. The results in this section are made non-dimensional as follows:

$${a_{33}}^* = \frac{a_{33}}{\rho A_r}, {b_{33}}^* = \frac{b_{33}}{\rho A_r}\sqrt{\frac{B}{2g}}, \zeta^* = \frac{\zeta_a}{\eta_{3a}}, \omega^* = \omega\sqrt{\frac{B}{2g}}$$

where all symbols are as described in the text and $A_r = BT_d$ is the submerged cross-sectional area of the model both for intact and damaged sections, and T_d is the mean draft in forced heave motion experiments. It means that, unless explicitly said, we always discuss dimensionless variables.

Figure 4.2 shows an example of FFT of the heave force for filling level FL 2 (also shown earlier in bottom left plot of figure 2.13) along with an enlarged view of the FFT. The presence of superharmonics (see section 3.1.1) can be observed with peaks occurring at multiples of the main forcing frequency. In the calculation of added mass and damping coefficients and wave probe RAOs, the linear forcing frequency component from the FFT analysis (i.e. corresponding to ω in the figure) of heave-force and wave-probe data is used. Therefore, assuming negligible the nonlinear effects on the wave-frequency responses, the results in this section can be interpreted as linear added mass, damping and wave elevation RAOs.
Figure 4.3 shows the 2^{nd} and 3^{rd} order force amplitudes associated with frequencies $2\omega, 3\omega$ and divided by the force amplitudes associated with the main forcing frequency ω from the experiments at filling level FL 1 and FL 2. It is observed that

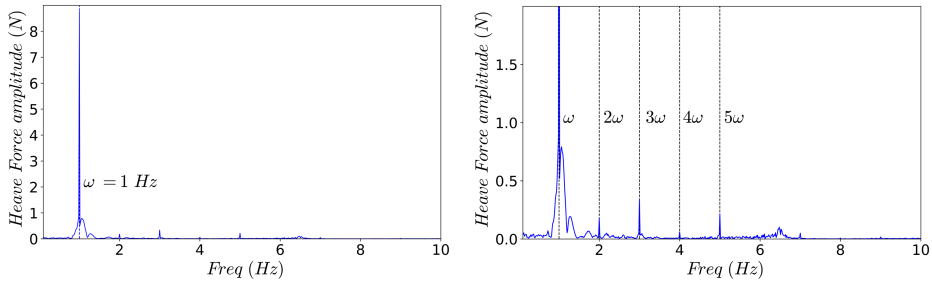

Figure 4.2: FFT analysis of force data (left) and enlarged view (right) for filling level FL 2 with $\eta_{3a} = 5$ mm and $\omega_f = 1$ Hz

FL 1 has higher nonlinear behavior as expected because of shallow-depth condition. For both filling levels, the nonlinear behavior is limited to less than 10% for the force amplitude. The nonlinear behavior is more pronounced for local flow features as compared with the heave force, for example steep nonlinear waves occur for filling level FL 1 inside the damaged compartment.

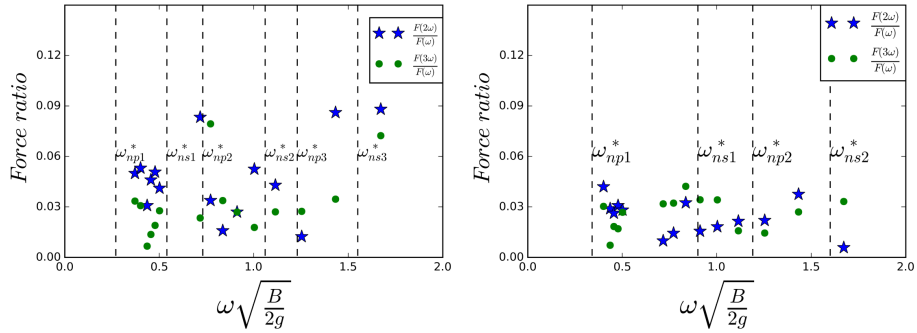

Figure 4.3: 2^{nd} $F(2\omega)$ and 3^{rd} $F(3\omega)$ order force amplitude components divided by the amplitude of the force component oscillating with forcing frequency for filling level FL 1 (left) and FL 2 (right) and forcing amplitude $\eta_{3a} = 5$ mm

4.2.1 Intact Condition

To quantify the influence of the damaged compartment on the hydrodynamic coefficients in heave motion, the model section was also tested in intact condition. A very thin wooden plate was used to cover the damage opening shown in figure 4.1 of the present model and sealed watertight. Figure 4.4 shows added mass and damping coefficients in heave from the present experiments for the two waterline conditions described in table 2.4. Within the examined frequency range, the experimental results indicate a limited effect of the non-dimensional frequency on the dimensionless added mass, while the damping coefficient is larger for lower frequencies. Higher damping values are observed for smaller drafts. This is a conse-

quence of the way the results made dimensionless. A similar behavior is observed for heave damping at different drafts of the 2D rectangular section in Vugts (1968). Numerical results from OpenFOAM for WL 1 are also given in figure 4.4. They have been obtained using the NWT setup for forced heave motions as described in section 3.2.2. The numerical results for WL 1 show a reasonable agreement with the corresponding experimental values with the difference between experimental and numerical added mass and damping coefficients being less than 18% and 28%, respectively.

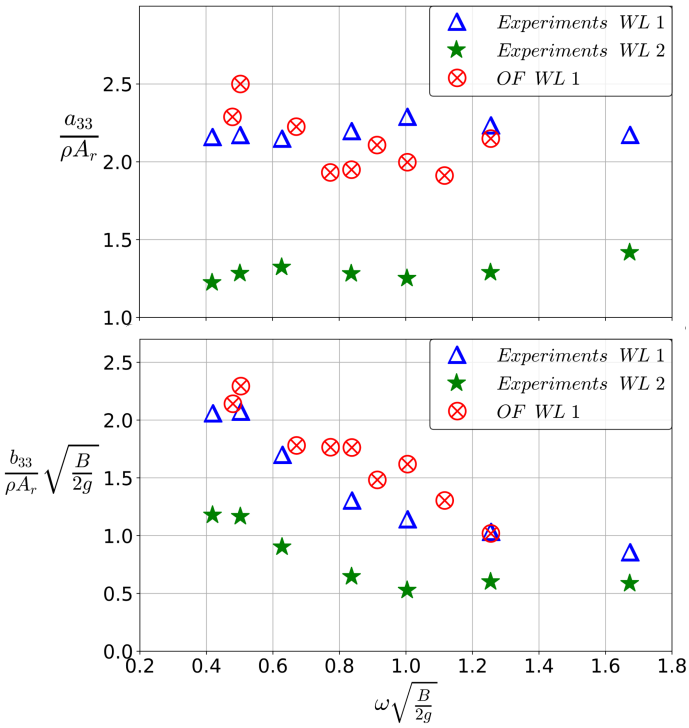

Figure 4.4: Added mass and damping coefficient in heave as a function of frequency for forced-heave motions of intact model in the present experiments

4.2.2 Damaged Condition

Forced heave motions are performed on the model with opening exposed to external water in various configurations as described in chapter 2. Faltinsen and Timokha (2009) documented that, according to linear theory, sloshing cannot be excited by heave motion of a partially-filled tank. However, in the damaged condition, the opening acts as a wave maker. This can excite sloshing and piston mode resonance. The effect of these resonance phenomena on heave added mass and damping for the damaged section depends on the symmetry properties of the

modeshapes about the centerplane (of the damaged compartment) for sloshing and piston mode resonance (see e.g. later figure 4.24).

Influence of filling depths inside damaged compartment

Filling level 1: If the forcing frequency is in the vicinity of the lowest natural sloshing frequency, Faltinsen and Timokha (2009) identify a shallow-depth condition for sloshing in a closed tank for $h/l \ll 0.1$, where h is the water depth in the tank and l is the tank breadth. In the present case, h/B_c =0.03/0.5 = 0.06 $\ll$ 0.1, therefore, a shallow water condition exists for the floodwater inside the damaged compartment. The wave systems in shallow water differ from those in higher filling depths for closed tanks. They were first described by Olsen and Johnsen (1975) and experimentally studied by Bouscasse et al. (2013) for a closed rectangular tank under harmonic forced oscillations in sway. These wave systems are found in the vicinity of the lowest sloshing frequency. In particular, Olsen and Johnsen (1975) classified four wave systems, in terms of the lowest sloshing frequency ω_{ns1}. Wave system I ($\omega/\omega_{ns1} = 0.645$), with standing waves, mainly occurs for smaller frequencies and is associated with small elevation inside the compartment. Wave system II ($\omega/\omega_{ns1} = 0.8$), with progressive waves travelling back and forth without breaking, involves water that moves towards the compartment wall and is reflected back with almost the same speed. Wave system III ($\omega/\omega_{ns1} = 1$), with progressive breaking waves similar to wave system II but with breaking occurring at or near the tank wall and wave system IV ($\omega/\omega_{ns1} = 1$), with hydraulic jumps travelling back and forth inside the compartment. Wave systems III and IV occur at the same forcing frequency depending on the ratio of the forcing amplitude and tank breadth. Wave system IV occurs for higher forcing amplitudes. A large water mass rises along the walls and the hump travels back and forth in the compartment. Bouscasse et al. (2013) reproduced typical free surface configurations as classified by Olsen and Johnsen (1975). They also highlighted nonlinear effects associated with shallow water sloshing in forced sway motions. It is interesting to note that forced heave motions on a damaged section also generate similar phenomena as classified by Olsen and Johnsen (1975) near the sloshing frequencies in table 3.1. Piston mode resonance is also observed near the frequencies documented in table 3.5. An important observation is the presence of travelling waves in the compartment at certain frequencies. These are associated with piston mode resonance frequencies, whereas, the standing waves are observed for sloshing resonance frequencies.

Figure 4.5 shows wave RAOs at WP 1 and WP 2 inside the damaged compartment for filling level FL 1. Figures 4.6-4.10 provide snapshots of the various wave systems occurring inside the damaged compartment for the shallow-water conditions examined in the present experiments. Figure 4.5 highlights peaks in wave amplitude inside the compartment near $\omega^* = 0.73$ and $\omega^* = 1.4$ with a magnification of around 1.2 to 1.8 times the forced heave amplitude. WP 2, which is close to the undamaged wall, has higher values at lower frequencies. The floodwater rises slowly inside the compartment along the wall and accumulates near the wall. After reflection from the wall, as the water reaches WP 1, which is close to the opening, it decays in magnitude because floodwater partially goes out of the

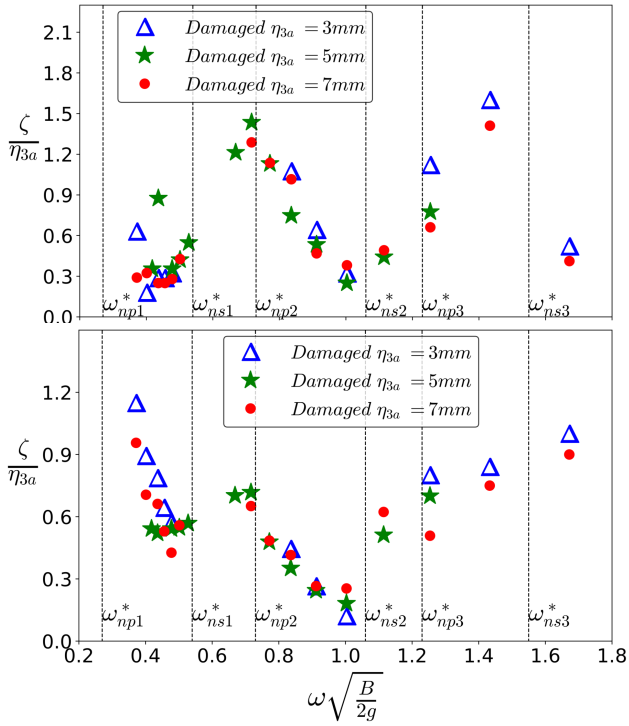

Figure 4.5: Wave probe RAOs at WP 1 (top) and WP 2 (bottom) inside damaged compartment as a function of non-dimensional frequency for three forced-heave amplitudes and filling level 1

compartment due to conservation of fluid mass, so smaller values are observed. At higher frequencies, the waves are reflected very quickly from the wall and do not have time to decay much until they reach WP 1. In the meanwhile, more water enters through the opening. As a result, the two waves, i.e. the one leaving and the one entering the damaged compartment, meet closer to WP 1 than to WP 2, rising locally the water level and resulting in a larger elevation for WP 1 with respect to WP 2 at higher frequencies. The behavior is similar to Olsen and Johnsen (1975) but since they have described results for forced sway motions, the frequencies of occurrence for the wave systems are not expected to be the same. Near the first sloshing resonance, i.e at $\omega^* = 0.55$, standing waves occur in the compartment (see figure 4.6), similar to wave system I identified by Olsen and Johnsen (1975). For higher frequencies, nonlinear progressive non-breaking waves are observed (see figures 4.7 and 4.8), similar to wave system II identified by Olsen and Johnsen (1975). At $\omega^* = 1$, the flow inside the compartment resembles the second natural mode of sloshing with high wave steepness. This is close to the theoretically calculated value of natural frequency for the second sloshing mode, $\omega^* = 1.06$ (see table 3.1). At $\omega^* = 1.43$, a higher order mode is observed. In some cases, the waves may impact the undamaged wall with splash up leading to water spray (see figure

4.9). At the second piston mode resonance and highest forcing amplitude, a scenario similar to wave system IV identified by Olsen and Johnsen (1975) occurs and is documented in figure 4.10. A large water mass rises near the undamaged wall and travels towards the opening but in the present case, a hydraulic jump was not observed. The wave amplitudes inside the compartment for the three examined forcing amplitudes are nonlinear as expected at this filling level (see figure 4.5). In addition, the waves generated at the smallest forcing amplitude are smaller and this may lead to larger measurement error from the wave probes.

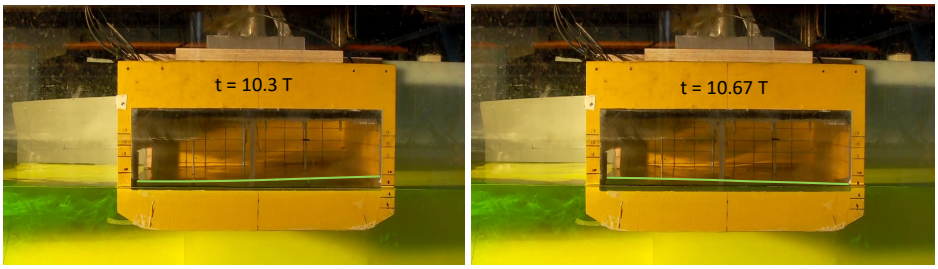

Figure 4.6: Scenario with standing waves at $\omega^* = 0.55$ and $\eta_{3a} = 5$ mm for FL 1, similar to wave system I identified by Olsen and Johnsen (1975)

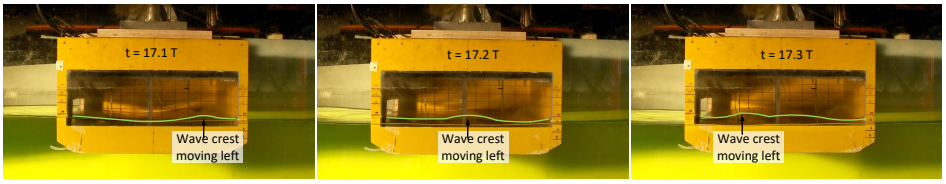

Figure 4.7: Progressive non-breaking waves at $\omega^* = 1$ and $\eta_{3a} = 5$mm for FL 1, similar to wave system II identified by Olsen and Johnsen (1975)

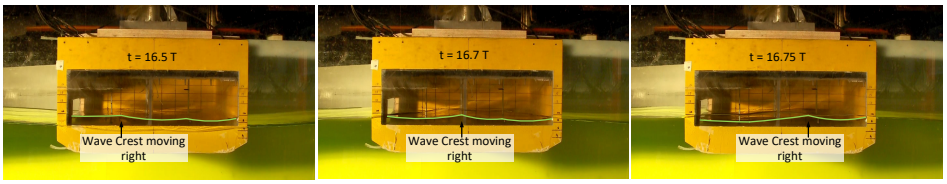

Figure 4.8: Progressive non-breaking waves at $\omega^* = 1.43$ and $\eta_{3a} = 5$mm for FL 1, similar to wave system II identified by Olsen and Johnsen (1975)

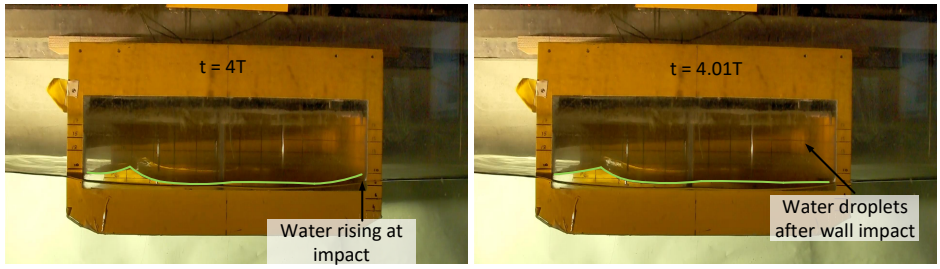

Figure 4.9: Progressive wave impacting the wall (left) with splash up leading to water spray (right) (not clear from the picture but visible in videos) for $\omega^* = 1.25$ and $\eta_{3a} = 5$mm for FL 1

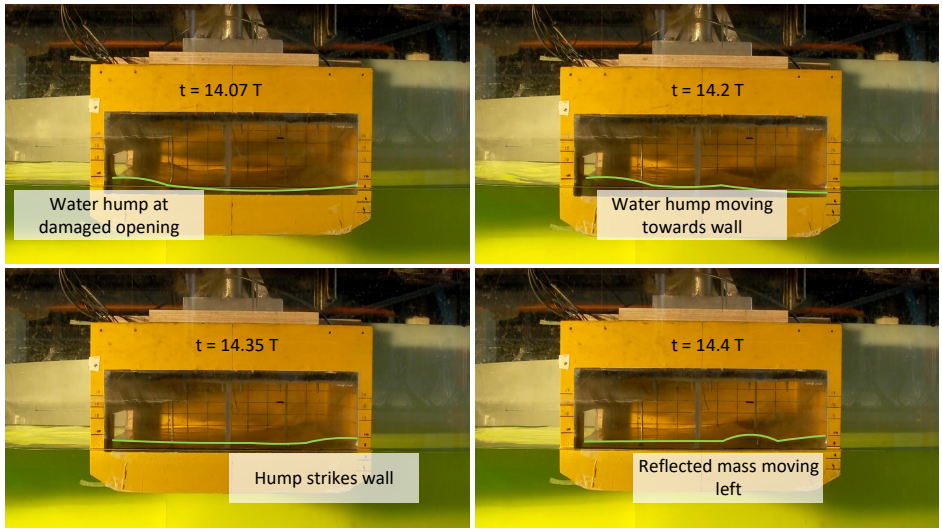

Figure 4.10: Second natural piston mode at $\omega^* = 0.72$ and $\eta_{3a} = 5$mm for FL 1, similar to wave system IV identified by Olsen and Johnsen (1975)

At certain frequencies and highest excitation amplitude $\eta_{3a} = 7$mm, breaking waves also occur in the middle of the tank as observed by Bouscasse et al. (2013). A similar behavior is observed at $\omega^* = 1.25$ and for the highest forcing amplitude, i.e., $\eta_{3a} = 7$mm, as shown in figure 4.11, where part of the progressive wave is reflected from the wall and meets the incoming wave from the opening. This causes a secondary splash near the middle of the tank. Such phenomena could cause high loading on an already damaged structure, in particular when wave breaking happens near an interior obstacle. To investigate the quantitative danger, the local loads induced on the compartment must be investigated. This has not been done here, as it would require a dedicated setup and suitable pressure sensors. This behavior is confirmed using 2D OF simulations at the same forcing frequency and amplitude in figures 4.12 and 4.13. The images from the simulation confirm the behavior described above using velocity vectors. Two crests, one at the opening

and the other at the undamaged wall move towards each other quickly (plots (c), (d)), merge to form a large peak (plot (e)) following which run-down is observed (plot (f)). The velocity of the two interacting waves can be estimated from the figures. The crest of each travelling wave is located at roughly 0.25 and 0.75 B in plot (c) of figure 4.12. These two meet in the middle of the compartment to form a peak at 8.25 T, each travelling a distance of 0.25 B. Thus, the waves travel with velocity $\approx 0.25B/0.25T = 0.625$ m/s. In full scale, this leads to a velocity of ≈8.3 m/s. Such a velocity is high enough to cause high local pressures on deck. Figure 4.14 shows the dynamic pressure obtained from OF numerical simulations using a pressure probe. The probe is placed at the center of the compartment on the deck. It is expected that the peak in pressure should occur just after the secondary splash up (or at start of run-down phase). From figure 4.13, a run-down is observed around 8.375 T (plot (e)). In general, this pressure peak should be periodic occurring at $nT + 3T/8$, for every n^{th} forced oscillation. Dashed lines in figure 4.14 are marked at every $3T/8$ and show the presence of a peak in pressure in the vicinity of these time instants. The peak pressure value is 1.9 times the hydrostatic pressure on the deck. This confirms the possibility of peaked local loads occurring on the deck.

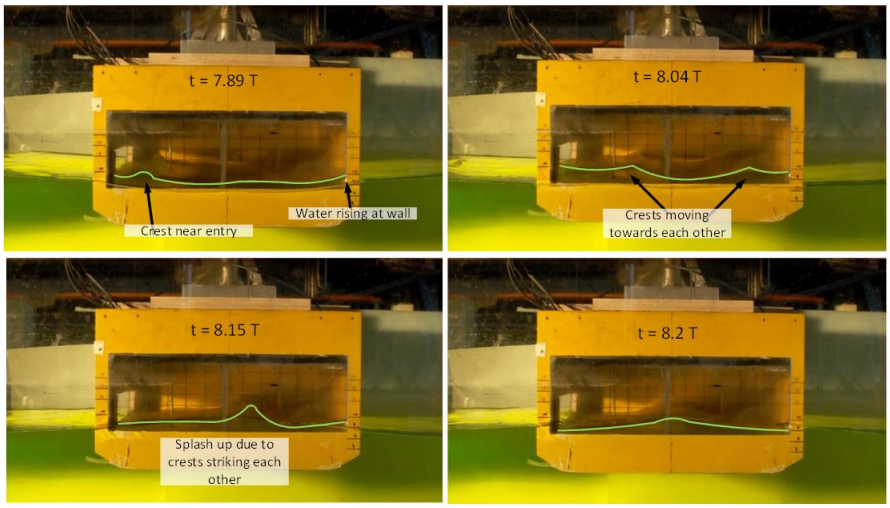

Figure 4.11: Secondary splash up in the middle of the tank at $\omega^* = 1.25$ and $\eta_{3a} =$ 7mm for FL 1 identified for the first time by Bouscasse et al. (2013)

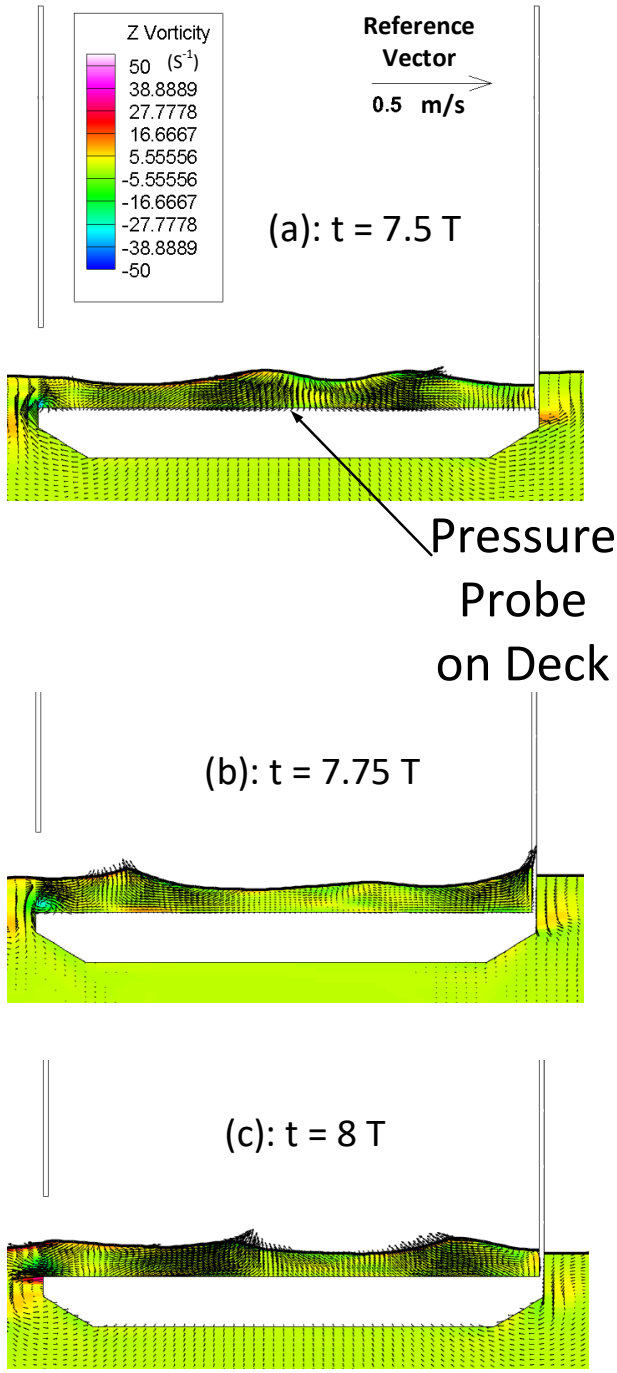

Figure 4.12: OF numerical results: Secondary splash up in the middle of the tank at $\omega^* = 1.25$ and $\eta_{3a} = 7$mm for FL 1 demonstrated through using OF. Vorticity (s^{-1}) field is shown along with velocity vectors

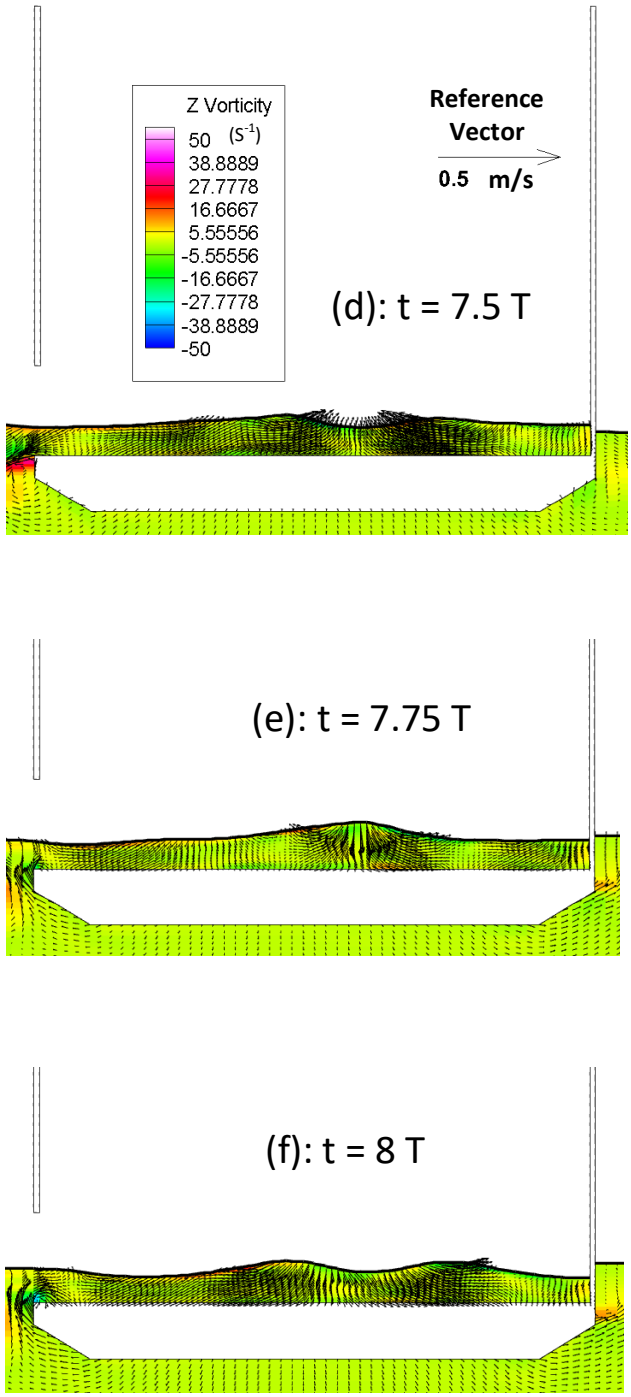

Figure 4.13: This is a continuation of figure 4.12

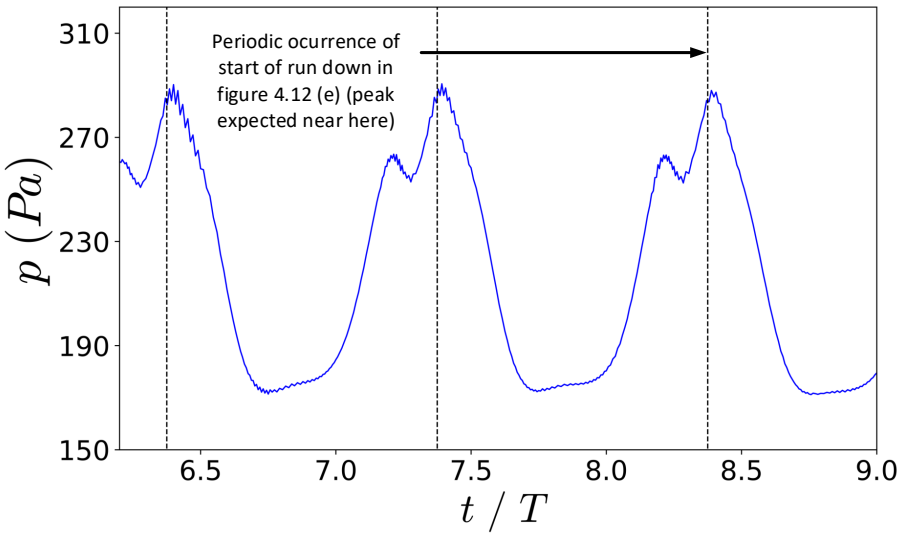

Figure 4.14: Dynamic pressure (using a probe in OpenFOAM) at the center of the damaged compartment

Figure 4.15 presents the non-dimensional added mass and damping coefficients in heave for filling level FL 1 obtained from eq. (4.8). The values of added mass at small frequencies show large negative values and large deviation from the behavior in intact condition at the same stationary draft. At higher frequencies, peaks are not observed but values are much smaller as compared to the intact section. The in/outflow of water through the opening is limited at higher frequencies with local floodwater effects being dominant. These do not cause a large change in the integrated heave force on the section when compared to an intact section. Also, it must be noted that the restoring coefficient for a damaged section is smaller as compared to an intact section. At smaller frequencies, especially near the first piston mode, large inflow/outflow causes large additional water mass to oscillate with the model. Large change in vertical force occurs, which, coupled with a smaller calculated restoring coefficient, leads to a negative added mass. Mathematically, this behavior can be confirmed using force amplitude and phase difference values shown in figure 4.16. The force amplitude shows peak near piston mode resonance frequencies. The phase difference decreases with decrease in frequency with a 90 degree phase difference occurring around the second piston mode resonance frequency. The added mass has large negative values below this frequency. Damping also increases at frequencies around the first and second piston mode i.e. $\omega^* = 0.27$ and $\omega^* = 0.73$ as compared to the intact ship section. This is related to the wave systems inside the damaged compartment, which help in wave generation capability of the damaged section. This can also be related to the force amplitude and phase values in figure 4.16. At the first piston mode resonance, large force values cause larger damping, whereas, near the second piston mode resonance a phase difference of 90 degree leads to a minor peak.

The behavior at the three forcing amplitudes is similar for the added mass except at the smallest forcing amplitude, especially for smaller frequencies. The damping shows much more nonlinear behavior. This may be related to nonlinear wave generation due to the damage opening.

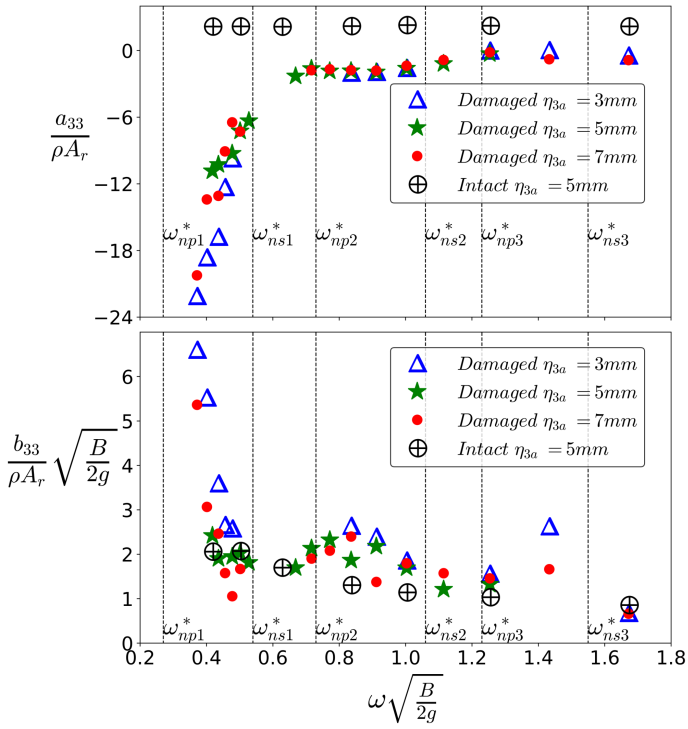

Figure 4.15: Added mass and damping coefficients in heave as a function of frequency for three forced-heave amplitudes and filling level FL 1

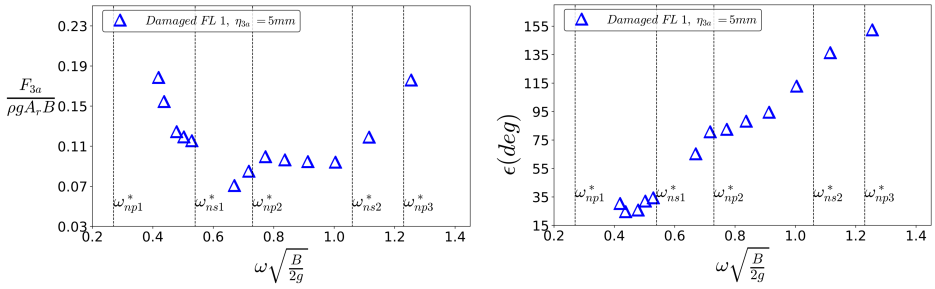

Figure 4.16: Heave force amplitude and phase difference (ϵ) as a function of frequency for filling level FL 1

Figure 4.17 compares the 2D added mass and damping coefficients in heave for a damaged section as given by eq. (4.11) with Newman et al. (1984) potential-

flow values from eq. (4.9). A good agreement is observed at higher frequencies. Newman et al. (1984) assumed the outside region has an infinite depth. At smaller frequencies, finite depth effects become non-negligible as mentioned earlier and deviation from the theoretical values is seen, for example for non-dimensional frequencies less than 0.6 the wavelength is 4 times as large as the water depth, therefore, non-negligible finite depth effects must be present below this frequency. Overall, the trend is predicted reasonably with large negative added mass values near first piston mode resonance, peak in damping near the first piston mode and a much smaller peak near the second piston mode resonance. In the present case, the non-dimensional resonance frequency for the first piston mode is around 0.27, which is much smaller than the frequencies studied in the experiments. Therefore, it is observed that values are going towards a peak but a large peak as for Newman et al. (1984) is not seen. Also, a small local peak, small to be seen in the figure, occurs near the second piston mode for the theoretical results based on Newman et al. (1984). This peak is confirmed by the experimental results and is actually higher for them.

Figure 4.18 compares the 2D added mass and damping coefficients in heave for a damaged section from experiments and OF. The general trend with change from positive to large negative values is captured by OF quite well. The damping values also match reasonably well with some differences for smaller frequencies.

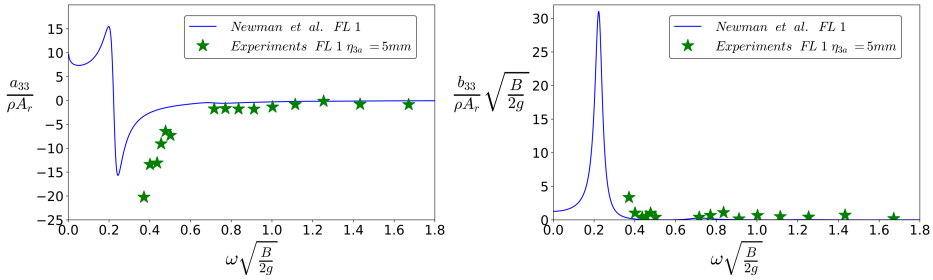

Figure 4.17: Added mass and damping coefficients in heave: comparison between experiments and Newman et al.'s expression for FL 1

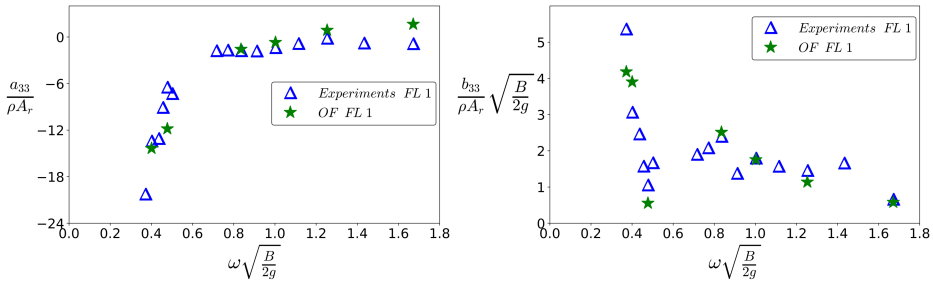

Figure 4.18: Added mass and damping coefficients in heave : comparison between experiments and OF for FL 1

Filling level 2: Piston mode and sloshing resonance modes are also observed for this filling level. The occurrence of these resonance phenomena are documented by the wave elevation RAO at WP 1 and WP 2 inside the damaged compartment shown in figure 4.19. A peak is observed near the first piston mode resonance frequency; correspondingly, a pumping piston mode occurs with a large in/outflow through the compartment (see figure 4.20). The values for WP 2 are higher than WP 1, this is also observed in the experimental images and occur because the antinode at the wall is close to WP 2 but there is almost a node-like condition near WP 1, as expected in case of the piston mode. A major peak is also seen at higher frequencies near the second piston mode frequency (see figure 4.21).

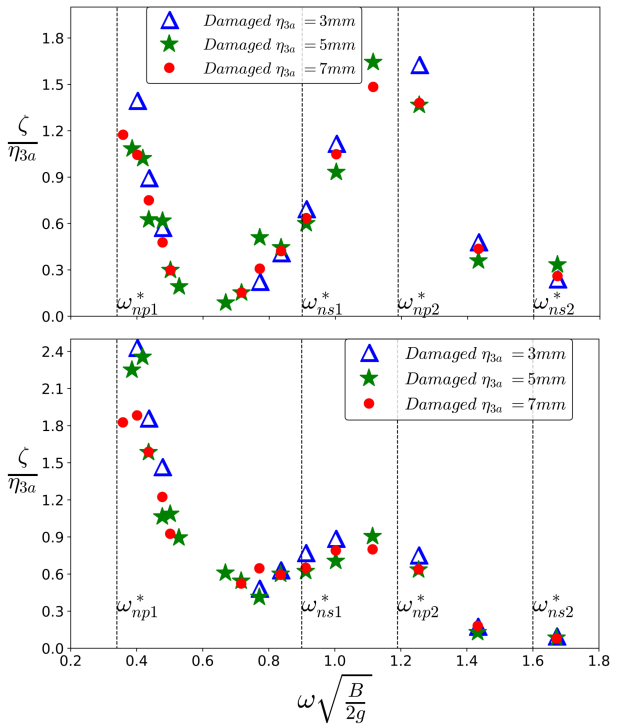

Figure 4.19: Wave probe RAOs at WP 1 (top) and WP 2 (bottom) inside damaged compartment as a function of frequency for three forced-heave amplitudes and filling level FL 2

In this case, WP 1 has higher values as compared to WP 2. This is because the location of the antinode is now changed and is closer to WP 1. The first sloshing mode is observed from video analysis, as documented in figure 4.22. In this case, WP 1 and WP 2 record RAO values between 0.6-0.8 without a large peak. The antinodes for piston modes are much closer to the wave probe locations as compared to sloshing modes. Also, for the second sloshing mode (see figure 4.23), the wave probes actually lie at the nodes and thus very small values are observed, as shown in figure 4.19.

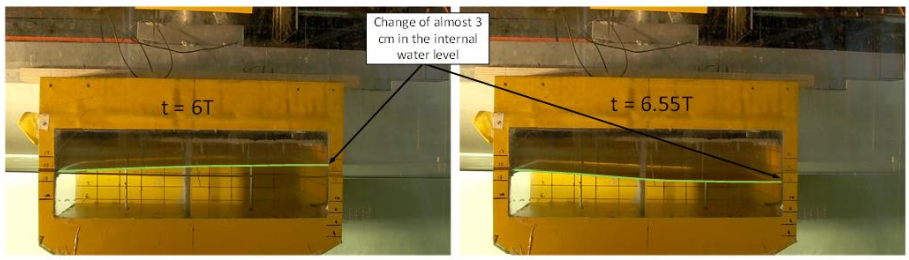

Figure 4.20: First natural piston mode resonance inside damaged compartment at $\omega^* = 0.41$ and $\eta_{3a} = 5$mm for FL 2

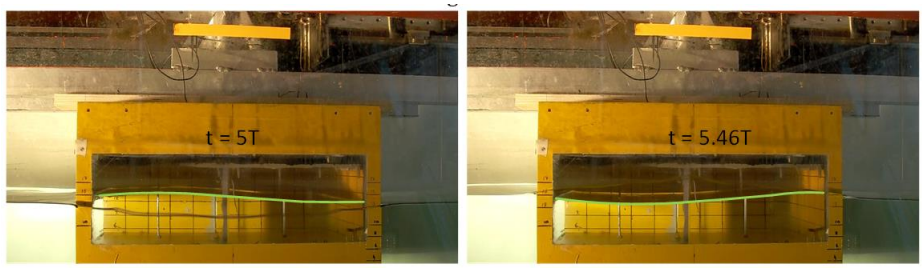

Figure 4.21: Second natural piston mode inside damaged compartment at $\omega^* = 1.25$ and $\eta_{3a} = 5$mm for FL 2

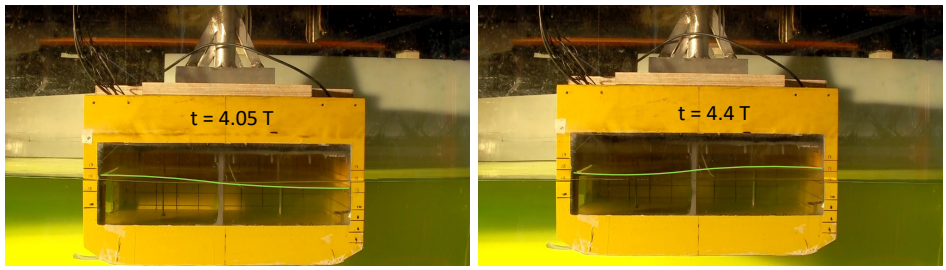

Figure 4.22: First natural sloshing mode inside damaged compartment at $\omega^* = 0.9$ and $\eta_{3a} = 5$mm for FL 2

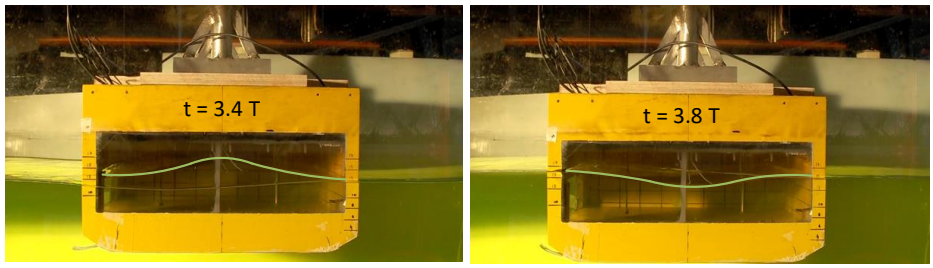

Figure 4.23: Second natural sloshing mode inside damaged compartment at $\omega^* = 1.67$ and $\eta_{3a} = 5$mm for FL 2

An illustration for the behavior of wave elevation measurements at sloshing and piston mode resonance, as describe above, is shown in figure 4.24. The RAOs generally document a linear behavior except for the smallest forcing amplitude and for small frequencies.

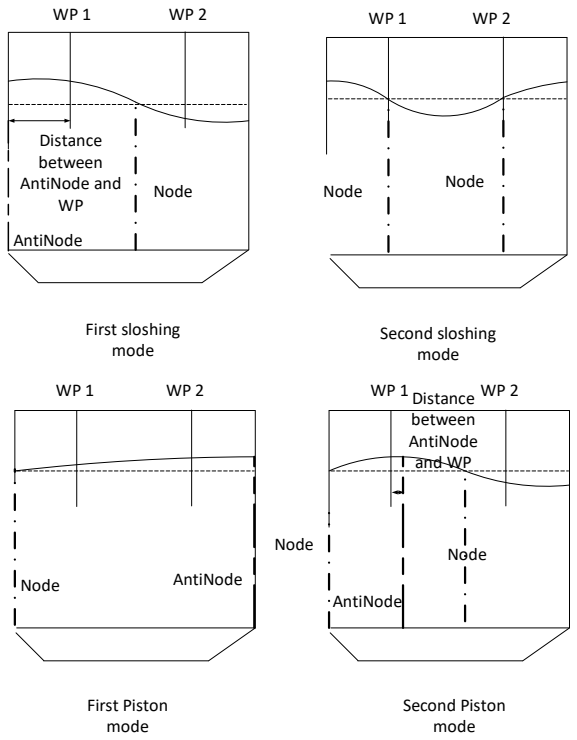

Figure 4.24: Illustration of wave amplitude measurements in various resonance conditions at the two wave probes

Figure 4.25 demonstrates snapshots at various time instants from OF simulations for $\omega^* = 0.41$, $\eta_{3a} = 5$mm and FL 2. The left plots show a significant change in internal water level at the undamaged wall as shown by experiments (see figure 4.20). Large vortex shedding is observed at the opening in plots (a) and (c) of figure 4.25, indicating cross-flow through the opening. This argument is complemented by plots (b), (d) showing a large inflow and outflow velocity. This is characteristic of piston mode resonance, confirming the description from the experimental observations.The large vortex shedding can lead to higher damping values as documented later. Figure 3.20 shows snapshots from OF simulations at $\omega^* = 1.67$ and $\eta_{3a} = 5$mm for FL 2, confirming the occurrence of second sloshing mode. They also confirm the statement, made in the previous experimental analysis, that small flow occurs through the opening near sloshing resonance frequencies. There are small positive velocities at the top of the opening and small negative velocities near the bottom resulting in a very small net inflow/outflow at both time instants.

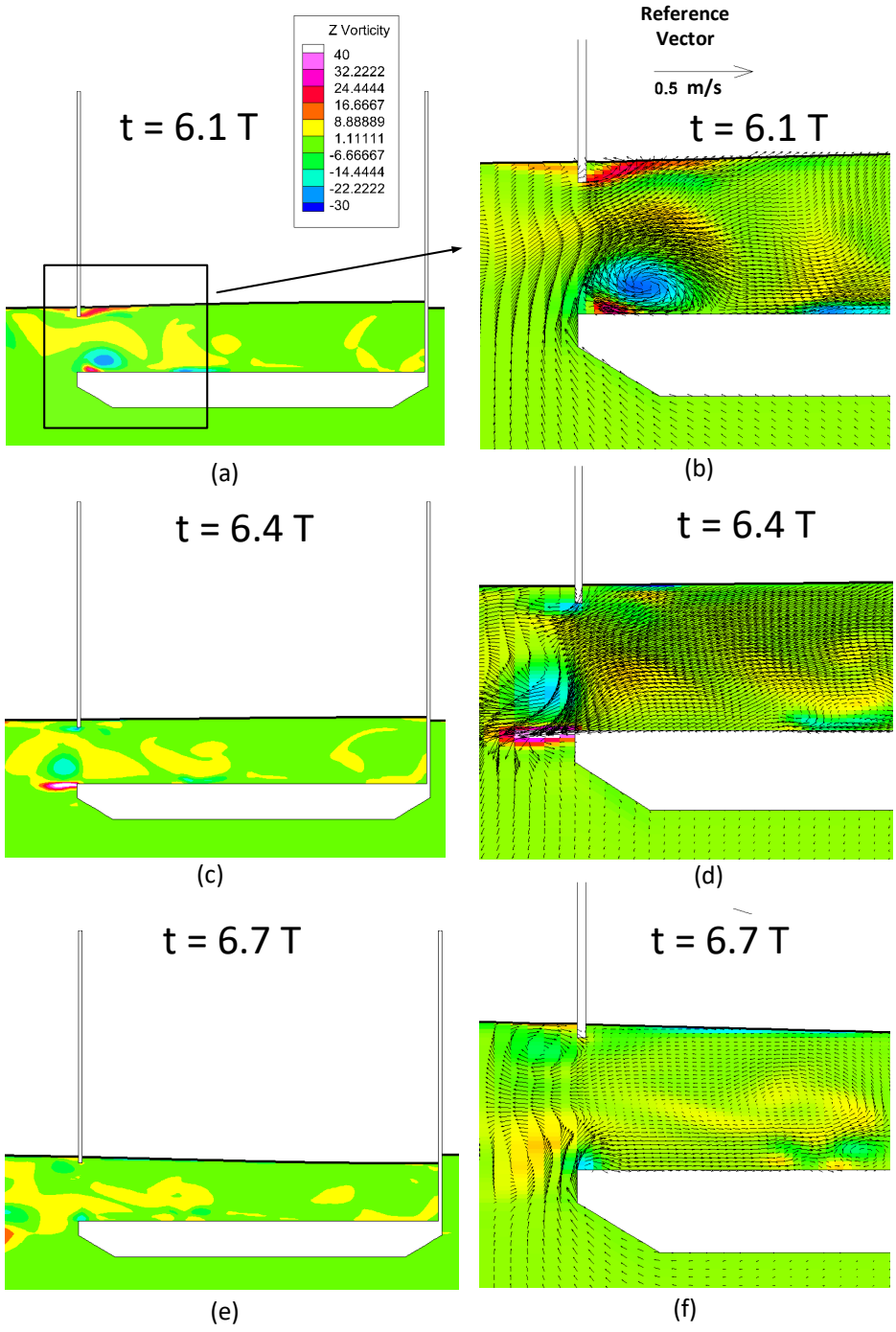

Figure 4.25: OF numerical results: First natural piston mode inside damaged compartment at $\omega^* = 0.41$ and $\eta_{3a} = 5$mm for FL 2 using OF. Vorticity (s^{-1}) field is shown in left plots with velocity vectors (enlarged opening view) in right plots

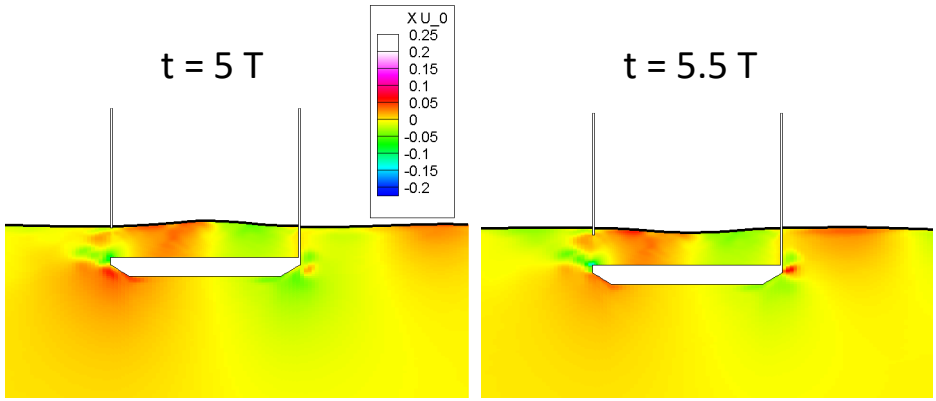

Figure 4.26: OF numerical results: Second natural sloshing mode inside damaged compartment at $\omega^* = 1.67$ and $\eta_{3a} = 5$mm for FL 2. Horizontal velocity (m/s) field is shown

At very high frequencies, 3D behavior inside the compartment is observed (figure 4.27). The first sloshing mode along the length L_c of the tank and a sloshing mode along the breadth B_c of the tank are seen. However, the amplitude associated with the mode along the length is much smaller as compared to the mode along the breadth.

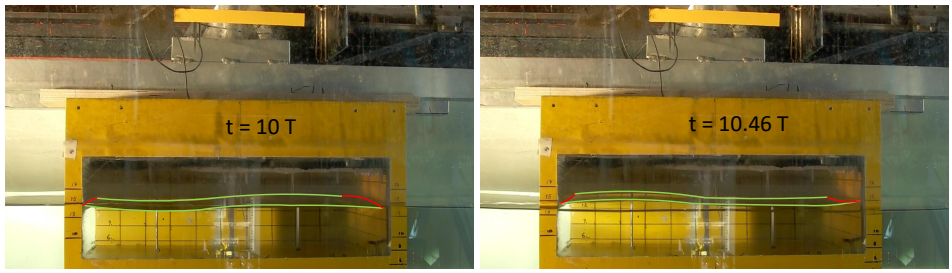

Figure 4.27: 3D sloshing mode inside damaged compartment at $\omega^* = 2$ and $\eta_{3a} = 5$mm for FL 2 (green lines show sloshing mode along the breadth and red lines show sloshing mode along the length of the model)

Figure 4.28 shows non-dimensional added mass and damping coefficients in heave for filling level 2. A sharp change in added mass values, i.e. negative to positive peak, occurs near the first piston mode resonance frequency and this is due to a large amount of water entering and leaving the damaged compartment and thus a large vertical force amplitude occurring at this resonance frequency. Also, at the first piston mode resonance change in phase occurs, which coupled with large force lead to large negative and positive added mass values. Similar behavior for heave added mass is documented in numerical studies carried out by Kong and Faltinsen (2010) and in the analysis presented in Newman et al. (1984). In the present case, near the first piston mode resonance, there can be change of almost 3 cm in the water level inside the compartment, see figure 4.20. It corresponds to a

change of 6 kg, i.e. 33% of floodwater mass inside the compartment at stationary position. This can cause a large change in the vertical force. At higher frequencies, positive but smaller values of added mass coefficients occur as compared with an intact section. The damping shows two peaks, a larger peak at the first piston mode resonance and a minor peak near the second piston mode frequency. The damping values are much higher when compared to those of an intact ship with the same draft near the first piston mode resonance. Large in/outflow occurs near piston mode resonance and, therefore, a large amount of energy is radiated at the first piston mode resonance. The curves for the non-dimensional hydrodynamic coefficients at different forcing amplitudes are practically superimposed except near the first piston mode resonance and highest forcing amplitude. This may be a consequence of vortex shedding at the opening top edge, which can have higher effect for higher forcing amplitudes.

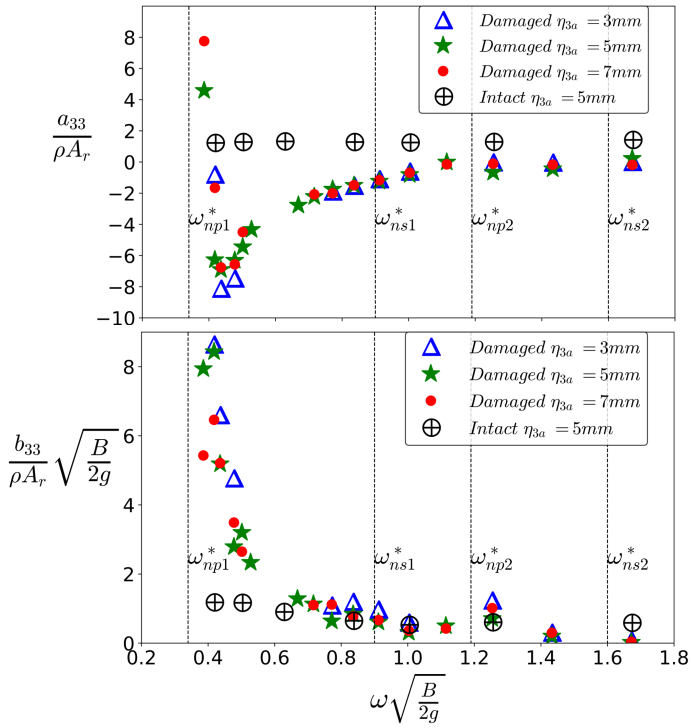

Figure 4.28: Added mass and damping coefficients in heave as a function of frequency for three forced-heave amplitudes and FL 2

Figure 4.29 shows the comparison between the 2D added mass and damping coefficients in heave for a damaged section at filling level FL 2 from eq. (4.11) and Newman et al. (1984) potential-flow values from eq. (4.9). Similar to filling level 1, good agreement is observed for higher frequencies but deviation occurs at smaller frequencies, as discussed earlier, due to finite depth effects. The agreement is better at this filling level compared to FL 1. This may be because Newman et al.

(1984) assumed linear free-surface condition and the nonlinearities are less strong for this filling level. The values from Newman et al. (1984) for the added mass show a jump from large negative to positive values at first piston mode resonance. The same is captured very well in the experiments. The peak in damping near the first piston mode and a small peak near the second piston mode are also similar to results by Newman et al. (1984). The peak in damping at second piston mode for Newman et al. (1984) expression is too small to be seen in the figure.

Figure 4.30 shows the comparison between the 2D added mass and damping coefficients in heave for a damaged section from experiments and OF for filling level FL 2. The general trend is captured reasonably by OF for both added mass and damping with better agreement being observed for the damping values.

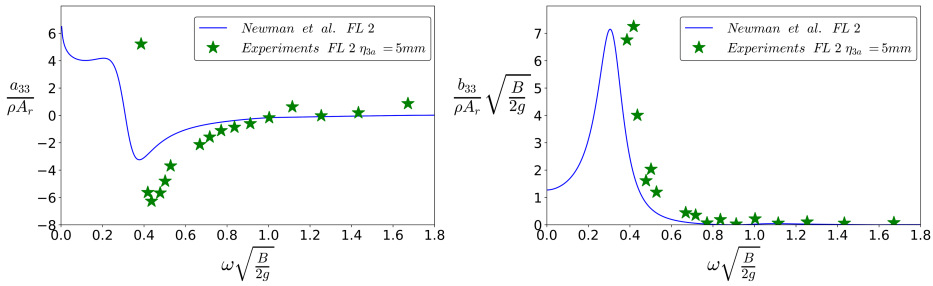

Figure 4.29: Added mass and damping coefficients in heave: comparison between experiments and Newman et al.'s expression for FL 2

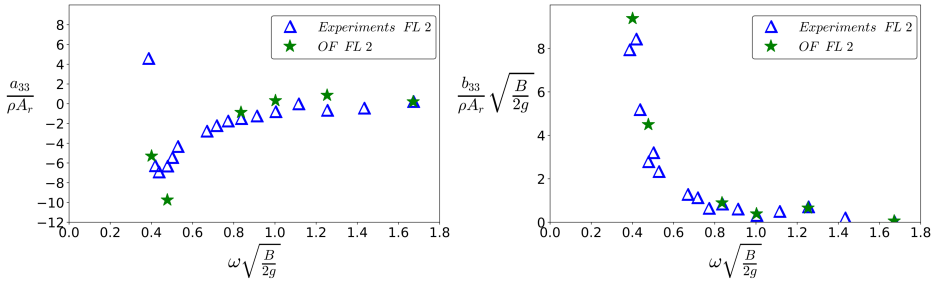

Figure 4.30: Added mass and damping coefficients in heave : comparison between experiments and OF for FL 2

Filling level 3: The wave elevation RAOs for WP1 and WP2 inside the compartment at filling level 3 are shown in figure 4.31. A similar behavior as observed for FL 2 is seen, with peaks near the piston mode resonance frequencies. Figure 4.32 provides the non-dimensional added mass and damping coefficients for this filling level. The non-dimensional added mass coefficient has similar trends as for filling level FL 2. The damping values are slightly smaller when compared with those for FL 2. This is because damping decreases with increase in draft, as mentioned earlier for an intact section. In addition, at smaller frequencies, nonlinear behavior is higher in this case as compared to FL 2.

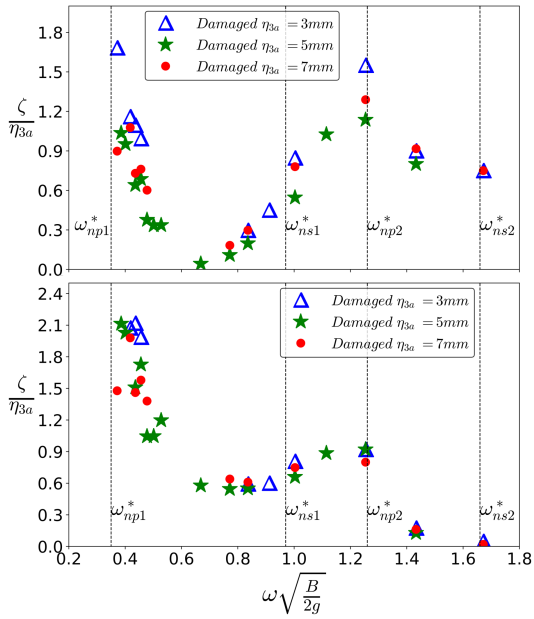

Figure 4.31: Wave probe RAOs at WP 1 (top) and WP 2 (bottom) inside damaged compartment as a function of frequency for three forced-heave amplitudes and FL 3

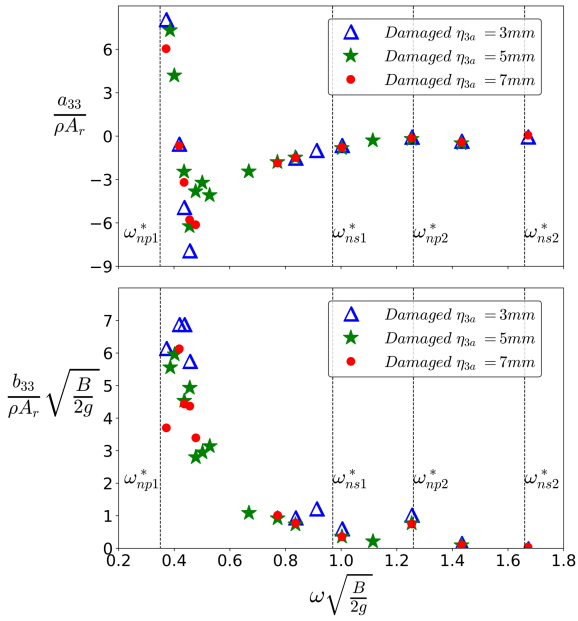

Figure 4.32: Added mass and damping coefficients in heave as a function of frequency for three forced-heave amplitudes and FL 3

In general, the damping for filling level FL 2 and 3 is higher than for FL 1. This is reasonable because for higher filling levels, the opening is completely submerged and vortex shedding occurs at the top and bottom edges of the opening. Numerical results from OF confirm this behavior when comparing results for filling levels FL 1 and 2 at the same forcing frequency and amplitude (see figure 4.33). Large vorticity values with opposite signs are observed at the opening for time instants when in/outflow occurs in the case of higher filling level. For FL 1, the vorticity is more or less constant and some vortices are observed near the bottom edge of the opening at the two time instants.

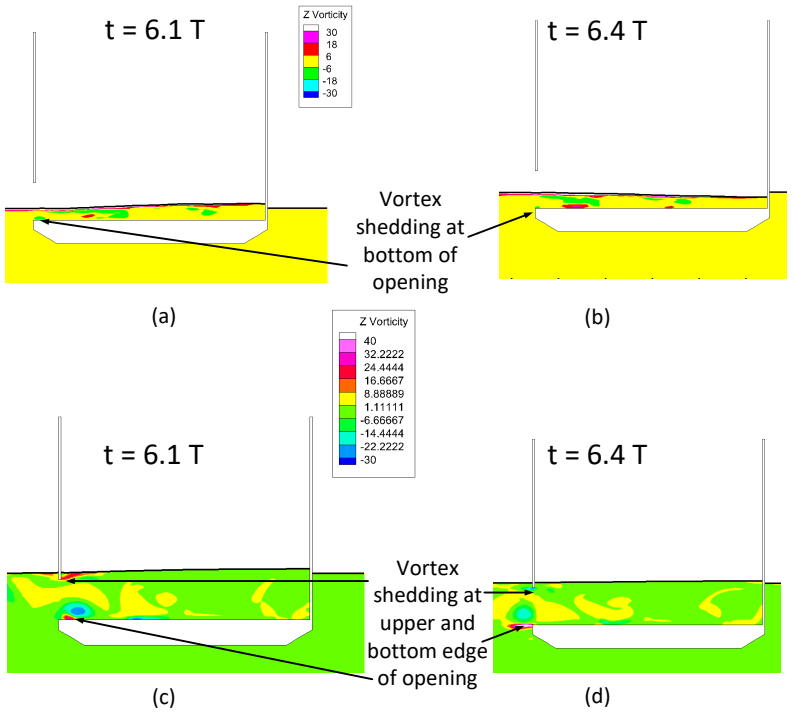

Figure 4.33: OF numerical results: Vorticity (s^{-1}) fields as a function of filling level. Results at the same non-dimensional time instants for FL 1 (top) and FL 2 (bottom) at $\omega^* = 0.41$ and $\eta_{3a} = 5$mm

Influence of air compressibility

As described in section 3.1.3, airtight condition has a strong influence on the wave scenarios inside the damaged compartment. Figures 4.34 and 4.35 show the wave elevation RAOs inside the compartment for airtight and ventilated cases at two filling levels, FL 2 and 3, respectively. The results demonstrate that piston mode resonance is almost completely absent for an airtight compartment (see figure 4.36), while it was clearly observed for ventilated compartment. Piston mode in-

volves a large change in volume of floodwater mass inside the compartment. This water displaces the air inside the compartment when it is ventilated. When the compartment is airtight, the air cannot escape leading to large overpressure limiting the water flow through the opening. Since sloshing resonance implies small change in air-cushion volume, the effect of air compressibility is less severe as evident from the combined free-surface condition in eq. (3.12). For example, in case of first sloshing mode, the volume above the water surface remains almost unchanged and less overpressure builds up in the compartment. Therefore, occurrence of sloshing resonance is not restricted. A clear peak at first sloshing resonances for filling level FL 2 and 3 is observed in case of the airtight compartment.

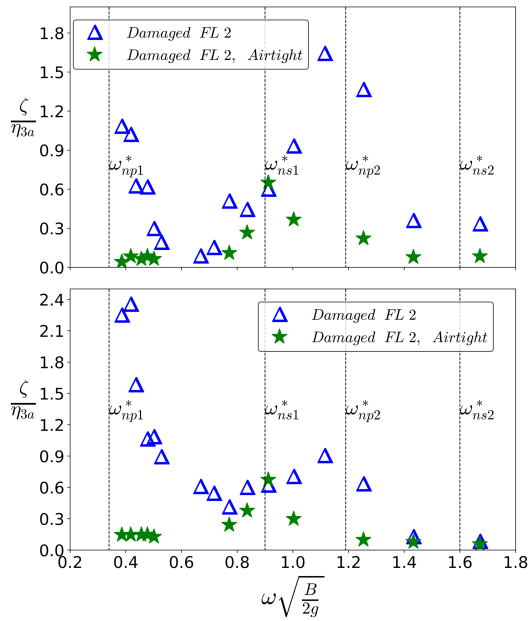

Figure 4.34: Wave probe RAOs WP 1 (top) and WP 2 (bottom) inside damaged compartment as a function of frequency, for ventilated and airtight conditions at FL 2

Figure 4.37 shows snapshots from OF simulations in airtight scenario at $\omega^* = 0.4$ and $\eta_{3a} = 5$mm for FL 2. The top plots provide the phase fraction (α) shaded for the water region ($\alpha >$0.5). The water level at the two examined time instants is almost unchanged, thus, piston mode resonance is absent just as observed in the experiments. The bottom plots of the figure give the velocity vectors near the opening for the same time instants as the top plots. It was shown earlier for a ventilated compartment at piston mode resonance that large inflow/outflow velocities occur at the opening. However, in this case, the velocities are small and not unidirectional. Positive velocity at the top of the opening and negative velocity near the bottom is observed. Therefore, small net flow through the opening occurs as hypothesized earlier. In addition, the behavior near the opening is almost similar for all time instants.

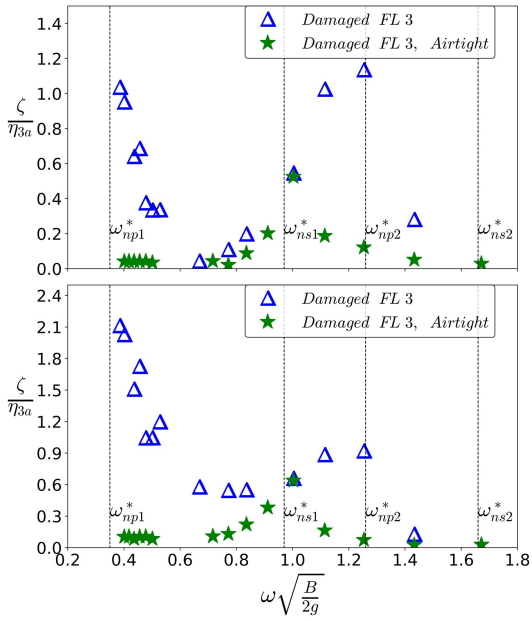

Figure 4.35: Wave probe RAOs WP 1 (top) and WP 2 (bottom) inside damaged compartment as a function of frequency, for ventilated and airtight conditions at FL 3

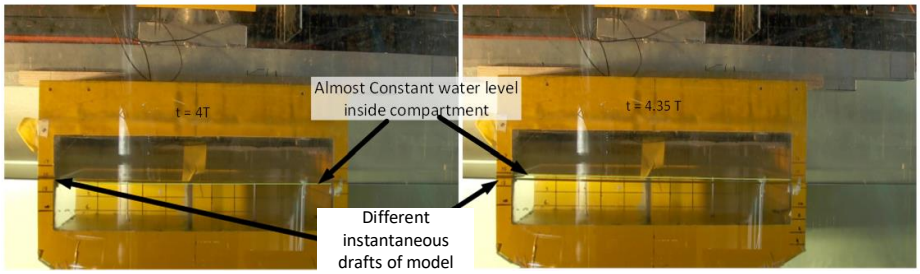

Figure 4.36: Water elevation (piston mode resonance absent) inside the airtight compartment for $\omega^* = 0.4$ and $\eta_{3a} = 5$mm for FL 2: the water level appears constant. Compare with figure 4.20 for the ventilated compartment in the same conditions.

Figures 4.38 and 4.39 show the non-dimensional added mass and damping coefficients in heave for filling levels FL 2 and 3, respectively, in airtight and ventilated conditions. The damping values are much lower for airtight cases, especially near the first and second piston mode resonance. Piston mode resonance is absent leading to small in/outflow through the opening and, therefore, small wave radiation outside the model. This behavior is consistent for both filling levels. The added mass coefficients for airtight condition have similar behavior as for intact

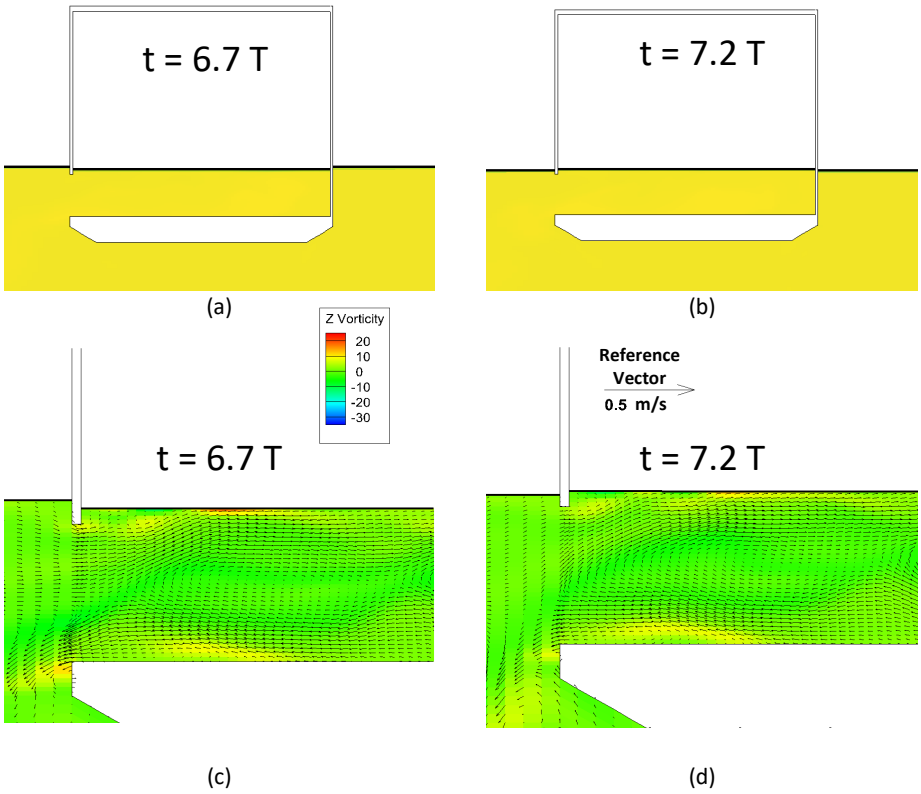

Figure 4.37: OF numerical results: Water elevation inside the airtight compartment for $\omega^* = 0.4$ and $\eta_{3a} = 5$mm for FL 2 (top plots) and vorticity (s^{-1}) field with vectors (bottom plots)

condition, as shown for FL 2, with slightly higher values at smaller frequencies. It must be emphasized that, as explained earlier in section 4.1.1, the restoring coefficient in this case is much larger as compared to a ventilated damaged section and, therefore, negative added mass values are not observed.

It is to be noted that effect of air compressibility in full scale might differ due to presence of small vent holes and difference in air-cushion stiffness. Making eq. (3.12) non-dimensional implies that, together with geometric similarity, both Froude number ($Fn = \frac{U}{\sqrt{Lg}}$) and Euler number ($Eu = \frac{p_0}{\rho U^2}$) must be same in model and full scale. Here U is the characteristic flow velocity and L is the characteristic length for a system. For instance, with the intended scale ratio of 1:40, ambient pressure in model scale has to be scaled down by 1:40 to ensure the same Eu value. Since cavitation must be avoided, there is an operational limit on how much the air pressure can be lowered in the experiments. The facilities in wave flumes do not allow for such an investigation in general but Ypma (2010) has presented experiments for a damaged scenario in vacuum conditions. This was out

of scope in the present work due to limitations in the wave flume. To avoid the problem of using depressurized setup and to circumvent the problem of scaling air stiffness from model to full scale, Ruponen et al. (2013) performed experiments on a full-scale ship to study the effect of air cavity on flooding. They concluded that air compressibility can slow down initial flooding largely and therefore can have a significant effect on ship motions. Air compressibility may be, therefore, important even in real-ship scenarios if the air-pipe vents are small or flooded.

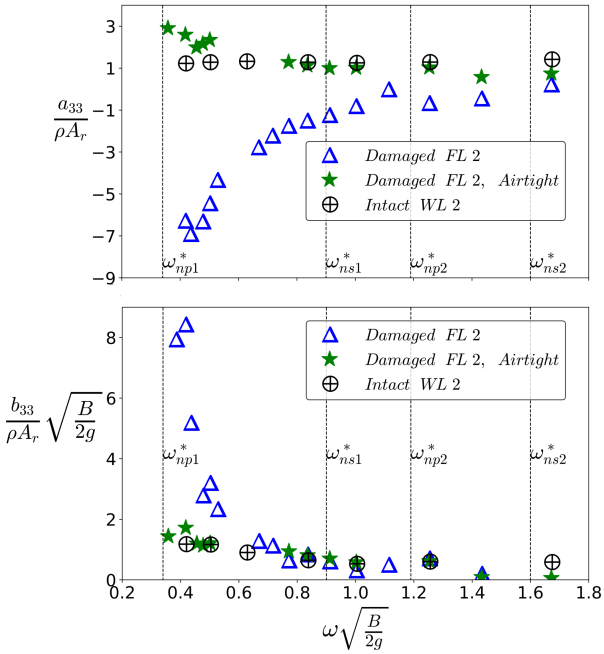

Figure 4.38: Added mass and damping coefficients in heave as a function of frequency, for ventilated and airtight conditions at FL 2

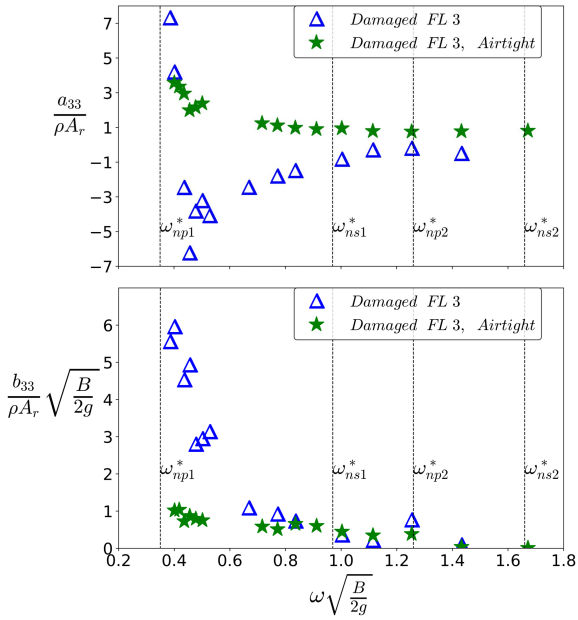

Figure 4.39: Added mass and damping coefficients in heave as a function of frequency, for ventilated and airtight conditions at FL 3

Influence of damage opening breadth

The effect of opening size is examined using opening sizes O1 and O2 as defined in chapter 2. The results discussed so far refer to opening size O1. Figures 4.40 and 4.41 show the wave amplitude RAOs inside the compartment for the two openings at filling levels 1 and 2, respectively. For FL 1, WP 1 has smaller values for opening O2 since the inflow is restricted to some extent and it is harder for the water to enter as compared to the larger opening. This effect is only observed for small frequencies because in this case it takes more time for inside wave systems to adjust to the outside water level and the smaller opening size acts as a barrier. Opposite behavior is observed for WP 2 as high frequency nonlinear waves may be trapped inside the compartment due to obstruction at the opening and cause higher values near the wall opposite to the opening. In case of filling level FL 2, wave elevations for both openings show a similar behavior except at some frequencies.

Figures 4.42 and 4.43 show non-dimensional added mass and damping coefficients in heave for opening O1 and O2 at filling FL 1 and 2, respectively. The added mass shows similar values for the two openings except near the first piston mode frequency. This may be because 3D effects are introduced due to the smaller opening. The damping shows similar behavior with slightly higher values for O2, mostly near the first piston mode resonance. Piston mode resonance is associated with large in/outflow through the opening and, therefore, for opening O2, there may be a significant effect of vortex shedding from the appendage edges.

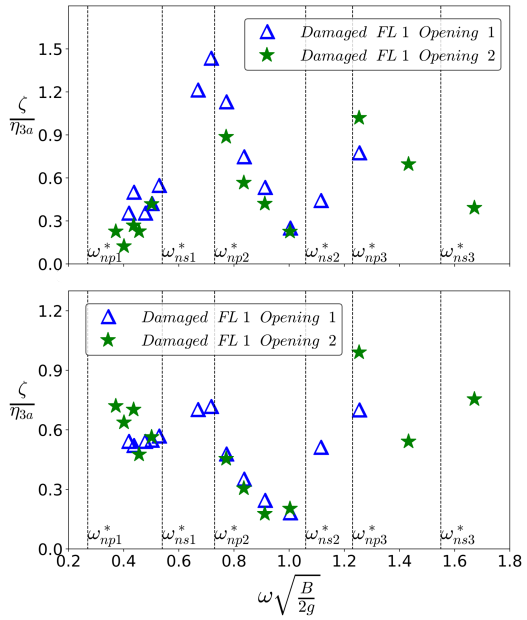

Figure 4.40: Wave probe RAOs at WP 1 (top) and WP 2 (bottom) inside damaged compartment as a function of frequency at $\eta_{3a} = 5$mm for O1 and O2 at FL 1

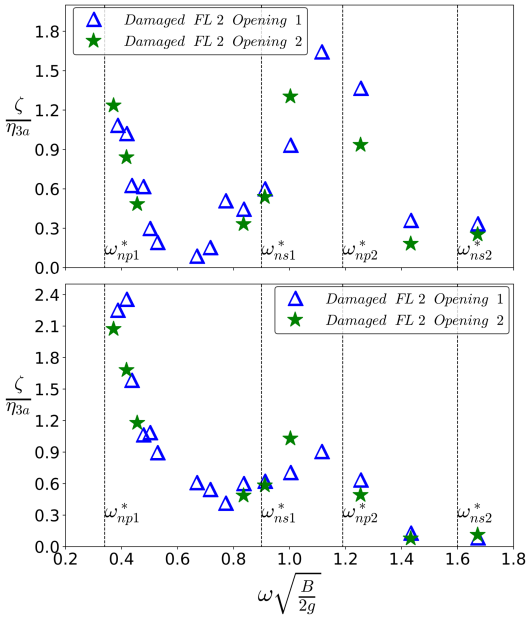

Figure 4.41: Wave probe RAOs at WP 1 (top) and WP 2 (bottom) inside damaged compartment as a function of frequency at $\eta_{3a} = 5$mm for O1 and O2 at FL 2

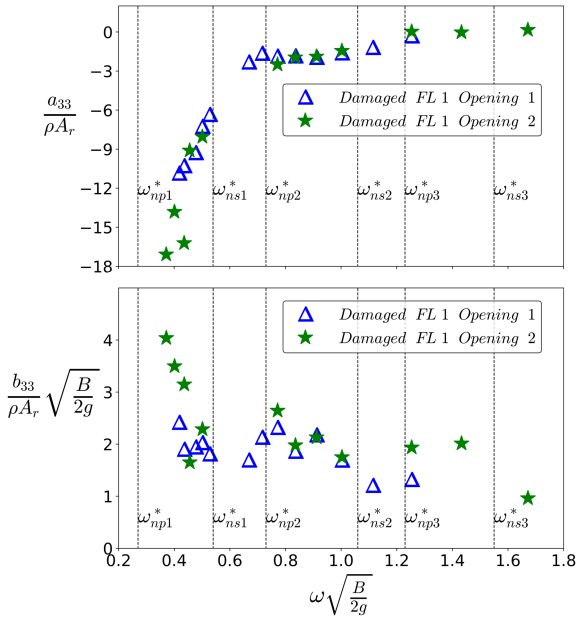

Figure 4.42: Added mass and damping coefficients in heave as a function of frequency at $\eta_{3a} = 5$mm for O1 and O2 at FL 1

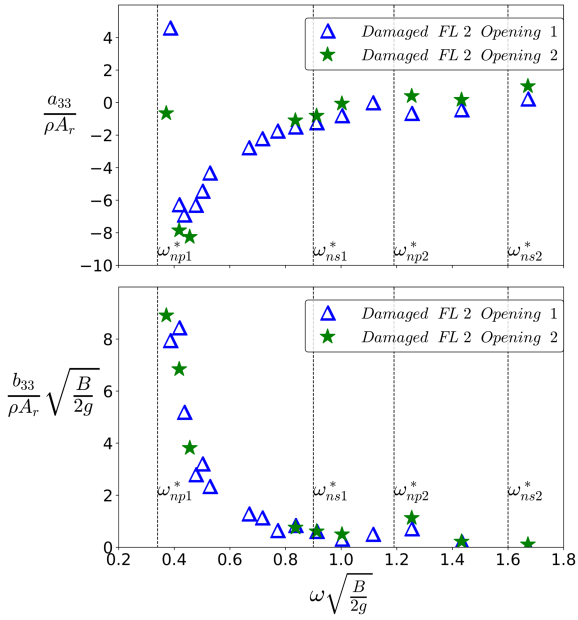

Figure 4.43: Added mass and damping coefficients in heave as a function of frequency at $\eta_{3a} = 5$mm for O1 and O2 at FL 2

Repeatability

Two sets of repetitions, in addition to the main tests, were performed to check for uncertainty and repeatability of the experiments. Repetition is not performed for all frequencies and cases because of the limited availability of lab resources. For FL 1, 5 frequencies were chosen to cover the range from small to high values along with some intermediate frequencies. Similarly, for FL 2, 6 frequencies were selected. Figure 4.44 shows mean values with deviation for added mass and damping coefficients in heave and wave elevation amplitudes at filling levels FL 1 and 2. The results show acceptable deviation for all measured values. Deviation from mean values in added mass and damping is larger at smaller frequencies with the maximum deviation being 18% and 17%, respectively. Wave elevation values show larger deviation as compared to added mass and damping values at most frequencies but are within an acceptable range. In particular, the maximum deviation is 23% and 20% for WP1 and WP2, respectively. Overall, the repeatability seems to be acceptable.

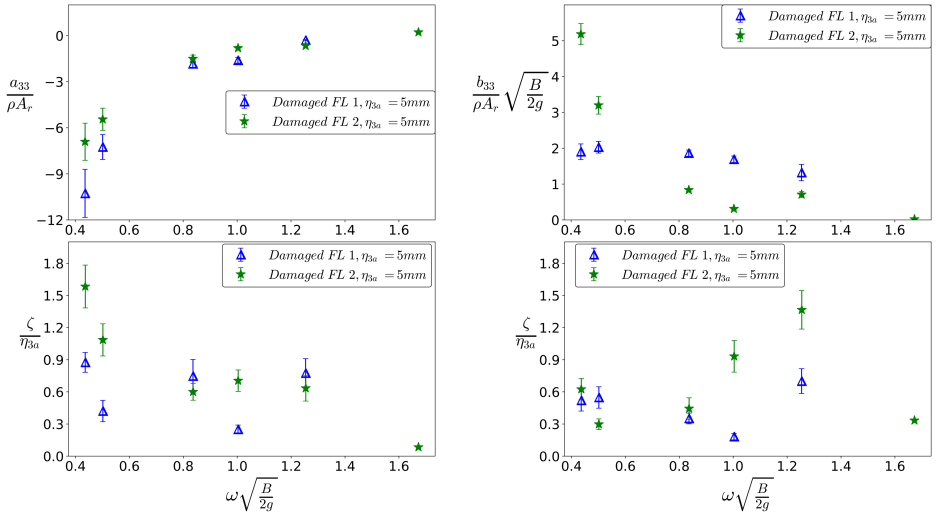

Figure 4.44: Deviation with mean values as a function of frequency in added mass, damping and wave elevation at WP1 (bottom left) and WP2 (bottom right) for $\eta_{3a} = 5$mm and two filling levels

4.3 Summary

Forced oscillatory heave tests in calm water have been carried out by varying the model-motion and damage-opening parameters. Analysis of images from videos, wave elevation inside the damaged compartment, and forces on the model was performed to investigate the wave systems and resonance conditions in the floodwater. The present experiments aim at demonstrating the complex behavior of hull and floodwater interaction. A single DoF constrained model will not capture

completely the complex physics of flooding and might amplify some dynamic effects. However, single DoF tests in heave are simple to implement with good reliability and are valuable in identifying important resonance phenomena. The outcomes of the physical investigation can be summarized as follows:

- Non-dimensional added mass and damping coefficients in heave for intact and damaged sections at identical drafts are considerably different, especially near piston mode resonance.
- Change in filling levels causes resonance frequencies and associated wave systems to vary considerably. Sloshing and piston mode resonances are observed inside the damaged compartment. Piston mode resonance causes a large effect on the added mass and damping coefficients.
- A reasonable agreement between theoretical estimates and experiments is observed both for the resonance frequencies and added mass and damping coefficients.
- Numerical results using OpenFOAM show reasonable agreement with the experiments for added mass and damping coefficients for FL 1 and 2. Snapshots from the simulations also show similar phenomena as observed in the images from experiments. Velocity and vorticity field from the simulations have been used to confirm the arguments derived based on experimental observations. For example, large vortex shedding at first piston mode resonance (see figure 4.25), absence of large in/outflow at sloshing resonance (see figure 4.26) etc. Numerical simulations from OF, thus, serve as an important tool in verifying and complementing the experiments so to enhance the physical understanding of involved phenomena.
- Air compressibility can have important effects. It limits the inflow/outflow of floodwater through the opening, which is especially evident near piston mode resonance where almost no water enters for an airtight damaged compartment. The damaged section behaves closer to an intact section with the same draft. However, air compressibility in full scale can be slightly different due to presence of vent holes.
- At certain heave excitation frequencies, some scenarios can lead to important local loads, e.g. secondary splash up as shown in figure 4.11. The presence of local loads is confirmed using OF numerical simulations.
- Damage-opening length influences the wave systems inside the damaged compartment. It does not show a considerable effect in the hydrodynamic forces acting on the body.
- Repeatability of the experiments can be viewed as acceptable.

Chapter 5

Freely-Floating Damaged Model In Waves

This chapter presents analysis and discussion for a freely-floating model in a small wave flume. The model, shown in chapter 2, is smaller than the flume breadth to achieve predominantly two-dimensional behavior in the experiments. Free-roll decay tests were preliminarily performed for intact and damaged sections to understand the effect of floodwater on roll natural period and roll damping of the model. Then, freely-floating tests in regular beam-sea waves were carried out on the model section in intact and damaged conditions. Video recordings and measurements of wave elevation inside the damaged compartment were performed in all experiments. Linear response amplitude operators (RAOs) for water elevation inside the model and model motions are presented and discussed. Effect of wave steepness, wave period, initial loading condition, damage-compartment division about centerplane (symmetric/asymmetric flooding), damage-opening size and air compressibility in the damaged compartment are examined. The presented results demonstrate occurrence of sloshing and piston mode resonances and their influence on damaged ship motions in waves is highlighted. A linearized strip theory method based on viscous flow is implemented, as explained in chapter 3, to cross-check and complement the experimental results.

In the first part of this chapter, free-roll decay analysis and tests are discussed followed by the investigation of intact and damaged section in beam-sea waves. Lastly, transient flooding behavior is discussed. A summary of the analysis and results is presented at the end of the chapter.

5.1 Results and Discussion

In this chpater, freely-floating section in intact and damaged condition is examined in beam-sea waves. The symbols and axis definitions used in this chapter are consistent with chapters 2 and 3. Results from roll decay tests for the intact and damaged sections and transient flooding in regular waves for the damaged model section are also presented. Hereafter, in this chapter, the term linear is used to indicate the contributions to the examined variables, extracted from the analysis,

that are associated with the incident-wave frequency. The results are documented in terms of linear wave elevation RAOs inside the damaged compartment and linear motion RAOs (sway, heave and roll) for the freely-floating section. To assess the influence of damage and resulting floodwater on the body motions, both intact and damaged conditions were examined. Intact tests were performed for one wave steepness i.e. kA=0.033. For the damaged section, two wave steepnesses i.e. kA=0.033 and 0.066 have been examined. These values seem to be small but at higher steepness 3D behavior was observed with yaw motions causing contact of model section with tank walls. Since 2D behavior was the main focus of present work, higher kA values were avoided. Also, higher values of the wave steepness may have caused capsizing. It must be noted that for the damaged condition, the coupled floodwater-body motion will always introduce nonlinearities. On the other hand, the focus of the present study is to analyze effect of sloshing and piston mode resonance on the linear response of a damaged ship. Therefore, based on the work in Begovic et al. (2013), the results in terms of linear RAOs (first-order harmonic) are presented, as they help in understanding relevant physical behavior. Sloshing and piston-mode resonance scenarios are presented using images from the tests with the green bold lines representing the 2D internal surface inside the damaged compartment. The results are made non-dimensional as follows:

$$\omega^* = \omega\sqrt{\frac{B}{2g}}; \zeta^* = \frac{\zeta_a}{A}; {\eta_i}^* = \frac{\eta_{ia}}{A}; {\eta_4}^* = \frac{\eta_{4a}}{kA}$$

here, η_{ia} denotes the motion amplitude with i=2 for sway and i=3 for heave motion, ζ_a is the wave elevation amplitude inside the damaged compartment and A is the incident wave amplitude.

It should be noted that intact and damaged conditions are considered for the same loading cases (LC 1 and LC 2). This is consistent with analyzing the change in seakeeping when an intact vessel is suddenly damaged. Therefore, the draft of the examined damaged model is much higher than that of the corresponding intact model. Vugts (1968) has demonstrated that the draft can affect the added mass and damping coefficients, especially for roll motions. To highlight the pure effect of the opening on the hydrodynamic coefficients, the added-mass and damping coefficients for the damaged ship could be compared against those of an intact ship with the same draft. This has not been examined using experiments. Therefore, OF simulations are used as complementary research tool to highlight this effect. Figure 5.1 shows heave damping coefficient for a 2D intact and damaged section at mean drafts corresponding to loading condition LC 2. OF results for an intact section at the same mean draft as the damaged section are also shown. The results confirm that the draft of an intact section affects the damping coefficient (as confirmed e.g. by results in figure 4.4) and a larger draft tends to reduce this hydrodynamic coefficient. The non-dimensional damping coefficient in heave for intact and damaged sections with the same draft have similar values at sufficiently large non-dimensional frequencies; this suggests that the presence of a damage plays a minor role at higher frequencies. At lower non-dimensional frequencies instead, the damping coefficient is greatly influenced by the presence of the damage and is much larger than that of an intact section with the same

loading condition and, therefore, with lower draft.

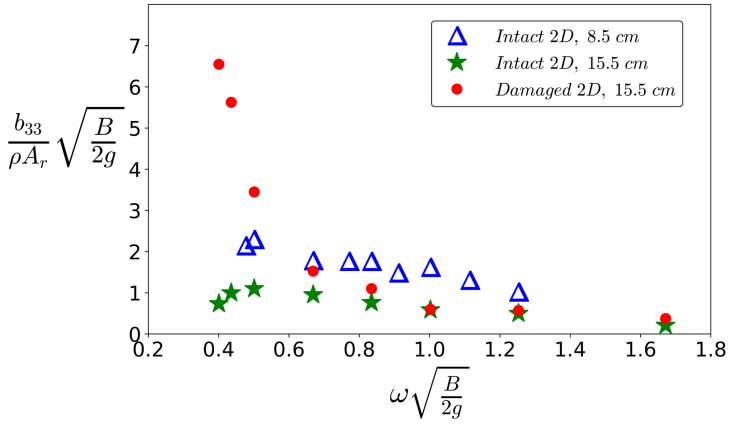

Figure 5.1: OF numerical simulations: Non-dimensional heave damping coefficient as a function of non-dimensional frequency for intact and damaged 2D section at different drafts corresponding to loading LC 2

5.1.1 Free-roll Decay Tests

Free-roll decay tests are performed to determine the natural roll period and roll damping for the model both in intact and damaged conditions. The tests were performed in calm water condition. For the damaged section, free-roll decay tests were carried out with three opening sizes (O1-3) and with opening O1 in airtight condition. In addition, free-roll decay tests were performed for cases with floodwater inside the damaged compartment for loading LC 1 and LC 2 but keeping the damage opening closed. This implies that no flow occurs through the opening and the floodwater mass inside the compartment is constant. The model is allowed to attain equilibrium after flooding in both loading conditions and the opening is then sealed using a very thin wooden plate. The damaged compartment, therefore, behaves as a closed partially-filled tank.

Neglecting coupling effects with the other degrees of freedom, the roll motion equation (assuming nonlinear damping) is assumed to be of the form

$$(I_{44} + A_{44})\ddot{\eta}_4 + B_{44l}\dot{\eta}_4 + B_{44,quad}\dot{\eta}_4\,|\dot{\eta}_4| + C_{44}\eta_4 = 0 \tag{5.1}$$

where I_{44} is the moment of inertia in roll about the x-axis through CoG, A_{44} is the added moment in roll, B_{44l} is the linear damping coefficient, $B_{44,quad}$ is the quadratic damping coefficient, C_{44} is the linear restoring coefficient and η_4 is the roll motion. The added moment A_{44} is estimated using $A_{44} = \left(\frac{2\pi}{T_{n4}}\right)^2 C_{44} - I_{44}$, where T_{n4} is the natural roll period, which is calculated as the mean of the first three oscillation periods in the experiments. Furthermore, I_{44} is defined in table 2.2 of chapter 2 and C_{44} is calculated as described in section 3.2.3. An optimization technique is used to find the best fit for the experimental data and, therefore, linear

and quadratic damping coefficients are calculated. Runge-Kutta 4th order scheme is used to solve for the roll angle in eq. (5.1). The results from this method are indicated as 'fitted data' in the comparison against experimentally measured free-roll decay data. The roll natural periods as well as linear and quadratic damping coefficients, estimated from the experiments for the various examined conditions are documented in table 5.1.

Model tests for free-roll decay of a RO-RO ship model in intact and damaged condition (described in benchmark studies, Papanikolaou, 2001; Papanikolaou and Spanos, 2004) demonstrated that the natural roll period and roll damping increase going from intact to damaged condition for the examined loading conditions (KGs). Other works, e.g. Acanfora and De Luca 2016, 2017; Begovic et al. 2013; Manderbacka et al. 2015b; Domeh et al. 2015, etc. have supported this finding. Such behavior is also confirmed by numerical studies in Papanikolaou (2001), although with deviations as compared to the experiments. Kong and Faltinsen (2010) also confirmed numerically that natural periods for roll and heave increase in damaged condition. A similar behavior was observed in the present experiments. A large change in the natural roll period occurs from intact to damaged condition. An important reason is the decrease of C_{44}. The damping is also considerably larger because of the inflow/outflow of the floodwater through the damage opening. Linear damping mainly consists of wave radiation damping, whereas quadratic damping is associated with viscous and vortex shedding effects. The dimensional value of linear damping increases from an intact section to a damaged section. If the non-dimensional values are considered in order to avoid the effect of increased draft in damaged condition, it is observed that the non-dimensional linear damping decreases slightly. The linear damping has similar values for all three damage opening sizes. It increases slightly for the smaller openings. The quadratic damping is not large for the intact section because there are no appendages or bilge keels. This contribution for the damaged section is believed to be mainly associated with the vortex shedding at the opening edges and its effect on the local pressure distribution. The strength of the shed vorticity depends on the magnitude of the inflow/outflow velocity through the opening as well as on the geometric details. Generally speaking, the damping for given inflow/outflow increases with decreasing interior body angle at the separation point. The magnitude of inflow/outflow velocity depends on the opening area because of continuity of water mass. Table 5.1 shows that the dimensional quadratic damping is largest for the damage opening O1 (largest opening) with ventilated compartment. If non-dimensional values of the quadratic damping with respect to the damaged opening area are considered, the order is reversed with opening O3 (smallest opening) having the largest quadratic damping coefficient. The quadratic damping decreases significantly for a damaged compartment in airtight condition as compared to the ventilated case. This suggests that the inflow/outflow is highly reduced, leading to limited vortex shedding at the opening and, therefore, much smaller quadratic damping.

Condition	Natural Roll Period T_{n4} (s)	Roll non-dimensional frequency $\omega_{n4}{}^{*} = \frac{2\pi}{T_{n4}}\sqrt{\frac{B}{2g}}$	Linear Damping Coefficient B_{44l} (kgm^2s^{-1})	$B^*_{44} = \frac{B_{44l}}{\rho B^3 L T_d}\sqrt{\frac{B}{2g}}$	Quadratic Damping Coefficient $B_{44,quad}$ (kgm^2rad^{-1})	$B^*_{44,quad} = \frac{B_{44,quad}}{\rho B^3 d h_d}$
Intact LC 1	0.92	1.09	0.63	0.02	0.56	-
Intact LC 2	0.94	1.067	0.6	0.016	0.56	-
Damaged LC 1 (O1)	4.03	0.249	0.4	0.008	3.43	1.15
Damaged LC 2 (O1)	2.45	0.409	1	0.0144	2.86	0.716
Damaged LC 2 (O2)	2.46	0.408	1.02	0.0147	2.29	0.76
Damaged LC 2 (O3)	2.43	0.412	1.02	0.012	2.0	1.0
Damaged LC 2 in airtight condition (O1)	2.6	0.386	0.8	0.010	1.15	0.29
Damaged LC 1 with Opening Closed	3.86	0.26	0.33	0.0067	1.15	-
Damaged LC 2 with Opening Closed	2.4	0.42	0.35	0.005	0.86	-

Table 5.1: Natural period for roll and linear and quadratic damping coefficient obtained from the free-roll decay tests

Figures 5.2-5.4 show a reasonable agreement between the measured and fitted roll time histories for the intact and damaged section in various conditions. The predicted curves for a damaged section have higher deviation as compared to an intact section but the overall data fit seem to be in reasonable agreement with the physical decay curves. They usually tend to have higher disagreement when the roll angle becomes small both for intact and damaged conditions. Figure 5.2 confirms similar natural period and damping in roll when the loading (draft) is changed for the intact ship section (see quantitative results in table 5.1). This is because the change in draft from loading LC 1 to LC 2 is not large, around 21%. Figure 5.3 illustrates that the roll motion dies out quicker for damaged section with loading LC 1 (smaller draft) as compared to loading LC 2. The quadratic damping is highest for the damaged condition with loading LC 1. This may be because for loading LC 1, the opening is partially submerged, whereas it is complete submerged for LC 2. This causes a 3D flow behavior of the free surface at the opening edges for LC 1 condition. Another reason can be the effect of smaller draft. As demonstrated in Vugts (1968) and also shown in figure 5.1, damping for smaller drafts is higher.

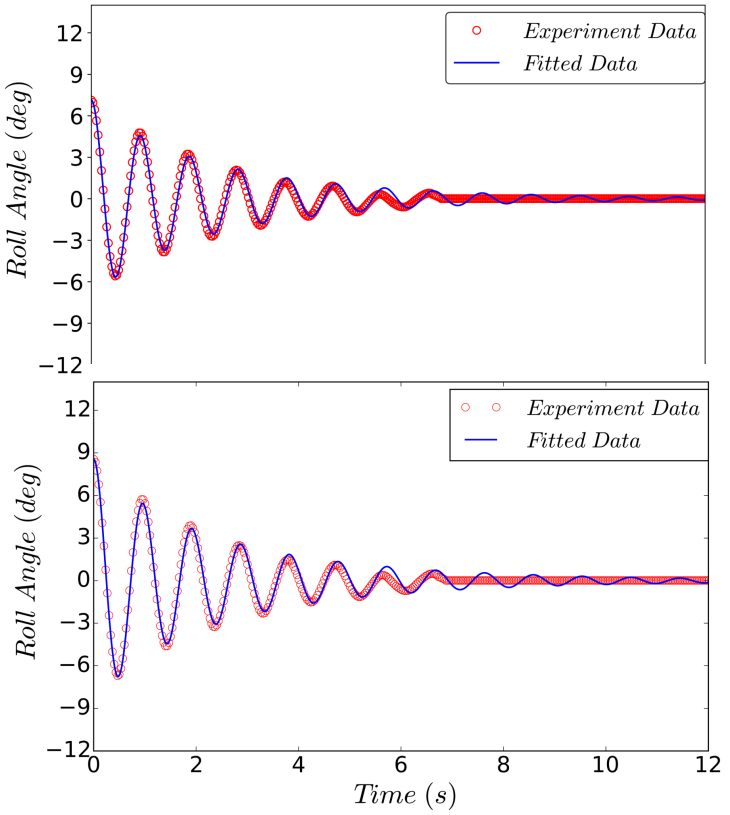

Figure 5.2: Time history of roll angle for intact section at loading LC 1 (top) and LC 2 (bottom)

Figures 5.2 and 5.3 show an increase of natural period and damping in roll when going from intact to damaged ship (in the same loading conditions). The increase in damping and natural period is much higher for the smaller loading. Figure 5.4 confirms that the damping is higher for the ventilated damaged condition than for the airtight damaged compartment. Also, as the damage opening size reduces, the net damping decreases. One important thing to note is that the natural period for a damaged section decreases slightly as the roll angle becomes smaller. This may be because of the transient dynamic effect of floodwater, which is not accounted for in the theoretical estimates. In addition, the damping for the first oscillation period is much higher as compared to the following periods.

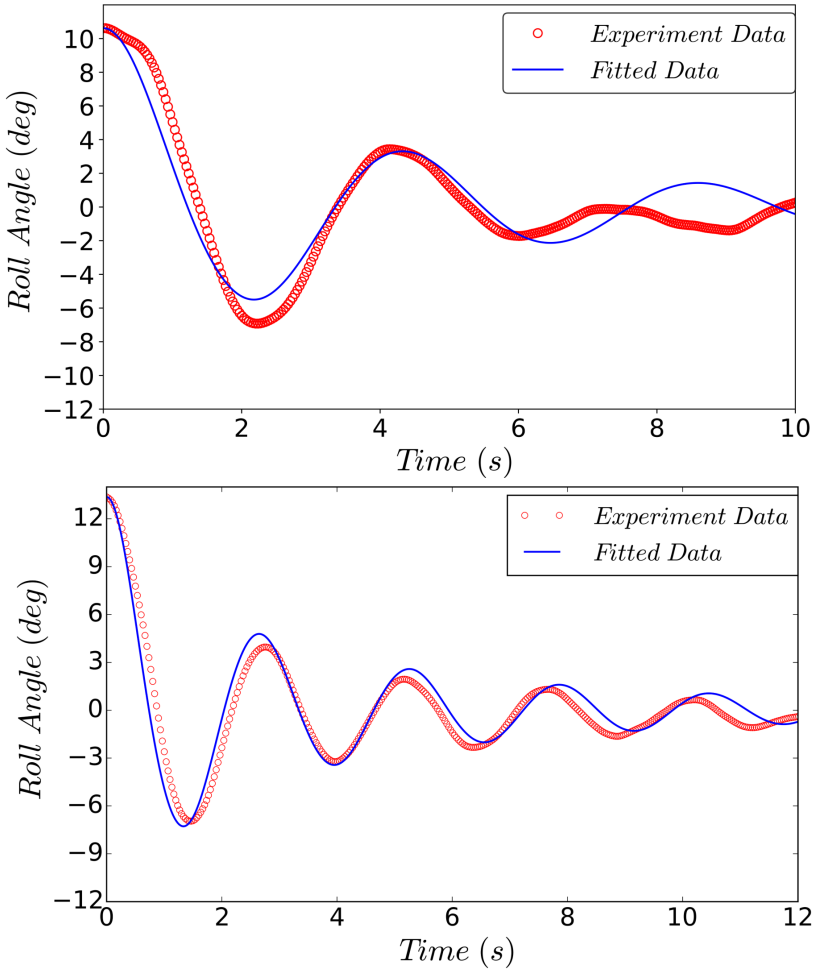

Figure 5.3: Time history of roll angle for damaged section with loading LC 1(top) and LC 2 (bottom) allowing inflow/outflow through the damage opening

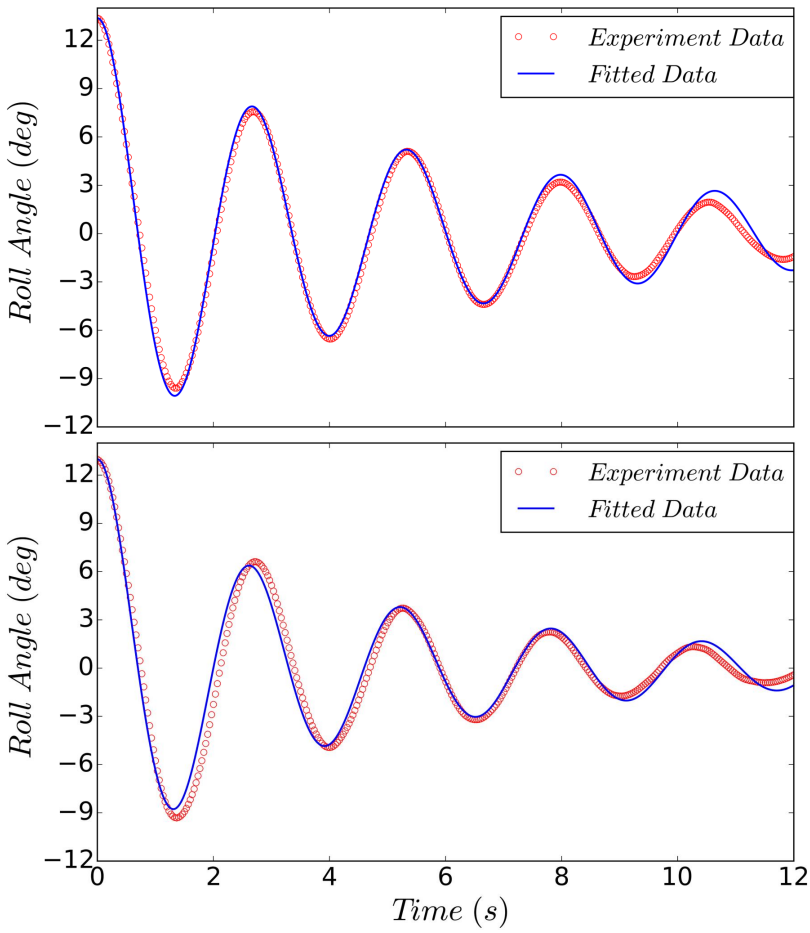

Figure 5.4: Time history of roll angle for damaged section with airtight compartment (top) and opening O3 (bottom) both at loading LC 2 allowing inflow/outflow through the damage opening

Figure 5.5 shows free-roll decay tests for the section with opening closed in loading LC 1 and 2 compared with the damaged scenario (inflow/outflow allowed). Natural roll periods for the two scenarios at both examined loading conditions are quite similar, a slight reduction occurs for the closed opening. The roll damping at both loading conditions is lower for the closed opening. This is because a closed tank provides damping effect (passive anti-roll tank) when the roll natural period of the section is close to the first natural sloshing mode in the tank (Faltinsen and Timokha, 2009). In case of LC 1, the natural sloshing period is 1.33 s and the natural roll period is around 4s (ω^*=0.25). For LC 2, the first natural sloshing period is around 1.05 s, whereas the natural roll period for the section is 2.4 s (ω^*=0.41). Thus, the closed tank is not able to provide a damping effect.

This can also be explained using forced roll OpenFOAM simulations with forcing frequency close to the natural roll frequency of the damaged sections with closed and open openings. The setup for the NWT is similar to the case of forced heave motions examined in chapter 4. Figure 5.6 shows a simple 2D section (similar to the experimental damaged cross-section) with a closed tank (left plots) and damaged compartment with inflow/outflow through the opening (right plots). The case with the closed tank has a small and uniformly distributed vorticity throughout the inner fluid domain. For the damaged case (open opening), there are pockets of large positive and negative vorticity in the floodwater with significant vortex shedding occurring at the opening. The opening also modifies flow structures near the opening with respect to the intact case, whereas, they are preserved towards the undamaged side. This large vortex shedding contributes significantly to the damping, especially quadratic damping.

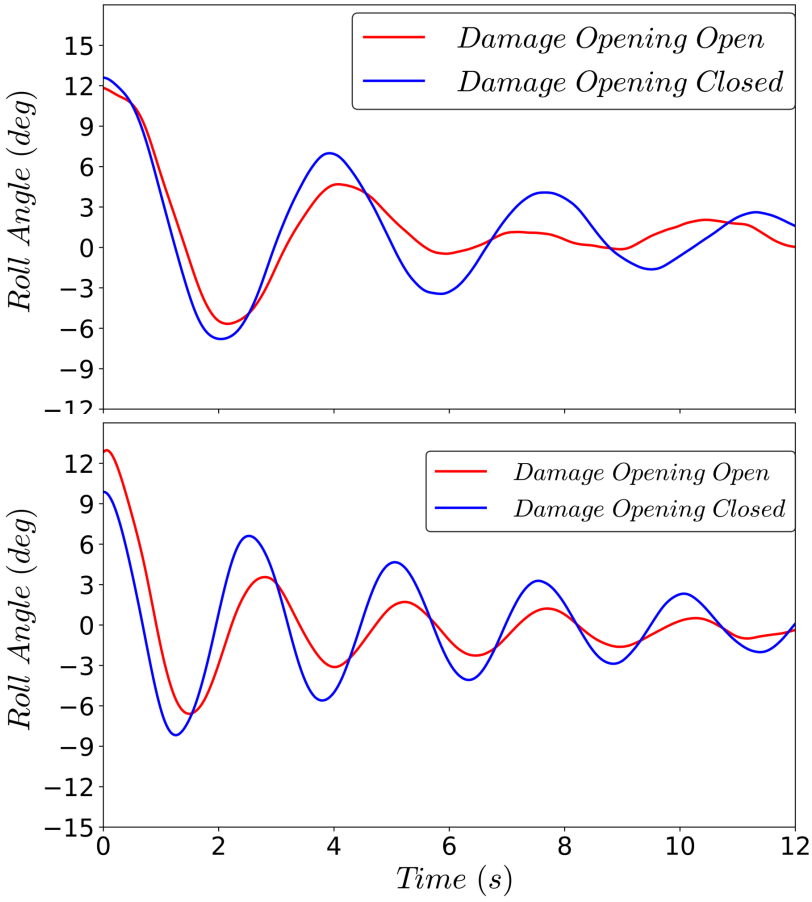

Figure 5.5: Time history of roll angle for damaged section with inflow/outflow through the damage opening restricted and allowed in loading LC 1 (top) and LC 2 (bottom)

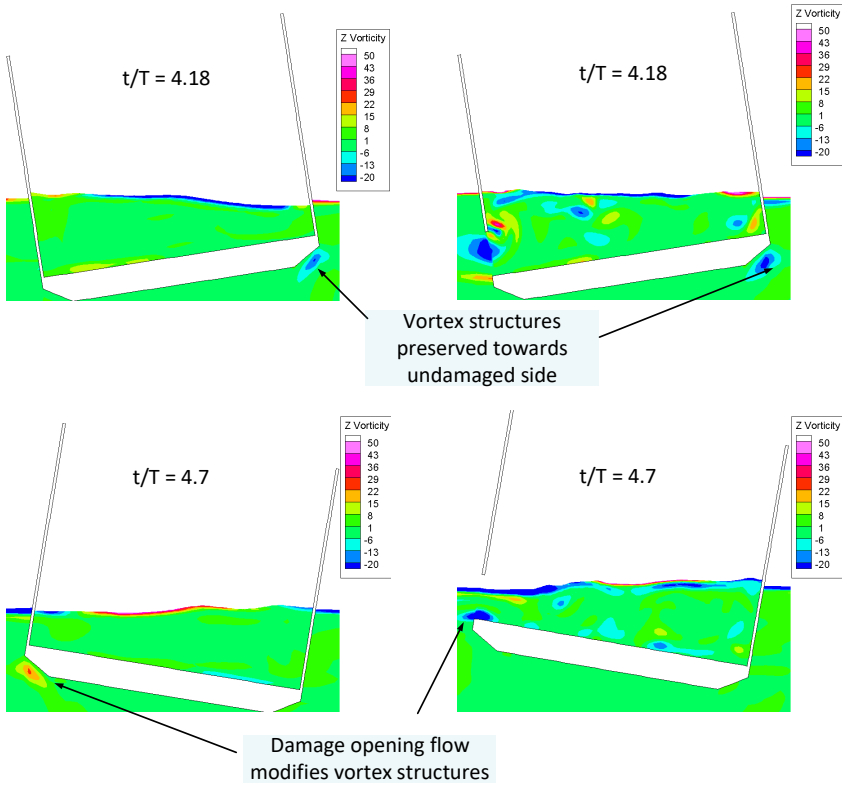

Figure 5.6: OF simulation: Forced roll motion at different time instants for a 2D damaged section with inflow/outflow through the damage opening restricted (left) and allowed (right) with mean draft 15.5 cm (LC 2). Vorticity (s^{-1}) field is shown

OF simulations were also performed for comparison with free-roll decay tests. In the intact condition, the cross-section is uniform along the length of the model, therefore, 2D simulations with a deforming mesh (DM) and overset grids were performed. The overset grid for the 2D condition is shown in chapter 3. For the damaged condition, a 2D simulation is not possible because a 2D damaged section does not have any physical restoring moment. A 3D simulation using the experimental damaged model (shown in figure 3.18) was performed. A structured overset grid was generated using ICEM© CFD tool. For both intact and damaged simulations, the setup for the NWT is the same as for forced heave motions. However, in this case, the body (2D/3D) is first rotated about the CoG to a fixed initial angle and then allowed to rotate freely about the CoG. The body is not allowed to move in sway or heave motions. Figure 5.7 shows comparison of OF results for free-roll decay with experiments. A reasonable agreement is observed for the intact case. The DM method gives a better comparison with the experiments as compared to the overset grid. OG gives a smaller period and damping compared to the experiments. This may be because the Euler scheme is used for OG and

may require a much smaller time-step than employed here. Use of a smaller time step has not been examined due to time limitations and is left for future studies. For the damaged case, a larger period as compared to the intact condition is obtained from the simulations. This behavior is consistent with the experiments. The damping from numerical simulations also shows reasonable agreement with the experiments.

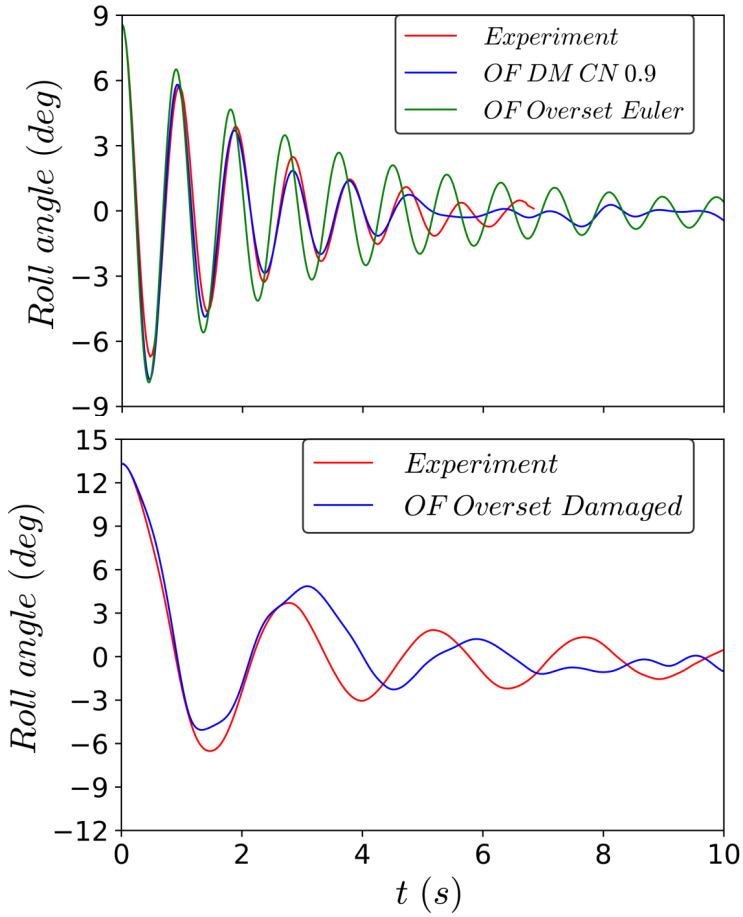

Figure 5.7: OF simulation: Comparison of OF free-roll decay results for intact section with loading LC 2 (top) and for damaged section (LC 2) with open damage opening O1 (bottom)

The free-roll decay simulations are sensitive to the CoG value used, especially for the damaged scenario. For simplification, the model is constrained to rotate only about the CoG in the numerical simulations. This can introduce some numerical errors. In the experiments, the model is free to move in sway and heave directions. The coupling with heave is limited in the intact condition but can be

significant for the damaged scenario. The heave motion was measured was for different experimental run of the free-roll decay tests. The roll and heave motion for the damaged model with loading LC 2 and both ventilated and airtight condition are shown in figure 5.8. It shows that the heave-roll coupling for the ventilated damaged model is much larger than for the airtight section. This is as expected since the ventilated condition allows for inflow/outflow of floodwater causing change in floodwater mass. The model, therefore, moves in the vertical direction to compensate for the change in floodwater mass. As the numerical simulations are locked in 1 DoF (roll about the CoG), they cannot capture this effect.

Table 5.2 gives the natural period and damping values calculated from the OF simulations. The symbols are as described in table 5.1. The table also provides the difference between numerical and experimental values. The agreement is reasonable for all variables in the examined cases (<15%) except for the linear damping in the damaged condition.

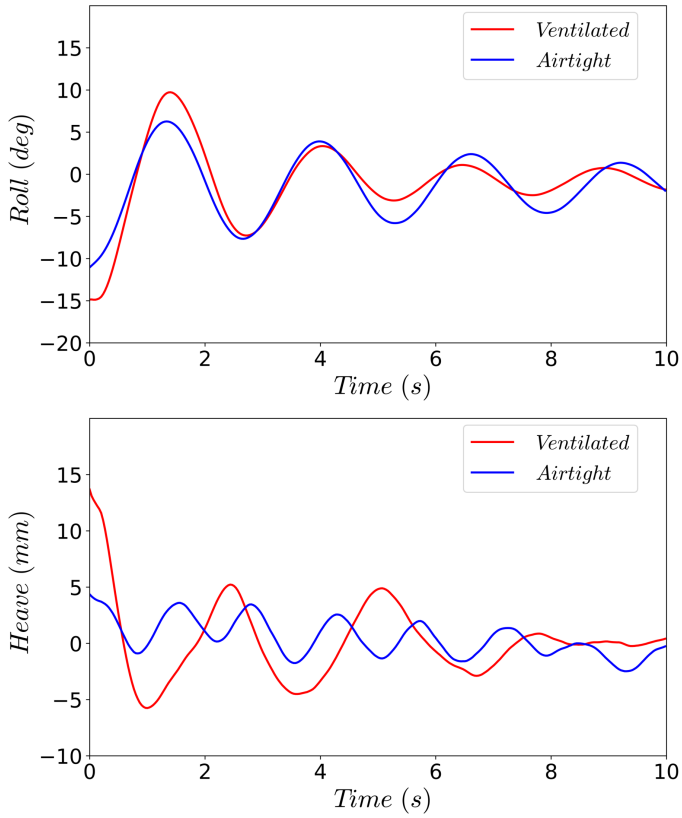

Figure 5.8: Time history of roll angle (top) and heave (bottom) for damaged section with inflow/outflow through the damage opening allowed in ventilated and airtight condition and loading LC 2

Condition	$T_{n4,N}$ (s)	$\delta T_{n4} = \frac{\lvert T_{n4} - T_{n4,N} \rvert}{T_{n4}}$	B_{44lN} (kgm^2s^{-1})	$\delta B_{44} = \frac{\lvert B_{44l} - B_{44lN} \rvert}{B_{44l}}$	$B_{44,quadN}$ (kgm^2rad^{-1})	$\delta B_{44,quad} = \frac{\lvert B_{44,quad} - B_{44,quadN} \rvert}{B_{44,quad}}$
Intact LC 2 OF DM O Grid	0.95	1.06%	0.65	8.33%	0.55	1.78%
Intact LC 2 OF Overset	0.89	5.32%	0.5	16.66%	0.5	10.71%
Damaged LC 2 (O1) OF Overset	2.75	12.24%	0.65	36.2%	2.8	2%

Table 5.2: Natural period for roll and linear and quadratic damping coefficient obtained from the free-roll decay OF simulations. Relative errors with respect to the corresponding experimental damping terms are also given

5.1.2 Intact Section in Waves

Tests in beam-sea waves with wave steepness kA=0.033 were performed for the intact section at two loading conditions LC 1 and LC 2 corresponding to drafts 7 cm and 8.5 cm, respectively. Figures 5.9- 5.11 show the RAOs for sway, heave and roll at the two experimental loadings, as well as the viscous strip-theory results for loading LC 2.

For the roll motions, both numerical and experimental results for LC 2 document a peak near a non-dimensional frequency of 1, which corresponds to a roll period of 1 s. This is consistent with the free-roll decay tests documenting a roll natural period of 0.94 s for this draft. A slight shift is usually observed due to sway-roll coupling as the free-decay tests assume a 1 DoF system, i.e. only roll motion about CoG is allowed. The natural roll period for loading LC 1 is also close to 1 s, as seen from figure 5.11. The resonant roll response is higher for LC 2 due to smaller damping. Consistently with the expected asymptotic behaviors, the motions approach zero for high frequencies due to decreasing wave excitation, whereas at smaller frequencies, the non-dimensional motion values tend to a value of 1. The comparison with the viscous strip theory seems reasonable for all RAOs, except near the roll resonance frequency where this theory shows an overprediction up to about 30%. The numerical method is able to capture the natural roll period, but the numerical roll motion is larger at the resonance period. An equivalent linearized damping term has not been included in the numerical simulations in the intact condition because of the small nonlinear damping obtained for this condition. The estimated damping from the numerical free-roll decay tests match well with the experimental values. However, as already mentioned, in the case of free-roll decay tests a 1 DoF system about the CoG is assumed. Due to presence of roll-sway coupling in the experimental setup for the freely-floating model in waves, hydrodynamic coefficients for sway and roll are modified as compared to single DoF free-decay tests. This also affects the sway motion.

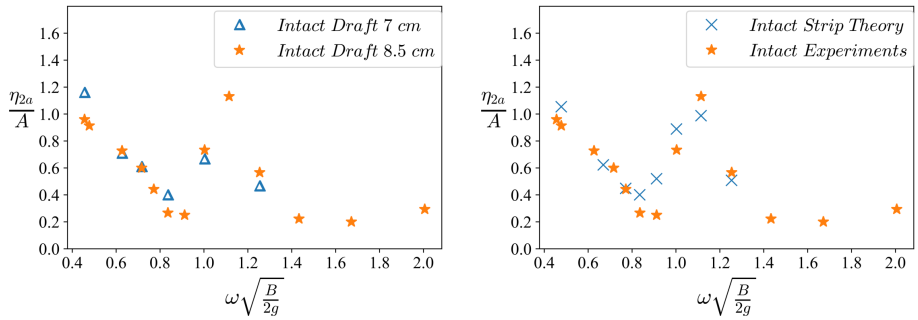

Figure 5.9: Experimental sway RAO as a function of frequency for the intact section at loadings LC 1 and LC 2 (left) and comparison with viscous strip-theory results for loading LC 2 (right)

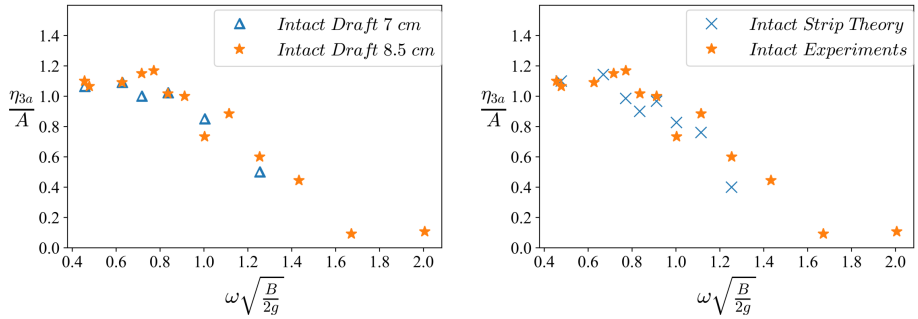

Figure 5.10: Experimental heave RAO as a function of frequency for the intact section at loadings LC 1 and LC 2 (left) and comparison with viscous strip-theory results for loading LC 2 (right)

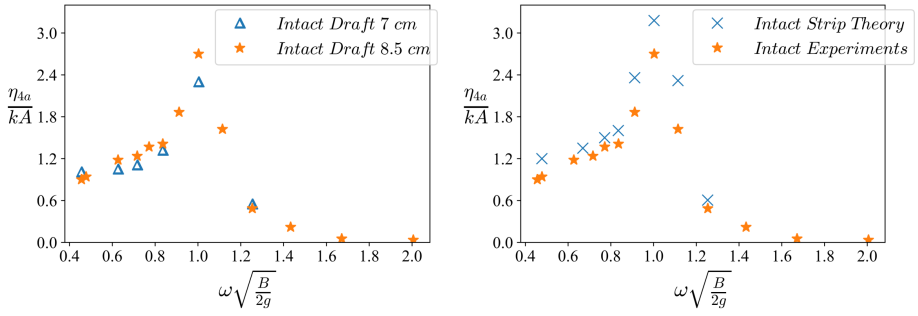

Figure 5.11: Experimental roll RAO as a function of frequency for the intact section at loadings LC 1 and LC 2 (left) and comparison with viscous strip-theory results for loading LC 2 (right)

5.1.3 Damaged Section in Waves

Full compartment flooding: Results are discussed for the case with the model damaged on the side facing the wavemaker and the damaged compartment encompasses the whole breadth of the model and is ventilated. Corresponding Hydrostatic characteristics corresponding to this condition are illustrated in table 2.2. Due to the intact regions at the ends, a reasonable value of GM is obtained in damaged condition. This is chosen so that capsizing does not take place in any of the examined wave conditions. The results for loading LC 2, with a damaged model draft of 15.5 cm and damage opening O1 are presented here. Figure 5.12 shows wave elevation RAOs inside the damaged compartment. The vertical dotted lines in the plots indicate the sloshing and piston-mode resonance frequencies.

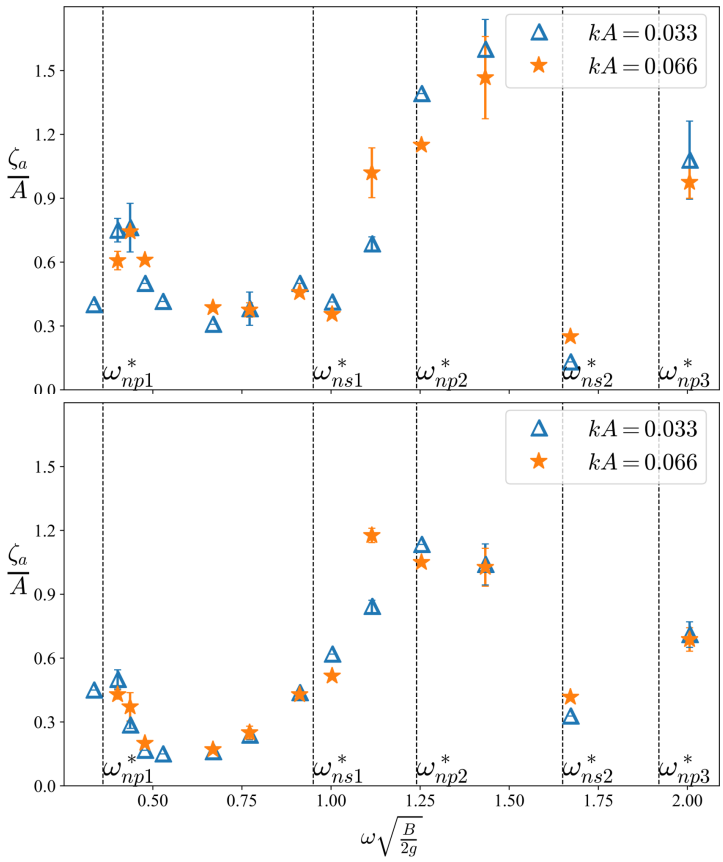

Figure 5.12: Wave probe RAOs at WP1 (top) and WP2 (bottom) inside the ventilated damaged compartment as a function of frequency for full compartment flooding (LC 2, O1) and two wave steepnesses

The largest measured wave elevations occur at higher frequencies with a maximum for WP 1 about 1.5 times the incident wave amplitude. At high frequencies,

incident waves do not cause large heave or roll motion. However, due to the damage opening, an external forcing exists, which excites resonance inside the flooded compartment. The wave elevation RAOs are small near the second sloshing mode (figure 5.13) because the wave probes are located far away from crest or trough of this sloshing mode. Near the second piston mode frequency, a large peak for both WP 1 and WP 2 measurements is observed. The piston mode and roll motion act as a coupled system causing high wave elevation values inside the compartment. The values for WP 1 are higher than for WP 2 since the crest is closer to WP 1 than to WP 2 (see figure 4.24 for an explanation). At ω^*=0.91, the first sloshing mode is excited (figure 5.14). At small frequencies, a small peak near the first piston mode frequency (figure 5.15) is seen. Five repetitions are performed for full compartment damage at LC 2 for six frequencies and two wave steepnesses. Error bars in the plots show the absolute deviation with mean values at the wave probes. The deviation for WP 2 is small and less than 15% for all cases. For WP 1, the maximum deviation is higher, around 20%.

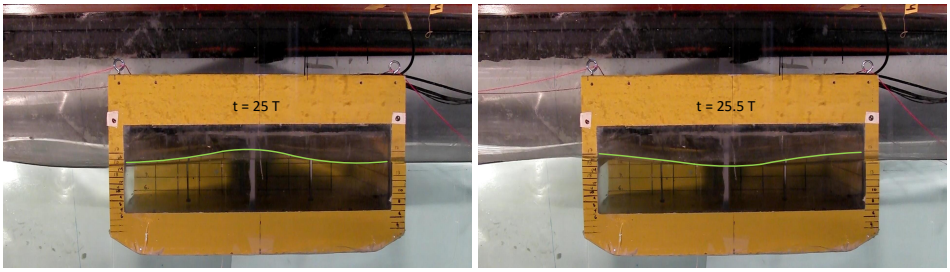

Figure 5.13: Second natural sloshing mode for ventilated damaged condition (LC 2) with opening O1 (at the left side of the model) in waves at kA=0.033 and ω^*=1.67

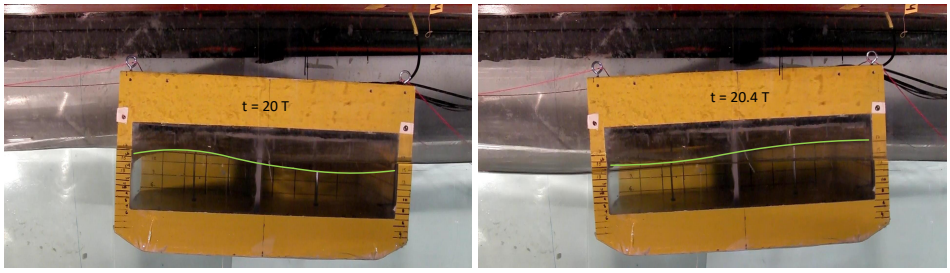

Figure 5.14: First natural sloshing mode for ventilated damaged condition (LC 2) with opening O1 (at the left side of the model) in waves at kA=0.033 and ω^*=0.91

Figures 5.16-5.18 provide the experimental sway, heave and roll RAOs for full compartment flooding at two steepnesses and the comparison with viscous strip-theory results. All motions are small at high frequencies similar to the intact model. Higher frequencies can excite higher sloshing modes inside the damaged compartment but do not cause large body motions. At smaller frequencies, the behavior is different as compared to an intact section with larger sway motions

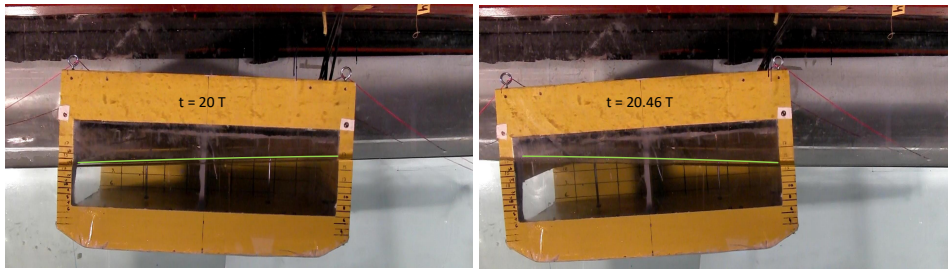

Figure 5.15: First natural piston mode for ventilated damaged condition (LC 2) with opening O1 (at the left side of the model) in waves at kA=0.033 and ω^*=0.33

occurring in the damaged case. The heave motion shows slightly larger values near the first piston mode frequency when compared to the intact model. The roll RAO is very different when compared to an intact section. A special feature of the roll RAO for a damaged ship section is that it has usually two peaks, i.e. a peak at the natural roll period for the damaged section and a minor peak close to the first sloshing mode resonance period. The natural roll period for the damaged ship section is calculated to be 2.43 s (ω^*=0.41) and matches quite well with the main peak in the roll RAO. The roll damping calculated from the experiments is higher for the damaged section when compared to the intact section, as previously discussed. However, the roll response at the natural period for the damaged section is higher than for the intact section at the corresponding natural period. In general, most experimental literature shows that the roll response for damaged condition is lower than for intact condition. It must, however, be noted that experiments for the whole ship experience a more limited change in draft due to flooding with respect to present case. In the present case, the draft and natural periods are almost doubled when going from intact to damaged scenario. Therefore, even though the absolute value of roll damping is higher for the damaged condition, the exciting roll moment from the waves at the much smaller frequency may be large enough to cause a larger response for the damaged ship.

The two examined wave steepness values may not be large enough to cause significant nonlinear behavior. Non-dimensional sway, heave and roll motions are practically superimposed for the two steepnesses. Consistently, the OF simulations show that nonlinear viscous damping matters mainly at roll resonance. Error bars show absolute deviation with mean values of the motions. The deviation is usually less than 10% for sway and heave at both steepnesses. The deviation is a bit higher for the roll RAO with a maximum value of 19%. The overall repeatability of the tests is acceptable with maximum deviation for all motion RAOs below 20%.

The comparison of experimental data with strip-theory numerical results is good except for the roll response at certain frequencies. A possible explanation of these identified differences is that 3D effects due to change from intact to damaged cross-sections at the opening edges is not accounted for by the strip theory. Furthermore, since 2D flow is assumed for radiation and diffraction problems for the damaged strip, possible 3D floodwater effects cannot be accounted for in this

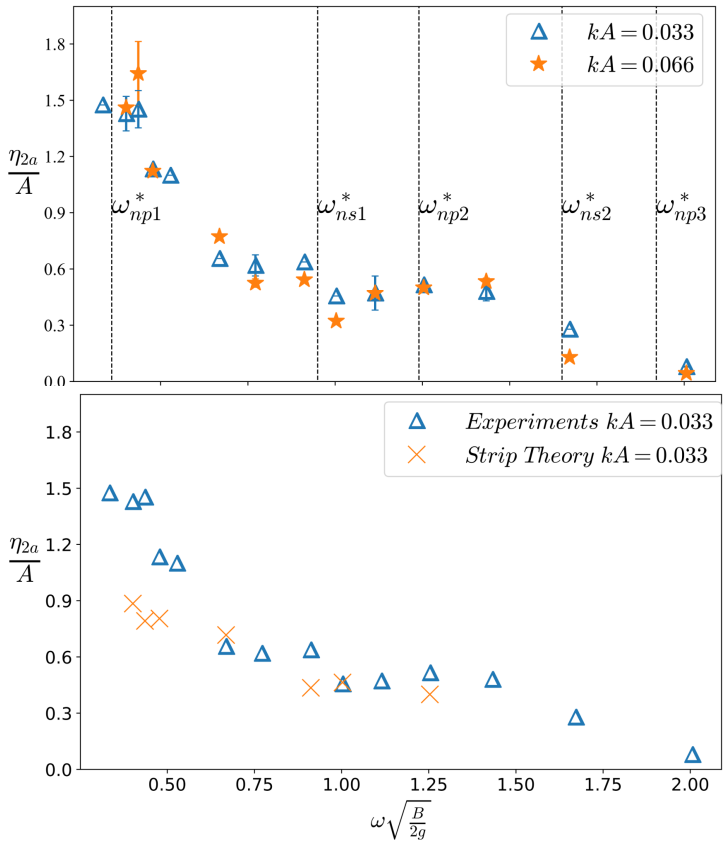

Figure 5.16: Sway RAO as a function of frequency for ventilated full compartment flooding (LC 2, O1) and two wave steepnesses (top) and comparison with viscous strip-theory results (bottom)

formulation.

The piston and sloshing mode resonances affect the body motions. For the damaged section in beam-sea waves, the major roll peak is located near the first piston mode frequency as seen in figure 5.18. This is a simple consequence of the restoring roll moment C_{44} being greatly reduced leading to a larger natural period. The natural roll period happens to be close to the first piston mode period. As a consequence, the internal free surface at natural roll period inclines along with the body (with a slight phase difference) resembling a piston mode, i.e. almost a node like condition at the opening and an antinode at the opposite wall. This behavior is also observed in the images from the free-decay tests in figure 5.19. The sway peak at roll natural period occurs due to coupling between roll and sway motions. The heave motion is quite similar to an intact section except near the first piston mode period which can be an effect of large mass inflow/outflow at the natural roll period.

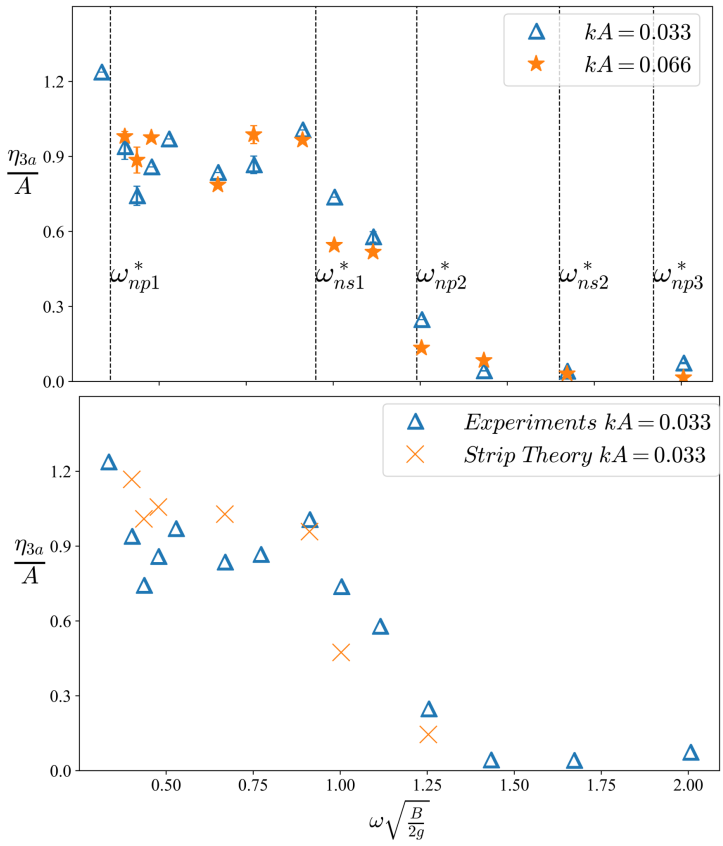

Figure 5.17: Heave RAO as a function of frequency for ventilated full compartment flooding (LC 2, O1) and two wave steepnesses (top) and comparison with viscous strip-theory results (bottom)

The influence of sloshing mode resonance on the motions of a damaged ship motions can be understood by comparing with the motions of a 3 DoF ship with an internal tank as discussed by Faltinsen and Timokha (2009). Rognebakke and Faltinsen (2003) also studied experimentally and numerically the influence on a model (with closed internal tank) that was allowed to move only in sway motion in regular beam-sea incident waves with frequencies in the vicinity of the lowest natural sloshing frequency. Since the contribution to sway added mass from sloshing becomes infinite at the sloshing natural frequency, the linear sway response becomes zero at the natural sloshing frequency. Furthermore, because of the strong frequency dependence of the sway added mass due to sloshing with large negative and positive values in the vicinity of the natural sloshing frequency, a maximum in sway response occurs at a frequency slightly higher than the lowest natural sloshing frequency. If the body with an internal tank is free to move in all rigid-body degrees of freedom, the motions in general will not be zero at the

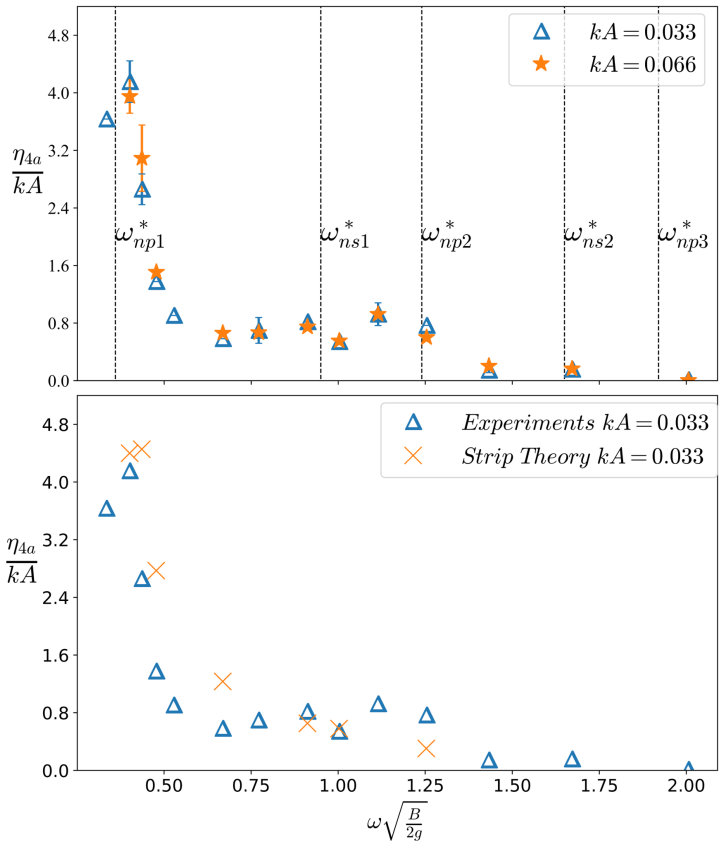

Figure 5.18: Roll RAO as a function of frequency for ventilated full compartment flooding (LC 2, O1) and two wave steepnesses (top) and comparison with viscous strip-theory results (bottom)

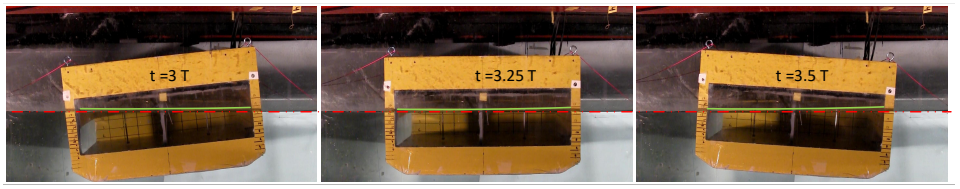

Figure 5.19: Internal water surface during different phases of free-roll decay test for ventilated damaged section with loading LC 2 and opening O1 (red dashed line indicate the external free surface and green solid s represent the internal free surface)

natural sloshing frequency. The latter is the consequence of hydrodynamic coupling properties and is proved by Faltinsen and Timokha (2009). Due to sway-roll coupling, at the first natural sloshing frequency a dip occurs for the roll RAO and

a nearby peak at frequency lower than the natural sloshing frequency is observed. Consistently, for the present case, large motions at sloshing resonance are not observed, but a small minor peak for roll and a small dip in sway motion occur near the first sloshing mode resonance frequency. This is similar to the behavior described for a body with closed internal tank in beam-sea waves, but the effect is not as large for this present case.

To demonstrate a case where the effect of sloshing resonance appears more clearly, experiments on a damaged model in beam-sea waves by Acanfora and De Luca (2016) are examined as an example. They presented motion RAOs for experiments on a ferry hull model in intact and damaged condition in beam-sea waves for side damage, bottom damage and floodwater with the opening closed (behaving as an internal closed tank). For the damage compartment in their case, natural sloshing resonance frequencies have been calculated here as described in chapter 3, while the piston mode frequencies have been obtained using the formulation for a harbor by Miles and Munk (1961). Figure 5.20 reproduces figure 15 from Acanfora and De Luca (2016), with the predicted values of the sloshing and piston mode frequencies given by the vertical dashed lines. The calculated first piston mode frequency (ω^*=1) and second sloshing frequency (ω^*=4.9) are out of their examined range. Two peaks in roll are observed and the effect of the first natural sloshing frequency is evident. Especially, the behavior for the case of flooding with closed opening (black line in figure 5.20) can be explained as discussed in figure 3.26 of Faltinsen and Timokha (2009) for 3 DoF body motions coupled with sloshing due to an internal tank. The two damage cases (side and bottom damage) in Acanfora and De Luca (2016) follow a similar behavior.

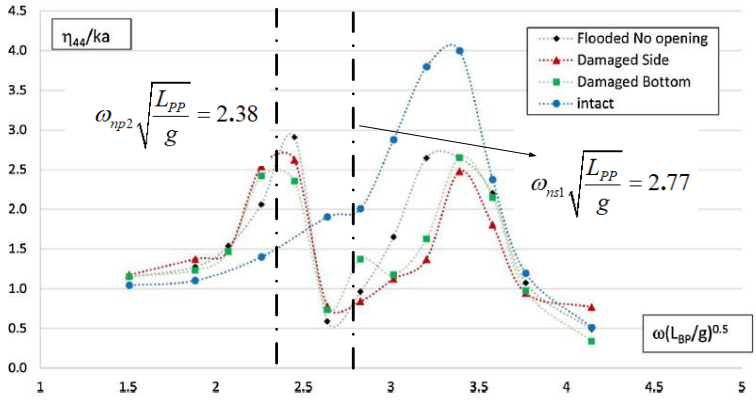

Figure 5.20: Figure 15 from Acanfora and De Luca (2016) along with marked the sloshing and piston mode resonance frequencies (here L_{BP} is the length between perpendiculars, i.e. L_{PP})

Effect of loading: Figure 5.21 shows wave elevation RAOs inside the compartment at loading LC 1, which corresponds to damaged model draft of 11 cm. In this case, the free-surface level is below the upper opening edge and not bounded by a wall on the opening side. As the filling level in the damaged compartment is

smaller, the sloshing and piston mode frequencies are modified. A large peak is observed around the second and third piston modes. Figures 5.22 and 5.23 show the second sloshing mode and second piston mode being excited in the compartment for this case.

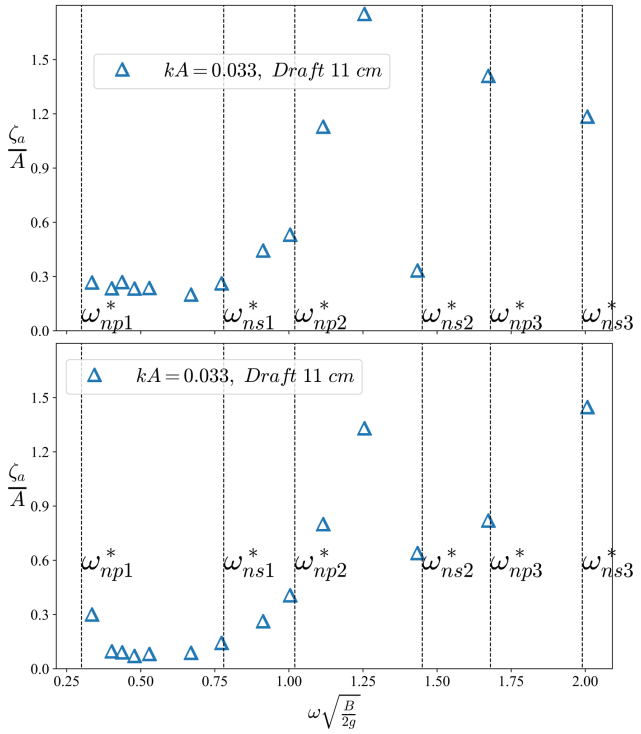

Figure 5.21: Wave probe RAOs at WP1 (left) WP2 (right) inside damaged compartment (LC 1, O1) as a function of frequency for full compartment flooding

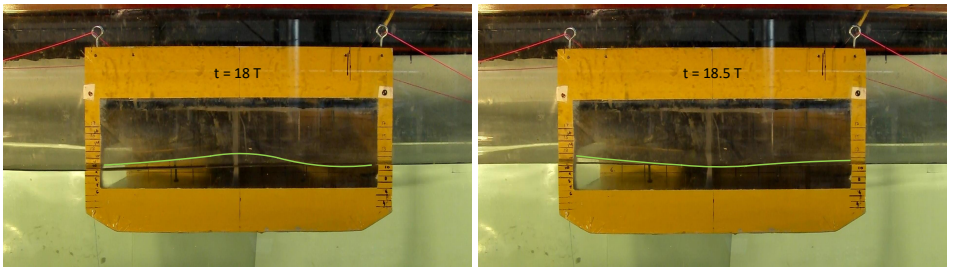

Figure 5.22: Second sloshing mode for a damaged model (LC 1, O1) in waves at kA=0.033 and ω^*=1.5

Figure 5.24 shows sway, heave and roll RAOs for full compartment flooding at LC 1 (11 cm draft). Sway behavior is significantly changed as compared to the loading LC 2 (referred to as higher filling level in this paragraph) shown in figure

5.16. A large peak is seen between the second piston and second sloshing mode frequencies. One factor may be the modified wave systems inside the damaged compartment striking the undamaged wall. The wave systems are similar to the shallow filling level discussed for forced heave motions in chapter 4. As discussed earlier, steep waves can occur for shallow filling conditions causing larger force on the wall opposite to the opening. Heave motion shows similar behavior as for the higher filling. Heave natural resonance period is governed by the waterplane area, which is the same for both damage cases. Therefore, similar heave behavior is expected for these filling levels. The roll motion is instead significantly different for the smaller filling level and, as seen earlier, presents a strong coupling with sway motion. In this loading condition, a relevant peak near the second piston mode frequency is observed and a smaller peak is seen approaching the first piston mode frequency. As seen in table 5.1, the roll natural period for this loading in damaged condition is quite high, around 4s (non-dimensional frequency 0.25). This is confirmed by the peak in the roll RAO. The RAO value near the first piston mode frequency is smaller compared to the higher filling level. This is because of the higher roll damping observed in the free-roll decay test. The roll wave-radiation damping is also larger due to higher beam to draft B/T ratio in this loading. Near the second piston mode, the roll motion is slightly larger than for the higher filling level. This is related to sway-roll coupling and larger sway motion near this frequency.

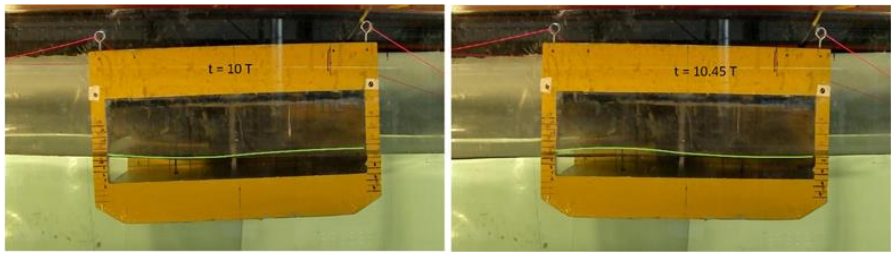

Figure 5.23: Second piston mode for a damaged model (LC 1, O1) in waves at kA=0.033 and ω^*=1.11

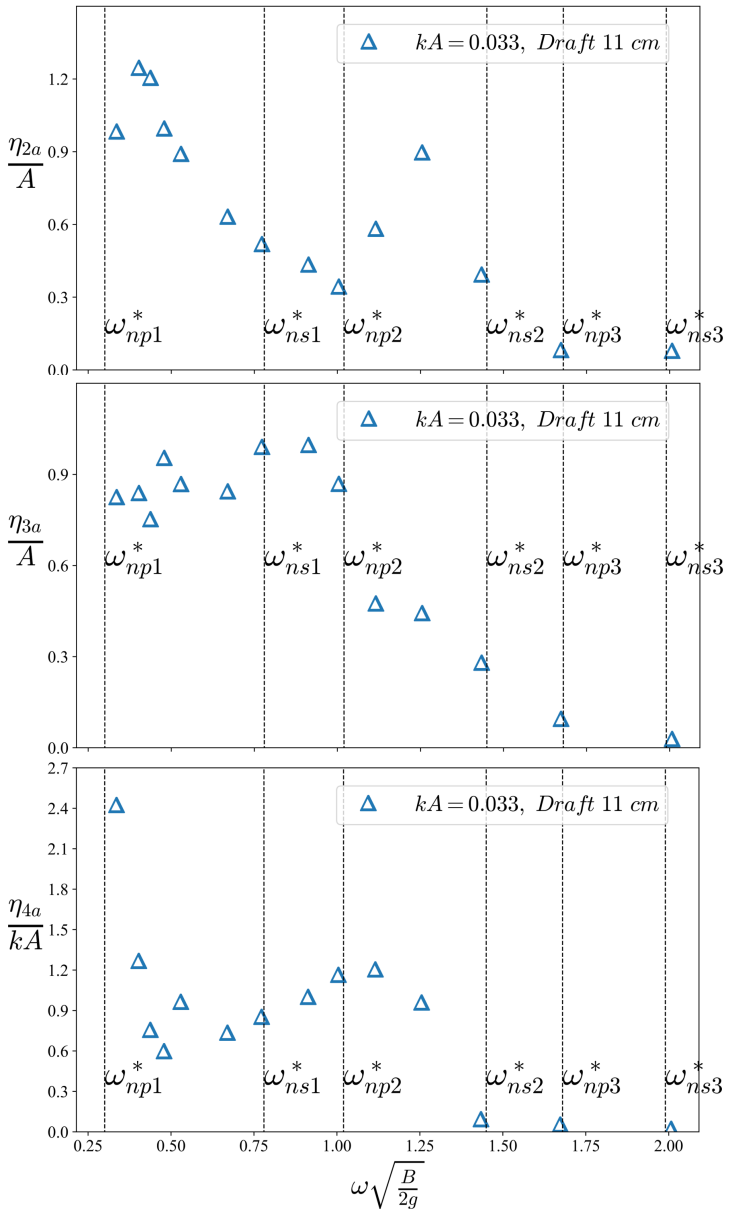

Figure 5.24: Sway, heave and roll RAOs as a function of frequency for full compartment flooding (LC 1, O1)

Effect of air compressibility: For an airtight compartment, the air compressibility in the damaged compartment acts as a strong spring and influences water inflow/outflow through the opening and, therefore, the motion responses. Air in the compartment slows down the flooding process as mentioned in Palazzi and

de Kat (2004) and Ruponen et al. (2013). As reported in chapter 4, when air cavities are involved, Euler number $Eu = p_0/\rho U^2$ matters in scaling from model tests to full scale (Faltinsen and Timokha, 2009). Here p_0, ρ and U are ambient air pressure, water density and characteristic flow velocity, respectively. To maintain Euler number similarity, depressurized conditions are needed in the flume which are out of scope of the present work. In the present scenario, the effect of air compressibility has been investigated experimentally by sealing all air exits and openings for the full compartment damage.

Figure 5.25 shows wave elevation RAOs inside the full-flooded compartment for ventilated and airtight conditions. Due to the air cushion acting as a spring, the wave elevation values for WP 1 and WP 2 inside the airtight compartment are lower as compared to the ventilated compartment. This effect is more pronounced at larger frequencies as compared to smaller frequencies. Figure 5.26 shows sway, heave and roll RAOs for ventilated and airtight compartments. Sway motion is not greatly affected by the air compressibility. Heave motions are highly modified due to the air cushion especially near ω^*=1. The motions are much larger at this frequency as compared to the ventilated compartment. The heave resonance frequency in airtight condition is modified and is calculated later in this section. As documented in figures 4.38 and 4.39, heave damping is lower for airtight damaged section as compared to a ventilated damaged section. Therefore, higher values of heave motion for the airtight section are observed near resonance. The roll RAO shows a similar trend as for the ventilated compartment. The only difference being that the roll motion in this case is larger near the natural roll frequency. This is because of smaller roll damping at roll resonance for the airtight compartment as demonstrated earlier in section 5.1.1. It was documented earlier in chapter 4 that piston mode resonance is absent for an airtight compartment for forced heave motions, whereas, sloshing resonance remains unaffected. WP 1 values show a reduction in values near the piston mode frequency in this case but the reduction is not as drastic as for the case of damaged section in forced heave motions. This is because of the heave-roll coupling for the freely-floating model; i.e. changes in air-cushion volume due to one mode of motion can be compensated by the other mode.

For a rough estimate of the heave resonance frequency in airtight condition, a single DoF system in forced heave motion can be considered for simplicity. It means that we need to evaluate the restoring and added-mass coefficients in heave. The restoring coefficient C_{33} is connected to the change in vertical force due to quasi-steady change $-\rho g \eta_3$ in hydrostatic pressure. The effect of the thin vertical side walls is neglected. Since the pressure can be assumed constant in the air cushion and the pressure at the interface between the air cushion and the water must be equal, there is a change of pressure equal to $-\rho g \eta_3$ in the air cushion. Therefore, C_{33} for an airtight section is equivalent to an intact section, therefore, $C_{33}^{2D} = \rho g B$ for a 2D cross-section. If it is integrated along length L of the model, $C_{33} = \rho g B L$. As for the added mass in heave, there is contribution from the internal and external flows. One contribution to heave added mass from the internal flow is simply the internal water mass. A first approximation of the external contribution to the heave added mass is that the sectional heave added mass is proportional to B^2, is the same as for the intact section (but draft equal to damaged

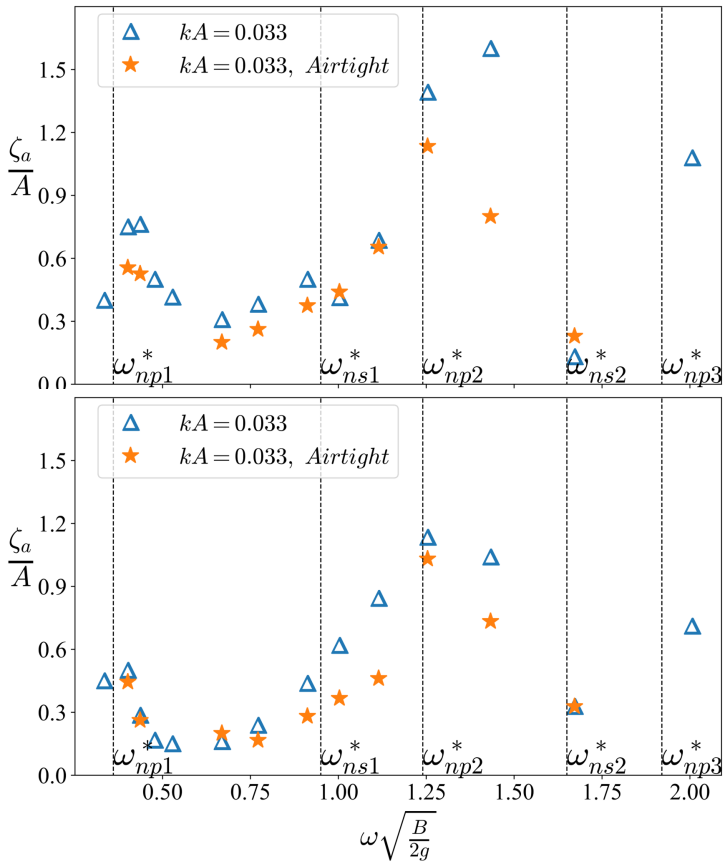

Figure 5.25: Wave probe RAOs at WP1 (left) and WP2 (right) inside the damaged compartment as a function of frequency for full compartment flooding in ventilated and airtight conditions (both with LC 2 and O1)

condition). Following this, the natural frequency for the damaged model with air cushion is found to be ω^*=0.94. Similar argument as for the restoring coefficient C_{33} in airtight condition can be made for the roll restoring coefficient C_{44}, as discussed in section 5.3 of the book by (Faltinsen, 2005) for a surface effect ship (SES).

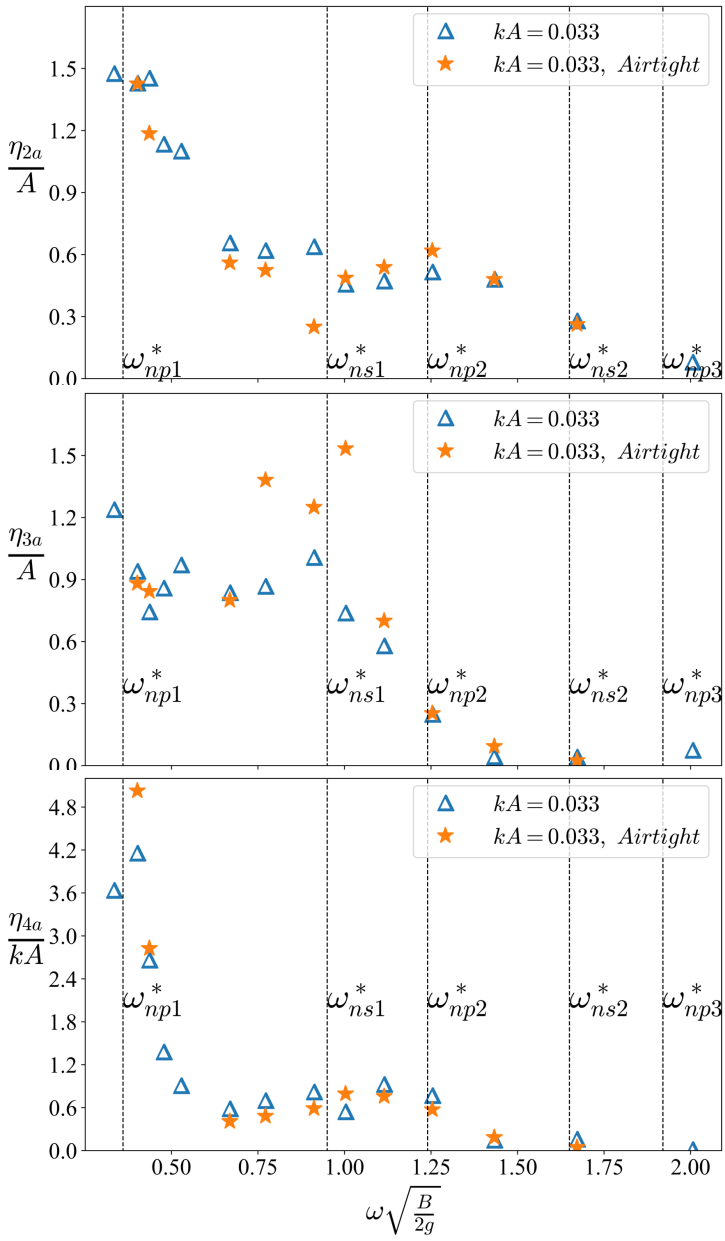

Figure 5.26: Sway, heave and roll RAOs as a function of frequency for full compartment flooding in ventilated and airtight conditions (both with LC 2 and O1)

Effect of damage-opening size: To study the effect of damage-opening size on the motions, three opening sizes were studied. The dimensions of the openings are described in table 2.3. Additional thin wooden plates were attached at the

original-opening sides to reduce the opening length leading to openings O2 and O3. Figure 5.27 shows the wave elevation RAOs inside the compartment for the three different opening sizes. These openings document similar trends. The RAOs of WP 1 and WP 2 for openings O2 and O3 are either quite similar or smaller than the values for O1. This is understandable as the inflow/outflow for the smaller openings is more restricted. It is, however, interesting to note that the values for the smaller openings are slightly larger near the first piston mode frequency.

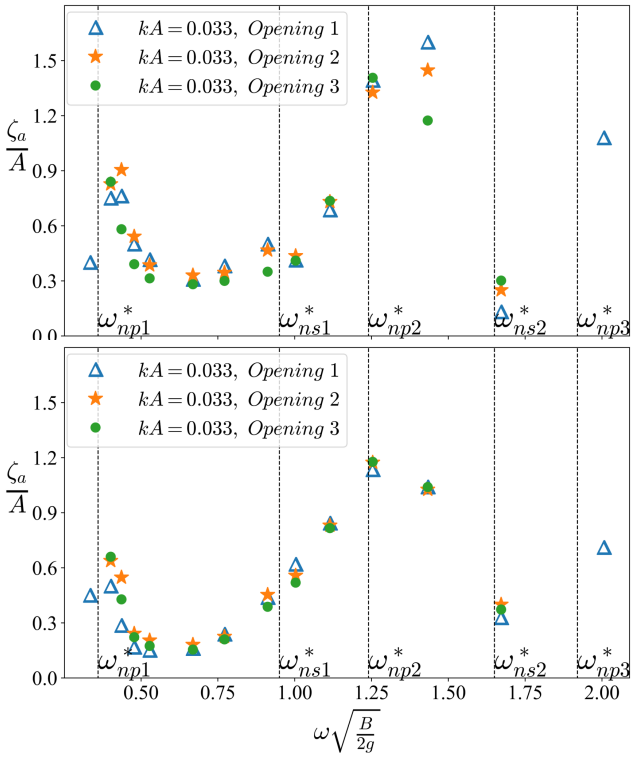

Figure 5.27: Wave probe RAOs at WP1 (left) and WP2 (right) inside ventilated damaged compartment (LC 2) as a function of frequency for three damage-opening sizes

Figure 5.28 shows sway, heave and roll RAOs for the three damage-opening sizes. The smallest opening (O3) behaves closer to a closed tank and is less affected by piston mode and associated damping. The reason is that the damaged compartment has cross-sectional parts closed to the external water, and the closed sections cannot have 2D piston mode. The largest opening (O1) has large inflow/outflow due to piston mode resonance and, therefore, larger associated damping. The sway behavior is mostly similar for all the three cases. However, near the first sloshing mode, as the opening size becomes smaller a reduction in sway motions is observed. This can be because the smaller opening compartment partly involves cross-sections not exposed directly to the external water. This matters especially at

sloshing resonance. As mentioned earlier, sloshing due to an internal closed tank reduces the sway motion considerably for a 3 DoF system. Heave motions display a similar trend for the three openings except at a few frequencies. Roll RAO values are also similar except at roll resonance frequency. The value for the smaller openings is larger due to the smaller total damping as shown in section 5.1.1.

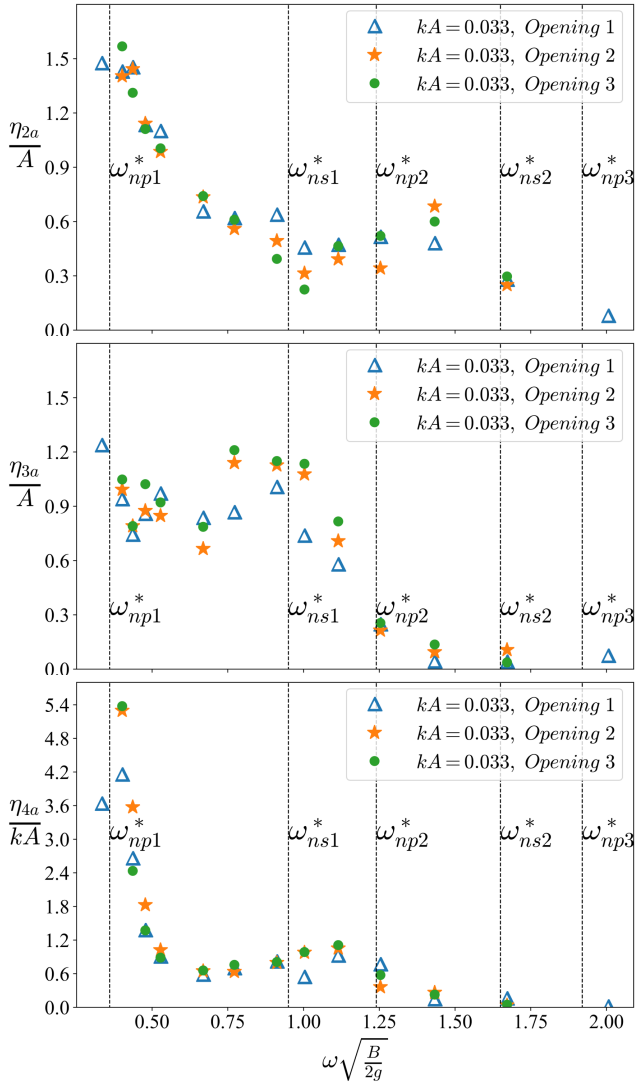

Figure 5.28: Sway, heave and roll RAOs as a function of frequency for ventilated full compartment flooding (LC 2) at three damage-opening sizes

Effect of damaged-compartment breath: Experiments were also performed on the model with damage only extending to half of the initially described compartment. A watertight plate was placed at the center plane of the compartment

for this case. The damaged region is now asymmetric with respect to the z-axis and leads to an initial equilibrium condition with non-zero heel angle (see right plot of figure 2.4). Two loading LC 1 and LC 2 are studied in this case. For the damaged condition, this leads to drafts of 12.5 cm and 16.5 cm, respectively, towards the damaged side. In this section, the two conditions are referred to using these two draft values. Since the breadth of the compartment is halved, the sloshing and piston mode frequencies are now much higher with only the first sloshing and piston mode lying within the range of examined frequencies. The values can be found in tables 3.3 and 3.7.

Figure 5.29 shows RAOs of heave and wave elevation for loading LC 2 (16.5 cm draft) with opening O1 and loading LC 1 (12.5 cm draft) with opening O1 and O3. In the figure, the subscript s and d in the natural frequency refer to the LC 1 and LC 2 loading cases, respectively. Heave RAO is mostly similar for the three cases (LC 1, O1; LC 1, O3 and LC 2, O1), except for small differences near the roll resonance frequency (ω^*=0.91). For LC 1 with the smaller opening (O3), heave values are slightly larger. The wave elevation RAO does not display a sharp peak for loading LC 2. The first sloshing mode is observed (see figure 5.30) but with very small wave elevation RAO values because WP 1 lies almost at the node. The wave elevation in the LC 1 case shows larger values because in this case steep travelling waves occur inside the damaged compartment (see figure 5.31). A large crest rises at the opening and is reflected as a large 'hump' from the non-damaged opposite 'centerline' wall. This can also cause large sway forces. For smaller opening, a similar trend is seen with slightly lower values.

Figure 5.32 shows sway and roll RAOs for loadings LC 2 (O1) and LC 1 (O1 and O3). The sway behavior is similar for the three cases, except near roll resonance. This can be explained due to the occurrence of travelling wave systems for the smaller submergence at these frequencies. The roll motion shows a peak at a non-dimensional frequency of 0.9, which seems to be the natural roll period for this case. This lies between the first piston and sloshing mode frequencies. It must be noted that there might be an error in the calculation of the piston mode frequency because, for simplicity, it was assumed that the heel angle does not affect the natural piston mode resonance. This is proven to be true for sloshing by Faltinsen and Timokha (2009) but may not hold for piston mode resonance. Also, as expected due to the initial heel angle and the asymmetric floating condition, the motions are highly damped compared to the full compartment damage case. The roll motions are, in general, similar for the two submergence cases, except near the roll resonance. At higher submergence, the peak in roll motion is sharper compared to the smaller submergence. A sharp peak implies that the slope of roll RAO for the smaller submergence values is higher between ω^*=0.91 and ω^*=1.25 as compared to the higher submergence. For the smaller loading, reduced opening size leads to a slightly larger roll motion at resonance. This is because the damping is smaller for the smaller opening size as discussed earlier for the full compartment damage.

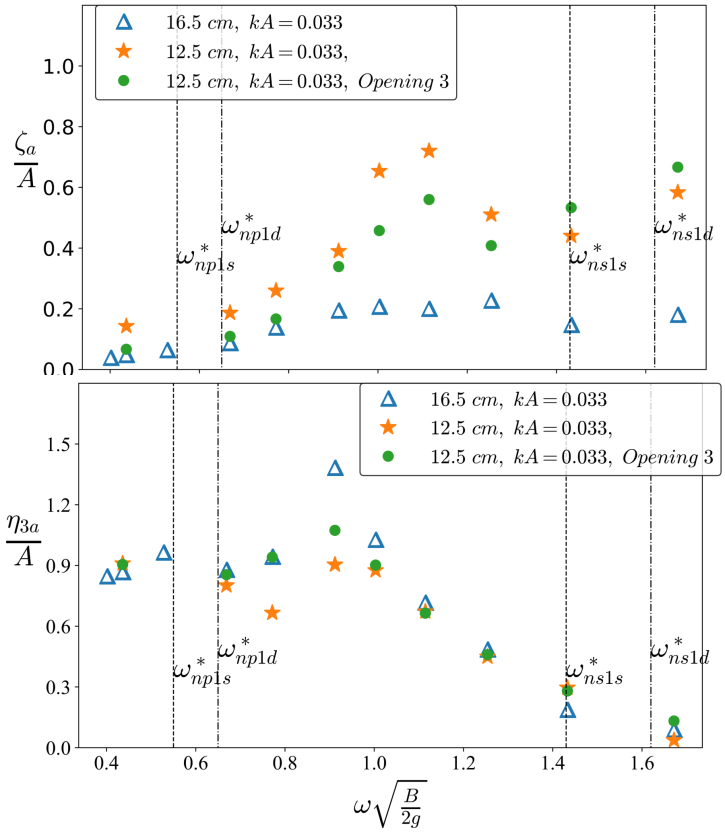

Figure 5.29: WP1 and heave RAO for half compartment damage at loading LC 1 (O1 and O3) and LC 2 (O1)

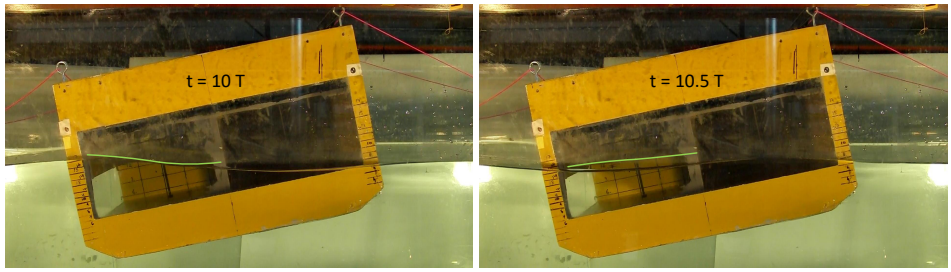

Figure 5.30: First sloshing mode in ventilated half compartment damage condition (LC 2, O1) at kA=0.033 and ω^*=1.66

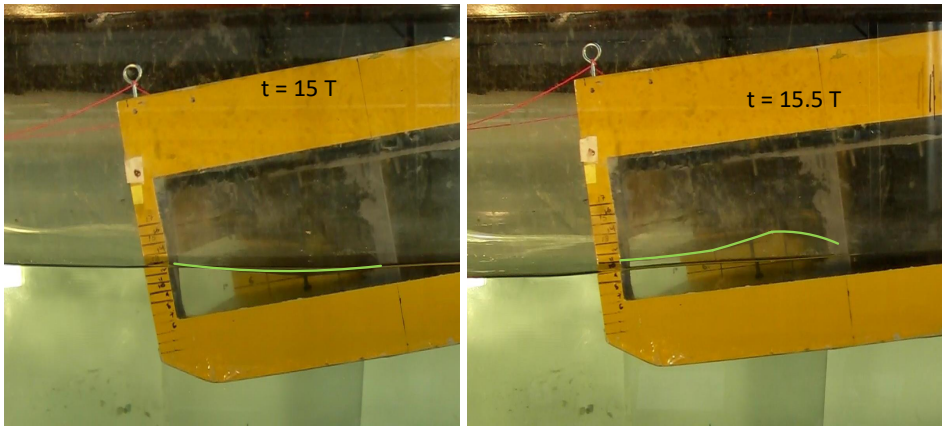

Figure 5.31: Travelling waves in half compartment damage (LC 1, O1) at kA=0.033 and ω^*=1.11

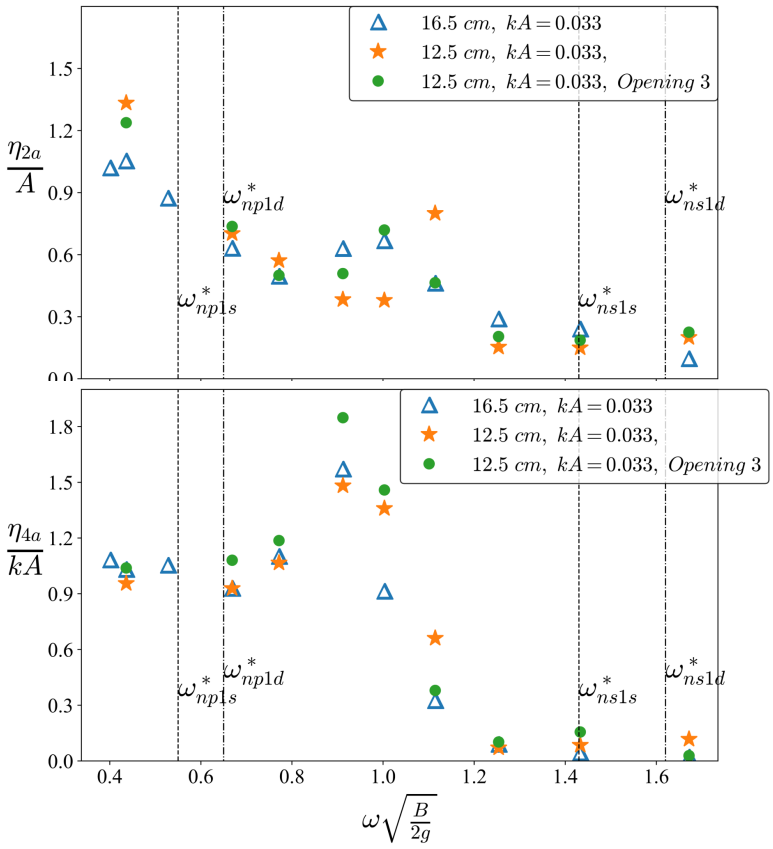

Figure 5.32: Sway and roll RAO for half compartment damage at loading LC 1 (O1 and O3) and LC 2 (O1)

5.1.4 Transient flooding

The transient flooding stage occurring immediately after a damage event, when the ship is exposed to incident waves, is very important as the largest motions take place in this stage and subsequent capsizing may be experienced. In the present tests, situations which can cause initial transient flooding due to the motions of the ship are examined. This can be the case when the damage opening is located above the initial waterline draft of the ship and is not sealed to external environment, like in the case of Estonia accident. Such a scenario was studied experimentally for bow flooding by Shimizu et al. (2000). They varied Froude number, wave period, wave height and bow opening size and reported that the wave height and wave periods were the dominant factors in determining flooding. A similar aspect has been investigated here but for a half compartment with side damage in beam-sea waves. The transient flooding is examined by varying three parameters i.e. KG, incident wave period and incident wave steepness. The examined model loading conditions are described in table 2.9. In particular, the loading LC 1 was used as basis to investigate the influence of incident wave steepness, ranging between 0.033 and 0.1, and incident-wave period, ranging between 0.7 and 1.5 s. Then, the effect of the loading was studied for incident-wave steepness kA = 0.066 and incident-wave periods 0.8, 0.9 and 1 s. Enough freeboard height is allowed so that flooding does not occur for all studied incident-wave periods and effect of varied parameters can be highlighted. The height of the opening edge of the compartment is increased using a small wooden plate 10 cm high from the bottom of the model leading to an initial freeboard of the opening edge of about 2.2 or 3 cm.

The case with the model in loading condition LC 1, opening O3 in incident waves with kA=0.066 and period T = 0.9 s is used to describe the typical features of flooding in the present tests. One should note, that in this case the roll natural period is 0.95 s before flooding. Figure 5.33 shows sudden transient flooding leading to a large sinkage and heel angle. The motions increase in magnitude and, just when flooding starts around t/T=35, a jump in roll and heave motions is observed. After the sudden jump, motions are large but stabilize around t/T=50 to a new equilibrium level. These results document similar behavior as in the stages identified by Ruponen (2007) and reported in section 2.1 of this thesis.

Figure 5.34 examines in detail the different stages of flooding for the same wave period and steepness. As the roll motion increases and gradually reaches a steady-state condition, the freeboard height of the opening relative to the external wave decreases and water starts entering the damaged opening. This inflow of water increases the floodwater weight in the damaged compartment and therefore causes a net mean roll moment towards the half-damaged compartment. The model tries to recover by rolling to the other side but the increase in roll moment towards the damaged side, coupled with reduction in GM due to the free surface in the compartment, further increases the roll motion. As a result, the magnitude of roll angle towards the damaged side increases over time and the model takes in more floodwater. The initial flooding may be slow for some incident wave-periods until when an abrupt flooding occurs with sudden large transient motions.

For loading condition LC 1, cases with kA=0.1 for four wave periods, T=

T (s)	Loading	kA	h_{fr} (cm)	A (cm)	t_{fl}/T	T/T_{n4}	Remarks
0.7	LC 1 (O1)	0.033	3	0.45		0.74	No Flooding
0.8	LC 1 (O1)	0.033	3	0.5		0.84	No Flooding
		0.066	3	1			No Flooding
0.9	LC 1 (O1)	0.033	3	0.65		0.95	Some splashes
		0.066	3	1.3	11.11		Flooding
1	LC 1 (O1)	0.033	3	0.8		1.05	No Flooding
		0.066	3	1.6	15		Flooding
1.2	LC 1 (O1)	0.033	3	1.1		1.26	No Flooding
		0.066	3	2.2			No Flooding
1.5	LC 1 (O1)	0.033	3	1.6		1.58	No Flooding
		0.066	3	3.2			No Flooding
0.8	LC 3 (O1)	0.066	3	1		0.86	Some splashes
0.9	LC 3 (O1)	0.066	3	1.3	12.8	0.97	Flooding
1	LC 3 (O1)	0.066	3	1.6		1.07	No Flooding
0.8	LC 4 (O1)	0.066	2.2	1	35	0.89	Flooding
0.9	LC 4 (O1)	0.066	2.2	1.3	17.77	1.01	Flooding
1	LC 4 (O1)	0.066	2.2	1.6	24	1.12	Flooding

Table 5.3: Summary of flooding scenarios for the performed transient flooding tests

0.8,0.9,1 and 1.5 s, were tested. Flooding was observed in all cases, demonstrating that at very large value of steepness, the wave height becomes the primary factor controlling flooding. The two smaller steepnesses help to examine the effect of other important parameters. Table 5.3 describes all examined flooding scenarios for kA=0.033 and 0.066 at three loading conditions and different incident wave periods. It is observed that shorter wave periods, relative to the natural roll period, with smaller wave amplitudes can cause flooding whereas longer waves with larger amplitudes may not cause flooding. Therefore, flooding depends not just on the wave height but also on the natural roll period of the ship model. This depends on the GM and therefore, KG of the model. Longer waves cause larger heave motions, but smaller roll response and the ship tends to follow the waves. Thus, even with the opening near the waterline, flooding does not occur. The wave steepness kA=0.033 is small enough to not cause flooding for any loading or in-

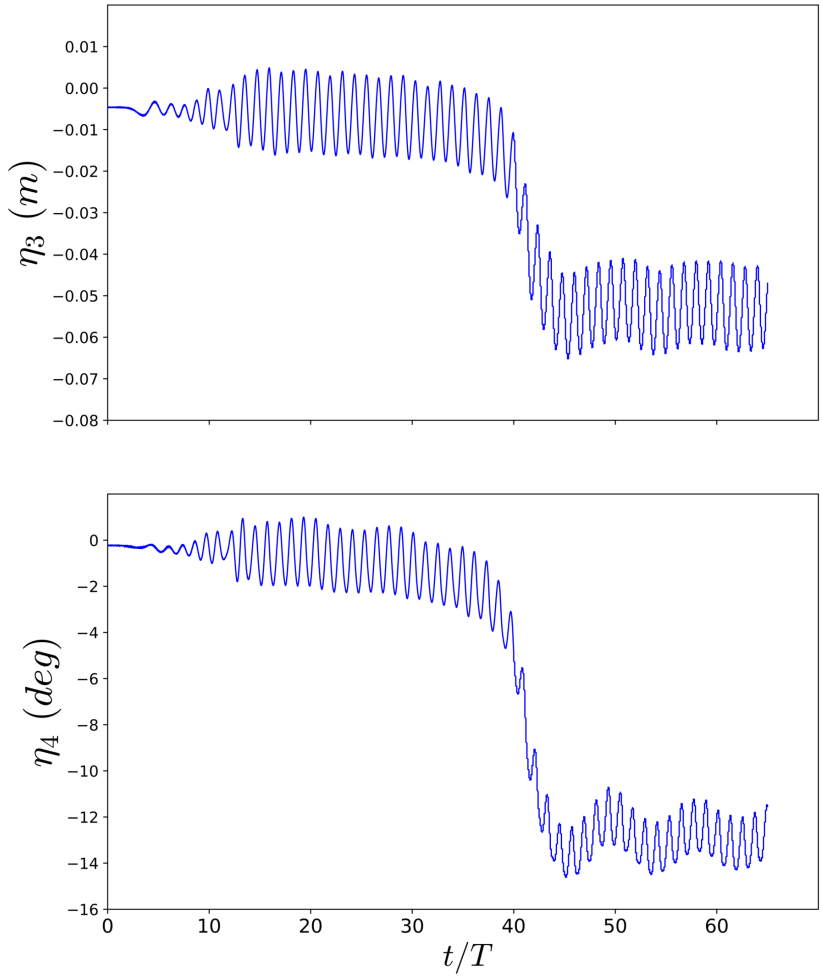

Figure 5.33: Heave (top) and roll (bottom) time histories for the model in loading condition LC 1 (O3) in waves with T=0.9 s and kA=0.066

cident wave period examined here. For LC 1, the roll natural period is around 0.95s and, therefore, flooding occurs for T=0.9 and 1 s at kA=0.066. For T=1.5 s, even though the wave amplitude is much larger than for T=0.9 or 1 s, the roll motions are not large enough to cause flooding. As GM increases, the natural roll period as expected decreases. For loading condition LC 4, all examined incident-wave periods are near the roll resonance period (0.89 s). Therefore, all of them at kA=0.066 cause flooding. The time t_{fl} in table 5.3 is defined as the time interval between start of entry of floodwater in the compartment and the attainment of final equilibrium position after flooding. In particular, the table gives the number

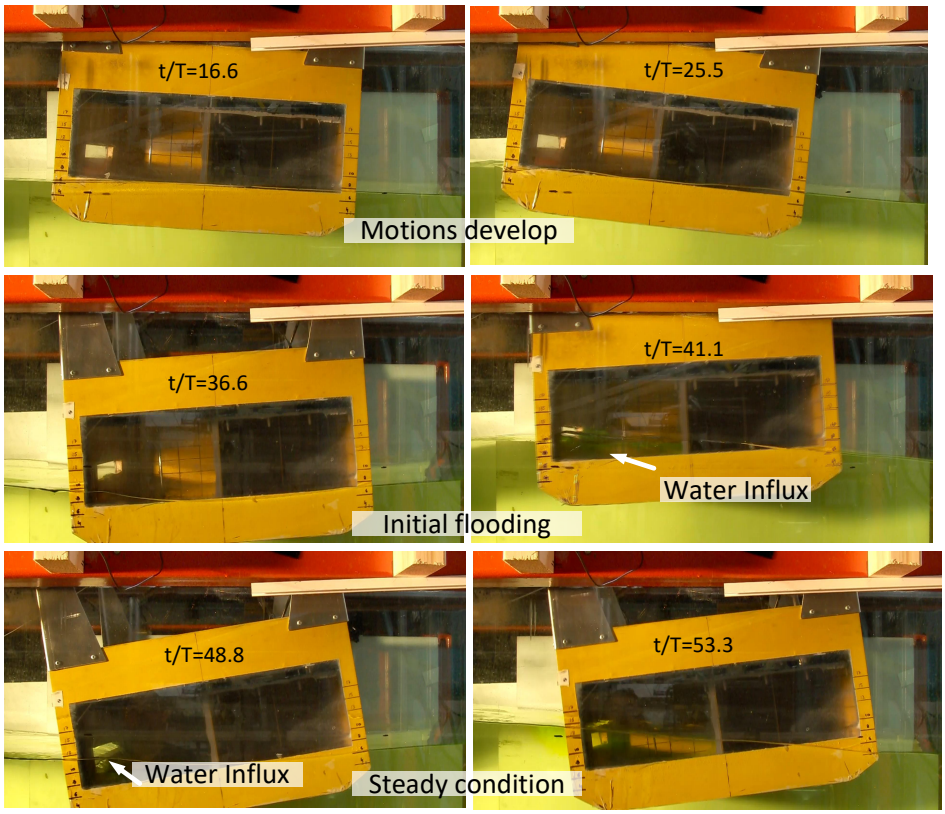

Figure 5.34: Sequence of flooding as it occurs over time for the model in loading condition LC 1, with opening O3 and in waves with T=0.9 s and kA=0.066. Time increases from left to right and from top to bottom

of incident-wave periods within t_{fl} for the defined flooding time. As expected, the value is smallest for the incident-wave period closest to the roll natural period and increases going far from this period. One interesting observation is that for T=0.9s, LC 1 with a higher freeboard has smaller values of t_{fl}/T than LC 4 with a lower freeboard.

Figure 5.35 shows the wave elevation inside the damaged compartment for the three flooding cases with loading condition LC 4. Since the loading condition and initial draft are the same, similar equilibrium floodwater level for the three incident-wave conditions is observed. The difference in t_{fl} is clearly visible. Figure 5.36 shows the wave elevation in the half compartment for T=0.8 s (top) and T=0.9 s (bottom) at different loading conditions for kA =0.066. For T=0.8 s, flooding only occurs for the highest GM value, i.e. for LC 4. Some water enters (green spikes) for LC 3, but it does not cause further flooding. For T=0.9 s, a clear difference between equilibrium wave probe values at LC 1 and LC 4 is seen, as expected because of the difference in initial loading condition. One should note that, because side damage and beam-sea scenarios are analyzed, roll motion is

seen to be the dominating factor. Roll motion may not always be the most important factor in other damage scenarios. Forward speed effects may also be relevant. Therefore, the presented results are applicable only to the studied scenario.

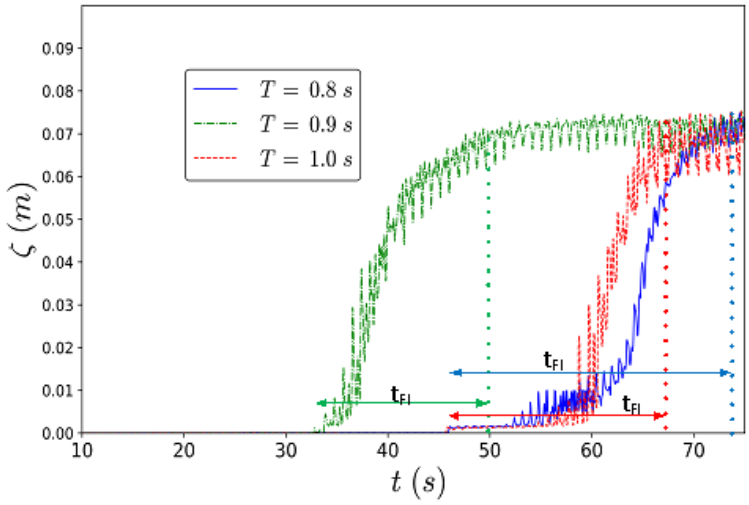

Figure 5.35: Wave elevation (WP 1) time histories for the model with loading LC4 in waves with different period and steepness kA=0.066

Greco et al. (2012) described an experimental and numerical study on a patrol ship in head-sea waves. They used a simple analysis to estimate the freeboard exceedance and to examine its link with the water-on-deck events. Following their work, a simplified calculation of freeboard exceedance is employed and its link to flooding occurrence is examined. The freeboard exceedance occurs when the relative vertical motion between the ship model and the local waves has an amplitude larger than the freeboard. If the local wave elevation associated with radiated and diffracted waves is neglected, the relative vertical motion at a position y can be approximated as in the present cases

$$\eta_r = \eta_3 + y\eta_4 - \zeta_w \tag{5.2}$$

Here ζ_w is the incident wave elevation at y. Freeboard exceedance occurs on the damage side of the model if condition

$$\eta_{ra} = \left| \eta_3 - \frac{B}{2}\eta_4 - \zeta_w \right| > h_{fr} \tag{5.3}$$

is satisfied. Here h_{fr} is the damage freeboard. The relative motion amplitude is estimated from the measurements for the intact test (LC 1) in beam-sea waves at kA=0.033 and assuming a linear behavior for its calculation at the other two

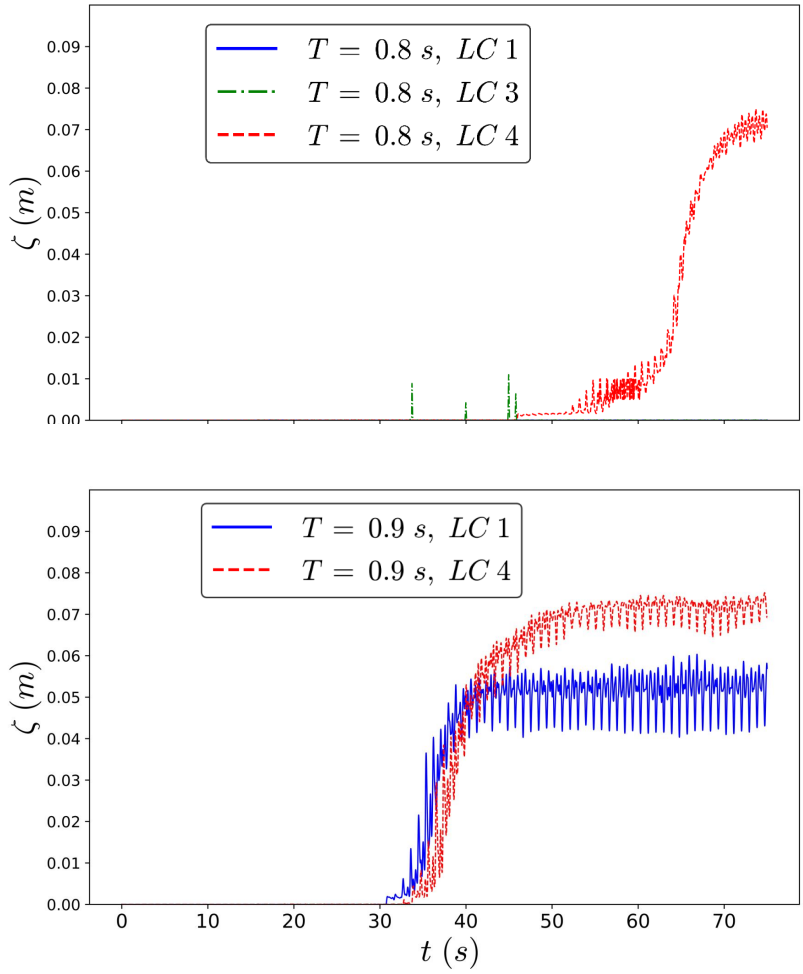

Figure 5.36: Wave elevation (WP 1) time histories for the damaged model at different loading conditions in waves with period $T = 0.8$ s (top) and 0.9 s (bottom) and steepness kA =0.066

steepnesses. Figure 5.37 presents the calculated non-dimensional relative motion parameter, $r = (\eta_{ra} - h_{fr})/h_{fr}$, against the non-dimensional incident wave frequency. The empty symbols represent experimental cases without flooding and full symbols represent those with flooding. From the figure, the simplified freeboard exceedance, i.e. $r>0$, corresponds well with the flooding occurrence in most of the examined cases. However, for few conditions associated with low positive r, experimentally flooding is not observed. This would suggest that for those cases local wave-body interaction matters. In particular, phase of the local wave near

the damage opening could play a role in avoiding the flooding occurrence.

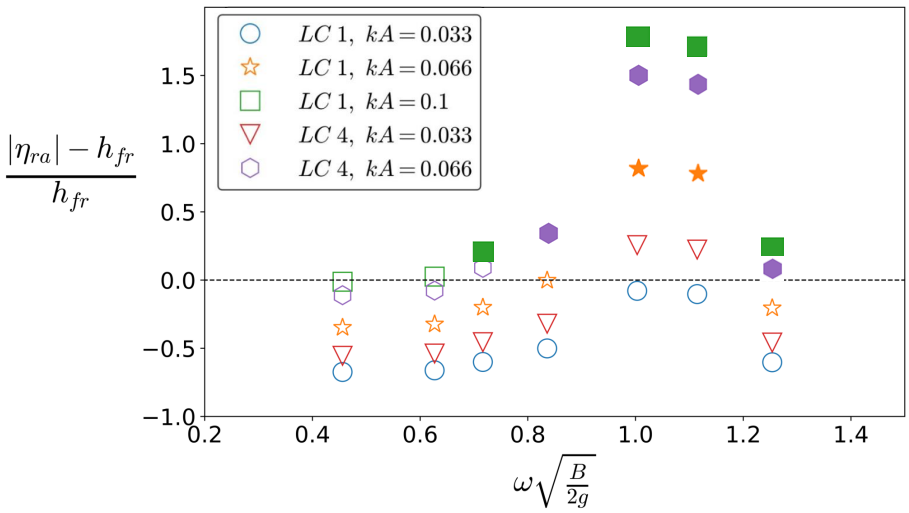

Figure 5.37: Non-dimensional flooding parameter as a function of non-dimensional frequency. The solid symbols represent flooding captured in experiments, the empty symbols represent no flooding

5.2 Summary

Free-roll decay tests for various conditions were performed for the intact and damaged ship model, both experimentally and numerically with OF. This was crucial to identify the roll natural periods and damping in the different examined scenarios and so to better analyze the behavior in waves. Then freely-floating tests in regular beam-sea waves on the damaged section have been carried out by varying the incident-wave parameters with 2D flow conditions. The damaged rectangular opening was located on the side facing the waves. Effect of loading condition, damage compartment size, air compressibility in airtight compartment, damage-opening size and initial transient flooding were examined. Video recordings and measurements inside the damage compartment, were performed in all experiments. Motions and internal floodwater heights were measured and analyzed. Repeatability tests were performed. The outcomes of the investigations can be summarized as follows:

- Free roll decay tests demonstrate that the damage scenario causes a large increase in roll damping and also increases the roll natural period relative to the intact case. Smaller damage opening decreases the total physical roll damping slightly, whereas for an airtight damaged compartment, the roll damping is highly reduced. OpenFOAM numerical results present a reasonable agreement with the experiments and can help in understanding the physical behavior of the damaged section.

- For the floating damaged section in waves, the floodwater behavior is highly coupled with body motions. The overall behavior is very different as compared to the intact condition. Heave and sway motions are affected to a smaller degree as compared to roll motions. Piston mode and sloshing resonance play an important role. A linear strip-theory approach, using the CFD solver OpenFOAM, provided a reasonable agreement with experiments but demonstrated the importance of incorporating nonlinear effects in roll damping for more quantitative comparison at roll resonance.
- Change in initial loading condition modifies the flooding behavior inside the compartment. In this case, the KG and draft are modified, thus, the natural resonance periods of rigid motions, piston and sloshing modes also shift towards higher values.
- Air compressibility can have important effects. It slows down the flooding inside the damaged compartment but it can excite larger motions in some cases as shown for heave motions. Air compressibility is, however, associated with scale effects with Euler number.
- Results from present transient-flooding tests show that flooding takes place in beam-sea waves near roll-resonance wave periods. Roll resonance varies with KG of the model section and the roll response is affected by the incident-wave period. Therefore, both KG and wave periods, and thus the ratio between the natural roll period and the incident wave period, have an important influence for a flooding case where damage opening lies above the water surface. Very high wave steepness can also cause flooding even if the wave period is not near roll resonance region. Effect of heave resonance period on transient flooding needs to be studied and is left for future investigations.
- Experimental repeatability is performed for a few cases and is shown to be acceptable (within 20%).

Chapter 6

Summary and Further Work

The behavior of a damaged ship section has been examined experimentally, theoretically and numerically. The main purpose of the work was to investigate the effect of piston and sloshing mode resonances on behavior of a damaged ship section. In addition, other features typical for the damaged condition were identified, quantified and compared with findings from previous works. The observed physical phenomena were verified with the use of theoretical and numerical tools, which also complemented the analysis.

Main findings from the work are summarized in section 6.1. Preliminary results for a domain decomposition (DD) technique combining a potential flow solver with a NS solver are presented in section 6.2. This study has been performed as part of present research work and is meant as first step towards more robust and efficient DD strategies. Other relevant topics for further work are proposed in section 6.3. These are also presented briefly in a table at the end of this chapter.

6.1 Summary of Present Work

Experiments were performed on a ship section (designed as a midship section) in intact and damaged conditions in a small wave flume. The model encompassed the entire breadth of the flume to have 2D flow conditions. Forced heave oscillation, free-roll decay tests in calm water and freely-floating model tests in beam-sea waves were performed. Experimental parameters were varied to identify important factors governing the flooded condition.

Forced heave motion experiments show that the damage has an important effect on the hydrodynamic heave added mass and damping coefficients. Sloshing mode resonance causes change in local flow features but no significant change in dynamic heave loads. First piston mode resonance causes large negative added mass and large damping values as compared to the intact condition. This is also confirmed using theoretical formulations from Newman et al. (1984) for submerged heaving bodies. This was adapted to study a 2D damaged section. Flow features for shallow filling level observed inside the damaged compartment were cross-checked with existing sloshing studies. Air compressibility in the damaged com-

partment changes the inflow/outflow at the opening. An important observation was the absence of piston mode and presence of sloshing modes for an airtight compartment. This was also supported by mathematical formulations.

Free-roll decay tests in intact and damaged condition have been performed. Natural roll period, linear and quadratic roll damping coefficients were calculated for all cases. It was found that presence of damage increases the natural roll period and damping for general scenarios. Quadratic damping was the dominating term in the damaged cases due to presence of a large opening. Airtight damage compartment further increase the roll period slightly as compared to a ventilated compartment but decreases the roll damping. This is due to limited flow through the opening for an airtight section confirming that flow near the opening plays an important role for roll damping. Change in damage-opening size mainly causes change in quadratic damping term without affecting natural roll period or linear damping. Initial loading condition also plays an important role in determining roll period and damping in the damaged condition. Smaller loading leads to larger natural roll period and damping. Free-roll decay tests were also preformed for an intact section with an internal tank (damage opening was closed). The natural roll period was similar to the damaged section with opening but the roll damping was much smaller. This shows purely the effect of damage opening on the roll damping behavior since all other parameters like the draft, free-surface effect etc. of the model with closed opening is same as the damaged section with inflow/outflow allowed.

For tests with the freely-floating model in beam-sea waves, the effect of piston and sloshing mode resonance was highlighted. Sloshing mode does not affect motions greatly but piston mode affects the body motions due to large inflow/outflow through the opening at these frequencies. Varying the initial loading condition has a significant effect on the behavior, mainly due to change in natural roll period and change in natural sloshing and piston mode resonance frequencies. Half-compartment (asymmetric) damage reduces the motions significantly due to additional heave and roll restoring moments on the non-damaged side. Damage-opening size has little influence on the motions in the present case. Air compressibility in the damaged compartment increases heave and roll motions because presence of air-cushion changes the heave and roll natural periods and damping.

Transient flooding tests were performed with the an initially dry freely-floating model in waves. The damage opening lies at a certain height above the floating draught depending on the loading condition. As the model undergoes motion, it can experience flooding. In beam-sea condition, as expected, roll motion was found to be the dominant factor governing flooding; in particular, a crucial parameter is the ratio of the incident-wave period and the roll natural period. This is indirectly related to the loading condition because the natural roll period depends on loading. Both the incident-wave period and steepness were found to be important factors for estimation of flooding occurrence and flooding time. The flooding behavior shown in figure 5.33 of the present work was found to be qualitatively similar to the transient flooding experiments documented in Bennett and Phillips (2017).

Detailed error analysis was performed for the experiments. The tests demon-

strated reasonable reapeatability for the analysed cases. These tests can serve as an important database for validation purposes due to the simplified model design and setup.

Theoretical formulations from Newman et al. (1984) were extended to study a 2D damaged section. Reasonable agreement for the piston mode frequencies and similar qualitative behavior for the hydrodynamic coefficients was obtained. Simulations from WAMIT also verified the presence of sloshing and piston mode resonance frequencies.

CFD simulations,using OpenFOAM, were performed to cross-check and complement experimental studies. A NWT was setup and validated against simple diffraction experiments in the wave flume. Convergence for space and time discretizations was demonstrated. The use of dynamic morphing vs overlapping grids was analyzed for moving bodies/boundaries. A detailed study was performed for proper selection of time-stepping schemes in OF. This analysis can guide researchers in proper selection of numerical parameters for OF. The use of overlapping grids proved to be useful for free-roll decay/forced roll simulations with reasonable results for intact and damaged condition. Reasonable agreement was observed for both the hydrodynamic force coefficients and the flow features (especially near opening) in case of forced heave motion simulations. Flow phenomena were explained in detail by means of simulation snapshots and they are consistent with the experimental findings. The simplified strip-theory formulation used for the simulation of freely-floating damaged ship motions also provided reasonable results.

Although, CFD is a very powerful tool, it is limited by the requirement of significant computational resources, especially in three-dimensional flow conditions. In an attempt to achieve efficiency while maintaining the advantages of the CFD solver, a preliminary study of a Domain Decomposition (DD) strategy is presented in the following section. This is meant to serve as a starting point for future research regarding a DD which can be implemented for complex simulations of damaged ships. Background and methodology for the DD along with initial results are discussed in the following section briefly. Details about implementation and other relevant information can be found in appendix C.

6.2 Preliminary Analysis of a Domain Decomposition Strategy

The analysis of damaged ship behavior (2D or 3D) is complex, involving exchange of floodwater and vortex shedding near the damaged opening edges, as demonstrated in chapters 4 and 5. Therefore, this wave-body interaction scenario requires the use of solvers which can provide detailed and accurate description of the flow features near the opening, for example, viscous-flow solvers which can take into account vortex-shedding effects. These effects do not matter far away from the body ($\sim$ 3-5B in 2D) due to diffusion and dissipation process. Therefore, sufficiently far from the structure the flow can be adequately described using potential-flow solvers.

The latter, such as BEM or Harmonic Polynomial Cell (HPC) methods, are more efficient and accurate than NS solvers when applicable, e.g. to simulate free-

surface wave propagation or seakeeping problems with minor viscous effects. On the other hand, NS solvers can account for viscous phenomena when they matter, but are computationally expensive. They require much finer mesh sizes and time steps as compared to potential-flow solvers. This leads to a high computational overhead. A simple diffraction case for 30-40 wave periods on a 2.2 GHz clock speed machine using 16-32 cores can take upto 10-15 hrs for a NS solver (see table 3.10). A domain decomposition (DD) method with a NS near the structure and a potential-flow solver in the rest of the domain can help preserving efficiency while retaining the features of NS solvers where needed.

Here, a 2-dimensional (2D) DD strategy is proposed coupling a NS solver with VoF technique for free-surface capturing (OF) with a potential-flow solver. For the latter, the HPC method, recently proposed by Shao and Faltinsen (2012, 2014), is selected, which proved to be very efficient and accurate. Shao and Faltinsen (2012, 2014) have demonstrated superior accuracy and efficiency for HPC as compared to BEM simulations with the same grid sizes.

The DD is setup here as an initial step towards efficient and accurate calculation of a radiation problem for a 2D damaged ship section. It is proposed to be extended for more complex damaged ship calculations (diffraction problem, freely-floating body in waves problem) and possibly for 3D damaged-ship scenarios as a future work.

6.2.1 2D Domain-Decomposition Methodology

A DD strategy could be useful to ensure accurate and efficient solution for a damaged ship section where vortex-shedding and viscous phenomena matter mainly near the body. Here, a simplified scenario is examined to prove its potentialities to be used for future research. A 2D DD strategy is proposed for radiation problems of a damaged ship section. The computational fluid domain is divided into two domains as shown in figure 6.1, so that forced body motions occur in the NS domain and waves travel outward through the HPC domain composed by two regions, respectively, at the left and right side of the NS domain. In the inner-domain region containing the damaged ship section, viscous effects and vortex shedding might be important; therefore, the NS solver (implemented in OF) is used. The setup and settings discussed in chapter 3 are also applicable here. The NS solver completely encloses the body and extends vertically from the computational top boundary in air to the bottom wall. For the OF domain, as described for the radiation problem in chapter 3, no-slip condition is used at the body boundaries and the bottom wall and CN 0.9 scheme is used for the time evolution. In the outer domain, where potential-flow theory describes the flow evolution adequately, the HPC method with a fixed grid is employed. No-penetration condition is enforced at the bottom. Semi-Langrangian markers are used to track the free-surface evolution, i.e. they are restricted to move along vertical gridlines. Nonlinear free-surface kinematic and dynamic boundary conditions are enforced at these markers. The time evolution is performed with the second order Runge-Kutta (RK2) scheme. More details for the HPC method are provided in appendix C. Within the DD, the grid strategy used in the NS and HPC domains contributes in limiting the com-

putational costs as the grid topology must be built only at the initial time step.

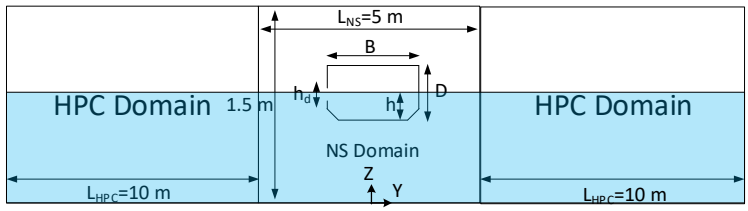

Figure 6.1: Domain-decomposition strategy: Sketch with dimensions of the two domains and definition of symbols used

The two domains are coupled at the left and right through non-overlapping vertical interfaces, as shown in figure 6.1. Continuity of pressure, velocity and free surface has to be maintained for the two solvers across the coupling interfaces spatially and temporally. For the present DD, information exchange between the two solvers is achieved by transferring read/write control to and from OpenFOAM using a Python executable file, rather than coding in OpenFOAM templates. This approach makes the DD implementation more straightforward, as the HPC solver is implemented in Python and because in this way we can treat the two solvers as separate. On the other hand, it is expected to lead to slower simulations with respect to the coding option due to the required read/write operations. Details of the information exchange for various variables at the coupling interface are described and shown in figure C.6 of appendix C.

The proposed DD is used here to study forced heave motions for a damaged 2D section. In this case, the primary aim of the outer domain is to propagate the radiated waves outwards and, therefore, a coarser grid can be used for the HPC domain. The NS domain should be large enough so that the vorticity reflected at the domain boundaries diffuses before reaching the body boundaries. The dimensions of the two domains and related symbols are provided in figure 6.1. The cell discretization in the NS solver is such that $\Delta Y = 0.02B$ and $\Delta Z = 0.01B$. For the HPC solver, $\Delta Y = 0.1B$ and $\Delta Z = 0.1B$ in both left and right HPC regions. Smaller cells in the NS domain help in obtaining a sharper air-water interface, with limited VoF smearing and better free-surface resolution.

Figure 6.2 demonstrates the comparison between added-mass and damping coefficients from experiments, from pure OF simulations and from DD simulations for forced heave motions at filling level FL 2. The pure OF simulations are performed using NWT settings given in chapter 3 with $\Delta Y = 0.02B$ and $\Delta Z = 0.01B$. The agreement of DD results with the experimental values is overall satisfactory, but differences are observed at smaller frequencies. The general trend of the experiments, i.e. negative added mass and large damping at smaller frequencies, is captured by the DD. The agreement between the DD and pure OF simulations is also reasonable except at smaller frequencies. At these frequencies, the wavelength becomes large with larger amplitudes. They carry larger energy

and even small differences in phase and amplitude at the coupling interface can cause significant changes in the added mass and damping coefficients. One major error source for this behavior of the DD is the coupling between the VoF technique used by OF to capture the air-water interface and the semi-Lagrangian free-surface markers employed in the HPC solver. Errors may also be introduced due to difference in spatial discretization schemes in the two domains. Increasing the size of OF domain for one frequency, ω^*=1.25, did not produce any difference in the hydrodynamic coefficients. This may not be the case for smaller frequencies and must to be investigated in detail in future works.

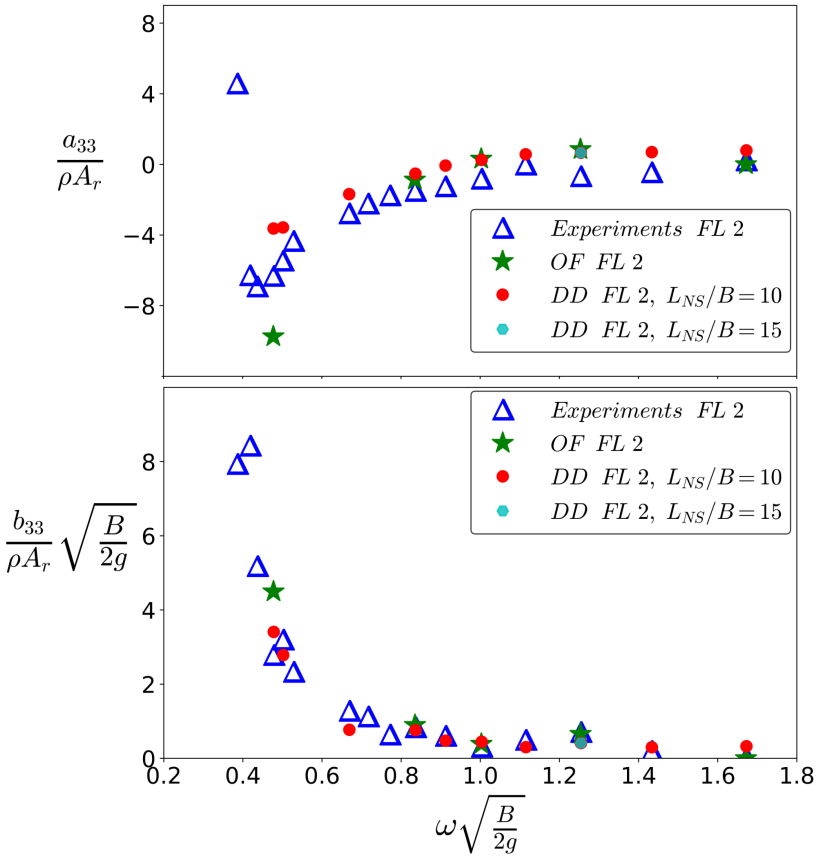

Figure 6.2: Non-dimensional experimental and numerical (pure OF and DD) added mass (top) and damping (bottom) non-dimensional coefficients for 5 mm heave amplitude at filling FL 2 as a function of normalized frequency. The symbols are consistent with those used in chapter 4

Figure 6.3 shows the vortical structures in the NS domain at filling level FL 2 for forcing frequency ω^* = 0.41 and forcing amplitude 5 mm. Significant vortex shedding is observed near the opening edges. The results are quite similar to the forced heave motion results obtained using pure OF simulations in chapter 4. This

shows that the DD can help in preserving flow features and viscous effects near the body.

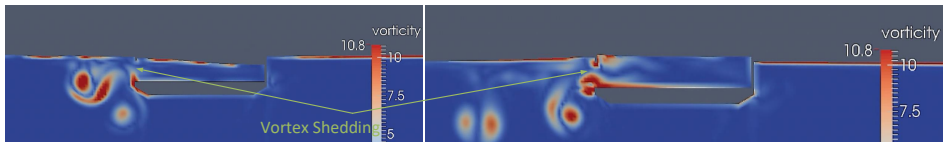

Figure 6.3: DD solution: vorticity (s^{-1}) in the inner domain (OF) at filling level FL 2 and forcing frequency ω^* = 0.41 and forcing amplitude η_{3a}=5mm

The DD gives reasonable accuracy for most frequencies while providing significant savings in computational time (CPU time). For the same forcing frequency (ω^*=1.25) and amplitude, using a serial process on a laptop (2.7 GHz, 4 cores), simulations were performed for the pure OF and DD cases with two OF domain sizes, i.e. L_{NS}/B=10 and 15, for 12 time periods. The CPU time required, of course, depends on the machine settings and can vary greatly. So, to ensure a proper comparison between pure OF and DD, their simulations were performed on the same machine. The results are shown in figure 6.4. The DD takes about 1/3 of the computational time as compared to pure OF simulations with the same overall domain size in the two cases. The decrease in computational time is not very high since the HPC solver is not optimized and also because the OF solver is initialized and stopped at each time step of the simulation by the external HPC solver. The savings can be improved by optimizing the HPC solver, see details provided in (Hanssen, 2019). It should also be noted that the savings will increase even more significantly for 3D simulations.

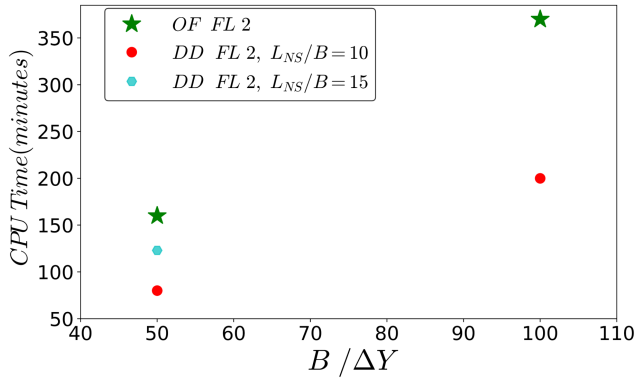

Figure 6.4: Computational time in minutes for forcing frequency with different sizes of OF domains and cell discretizations for ω^*=1.25 and forcing amplitude η_{3a}=5mm

6.2.2 Challenges and Limitations for the DD

Some challenges in the coupling of the two solvers used in the present DD are mentioned in this section. Discussion about possible shortcomings for a DD between the HPC and OF solver is also provided in detail in Hanssen (2019).

Firstly, the HPC solves a single-phase problem in the fluid domain, whereas OpenFOAM uses a multiphase solver and both air and water domains are solved. This causes a large gradient in dynamic pressure and horizontal velocities in OF near the free surface. Therefore, special consideration has to be given to the free surface cell in OF at the coupling interface. As mentioned earlier, a major issue is related to the VoF method employed for OF. OF uses a simplified VoF method, where the volume fraction in a cell is defined but the free surface is always horizontal or perpendicular to the gravity vector. This phase fraction can only be defined at the interface patch for OF but the slope of the free-surface cannot be defined (see example case in figure 6.5). Therefore, the cell size has to be very small in OF domain for maintaining the local slope almost similar to the one in the HPC domain.

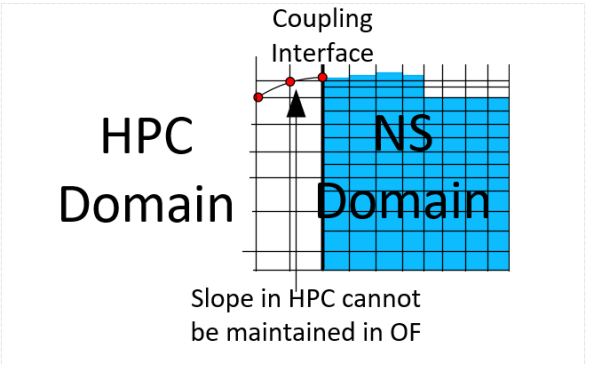

Figure 6.5: Issue of maintaining slope continuity in OF domain

Lastly, the presented coupling is a weak coupling. To obtain a stronger coupling between the domains, an iterative procedure for exchange of boundary condition information must be employed. To efficiently implement such a solution, iterations inside the OF solver loop have to performed. This requires coding in OpenFOAM which is out of the scope for this work. Although the presented strategies work well in certain cases, more robust techniques have to be developed for general scenarios. Hanssen (2019) has shown a DD strategy for the HPC solver with the in-house NSLS code from Colicchio et al. (2006), discussed in chapter 3. They have shown promising results and demonstrated that, for a more effective and robust DD, it is an advantage to have full control of both solvers and being able to couple them also within the sub-steps of the used temporal schemes. This represents a challenge for OpenFOAM because it requires to dive into and modify adequately the inner levels of OF implementation.

The present study proved the potential applications of a DD strategy for the problem of interest. Its practical use needs its extension for more complex dam-

aged ship calculations (diffraction problem, freely-floating body in waves problem) and possibly 3D damaged-ship scenarios. This is left for future research.

6.3 Suggestions for Future Research

Main areas identified for further research during the course of the present work are as follows:

- Experiments for forced roll and heave motions of a damaged model with realistic internal compartment layout effect can be important for more in-depth understanding of the effect of damage on hydrodynamic coefficients in real scenarios, especially for roll motion. Effect of damage compartment size can also be examined and can provide interesting insights into occurence and effect of of sloshing and piston mode resonance.
- Dedicated experiments are suggested for a complete 6 DoF model of a RO-RO ship in waves with head, beam and quartering sea headings. This will help to identify the 3D effect of sloshing and piston mode resonance on ship motions. The damage opening size must be selected according to International Maritime Organization (IMO) rules. Modelling of internal structures, for example, engine room and decks precisely can help in reproducing realistic phenomena. This can also help to identify the effect of local floodwater loading on these structures. Forward-speed effects in waves must also be considered. These experiments would serve as an important benchmark for numerical studies and also help researchers develop protocols and guidelines on operations of ships in damaged condition.
- Incorporation of roll damping from experiments in theoretical formulations/ WAMIT to check if faster and efficient solutions can provide reasonable agreement with experiments.
- CFD simulations in 3D, though computationally expensive, can be important to study cases when experiments are not directly possible/available. In this regard, overset grids seem to be a very attractive option and can be investigated with more complex grid types, especially with open-source solvers like OpenFOAM. 3D simulations can also help study local flow behavior inside the damaged compartment.
- A preliminary analysis for a DD scheme is discussed in the present work to demonstrate its potential. This can be extended to involve more complex scenarios and possibly 3D simulations. A 3D DD will help reduce computational cost significantly.
- Finally, a research effort should be made to provide suggestions for the formulation of rules and guidelines on operations, handling of damage scenarios and return to nearest port for damaged ships. Research on damaged ships has led to newer IMO and Safety-of-Life-At-Sea (SOLAS) regulations. Further development in research and understanding of damaged ship behavior can help to reduce loss of life/property after ship damage incidents.

Main findings of the present work and relevant suggestions for future research are outlined in table 6.1

Present Work	Important Findings	Suggestions for future studies
Experiments		
Forced motions Roll		Effect of airtightness, damage-opening size, compartment size and comparison with free-roll decay tests
Heave	Hydrodynamic behavior of a 2D damaged section is significantly different from intact condition	Possible studies on a 3D model to understand effect of 3D flow on piston and sloshing modes, realistic internal compartment layout
Sloshing and piston mode resonance	Piston mode resonance affects the added mass and damping significantly while sloshing affects local flow behavior. Large negative added mass and large damping values are observed near first the piston mode	
Effect of variation in experimental parameters	Airtightness can cause the damaged section to behave similarly as an intact section. Change in opening size does not affect heave hydrodynamic coefficients greatly	Study effect of change in compartment size and modelling realistic layout inside the compartments
Free-roll decay tests	Damage increases roll natural period and damping. Airtightness in damaged compartment reduces the roll damping and increases the natural period. Smaller initial loading results in a larger natural period and larger damping in the damaged condition. An intact section with an internal tank has similar natural roll period as a damaged section with an opening but much smaller roll damping	Free-roll decay tests for a 6 DoF model with similar parameters
Freely-floating model in waves 3 DoF damaged model in beam-sea waves	Roll behavior changes significantly for the damaged condition	6 DoF model in an at least three wave headings

Sloshing and piston mode resonance	For the damaged condition, change in motions/behavior as compared to intact condition is observed near the first piston mode. The change in motions is not as drastic as the change in heave hydrodynamic coefficients	Analyze effect of these resonance on a 6 DoF model in 3D flow conditions
Effect of variation in experimental parameters	Airtightness in damaged compartment increases heave and roll motions compared to ventilated damaged section but slows down flooding. Asymmetric damage significantly reduces motions. Change in opening size does not have a large effect on motions	Effect of airtightness, opening sizes, realistic internal compartment layout in a 6 DoF model
Transient flooding tests	Flooding is observed for incident waves with periods close to the natural roll period. At higher wave periods, waves with even larger amplitudes may not cause flooding. Flooding time depends on the initial loading condition, wave period and steepness	Extend the present work to a 6 DoF model/ possible damage opening mechanism
Numerical Work		
Theoretical formulations	Good estimate obtained for sloshing and piston mode resonance frequency values	
WAMIT	Good estimate obtained for sloshing and piston mode resonance frequency values	Apply roll damping from experiments to check if reasonable results can be obtained
CFD	Forced heave motion simulations show reasonably good agreement capturing large damping at piston mode resonance for a damaged section. Free-roll decay simulations also display a reasonable agreement with experiments. The large natural roll period and damping for the damaged condition are captured by the simulations with reasonable differences against experiments.	3D freely-floating model in waves using Overset grids. Use of oct-tree grids

	Strip-theory results show reasonable agreement with experiments. Difference occurs near roll resonance frequency due to possible 3D effect that not captured by the strip-theory method	
DD	Encouraging results are obtained for forced heave motion simulations with differences at smaller forcing frequencies	Extend DD to an in-house solver, possibly a LS method, to simulate more complex problems and to have greater control over solvers and implementation. 3D DD to perform CFD simulations providing significant computational savings

Table 6.1: Summary of main findings from present work and some suggestions for future studies

Appendices

Appendix A

Lost Buoyancy Method

Following flooding, a damaged ship can reach equilibrium condition. Two methods are used for calculation of static ship condition after flooding: Lost buoyancy method and added weight method (Biran and Pulido, 2013). In the present work, the lost buoyancy method was used and is described in this appendix. The symbols used in the text are as defined in chapter 2.

In the lost buoyancy method, it is assumed that the flooded region/compartment does not provide any buoyancy. However, the weight of the ship structure remains the same. Therefore, the ship must reach a new equilibrium condition until the forces/moments are balanced. Figure A.1 shows the change in waterplane area after damage for the experimental model used in this work.

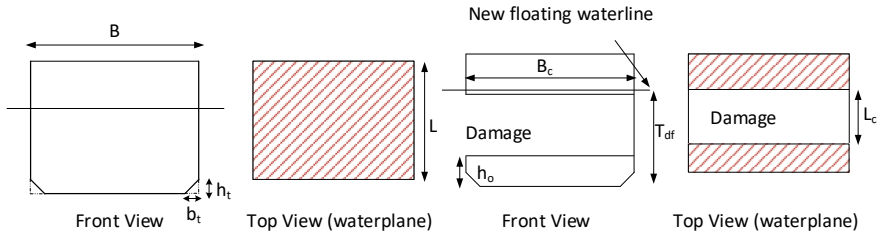

Figure A.1: Illustration of the change in floating condition and lost waterplane area after damage from intact (left plots) to damaged condition (right plots)

The damaged waterplane area is $a_{wp}^{dam} = LB - \mathrm{B_c L_c}$
Assuming a new floating draft, $\mathrm{T_{df}}$, after damage, new equilibrium force balance condition is

$$\mathrm{M} + \mathrm{M_B} = \rho[{a_{wp}}^{dam}(\mathrm{T_{df}} - h_o) + LBh_o - 2LAr_t] \tag{A.1}$$

where, $\mathrm{M} + \mathrm{M_B}$ is the total mass of model in intact condition and $Ar_t = \frac{b_t h_t}{2}$, i.e., the area of triangular sections shown in figure A.1. All other quantities are known, therefore, $\mathrm{T_{df}}$ can be found from eq. (A.1).

The new height of centre of buoyancy from keel, KB_n, is given by

$$KB_n = \frac{\rho[({a_{wp}}^{dam}\mathrm{T_{df}} - 2LAr_t)\frac{\mathrm{T_{df}}}{2} + (\mathrm{L_cB_c}h_o - 2LAr_t)\frac{h_o}{2}]}{\mathrm{M} + \mathrm{M_B}} \tag{A.2}$$

Since, the damage is symmetrical about the center-line, the area of moment of waterplane after damage becomes $I_l = \frac{(L-\mathrm{L_c})B^3}{12}$.

Therefore, the metacentric radius is, $BM_n = \frac{I}{\Delta} = \frac{\rho I_l}{(\mathrm{M}+\mathrm{M_B})}$.

The corresponding metacentric height is, $GM = KB_n + BM_n - KG$, where KG is the initial centre of gravity from keel for the model before flooding.

Appendix B

Calculation of added mass and damping coefficients

Both forced-heave motion experiments and simulations have been performed in the present work. The calculations for obtaining heave added mass and damping from heave force was presented in chapter 4. For the strip-theory calculations in chapter 5, forced motion simulations were performed for all three modes of motion. Two methods for calculation of added mass and damping coefficients in sway and roll are presented in this appendix. More details can be found in Vugts (1968) and Faltinsen (1990).

Method I
Assuming that heave motion is decoupled from sway and roll, the equations of motion for a coupled sway-roll system can be written as

$$\begin{aligned}(m + a_{22})\ddot{\eta}_2 + a_{24}\ddot{\eta}_4 + b_{22}\dot{\eta}_2 + b_{24}\dot{\eta}_4 &= F_2 \\ a_{42}\ddot{\eta}_2 + (I_{44} + a_{44})\ddot{\eta}_4 + b_{42}\dot{\eta}_2 + b_{44}\dot{\eta}_4 + c_{44}\eta_4 &= F_4\end{aligned} \tag{B.1}$$

where all symbols are as defined before in this text (Chapter 5).
In each simulation, it is assumed that the body is forced to oscillate in one degree of freedom only, e.g.

$\eta_2 = \eta_{2a}\sin(\omega t), \eta_3 = \eta_4 = 0;$
$\eta_2 = \eta_3 = 0, \eta_4 = \eta_{4a}\sin(\omega t)$

During each simulation, the sway force and roll moment are measured and can be written as, $F_k = F_{ka}\sin(\omega t + \varepsilon_k)$, where k=2,4 and ε_k is the phase relative to the forced oscillation. Substituting η_k and F_k in eqs. (B.1) gives the added mass and damping coefficients as

$$\begin{aligned}a_{22} &= \frac{-F_{2a}\cos(\varepsilon_2)}{\eta_{2a}\omega^2} - m \\ b_{22} &= \frac{F_{2a}\sin(\varepsilon_2)}{\eta_{2a}\omega}\end{aligned} \tag{B.2}$$

$$
\begin{aligned}
a_{42} &= \frac{-F_{4a}\cos(\varepsilon_4)}{\eta_{2a}\omega^2} \\
b_{42} &= \frac{F_{4a}\sin(\varepsilon_4)}{\eta_{2a}\omega} \\
a_{44} &= \frac{c_{44} - \frac{F_{4a}}{\eta_{4a}}\cos(\varepsilon_4)}{\omega^2} - I_{44} \\
b_{44} &= \frac{F_{4a}\sin(\varepsilon_4)}{\eta_{4a}\omega} \\
a_{24} &= \frac{-F_{2a}\cos(\varepsilon_2)}{\eta_{4a}\omega^2} \\
b_{24} &= \frac{F_{2a}\sin(\varepsilon_2)}{\eta_{4a}\omega}
\end{aligned}
$$

Method II (Time-Domain Method)
Another method can be used to calculate added mass and damping coefficients as shown in Faltinsen (1990). Excluding hydrostatic pressure, the linear hydrodynamic radiation force $F_{rad,kj}$ in k-th direction due to forced motion,η_j, in j-th direction, can be written as

$$F_{rad,kj} = -a_{kj}\ddot{\eta}_j - b_{kj}\dot{\eta}_j \tag{B.3}$$

where, a_{kj}, b_{kj} are frequency dependent added mass and damping coefficients, respectively. a_{kj}, b_{kj} can then be evaluated using

$$
\begin{aligned}
a_{kj}(\omega) &= -\frac{\int_0^{nT} F_{rad,kj}\ddot{\eta}_j dt}{\int_0^{nT} \ddot{\eta}_j{}^2 dt} \\
b_{kj}(\omega) &= -\frac{\int_0^{nT} F_{rad,kj}\dot{\eta}_j dt}{\int_0^{nT} \dot{\eta}_j{}^2 dt}
\end{aligned}
\tag{B.4}
$$

Here, n is a whole number, i.e. nT is a whole number of time periods.In the present work, it was found n=5-10 gives good results.

In general, the comparison between the two methods described here was found to be good (difference of less than 5%). However, it depends on the accuracy of phase difference measurement for method I and time-integration of motion and velocity in method II.

Appendix C

Domain Decomposition: Additional details

A DD is discussed in chapter 6 as an initial step towards efficient and accurate simulation of a radiation problem for a 2D damaged ship section. A brief description of the HPC method, potential-flow solver used in the DD, and additional information about the coupling strategy are provided in this appendix.

C.1 Harmonic Polynomial Cell Method

The HPC method can efficiently solve hydrodynamic problems. This is a field solver for potential-flow problems. It has been earlier used for electrodynamics problems and other physical problems which involve the Laplace equation as governing equation. For hydrodynamic problems involving floating bodies and deforming free surface, it is used to solve boundary value problems (BVP) for the velocity potential governed by the Laplace equation and completed by Dirichlet (along the free surface) and Neumann (along bodies/walls) boundary conditions. The BVP solution is coupled with a suitable temporal scheme to prolong the geometry and boundary conditions in time, within a Mixed Eulerian-Lagrangian strategy (Ogilvie, 1967; Longuett-Higgins and Cokelet, 1976). An important feature of the HPC method is that the Laplace equation is automatically satisfied by expressing the velocity potential in terms of harmonic polynomials, i.e. functions everywhere analytic and solutions of the Laplace equation. At discrete level, it leads to sparse matrix systems which can be solved very efficiently. Basic details of the HPC method and its implementation can be found in Shao and Faltinsen (2012, 2014). Detailed analysis on the global and local properties of the HPC method, associated grid types, configurations etc. is described in Ma et al. (2018a). The refinement using quad-tree grids (right plot of figure C.1) documented in the latter work, as well as discussion on rectangular HPC grids, was developed as a part of the present learning and training on the HPC method. The HPC method was extended for simulation of body motions and nonlinear waves with overlapping grids by Hanssen (2019); Hanssen et al. (2018). They have provided a very detailed description of nonlinear wave generation and propagation. Here, only

information relevant to the DD, necessary basic details and some results are presented to highlight the accuracy of the method.

A standard HPC cell along with some modifications with respect to the original formulation are represented in figure C.1. The velocity potential in the cell (left plot of figure C.1) is described as a linear combination of eight harmonic polynomials, i.e.

$$\varphi(y,z) = \sum_{j=1}^{8} b_j f_j(y,z) \tag{C.1}$$

All harmonic polynomials up to third order and one fourth-order (first eight polynomials) are included, which leads to a spatial accuracy of the velocity potential between third and fourth order. Here, a local Cartesian coordinate system (y,z)is used with origin at node 9 of the cell. In addition, a global coordinate (Y,Z) system is used for the solution of the global problem. If the velocity potential is known at the nodes i=1-8 of a generic HPC cell (Dirichlet condition), then substituting (y,z) in eq. (C.1) with the locations (y_i,z_i) of the nodes i =1-8 and their respective potential values, φ_i (Dirichlet condition), leads to

$$\varphi_i = \sum_{j=1}^{8} d_{i,j} b_j \tag{C.2}$$

where $d_{i,j} = f_j(y_i,z_i)$. The coefficients, b_j in eq. (C.1) can, by matrix inversion, be written as $b_j = \sum_{j=1}^{8} c_{j,i}\varphi_j$. Substituting this relation in eq. (C.2) gives

$$\varphi(y,z) = \sum_{i=1}^{8}\sum_{j=1}^{8} c_{j,i} f_j(y,z)\varphi_i \tag{C.3}$$

Enforcing equation (C.3) at the center of each cell, i.e. at the node 9, gives an equation to estimate the velocity potential there. Moreover, the HPC cells are defined as overlapped so that node 9 of one cell is a boundary node for the neighboring overlapping cells and the continuity of velocity potential is ensured through the entire computational domain. This, together, with the fact that the first eight polynomials have a value of 1, 0, 0 ... at node 9 ($y=0, z=0$) results in the global matrix having constant entries for all internal fluid nodes, i.e. nodes that do not lie at the boundary. This helps to calculate coefficients for center nodes of HPC cells just once at the beginning of time-dependent problems, with substantial computational savings. A Dirichlet condition at the boundaries can be enforced by specifying the values of velocity potential at boundary nodes. To enforce a Neumann condition, the derivatives of the potential can be calculated analytically. In a NWT simulation, at any time instant zero normal velocity is enforced at the bottom, zero velocity is enforced horizontally far away, known normal velocity is enforced along a wavemaker/body and known velocity potential is enforced along the free surface. The BVP solution provides the velocity potential at the grid nodes at the examined time instant. In general, for the HPC simulations documented here, an Eulerian structured grid is employed. This differs from the original HPC method

where a boundary-fitted approach is used. It means that an additional technique is required for the evolution of the free surface. Here, similarly as proposed by Hanssen (2019), semi-Langrangian markers are used to track the free surface. The latter means that the markers are restricted to move vertically. Moreover, they are distributed horizontally so to be at the grid lines. Nonlinear free-surface kinematic and dynamic boundary conditions are enforced at the free-surface markers. They allow to update in time the velocity potential and the position of the free surface. Here the time evolution is performed with the fourth/second order Runge-Kutta (RK4/RK2) scheme. The velocity potential solved from the boundary value problem is stored at the nodes. The code was implemented in Python. More details on the extended version of the original HPC adopted here, can be found in Ma et al. (2018a).

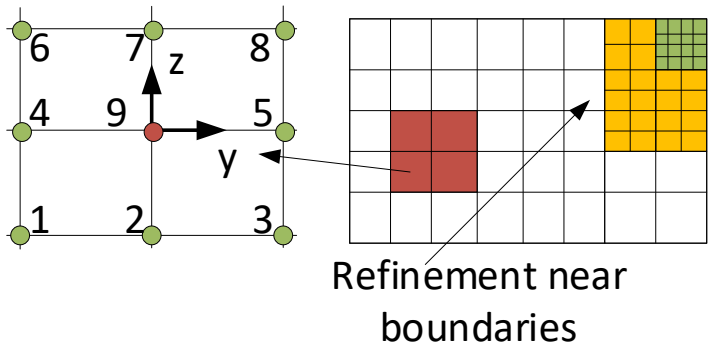

Figure C.1: The standard HPC cell (left), and quad tree refinement (right)

A simple case is presented here to demonstrate the wave propagation abilities of the HPC method. The latter is compared against the OF solver described in chapter 3. The computational field is shown in figure C.2. Dimensions for the NWT are length L_a =20 m, height d_a =2 m with a water depth of h_a = 1m. A Neumann condition is applied at the left end, representing a vertical control surface through which incident waves enter the domain with horizontal velocity $U = A\omega \cosh(k(h_a + Y))/\cosh(kh_a)\sin(\omega t)$. Here, A is amplitude of oscillation, ω is angular frequency of oscillation, k is wave number and h_a is depth of water. The boundary condition at the bottom wall is zero vertical velocity and the right end has a zero horizontal velocity condition. A NWT with the same dimensions was also implemented in OF to complement and check HPC results. The settings are the same as for the diffraction case presented in section 3.2 except at the left end. Here, instead of an oscillating wavemaker, a velocity condition at a fixed vertical control surface , i.e. a surface transparent to the water flow, is applied. The simulation parameters are such that ω =6.4 rad/s, $T = 2\pi/\omega$ =0.98s, A =0.025m and $kA = 0.10475$. The discretization values are $\Delta Y = \Delta Z = L_a/200 = 0.1m$ and $\Delta t = 0.05s \approx T/20$ for the HPC solver. For the OF solver, $\Delta Y = L_a/400 = 0.05m, \Delta Z = L_a/800 = 0.025m$ and $\Delta t = 0.01s \approx T/98$. The grid was refined

near the free-surface from 0.9 m $< Z <$ 1.1 m with $\Delta Y = A/10 = 0.0025m$, i.e. 10 cells per wave height. Numerical convergence, though not demonstrated here, was ensured for the HPC solver, while it has already been presented for the OF solver in chapter 3.

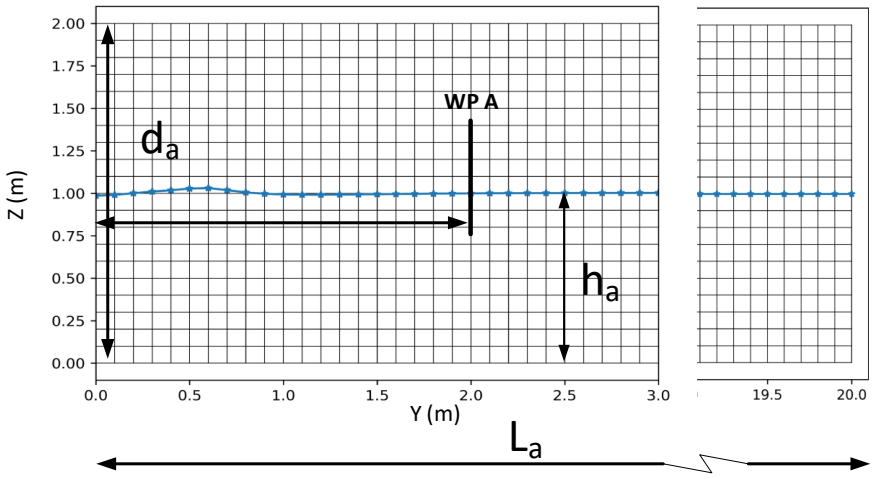

Figure C.2: Computational domain used for the examined wave propagation case. The shown free surface corresponds to the time instant t=0.14 s. The symbols used for the NWT are shown along with free-surface markers

A wave probe was used to measure the wave elevation at 2m (WP A, see definition in figure C.2) from the control surface to analyze the wave propagation from the two solvers, as shown in figure C.3. The numerical results are compared against the linear finite-water wave solution because the involved steepness is limited and therefore linear effects should be dominant. The wave elevation at WP A, which is at almost 1.5 wavelengths from the left boundary, documents a fair agreement between the two numerical results and the theoretical solution. The HPC solver is much closer to the theoretical solution with very small difference in the trough amplitudes and negligible phase difference. For the OF results, a slight phase shift is observed with respect to HPC and theoretical results. A small difference in amplitude (5%) is also present. This may be due to how the free surface evolution is handled in the OF solver. The VoF causes some smearing across the water-air interface. A very fine grid is required for accurate description of the free-surface.

In the following a wave-body interaction case is examined. The HPC results have been kindly provided as personal communication by Dr. Hanssen (2020). They have been obtained using his HPC solver documented in Hanssen (2019); Hanssen et al. (2018). Forced roll simulations were performed for the intact 2D section used in the present work (see chapter 3) by both HPC and OF solvers. Their setup is shown in figure C.4. Both solvers use an overlapping grid for these

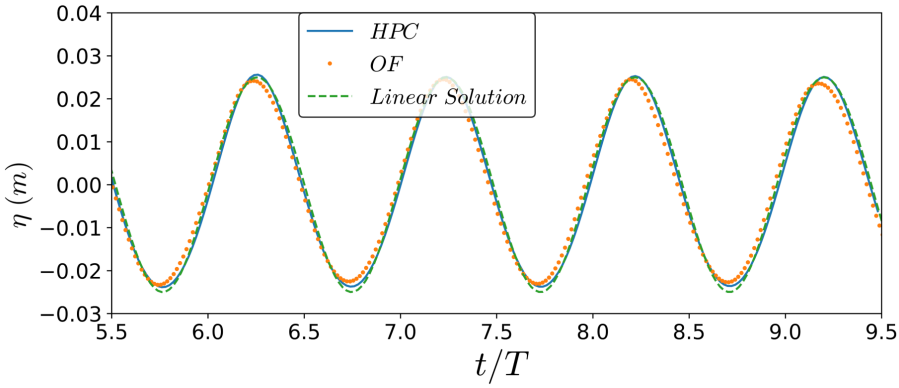

Figure C.3: HPC and OF time evolution of the wave elevation at the probe WP A defined in figure 6.2. The results are compared with the linear finite-water wave solution

simulations. Details of the implementation for the HPC overlapping grids can be found in Hanssen (2019). The settings for the OF solver are the same as for the radiation problem described in section 3.2.3. Figure C.5 shows the results for forced roll amplitude 0.1 and 0.135 radians, and oscillation frequency ω =6.28 rad/s. The HPC simulations were performed with dY=$B/20$, dZ=$B/20$ for the background grid and dY=$B/50$, dZ=$B/50$ for the overlapping grid and dt=0.02-0.05s. The OF simulations were obtained with dY=$B/50$, dZ=$B/100$ in the background grid and dY=$B/100$, dZ=$B/100$ for the overlapping grids (OG) with dt =0.005s. Their comparison shows a very good agreement in the steady-state region. This implies that for the intact ship section, the viscous effects are not important for the examined forcing amplitudes and frequency. This is also evident from the quadratic damping values obtained using free-roll decay tests for this ship-section scenario (see chapter 5). The CPU-time for the HPC simulations is less than 1/10 of the OF simulations.

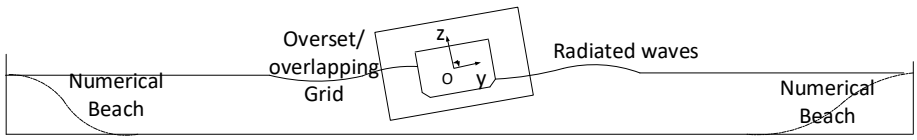

Figure C.4: Sketch of the numerical setup for the forced roll motions in calm water by the HPC/OF solvers

The two study cases examined here demonstrate the efficiency and accuracy of the HPC solver. In the next section, this is proposed as potential-flow solver to be coupled with the NS solver from OF within a 2D DD strategy for a damaged ship section.

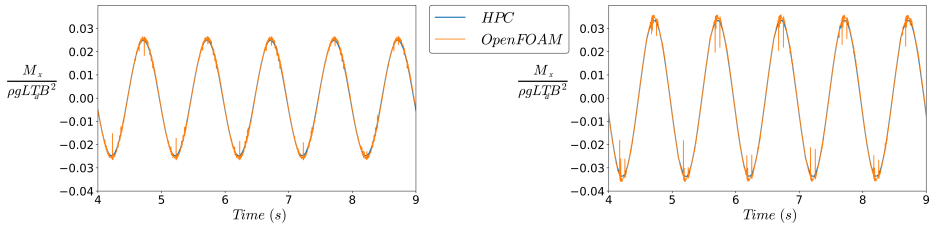

Figure C.5: Roll moment on the intact ship section due to forced roll motion at frequency ω =6.28 rad/s and amplitudes θ_0 =0.1 radians (left) and θ_0 =0.135 radians (right). Here, T_d is the draft and the other symbols are as described in chapter 2

C.2 2D Domain-Decomposition Strategy: Details

The two domains (HPC and OF) are coupled at the left and right through non-overlapping vertical interfaces. Details of the information exchange for various variables at the coupling interface are provided next and also illustrated in figure C.6.

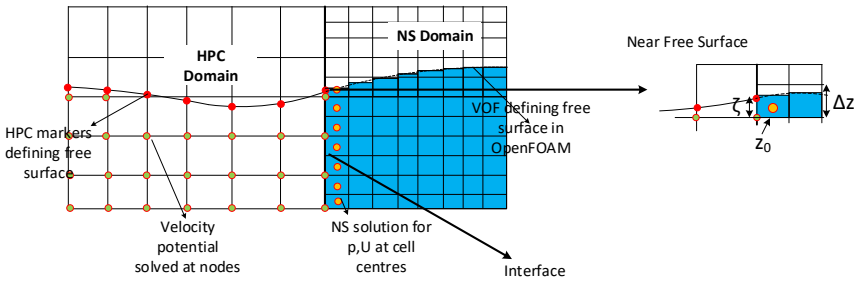

Figure C.6: Illustration of coupling between HPC and OF domains using a non-overlapping coupling interface. The sketch refers to the interface on the left of the VoF domain. The enlarged view in the right of the figure shows the dimension of a generic OF cell, Δz, the Z position z_0 of the bottom face of the cell containing the free surface closest to the interface and the vertical position of the free surface (at the interface), ζ, from the bottom of the cell

Data transfer from OF to HPC- The velocity calculated from OF is passed as input to the HPC solver in the form of a Neumann condition i.e. $\nabla\varphi.n = U.n$, where $U$is the OF velocity vector, n is normal vector to the coupling boundary and φ is the velocity potential to be solved in the HPC domain. To identify the free-surface, the vertical gradient of α in the cells adjoining the coupling boundary is computed. The cell closest to the maximum gradient is taken as the one with free surface location and its phase fraction is used to define the HPC marker location (see right plot of figure C.6). The values of the HPC marker can be written as

$\zeta = \alpha\Delta z$

Data transfer from HPC to OF- The velocity along the interface and the free-

surface marker location at the interface are calculated from the HPC solver and passed to OpenFOAM (OF) as boundary conditions. Phase fraction (α) and velocity are supplied at the start of each time step, as follows :

$$\alpha = \begin{cases} 1 & \text{completely filled cells} \\ \frac{\zeta}{\Delta z} & \text{partially filled cell} \\ 0 & \text{completely dry cells} \end{cases} \qquad U = \begin{cases} \nabla\varphi & \text{completely filled cells} \\ \nabla\varphi\ (\alpha) & \text{partially filled cell} \\ 0 & \text{completely dry cells} \end{cases}$$

The definition of the variables is provided in figure C.6. It should be noted that the NS solver requires input values of pressure and velocity at the cell centers whereas the HPC solver requires the information at the cell nodes. Therefore, third order interpolation schemes are used to interpolate velocity and pressure values back and forth between the two solvers.

Figure C.7 demonstrates graphically the time stepping procedure used in the DD. The starting solver is the domain where initial disturbance takes place. In the present DD application, it coincides with the NS solver, while for wave-body interaction problems it would coincide with the HPC solver. In the rare case of initial perturbation in both domains, then an initial iteration process must be carried out to make the flow conditions at common interfaces consistent for the two solvers. Each solver is stepped in time independently and boundary conditions are passed from one solver to the other alternately. For example, in case of forced heave motions, the NS solver will provide initial conditions at n^{th} time step to the HPC domain. Both solvers then march in time independently. The boundary conditions obtained from HPC domain solution at $(n+1)^{th}$ step are passed to the NS domain and serve as corrected boundary conditions for the NS solver at the next time step.

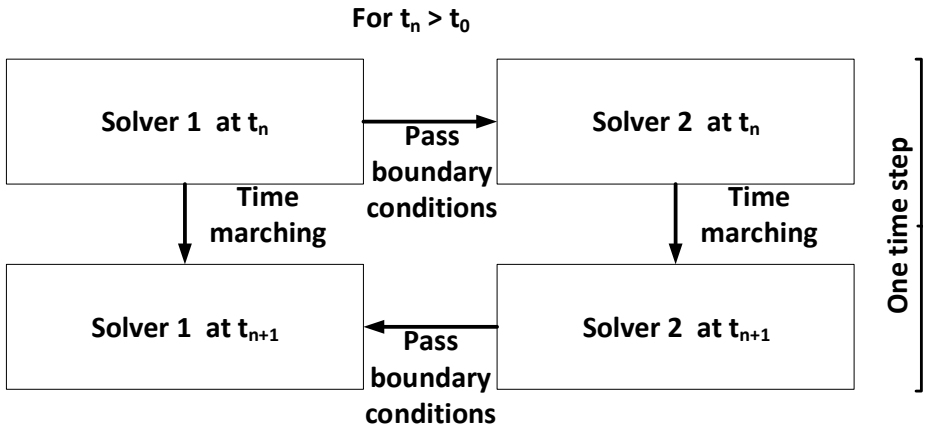

Figure C.7: Time stepping used for the numerical DD

The DD helps in limiting the size of the NS domain. A smaller inner domain allows to use a finer grid leading to better flow features resolution in the NS solver,

as shown in Colicchio et al. (2006). Using three different grid sizes they demonstrated that finer grids in the NS solver help in obtaining better flow capturing. The grid size for the HPC domain can be much coarser than for the NS solver since it has a higher spatial accuracy , as examined in section C.1. Colicchio et al. (2006) used an overlapping region where the solutions from the two domains overlap instead of a sharp interface. This makes the coupling between the domains more flexible and can be more stable. For forced motions, since the radiated waves propagate outwards, a single interface works well but an overlapping domain is suggested as future work for general problems.

Appendix D

Free Surface Identification in Experimental Images

The free-surface inside the damaged compartment is identified to demonstrate the modeshapes of sloshing and piston mode resonances. This was done manually using magnified images. There is also an external free-surface in the gap between the model and the flume wall. When the two are close to each other, it can be confusing to identify each surface accurately. In this appendix, two examples are presented with an without tracing of the free surface.

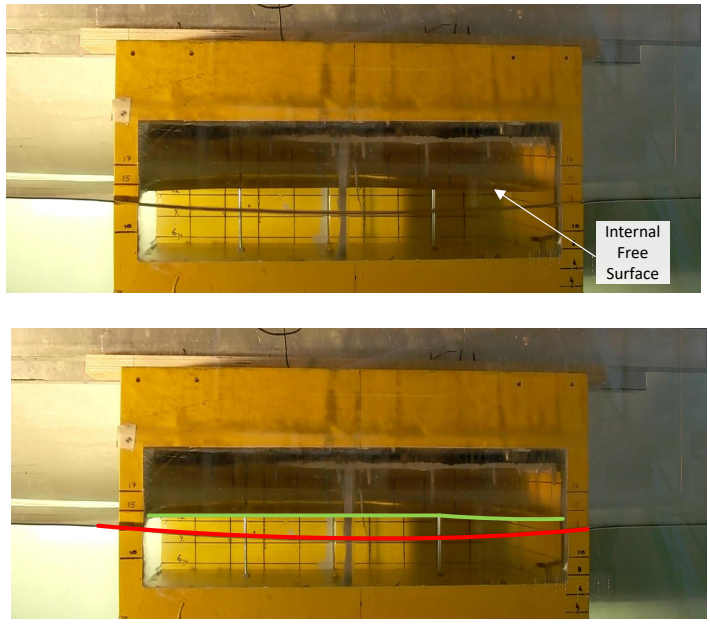

Figure D.1: Free surface identification for forced heave motion tests at filling level FL 2: clean image (top), image with traced internal and external free-surface (bottom)

In the first example (figure D.1), the internal and external free surface are far apart, whereas they are much closer in the second example (figure D.2). In latter situations, one needs to be careful in identification of the internal free surface.

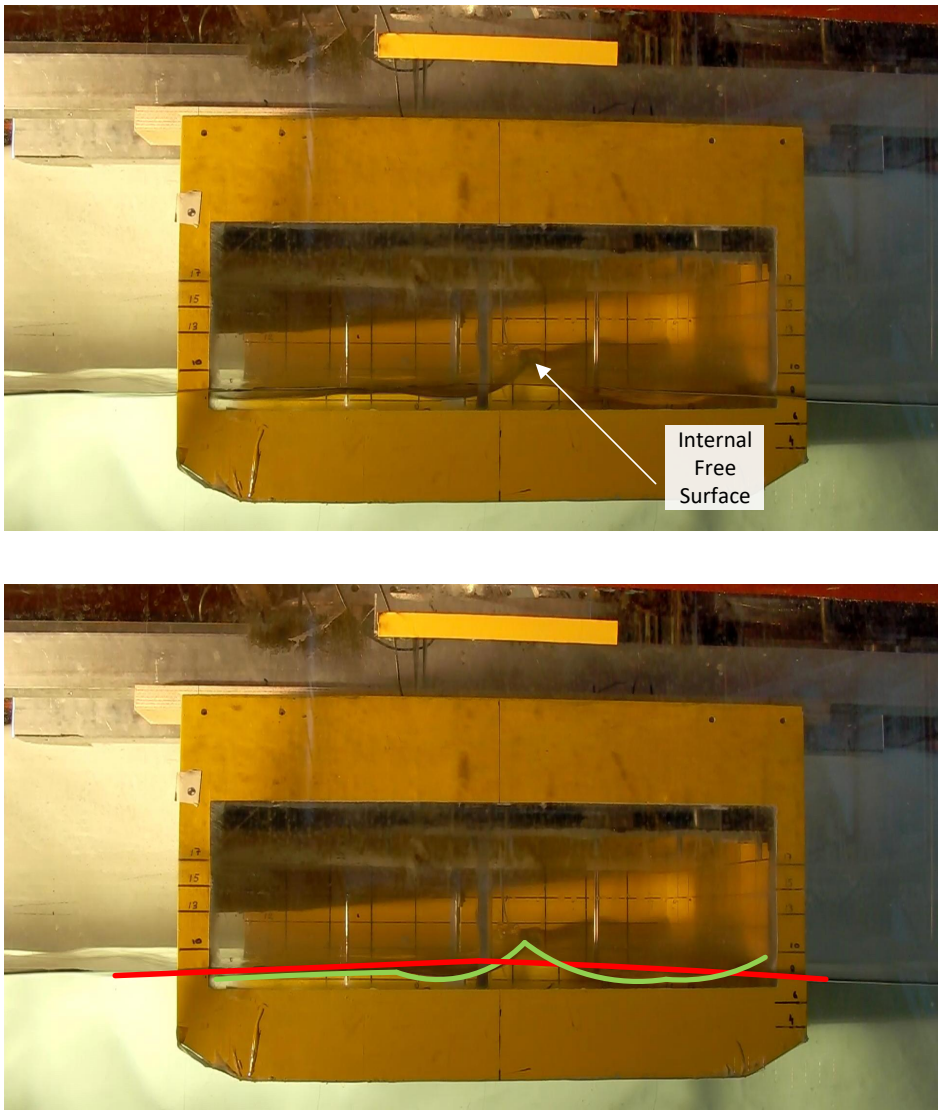

Figure D.2: Free surface identification for forced heave motion tests at filling level FL 1: clean image (top), image with traced internal and external free-surface (bottom)

Bibliography

M. Acanfora and A. Cirillo. A simulation model for ship response in flooding scenario. *Proceedings of the Institution of Mechanical Engineers, Part M: Journal of Engineering for the Maritime Environment*, 231(1):153–164, 2017.

M. Acanfora and F. De Luca. An experimental investigation into the influence of the damage openings on ship response. *Applied Ocean Research*, 58:62–70, 2016.

M. Acanfora and F. De Luca. An experimental investigation on the dynamic response of a damaged ship with a realistic arrangement of the flooded compartment. *Applied Ocean Research*, 69:191–204, 2017.

M. Acanfora, E. Begovic, and F. De Luca. A fast simulation method for damaged ship dynamics. *J. Mar. Sci. Eng.*, 7,111:47–65, 2019.

E. Begovic, G. Mortola, A. Incecik, and A. Day. Experimental assessment of intact and damaged ship motions in head, beam and quartering seas. *Ocean Engineering*, 72(1):209–226, 2013.

E. Begovic, A. Day, A. Incecik, S. Mancini, and D. Pizzirusso. Roll damping assessment of intact and damaged ship by CFD and EFD methods. In *Proceedings of the 12th International Conference on the Stability of Ships and Ocean Vehicles*, 2015.

E. Begovic, A. Day, and I. A. An experimental study of hull girder loads on an intact and damaged naval ship. *Ocean Engineering*, 133:47–65, 2017.

S. Bennett and A. Phillips. Experimental investigation of the influence of floodwater due to ship grounding on motions and global loads. *Ocean Engineering*, 130(1):49–63, 2017.

A. Biran and R. L. Pulido. *Ship Hydrostatics and Stability*. Elsevier Ltd., 2013.

L. Bonfiglio, S. Brizzolara, and C. Chryssostomidis. Added mass and damping of oscillating bodies: a fully viscous numerical approach. In *Recent Advances in Fluid Mechanics, Heat Mass Transfer and Biology*, 2011.

B. Bouscasse, M. Antuono, A. Colagrossi, and C. Lugni. Numerical and experimental investigation of nonlinear shallow water sloshing. *Int. J. Nonlinear Sci. Numer. Simul*, 14(2):123–138, 2013.

B.-C. Chang. On the damage survivability of Ro-Ro ships investigated by motion simulation in a seaway. *Schiffstechnik-Ship Technology Research*, 46:192–207, 1999.

H. Chen and E. Christensen. Computation of added mass and damping coefficient of a horizontal circular cylinder in OpenFOAM. In *Proceedings of the 35th International Conference on Ocean, Offshore and Arctic Engineering*, 2016.

J. Cichowicz, D. Vassalos, and A. Jasionowski. Experiments on a floating body subjected to forced oscillation in calm water at the presence of an open-to-sea compartment. In *Proceedings of the 12th International Ship Stability Workshop*, 2011.

G. Colicchio, M. Landrini, and J. Chaplin. Level-set computations of free surface rotational flows. *Journal of Fluids Engineering*, 127(6):1111–1121, 2005.

G. Colicchio, M. Greco, and O. M. Faltinsen. A BEM-level set domain decomposition strategy for nonlinear and fragmented interfacial flows. *Int. Journal Numer. Meth. Engng*, 67(10), 2006.

J. O. de Kat. The numerical modeling of ship motions and capsizing in severe seas. *J Ship Research*, 34:289–301, 1990.

J. O. de Kat. Dynamics of a ship with a partially flooded compartment. In *Contemporary Ideas on Ship Stability*. Elsevier Science Ltd., 2000.

R. G. Dean and R. A. Dalrymple. *Water wave mechanics for engineers and scientists*,, volume 2 of Advanced series on Ocean Engineering. World Scientific, 1984.

V. D. K. Domeh, A. J. Sobey, and D. A. Hudson. A preliminary experimental investigation into the influence of compartment permeability on damaged ship response in waves. *Applied Ocean Research*, 52:27–36, 2015.

Estonia. *Final report on the MV Estonia disaster of 28 September 1994*. The Joint Accident Investigation Commission of MV ESTONIA and Edita Ltd., 1997.

O. M. Faltinsen. *Sea Loads on Ships and Offshore Structures*. Cambridge University Press., 1990.

O. M. Faltinsen. *Hydrodynamics of High-Speed Marine Vehicles*. Cambridge University Press, 2005.

O. M. Faltinsen and A. N. Timokha. *Sloshing*. Cambridge University Press., 2009.

O. M. Faltinsen, O. F. Rognebakke, and A. Timokha. Two-dimensional resonant piston-like sloshing in a moonpool. *Journal of Fluid Mechanics*, 575:359–397, 2007.

J. H. Ferziger and M. Peric. *Computational Methods for Fluid Dynamics*. Springer 3rd Edition, 2010.

A. G. Fredriksen, T. Kristiansen, and O. M. Faltinsen. Experimental and numerical investigation of wave resonance in moonpools at low forward speed. *Applied Ocean Research*, 47:28–46, 2014.

Q. Gao and D. Vassalos. Numerical study of damage ship hydrodynamics. *Ocean Engineering*, 55:199–205, 2012.

Z. Gao, Q. Gao, and D. Vassalos. Numerical study of damaged ship flooding in beam seas. *Ocean Engineering*, 61:77–87, 2013.

M. Greco, O. Faltinsen, and M. Landrini. Shipping of water on a two-dimensional structure. *Journal of Fluid Mechanics*, 525, 2005.

M. Greco, B. Bouscasse, and C. Lugni. 3-D seakeeping analysis with water on deck and slamming. Part 2: Experiments and physical investigation. *Journal of Fluids and Structures*, 33:148–179, 2012.

Y. Gu, A. Day, E. Boulougouris, and S. Dai. Experimental investigation on stability of intact and damaged combatant ship in a beam sea. *Ships and Offshore Structures*, 13(1):322–338, 2018.

F.-C. W. Hanssen. *Non-Linear Wave-Body Interaction in Severe Waves*. PhD thesis, Norwegian University of Science and Technology, Trondheim, Norway, 2019.

F.-C. W. Hanssen. Private Communication-'Simulations for the HPC method', 2020.

F.-C. W. Hanssen, A. Bardazzi, C. Lugni, and M. Greco. Free-surface tracking in 2d with the harmonic polynomial cell method: Two alternative strategies. *International Journal for Numerical Methods in Engineering*, 113, 2018.

H. Hashimoto, K. Kawamura, and M. Sueyoshi. A numerical simulation method for transient behavior of damaged ships associated with flooding. *Ocean Engineering*, 143:282–294, 2017.

P. Higuera, J. L. Lara, and I. J. Losada. Realistic wave generation and active wave absorption for navier-stokes models. application to OpenFOAM®. *Coastal Engineering*, 71:102–118, 2013.

C. W. Hirt and B. D. Nichols. Volume of fluid (VOF) method for the dynamics of free boundaries. *Journal of Computational Physics*, 39:201–225, 1981.

N. G. Jacobsen, D. R. Fuhrman, and J. Fredsoe. A wave generation toolbox for the open-source library: OpenFoam . *Int J Numer Methods Fluids*, 70(9), 2012.

F. Jaouen, A. Koop, and G. Vaz. Predicting Roll Added Mass and Damping of a Ship Hull Section Using CFD. In *Proceedings of the 30th International Conference on Ocean, Offshore and Arctic Engineering.*, 2011.

H. Jasak. *Error Analysis and Estimation for the Finite Volume Method with Applications to Fluid Flows*. PhD thesis, Imperial College, 1996.

H. Jasak and Z. Tukovic. Automatic mesh motion for the unstructured Finite Volume Method. *Transactions of FAMENA*, 30:1–20, 2006.

A. Jasionowski. *An integrated approach to damage ship survivability assessment*. PhD thesis, University of Strathclyde, Scotland, 2001.

T. Karppinen and K. Rahka. Investigation and causes of the sinking of MV Estonia. *Technology, Law and Insurance*, 3(2):149–162, 1998.

T. Katayama, Y. Takeuchi, and Y. Ikeda. An experimental study on roll motion of a damaged large passenger ship in intermediate stages of flooding. *Journal of the Kansai Society of Naval Architects of Japan*, 243, 2005.

C. Khaddaj-Mallat, B. Alessandrini, J. Rousset, and P. Ferrant. An experimental study on the flooding of a damaged passenger ship. *Ships and Offshore Structures*, 7(1):55–71, 2012.

H. King and E. Brater. *Handbook of Hydraulics, Fifth Edition*. McGraw Hill Book Company, 1963.

X. J. Kong. *A Numerical Study of a Damaged Ship in Beam Sea Waves*. PhD thesis, Department of Marine Technology, Norwegian University of Science and Technology, Trondheim, Norway, 2009.

X. J. Kong and O. M. Faltinsen. Piston mode and sloshing resonances in a damaged ship. In *Proceedings of the ASME 29th International Conference on Ocean, Offshore and Arctic Engineering*, volume 3, Shanghai, China, June 6–11 2010.

E. Korkut, M. Altar, and A. Incecik. An experimental study of motion behavior with an intact and damaged Ro-Ro ship model. *Ocean Engineering*, 31:483–512, 2004.

E. Korkut, M. Atlar, and A. Incecik. An experimental study of global loads acting on an intact and damaged Ro–Ro ship model. *Ocean Engineering*, 32:1370–1403, 2005.

T. Kristiansen and O. M. Faltinsen. A two-dimensional numerical and experimental study of resonant coupled ship and piston-mode motion. *Applied Ocean Research*, 32(2):158–176, 2010.

C.-H. Lee. *WAMIT Theory Manual, Report 95-2*. Dept. of Ocean Engineering, MIT, 1995.

C. H. Lee and J. N. Newman. Computation of wave effects using the panel method. In S. Chakrabarti, editor, *Numerical Modeling in Fluid-Structure Interaction*. WIT Press, 2004.

D. Lee, S. Hong, and G.-J. Lee. Theoretical and experimental study on dynamic behavior of a damaged ship in waves. *Ocean Engineering*, 34(1):21–31, 2007.

S. Lee, J.-M. You, H.-H. Lee, T. Lim, S. Park, J. Seo, S. Ree, and K.-P. Rhee. Experimental study on the six degree-of-freedom motions of a damaged ship floating in regular waves. *IEEE Journal of Oceanic Engineering*, 41:40–49, 2015.

M. S. Longuett-Higgins and E. D. Cokelet. The deformation of steep surface waves on water. I. A numerical method of computation. *In Pro c. R. Soc. London A, Volume*, 350, 1976.

C. Lugni, M. Brocchini, and O. M. Faltinsen. Evolution of the air cavity during a depressurized wave impact. ii. the dynamic field. *Physics of Fluids*, 22, 2010a.

C. Lugni, M. Miozzi, M. Brocchini, and O. M. Faltinsen. Evolution of the air cavity during a depressurized wave impact. i. the kinematic flow field. *Physics of Fluids*, 22, 2010b.

S. Ma, F. W. Hanssen, M. A. Siddiqui, M. Greco, and O. M. Faltinsen. Local and global properties of the harmonic polynomial cell method: In-depth analysis in two dimensions. *Int. Journal Numer. Meth. Engng*, 113(4):618–718, 2018a.

Z. Ma, L. Ha, Qian, P. J. Martinez-Ferrer, D. M. Causon, C. G. Mingham, and W. , Bai. An overset mesh based multiphase flow solver for water entry problems. *Computer and Fluids*, 172:689–705, 2018b.

S. Malenica and M. Zalar. An alternative method for linear hydrodynamics of air cushion supported floating bodies. In *Proceedings of the 15th International Workshop on Water Waves and Floating Bodies*, March 2000.

S. Mancini, E. Begovic, A. Day, and A. Incecik. Verification and validation of numerical modelling of dtmb 5415 roll decay. *Ocean Engineering*, 162:209 – 223, 2018.

T. Manderbacka, T. Mikkola, P. Ruponen, and J. Matusiak. Transient response of a ship to an abrupt flooding accounting for the momentum flux. *Journal of Fluids and Structures*, 57, 2015a.

T. Manderbacka, P. Ruponen, J. Kulovesi, and J. Matusiak. Model experiments of the transient response to flooding of the box shaped barge. *Journal of Fluids and Structures*, 57, 2015b.

J. Miles and W. Munk. Harbor Paradox. *Jour. Waterways and Harbors Div., Proc. ASCE*, 87(WW3), 1961.

B. Molin. On the piston and sloshing modes in moonpools. *Journal of Fluid Mechanics*, 430:27–50, 2001.

J. N. Newman. *Marine Hydrodynamics*. MIT Press, 1977.

J. N. Newman. Resonant response of a moonpool with a recess. *Applied Ocean Research*, 76(1):98–109, 2018.

J. N. Newman and P. D. Sclavounos. The computation of wave loads on large offshore structures. In *5th International Conference on the Behaviour of Offshore Structures BOSS*, Trondheim, Norway, 1988.

J. N. Newman, B. Sortnad, and T. Vinje. Added mass and damping of rectangular bodies close to the free surface. *Journal of Ship Research*, 28(4):219–225, 1984.

T. F. Ogilvie. Nonlinear high-Froude-number free surface problems. *J. of Engineering Mathematics*, 1(3), 1967.

H. Olsen and K. Johnsen. Nonlinear sloshing in rectangular tanks: a pilot study on the applicability of analytical models. Technical report, Det Norske Veritas (DNV), Høvik, Norway, 1975.

OpenFOAM. *The Open Source CFD Toolbox v1906*, 2019. URL https://www.openfoam.com/releases/openfoam1906/documentation.php.

Y. Ouelett and I. Datta. A survey of wave absorbers. *Journal of Hydraulic Research*, 24:265–279, 1986.

L. Palazzi and J. O. de Kat. Model experiments and simulations of a damaged ship with airflow taken into account. *Marine Technology*, 41(1):38–44, 2004.

A. Papanikolaou. Benchmark study on the capsizing of a damaged RO-RO passenger ship in waves. Technical report, 23rd ITTC Specialist Committee on the Prediction of Extreme Motions and Capsizing, 2001.

A. Papanikolaou and D. Spanos. 24th ITTC benchmark study on the numerical prediction of damage ship stability in waves – Preliminary Analysis of results. In *Proc. 7th Int. Workshop on Stability and Operational Safety of Ships, Shanghai*, 2004.

A. Papanikolaou and D. Spanos. Benchmark Study on Numerical Codes for the Prediction of Damage Ship Stability in Waves. In *Proceedings of the 10th International Ship Stability Workshop*, 2008.

A. Papanikolaou, G. Zaraphonitis, D. Spanos, V. Boulougouris, and E. E. Investigation into the capsizing of damaged ro-ro passenger ships in waves. In *7th Inter. Conf. On Stability of Ships Ocean Vehicles STAB2000, Australia, Tasmania*, 2000.

A. Papanikolau, K. Bitha, E. Eliopoulou, and N. Ventikos. Statistical analysis of ship accidents that occurred in the period 1990-2012 and assessment of safety level of ship types. In *Maritime Technology And Engineering- Guedes Soares and Santos*. Taylor Francis Group, London, 2015.

J. Parunov, M. Corak, C. Guedes Soares, H. Jafaryeganeh, S. Kalske, Y. Lee, S. Liu, A. Papanikolaou, D. Prentice, J. Prpic-Orsic, P. Ruponen, and N. Vitali. Benchmark study and uncertainty assessment of numerical predictions of global wave loads on damaged ships. *Ocean Engineering*, 197(106876), 2020.

P. Roache. *Verification and Validation in Computational Science and Engineering*. Hermosa Publishers, New Mexico, 1998.

O. F. Rognebakke and O. M. Faltinsen. Coupling of sloshing and ship motions. *Journal of Ship Research*, 47(3):208–221, 2003.

P. Ruponen. *Progressive flooding of a damaged passenger ship*. PhD thesis, Helsinki University of Technology, Helsinki, 2007.

P. Ruponen, P. Kurvinen, I. Saisto, and J. Harras. Air compression in a flooded tank of a damaged ship. *Ocean Engineering*, 57:64–71, 2013.

H. Sadat-Hosseini, D.-H. Kim, P. Carrica, S. Rhee, and F. Stern. URANS simulations for a flooded ship in calm water and regular beam waves. *Ocean Engineering*, 120:318–330, 2016.

N. Salvesen, E. Tuck, and O. M. Faltinsen. Ship motions and sea loads. *Society of Naval Architects and Marine Engineers*, 1970.

T. Santos and C. Guedes Soares. Study of damaged ship motions taking into account floodwater dynamics. *Journal of Marine Science and Technology*, 13(3):291–307, 2008.

Y. L. Shao and O. M. Faltinsen. Towards efficient fully-nonlinear potential-flow solvers in marine hydrodynamics. In *In ASME 2012 31st International Conference on Ocean, Offshore and Arctic Engineering*, 2012.

Y. L. Shao and O. M. Faltinsen. A harmonic polynomial cell (HPC) method for 3D Laplace equation with application in marine hydrodynamics. *Journal of Computational Physics*, 274:312–332, 2014.

N. Shimizu, R. Kambisseri, and Y. Ikeda. An experimental study on flooding into the car deck of a RORO ferry through damaged bow door. In *Contemporary Ideas on Ship Stability*. Elsevier Science Ltd., 2000.

T. W. P. Smith, K. R. Drake, and P. Wrobel. Experiments on a damaged ship section. In *Analysis and Design of Marine Structures*. CRC Press, 2009.

D. Spanos and A. Papanikolaou. On the stability of fishing vessels with trapped water on deck. *Ship Technology Research*, 48:124–133, 2001.

D. Spanos, A. Papanikolaou, and G. Tzabiras. On the effect of water on deck on ship motion. In *Proceedings of the International Conference on Offshore Mechanics and Arctic Engineering - OMAE*, 2002.

J. R. Spouge. The technical investigation of the sinking of the Ro-Ro ferry european gateway. *Transactions of the Royal Institution of Naval Architects*, 128:49–72, 1986.

O. Thilleul, A. Babarit, A. Drouet, and S. Le Floch. Validation of CFD for the Determination of Damping Coefficients for the Use of Wave Energy Converters Modelling. In *Proceedings of the 32nd International Conference on Ocean, Offshore and Artic Engineering*, 2013.

O. Turan and D. Vassalos. Dynamic stability assessment of damaged passenger ships. *Transactions of the Royal Institution of Naval Architects*, 135:79–104, 1993.

D. Vassalos and A. Papanikolaou. Stockholm agreement—past, present, future (part 1). *Marine Technology*, 39(3):137–158, 2002.

H. K. Versteeg and W. Malalasekera. *Computational Fluid Dynamics*. Prentice Hall; 2 edition, 2007.

A. W. Vredeveldt and J. M. J. Journée. Roll motions of ships due to sudden water ingress, calculations and experiments. In *Proceedings of the International Conference on Ro-Ro Safety and Vulnerability the Way Ahead*, London, 1991.

I. J. H. Vugts. The hydrodynamic coefficients for swaying, heaving and rolling cylinders in a free surface, report 112s, 1968.

C. Windt, J. Davidson, P. Schmitt, and J. Ringwood. On the assessment of numerical wave makers in CFD simulations. *J. Mar. Sci. Eng*, 7-47, 2019.

E. Ypma. Model tests in atmospheric and vacuum conditions. Technical report, Project FLOODSTAND Deliverable D2.5b., 2010.

Previous PhD theses published at the Department of Marine Technology (earlier: Faculty of Marine Technology) NORWEGIAN UNIVERSITY OF SCIENCE AND TECHNOLOGY

Report No.	Author	Title
	Kavlie, Dag	Optimization of Plane Elastic Grillages, 1967
	Hansen, Hans R.	Man-Machine Communication and Data-Storage Methods in Ship Structural Design, 1971
	Gisvold, Kaare M.	A Method for non-linear mixed -integer programming and its Application to Design Problems, 1971
	Lund, Sverre	Tanker Frame Optimalization by means of SUMT-Transformation and Behaviour Models, 1971
	Vinje, Tor	On Vibration of Spherical Shells Interacting with Fluid, 1972
	Lorentz, Jan D.	Tank Arrangement for Crude Oil Carriers in Accordance with the new Anti-Pollution Regulations, 1975
	Carlsen, Carl A.	Computer-Aided Design of Tanker Structures, 1975
	Larsen, Carl M.	Static and Dynamic Analysis of Offshore Pipelines during Installation, 1976
UR-79-01	Brigt Hatlestad, MK	The finite element method used in a fatigue evaluation of fixed offshore platforms. (Dr.Ing. Thesis)
UR-79-02	Erik Pettersen, MK	Analysis and design of cellular structures. (Dr.Ing. Thesis)
UR-79-03	Sverre Valsgård, MK	Finite difference and finite element methods applied to nonlinear analysis of plated structures. (Dr.Ing. Thesis)
UR-79-04	Nils T. Nordsve, MK	Finite element collapse analysis of structural members considering imperfections and stresses due to fabrication. (Dr.Ing. Thesis)
UR-79-05	Ivar J. Fylling, MK	Analysis of towline forces in ocean towing systems. (Dr.Ing. Thesis)
UR-80-06	Nils Sandsmark, MM	Analysis of Stationary and Transient Heat Conduction by the Use of the Finite Element Method. (Dr.Ing. Thesis)
UR-80-09	Sverre Haver, MK	Analysis of uncertainties related to the stochastic modeling of ocean waves. (Dr.Ing. Thesis)
UR-81-15	Odland, Jonas	On the Strength of welded Ring stiffened cylindrical Shells primarily subjected to axial Compression
UR-82-17	Engesvik, Knut	Analysis of Uncertainties in the fatigue Capacity of

		Welded Joints
UR-82-18	Rye, Henrik	Ocean wave groups
UR-83-30	Eide, Oddvar Inge	On Cumulative Fatigue Damage in Steel Welded Joints
UR-83-33	Mo, Olav	Stochastic Time Domain Analysis of Slender Offshore Structures
UR-83-34	Amdahl, Jørgen	Energy absorption in Ship-platform impacts
UR-84-37	Mørch, Morten	Motions and mooring forces of semi submersibles as determined by full-scale measurements and theoretical analysis
UR-84-38	Soares, C. Guedes	Probabilistic models for load effects in ship structures
UR-84-39	Aarsnes, Jan V.	Current forces on ships
UR-84-40	Czujko, Jerzy	Collapse Analysis of Plates subjected to Biaxial Compression and Lateral Load
UR-85-46	Alf G. Engseth, MK	Finite element collapse analysis of tubular steel offshore structures. (Dr.Ing. Thesis)
UR-86-47	Dengody Sheshappa, MP	A Computer Design Model for Optimizing Fishing Vessel Designs Based on Techno-Economic Analysis. (Dr.Ing. Thesis)
UR-86-48	Vidar Aanesland, MH	A Theoretical and Numerical Study of Ship Wave Resistance. (Dr.Ing. Thesis)
UR-86-49	Heinz-Joachim Wessel, MK	Fracture Mechanics Analysis of Crack Growth in Plate Girders. (Dr.Ing. Thesis)
UR-86-50	Jon Taby, MK	Ultimate and Post-ultimate Strength of Dented Tubular Members. (Dr.Ing. Thesis)
UR-86-51	Walter Lian, MH	A Numerical Study of Two-Dimensional Separated Flow Past Bluff Bodies at Moderate KC-Numbers. (Dr.Ing. Thesis)
UR-86-52	Bjørn Sortland, MH	Force Measurements in Oscillating Flow on Ship Sections and Circular Cylinders in a U-Tube Water Tank. (Dr.Ing. Thesis)
UR-86-53	Kurt Strand, MM	A System Dynamic Approach to One-dimensional Fluid Flow. (Dr.Ing. Thesis)
UR-86-54	Arne Edvin Løken, MH	Three Dimensional Second Order Hydrodynamic Effects on Ocean Structures in Waves. (Dr.Ing. Thesis)
UR-86-55	Sigurd Falch, MH	A Numerical Study of Slamming of Two-Dimensional Bodies. (Dr.Ing. Thesis)
UR-87-56	Arne Braathen, MH	Application of a Vortex Tracking Method to the Prediction of Roll Damping of a Two-Dimension Floating Body. (Dr.Ing. Thesis)

UR-87-57	Bernt Leira, MK	Gaussian Vector Processes for Reliability Analysis involving Wave-Induced Load Effects. (Dr.Ing. Thesis)
UR-87-58	Magnus Småvik, MM	Thermal Load and Process Characteristics in a Two-Stroke Diesel Engine with Thermal Barriers (in Norwegian). (Dr.Ing. Thesis)
MTA-88-59	Bernt Arild Bremdal, MP	An Investigation of Marine Installation Processes – A Knowledge - Based Planning Approach. (Dr.Ing. Thesis)
MTA-88-60	Xu Jun, MK	Non-linear Dynamic Analysis of Space-framed Offshore Structures. (Dr.Ing. Thesis)
MTA-89-61	Gang Miao, MH	Hydrodynamic Forces and Dynamic Responses of Circular Cylinders in Wave Zones. (Dr.Ing. Thesis)
MTA-89-62	Martin Greenhow, MH	Linear and Non-Linear Studies of Waves and Floating Bodies. Part I and Part II. (Dr.Techn. Thesis)
MTA-89-63	Chang Li, MH	Force Coefficients of Spheres and Cubes in Oscillatory Flow with and without Current. (Dr.Ing. Thesis
MTA-89-64	Hu Ying, MP	A Study of Marketing and Design in Development of Marine Transport Systems. (Dr.Ing. Thesis)
MTA-89-65	Arild Jæger, MH	Seakeeping, Dynamic Stability and Performance of a Wedge Shaped Planing Hull. (Dr.Ing. Thesis)
MTA-89-66	Chan Siu Hung, MM	The dynamic characteristics of tilting-pad bearings
MTA-89-67	Kim Wikstrøm, MP	Analysis av projekteringen for ett offshore projekt. (Licenciat-avhandling)
MTA-89-68	Jiao Guoyang, MK	Reliability Analysis of Crack Growth under Random Loading, considering Model Updating. (Dr.Ing. Thesis)
MTA-89-69	Arnt Olufsen, MK	Uncertainty and Reliability Analysis of Fixed Offshore Structures. (Dr.Ing. Thesis)
MTA-89-70	Wu Yu-Lin, MR	System Reliability Analyses of Offshore Structures using improved Truss and Beam Models. (Dr.Ing. Thesis)
MTA-90-71	Jan Roger Hoff, MH	Three-dimensional Green function of a vessel with forward speed in waves. (Dr.Ing. Thesis)
MTA-90-72	Rong Zhao, MH	Slow-Drift Motions of a Moored Two-Dimensional Body in Irregular Waves. (Dr.Ing. Thesis)
MTA-90-73	Atle Minsaas, MP	Economical Risk Analysis. (Dr.Ing. Thesis)
MTA-90-74	Knut-Aril Farnes, MK	Long-term Statistics of Response in Non-linear Marine Structures. (Dr.Ing. Thesis)
MTA-90-75	Torbjørn Sotberg, MK	Application of Reliability Methods for Safety Assessment of Submarine Pipelines. (Dr.Ing.

		Thesis)
MTA-90-76	Zeuthen, Steffen, MP	SEAMAID. A computational model of the design process in a constraint-based logic programming environment. An example from the offshore domain. (Dr.Ing. Thesis)
MTA-91-77	Haagensen, Sven, MM	Fuel Dependant Cyclic Variability in a Spark Ignition Engine - An Optical Approach. (Dr.Ing. Thesis)
MTA-91-78	Løland, Geir, MH	Current forces on and flow through fish farms. (Dr.Ing. Thesis)
MTA-91-79	Hoen, Christopher, MK	System Identification of Structures Excited by Stochastic Load Processes. (Dr.Ing. Thesis)
MTA-91-80	Haugen, Stein, MK	Probabilistic Evaluation of Frequency of Collision between Ships and Offshore Platforms. (Dr.Ing. Thesis)
MTA-91-81	Sødahl, Nils, MK	Methods for Design and Analysis of Flexible Risers. (Dr.Ing. Thesis)
MTA-91-82	Ormberg, Harald, MK	Non-linear Response Analysis of Floating Fish Farm Systems. (Dr.Ing. Thesis)
MTA-91-83	Marley, Mark J., MK	Time Variant Reliability under Fatigue Degradation. (Dr.Ing. Thesis)
MTA-91-84	Krokstad, Jørgen R., MH	Second-order Loads in Multidirectional Seas. (Dr.Ing. Thesis)
MTA-91-85	Molteberg, Gunnar A., MM	The Application of System Identification Techniques to Performance Monitoring of Four Stroke Turbocharged Diesel Engines. (Dr.Ing. Thesis)
MTA-92-86	Mørch, Hans Jørgen Bjelke, MH	Aspects of Hydrofoil Design: with Emphasis on Hydrofoil Interaction in Calm Water. (Dr.Ing. Thesis)
MTA-92-87	Chan Siu Hung, MM	Nonlinear Analysis of Rotordynamic Instabilities in Highspeed Turbomachinery. (Dr.Ing. Thesis)
MTA-92-88	Bessason, Bjarni, MK	Assessment of Earthquake Loading and Response of Seismically Isolated Bridges. (Dr.Ing. Thesis)
MTA-92-89	Langli, Geir, MP	Improving Operational Safety through exploitation of Design Knowledge - an investigation of offshore platform safety. (Dr.Ing. Thesis)
MTA-92-90	Sævik, Svein, MK	On Stresses and Fatigue in Flexible Pipes. (Dr.Ing. Thesis)
MTA-92-91	Ask, Tor Ø., MM	Ignition and Flame Growth in Lean Gas-Air Mixtures. An Experimental Study with a Schlieren System. (Dr.Ing. Thesis)
MTA-86-92	Hessen, Gunnar, MK	Fracture Mechanics Analysis of Stiffened Tubular Members. (Dr.Ing. Thesis)

MTA-93-93	Steinebach, Christian, MM	Knowledge Based Systems for Diagnosis of Rotating Machinery. (Dr.Ing. Thesis)
MTA-93-94	Dalane, Jan Inge, MK	System Reliability in Design and Maintenance of Fixed Offshore Structures. (Dr.Ing. Thesis)
MTA-93-95	Steen, Sverre, MH	Cobblestone Effect on SES. (Dr.Ing. Thesis)
MTA-93-96	Karunakaran, Daniel, MK	Nonlinear Dynamic Response and Reliability Analysis of Drag-dominated Offshore Platforms. (Dr.Ing. Thesis)
MTA-93-97	Hagen, Arnulf, MP	The Framework of a Design Process Language. (Dr.Ing. Thesis)
MTA-93-98	Nordrik, Rune, MM	Investigation of Spark Ignition and Autoignition in Methane and Air Using Computational Fluid Dynamics and Chemical Reaction Kinetics. A Numerical Study of Ignition Processes in Internal Combustion Engines. (Dr.Ing. Thesis)
MTA-94-99	Passano, Elizabeth, MK	Efficient Analysis of Nonlinear Slender Marine Structures. (Dr.Ing. Thesis)
MTA-94-100	Kvålsvold, Jan, MH	Hydroelastic Modelling of Wetdeck Slamming on Multihull Vessels. (Dr.Ing. Thesis)
MTA-94-102	Bech, Sidsel M., MK	Experimental and Numerical Determination of Stiffness and Strength of GRP/PVC Sandwich Structures. (Dr.Ing. Thesis)
MTA-95-103	Paulsen, Hallvard, MM	A Study of Transient Jet and Spray using a Schlieren Method and Digital Image Processing. (Dr.Ing. Thesis)
MTA-95-104	Hovde, Geir Olav, MK	Fatigue and Overload Reliability of Offshore Structural Systems, Considering the Effect of Inspection and Repair. (Dr.Ing. Thesis)
MTA-95-105	Wang, Xiaozhi, MK	Reliability Analysis of Production Ships with Emphasis on Load Combination and Ultimate Strength. (Dr.Ing. Thesis)
MTA-95-106	Ulstein, Tore, MH	Nonlinear Effects of a Flexible Stern Seal Bag on Cobblestone Oscillations of an SES. (Dr.Ing. Thesis)
MTA-95-107	Solaas, Frøydis, MH	Analytical and Numerical Studies of Sloshing in Tanks. (Dr.Ing. Thesis)
MTA-95-108	Hellan, Øyvind, MK	Nonlinear Pushover and Cyclic Analyses in Ultimate Limit State Design and Reassessment of Tubular Steel Offshore Structures. (Dr.Ing. Thesis)
MTA-95-109	Hermundstad, Ole A., MK	Theoretical and Experimental Hydroelastic Analysis of High Speed Vessels. (Dr.Ing. Thesis)
MTA-96-110	Bratland, Anne K., MH	Wave-Current Interaction Effects on Large-Volume Bodies in Water of Finite Depth. (Dr.Ing. Thesis)
MTA-96-111	Herfjord, Kjell, MH	A Study of Two-dimensional Separated Flow by a Combination of the Finite Element Method and

		Navier-Stokes Equations. (Dr.Ing. Thesis)
MTA-96-112	Æsøy, Vilmar, MM	Hot Surface Assisted Compression Ignition in a Direct Injection Natural Gas Engine. (Dr.Ing. Thesis)
MTA-96-113	Eknes, Monika L., MK	Escalation Scenarios Initiated by Gas Explosions on Offshore Installations. (Dr.Ing. Thesis)
MTA-96-114	Erikstad, Stein O., MP	A Decision Support Model for Preliminary Ship Design. (Dr.Ing. Thesis)
MTA-96-115	Pedersen, Egil, MH	A Nautical Study of Towed Marine Seismic Streamer Cable Configurations. (Dr.Ing. Thesis)
MTA-97-116	Moksnes, Paul O., MM	Modelling Two-Phase Thermo-Fluid Systems Using Bond Graphs. (Dr.Ing. Thesis)
MTA-97-117	Halse, Karl H., MK	On Vortex Shedding and Prediction of Vortex-Induced Vibrations of Circular Cylinders. (Dr.Ing. Thesis)
MTA-97-118	Igland, Ragnar T., MK	Reliability Analysis of Pipelines during Laying, considering Ultimate Strength under Combined Loads. (Dr.Ing. Thesis)
MTA-97-119	Pedersen, Hans-P., MP	Levendefiskteknologi for fiskefartøy. (Dr.Ing. Thesis)
MTA-98-120	Vikestad, Kyrre, MK	Multi-Frequency Response of a Cylinder Subjected to Vortex Shedding and Support Motions. (Dr.Ing. Thesis)
MTA-98-121	Azadi, Mohammad R. E., MK	Analysis of Static and Dynamic Pile-Soil-Jacket Behaviour. (Dr.Ing. Thesis)
MTA-98-122	Ulltang, Terje, MP	A Communication Model for Product Information. (Dr.Ing. Thesis)
MTA-98-123	Torbergsen, Erik, MM	Impeller/Diffuser Interaction Forces in Centrifugal Pumps. (Dr.Ing. Thesis)
MTA-98-124	Hansen, Edmond, MH	A Discrete Element Model to Study Marginal Ice Zone Dynamics and the Behaviour of Vessels Moored in Broken Ice. (Dr.Ing. Thesis)
MTA-98-125	Videiro, Paulo M., MK	Reliability Based Design of Marine Structures. (Dr.Ing. Thesis)
MTA-99-126	Mainçon, Philippe, MK	Fatigue Reliability of Long Welds Application to Titanium Risers. (Dr.Ing. Thesis)
MTA-99-127	Haugen, Elin M., MH	Hydroelastic Analysis of Slamming on Stiffened Plates with Application to Catamaran Wetdecks. (Dr.Ing. Thesis)
MTA-99-128	Langhelle, Nina K., MK	Experimental Validation and Calibration of Nonlinear Finite Element Models for Use in Design of Aluminium Structures Exposed to Fire. (Dr.Ing. Thesis)
MTA-99-	Berstad, Are J., MK	Calculation of Fatigue Damage in Ship Structures.

129		(Dr.Ing. Thesis)
MTA-99-130	Andersen, Trond M., MM	Short Term Maintenance Planning. (Dr.Ing. Thesis)
MTA-99-131	Tveiten, Bård Wathne, MK	Fatigue Assessment of Welded Aluminium Ship Details. (Dr.Ing. Thesis)
MTA-99-132	Søreide, Fredrik, MP	Applications of underwater technology in deep water archaeology. Principles and practice. (Dr.Ing. Thesis)
MTA-99-133	Tønnessen, Rune, MH	A Finite Element Method Applied to Unsteady Viscous Flow Around 2D Blunt Bodies With Sharp Corners. (Dr.Ing. Thesis)
MTA-99-134	Elvekrok, Dag R., MP	Engineering Integration in Field Development Projects in the Norwegian Oil and Gas Industry. The Supplier Management of Norne. (Dr.Ing. Thesis)
MTA-99-135	Fagerholt, Kjetil, MP	Optimeringsbaserte Metoder for Ruteplanlegging innen skipsfart. (Dr.Ing. Thesis)
MTA-99-136	Bysveen, Marie, MM	Visualization in Two Directions on a Dynamic Combustion Rig for Studies of Fuel Quality. (Dr.Ing. Thesis)
MTA-2000-137	Storteig, Eskild, MM	Dynamic characteristics and leakage performance of liquid annular seals in centrifugal pumps. (Dr.Ing. Thesis)
MTA-2000-138	Sagli, Gro, MK	Model uncertainty and simplified estimates of long term extremes of hull girder loads in ships. (Dr.Ing. Thesis)
MTA-2000-139	Tronstad, Harald, MK	Nonlinear analysis and design of cable net structures like fishing gear based on the finite element method. (Dr.Ing. Thesis)
MTA-2000-140	Kroneberg, André, MP	Innovation in shipping by using scenarios. (Dr.Ing. Thesis)
MTA-2000-141	Haslum, Herbjørn Alf, MH	Simplified methods applied to nonlinear motion of spar platforms. (Dr.Ing. Thesis)
MTA-2001-142	Samdal, Ole Johan, MM	Modelling of Degradation Mechanisms and Stressor Interaction on Static Mechanical Equipment Residual Lifetime. (Dr.Ing. Thesis)
MTA-2001-143	Baarholm, Rolf Jarle, MH	Theoretical and experimental studies of wave impact underneath decks of offshore platforms. (Dr.Ing. Thesis)
MTA-2001-144	Wang, Lihua, MK	Probabilistic Analysis of Nonlinear Wave-induced Loads on Ships. (Dr.Ing. Thesis)
MTA-2001-145	Kristensen, Odd H. Holt, MK	Ultimate Capacity of Aluminium Plates under Multiple Loads, Considering HAZ Properties. (Dr.Ing. Thesis)
MTA-2001-146	Greco, Marilena, MH	A Two-Dimensional Study of Green-Water

		Loading. (Dr.Ing. Thesis)
MTA-2001-147	Heggelund, Svein E., MK	Calculation of Global Design Loads and Load Effects in Large High Speed Catamarans. (Dr.Ing. Thesis)
MTA-2001-148	Babalola, Olusegun T., MK	Fatigue Strength of Titanium Risers – Defect Sensitivity. (Dr.Ing. Thesis)
MTA-2001-149	Mohammed, Abuu K., MK	Nonlinear Shell Finite Elements for Ultimate Strength and Collapse Analysis of Ship Structures. (Dr.Ing. Thesis)
MTA-2002-150	Holmedal, Lars E., MH	Wave-current interactions in the vicinity of the sea bed. (Dr.Ing. Thesis)
MTA-2002-151	Rognebakke, Olav F., MH	Sloshing in rectangular tanks and interaction with ship motions. (Dr.Ing. Thesis)
MTA-2002-152	Lader, Pål Furset, MH	Geometry and Kinematics of Breaking Waves. (Dr.Ing. Thesis)
MTA-2002-153	Yang, Qinzheng, MH	Wash and wave resistance of ships in finite water depth. (Dr.Ing. Thesis)
MTA-2002-154	Melhus, Øyvin, MM	Utilization of VOC in Diesel Engines. Ignition and combustion of VOC released by crude oil tankers. (Dr.Ing. Thesis)
MTA-2002-155	Ronæss, Marit, MH	Wave Induced Motions of Two Ships Advancing on Parallel Course. (Dr.Ing. Thesis)
MTA-2002-156	Økland, Ole D., MK	Numerical and experimental investigation of whipping in twin hull vessels exposed to severe wet deck slamming. (Dr.Ing. Thesis)
MTA-2002-157	Ge, Chunhua, MK	Global Hydroelastic Response of Catamarans due to Wet Deck Slamming. (Dr.Ing. Thesis)
MTA-2002-158	Byklum, Eirik, MK	Nonlinear Shell Finite Elements for Ultimate Strength and Collapse Analysis of Ship Structures. (Dr.Ing. Thesis)
IMT-2003-1	Chen, Haibo, MK	Probabilistic Evaluation of FPSO-Tanker Collision in Tandem Offloading Operation. (Dr.Ing. Thesis)
IMT-2003-2	Skaugset, Kjetil Bjørn, MK	On the Suppression of Vortex Induced Vibrations of Circular Cylinders by Radial Water Jets. (Dr.Ing. Thesis)
IMT-2003-3	Chezhian, Muthu	Three-Dimensional Analysis of Slamming. (Dr.Ing. Thesis)
IMT-2003-4	Buhaug, Øyvind	Deposit Formation on Cylinder Liner Surfaces in Medium Speed Engines. (Dr.Ing. Thesis)
IMT-2003-5	Tregde, Vidar	Aspects of Ship Design: Optimization of Aft Hull with Inverse Geometry Design. (Dr.Ing. Thesis)
IMT-	Wist, Hanne Therese	Statistical Properties of Successive Ocean Wave

2003-6		Parameters. (Dr.Ing. Thesis)
IMT-2004-7	Ransau, Samuel	Numerical Methods for Flows with Evolving Interfaces. (Dr.Ing. Thesis)
IMT-2004-8	Soma, Torkel	Blue-Chip or Sub-Standard. A data interrogation approach of identity safety characteristics of shipping organization. (Dr.Ing. Thesis)
IMT-2004-9	Ersdal, Svein	An experimental study of hydrodynamic forces on cylinders and cables in near axial flow. (Dr.Ing. Thesis)
IMT-2005-10	Brodtkorb, Per Andreas	The Probability of Occurrence of Dangerous Wave Situations at Sea. (Dr.Ing. Thesis)
IMT-2005-11	Yttervik, Rune	Ocean current variability in relation to offshore engineering. (Dr.Ing. Thesis)
IMT-2005-12	Fredheim, Arne	Current Forces on Net-Structures. (Dr.Ing. Thesis)
IMT-2005-13	Heggernes, Kjetil	Flow around marine structures. (Dr.Ing. Thesis
IMT-2005-14	Fouques, Sebastien	Lagrangian Modelling of Ocean Surface Waves and Synthetic Aperture Radar Wave Measurements. (Dr.Ing. Thesis)
IMT-2006-15	Holm, Håvard	Numerical calculation of viscous free surface flow around marine structures. (Dr.Ing. Thesis)
IMT-2006-16	Bjørheim, Lars G.	Failure Assessment of Long Through Thickness Fatigue Cracks in Ship Hulls. (Dr.Ing. Thesis)
IMT-2006-17	Hansson, Lisbeth	Safety Management for Prevention of Occupational Accidents. (Dr.Ing. Thesis)
IMT-2006-18	Zhu, Xinying	Application of the CIP Method to Strongly Nonlinear Wave-Body Interaction Problems. (Dr.Ing. Thesis)
IMT-2006-19	Reite, Karl Johan	Modelling and Control of Trawl Systems. (Dr.Ing. Thesis)
IMT-2006-20	Smogeli, Øyvind Notland	Control of Marine Propellers. From Normal to Extreme Conditions. (Dr.Ing. Thesis)
IMT-2007-21	Storhaug, Gaute	Experimental Investigation of Wave Induced Vibrations and Their Effect on the Fatigue Loading of Ships. (Dr.Ing. Thesis)
IMT-2007-22	Sun, Hui	A Boundary Element Method Applied to Strongly Nonlinear Wave-Body Interaction Problems. (PhD Thesis, CeSOS)
IMT-2007-23	Rustad, Anne Marthine	Modelling and Control of Top Tensioned Risers. (PhD Thesis, CeSOS)
IMT-2007-24	Johansen, Vegar	Modelling flexible slender system for real-time simulations and control applications
IMT-2007-25	Wroldsen, Anders Sunde	Modelling and control of tensegrity structures.

		(PhD Thesis, CeSOS)
IMT-2007-26	Aronsen, Kristoffer Høye	An experimental investigation of in-line and combined inline and cross flow vortex induced vibrations. (Dr. avhandling, IMT)
IMT-2007-27	Gao, Zhen	Stochastic Response Analysis of Mooring Systems with Emphasis on Frequency-domain Analysis of Fatigue due to Wide-band Response Processes (PhD Thesis, CeSOS)
IMT-2007-28	Thorstensen, Tom Anders	Lifetime Profit Modelling of Ageing Systems Utilizing Information about Technical Condition. (Dr.ing. thesis, IMT)
IMT-2008-29	Refsnes, Jon Erling Gorset	Nonlinear Model-Based Control of Slender Body AUVs (PhD Thesis, IMT)
IMT-2008-30	Berntsen, Per Ivar B.	Structural Reliability Based Position Mooring. (PhD-Thesis, IMT)
IMT-2008-31	Ye, Naiquan	Fatigue Assessment of Aluminium Welded Box-stiffener Joints in Ships (Dr.ing. thesis, IMT)
IMT-2008-32	Radan, Damir	Integrated Control of Marine Electrical Power Systems. (PhD-Thesis, IMT)
IMT-2008-33	Thomassen, Paul	Methods for Dynamic Response Analysis and Fatigue Life Estimation of Floating Fish Cages. (Dr.ing. thesis, IMT)
IMT-2008-34	Pákozdi, Csaba	A Smoothed Particle Hydrodynamics Study of Two-dimensional Nonlinear Sloshing in Rectangular Tanks. (Dr.ing.thesis, IMT/ CeSOS)
IMT-2007-35	Grytøyr, Guttorm	A Higher-Order Boundary Element Method and Applications to Marine Hydrodynamics. (Dr.ing.thesis, IMT)
IMT-2008-36	Drummen, Ingo	Experimental and Numerical Investigation of Nonlinear Wave-Induced Load Effects in Containerships considering Hydroelasticity. (PhD thesis, CeSOS)
IMT-2008-37	Skejic, Renato	Maneuvering and Seakeeping of a Singel Ship and of Two Ships in Interaction. (PhD-Thesis, CeSOS)
IMT-2008-38	Harlem, Alf	An Age-Based Replacement Model for Repairable Systems with Attention to High-Speed Marine Diesel Engines. (PhD-Thesis, IMT)
IMT-2008-39	Alsos, Hagbart S.	Ship Grounding. Analysis of Ductile Fracture, Bottom Damage and Hull Girder Response. (PhD-thesis, IMT)
IMT-2008-40	Graczyk, Mateusz	Experimental Investigation of Sloshing Loading and Load Effects in Membrane LNG Tanks Subjected to Random Excitation. (PhD-thesis, CeSOS)
IMT-2008-41	Taghipour, Reza	Efficient Prediction of Dynamic Response for Flexible amd Multi-body Marine Structures. (PhD-

		thesis, CeSOS)
IMT-2008-42	Ruth, Eivind	Propulsion control and thrust allocation on marine vessels. (PhD thesis, CeSOS)
IMT-2008-43	Nystad, Bent Helge	Technical Condition Indexes and Remaining Useful Life of Aggregated Systems. PhD thesis, IMT
IMT-2008-44	Soni, Prashant Kumar	Hydrodynamic Coefficients for Vortex Induced Vibrations of Flexible Beams, PhD thesis, CeSOS
IMT-2009-45	Amlashi, Hadi K.K.	Ultimate Strength and Reliability-based Design of Ship Hulls with Emphasis on Combined Global and Local Loads. PhD Thesis, IMT
IMT-2009-46	Pedersen, Tom Arne	Bond Graph Modelling of Marine Power Systems. PhD Thesis, IMT
IMT-2009-47	Kristiansen, Trygve	Two-Dimensional Numerical and Experimental Studies of Piston-Mode Resonance. PhD-Thesis, CeSOS
IMT-2009-48	Ong, Muk Chen	Applications of a Standard High Reynolds Number Model and a Stochastic Scour Prediction Model for Marine Structures. PhD-thesis, IMT
IMT-2009-49	Hong, Lin	Simplified Analysis and Design of Ships subjected to Collision and Grounding. PhD-thesis, IMT
IMT-2009-50	Koushan, Kamran	Vortex Induced Vibrations of Free Span Pipelines, PhD thesis, IMT
IMT-2009-51	Korsvik, Jarl Eirik	Heuristic Methods for Ship Routing and Scheduling. PhD-thesis, IMT
IMT-2009-52	Lee, Jihoon	Experimental Investigation and Numerical in Analyzing the Ocean Current Displacement of Longlines. Ph.d.-Thesis, IMT.
IMT-2009-53	Vestbøstad, Tone Gran	A Numerical Study of Wave-in-Deck Impact usin a Two-Dimensional Constrained Interpolation Profile Method, Ph.d.thesis, CeSOS.
IMT-2009-54	Bruun, Kristine	Bond Graph Modelling of Fuel Cells for Marine Power Plants. Ph.d.-thesis, IMT
IMT 2009-55	Holstad, Anders	Numerical Investigation of Turbulence in a Sekwed Three-Dimensional Channel Flow, Ph.d.-thesis, IMT.
IMT 2009-56	Ayala-Uraga, Efren	Reliability-Based Assessment of Deteriorating Ship-shaped Offshore Structures, Ph.d.-thesis, IMT
IMT 2009-57	Kong, Xiangjun	A Numerical Study of a Damaged Ship in Beam Sea Waves. Ph.d.-thesis, IMT/CeSOS.
IMT 2010-58	Kristiansen, David	Wave Induced Effects on Floaters of Aquaculture Plants, Ph.d.-thesis, CeSOS.

IMT 2010-59	Ludvigsen, Martin	An ROV-Toolbox for Optical and Acoustic Scientific Seabed Investigation. Ph.d.-thesis IMT.
IMT 2010-60	Hals, Jørgen	Modelling and Phase Control of Wave-Energy Converters. Ph.d.thesis, CeSOS.
IMT 2010- 61	Shu, Zhi	Uncertainty Assessment of Wave Loads and Ultimate Strength of Tankers and Bulk Carriers in a Reliability Framework. Ph.d. Thesis, IMT/ CeSOS
IMT 2010-62	Shao, Yanlin	Numerical Potential-Flow Studies on Weakly-Nonlinear Wave-Body Interactions with/without Small Forward Speed, Ph.d.thesis,CeSOS.
IMT 2010-63	Califano, Andrea	Dynamic Loads on Marine Propellers due to Intermittent Ventilation. Ph.d.thesis, IMT.
IMT 2010-64	El Khoury, George	Numerical Simulations of Massively Separated Turbulent Flows, Ph.d.-thesis, IMT
IMT 2010-65	Seim, Knut Sponheim	Mixing Process in Dense Overflows with Emphasis on the Faroe Bank Channel Overflow. Ph.d.thesis, IMT
IMT 2010-66	Jia, Huirong	Structural Analysis of Intect and Damaged Ships in a Collission Risk Analysis Perspective. Ph.d.thesis CeSoS.
IMT 2010-67	Jiao, Linlin	Wave-Induced Effects on a Pontoon-type Very Large Floating Structures (VLFS). Ph.D.-thesis, CeSOS.
IMT 2010-68	Abrahamsen, Bjørn Christian	Sloshing Induced Tank Roof with Entrapped Air Pocket. Ph.d.thesis, CeSOS.
IMT 2011-69	Karimirad, Madjid	Stochastic Dynamic Response Analysis of Spar-Type Wind Turbines with Catenary or Taut Mooring Systems. Ph.d.-thesis, CeSOS.
IMT - 2011-70	Erlend Meland	Condition Monitoring of Safety Critical Valves. Ph.d.-thesis, IMT.
IMT – 2011-71	Yang, Limin	Stochastic Dynamic System Analysis of Wave Energy Converter with Hydraulic Power Take-Off, with Particular Reference to Wear Damage Analysis, Ph.d. Thesis, CeSOS.
IMT – 2011-72	Visscher, Jan	Application of Particla Image Velocimetry on Turbulent Marine Flows, Ph.d.Thesis, IMT.
IMT – 2011-73	Su, Biao	Numerical Predictions of Global and Local Ice Loads on Ships. Ph.d.Thesis, CeSOS.
IMT – 2011-74	Liu, Zhenhui	Analytical and Numerical Analysis of Iceberg Collision with Ship Structures. Ph.d.Thesis, IMT.
IMT – 2011-75	Aarsæther, Karl Gunnar	Modeling and Analysis of Ship Traffic by Observation and Numerical Simulation. Ph.d.Thesis, IMT.

Imt – 2011-76	Wu, Jie	Hydrodynamic Force Identification from Stochastic Vortex Induced Vibration Experiments with Slender Beams. Ph.d.Thesis, IMT.
Imt – 2011-77	Amini, Hamid	Azimuth Propulsors in Off-design Conditions. Ph.d.Thesis, IMT.
IMT – 2011-78	Nguyen, Tan-Hoi	Toward a System of Real-Time Prediction and Monitoring of Bottom Damage Conditions During Ship Grounding. Ph.d.thesis, IMT.
IMT- 2011-79	Tavakoli, Mohammad T.	Assessment of Oil Spill in Ship Collision and Grounding, Ph.d.thesis, IMT.
IMT- 2011-80	Guo, Bingjie	Numerical and Experimental Investigation of Added Resistance in Waves. Ph.d.Thesis, IMT.
IMT- 2011-81	Chen, Qiaofeng	Ultimate Strength of Aluminium Panels, considering HAZ Effects, IMT
IMT- 2012-82	Kota, Ravikiran S.	Wave Loads on Decks of Offshore Structures in Random Seas, CeSOS.
IMT- 2012-83	Sten, Ronny	Dynamic Simulation of Deep Water Drilling Risers with Heave Compensating System, IMT.
IMT- 2012-84	Berle, Øyvind	Risk and resilience in global maritime supply chains, IMT.
IMT- 2012-85	Fang, Shaoji	Fault Tolerant Position Mooring Control Based on Structural Reliability, CeSOS.
IMT- 2012-86	You, Jikun	Numerical studies on wave forces and moored ship motions in intermediate and shallow water, CeSOS.
IMT- 2012-87	Xiang ,Xu	Maneuvering of two interacting ships in waves, CeSOS
IMT- 2012-88	Dong, Wenbin	Time-domain fatigue response and reliability analysis of offshore wind turbines with emphasis on welded tubular joints and gear components, CeSOS
IMT- 2012-89	Zhu, Suji	Investigation of Wave-Induced Nonlinear Load Effects in Open Ships considering Hull Girder Vibrations in Bending and Torsion, CeSOS
IMT- 2012-90	Zhou, Li	Numerical and Experimental Investigation of Station-keeping in Level Ice, CeSOS
IMT- 2012-91	Ushakov, Sergey	Particulate matter emission characteristics from diesel enignes operating on conventional and alternative marine fuels, IMT
IMT- 2013-1	Yin, Decao	Experimental and Numerical Analysis of Combined In-line and Cross-flow Vortex Induced Vibrations, CeSOS

IMT-2013-2	Kurniawan, Adi	Modelling and geometry optimisation of wave energy converters, CeSOS
IMT-2013-3	Al Ryati, Nabil	Technical condition indexes doe auxiliary marine diesel engines, IMT
IMT-2013-4	Firoozkoohi, Reza	Experimental, numerical and analytical investigation of the effect of screens on sloshing, CeSOS
IMT-2013-5	Ommani, Babak	Potential-Flow Predictions of a Semi-Displacement Vessel Including Applications to Calm Water Broaching, CeSOS
IMT-2013-6	Xing, Yihan	Modelling and analysis of the gearbox in a floating spar-type wind turbine, CeSOS
IMT-7-2013	Balland, Océane	Optimization models for reducing air emissions from ships, IMT
IMT-8-2013	Yang, Dan	Transitional wake flow behind an inclined flat plate-----Computation and analysis, IMT
IMT-9-2013	Abdillah, Suyuthi	Prediction of Extreme Loads and Fatigue Damage for a Ship Hull due to Ice Action, IMT
IMT-10-2013	Ramìrez, Pedro Agustìn Pèrez	Ageing management and life extension of technical systems- Concepts and methods applied to oil and gas facilities, IMT
IMT-11-2013	Chuang, Zhenju	Experimental and Numerical Investigation of Speed Loss due to Seakeeping and Maneuvering. IMT
IMT-12-2013	Etemaddar, Mahmoud	Load and Response Analysis of Wind Turbines under Atmospheric Icing and Controller System Faults with Emphasis on Spar Type Floating Wind Turbines, IMT
IMT-13-2013	Lindstad, Haakon	Strategies and measures for reducing maritime CO2 emissons, IMT
IMT-14-2013	Haris, Sabril	Damage interaction analysis of ship collisions, IMT
IMT-15-2013	Shainee, Mohamed	Conceptual Design, Numerical and Experimental Investigation of a SPM Cage Concept for Offshore Mariculture, IMT
IMT-16-2013	Gansel, Lars	Flow past porous cylinders and effects of biofouling and fish behavior on the flow in and around Atlantic salmon net cages, IMT
IMT-17-2013	Gaspar, Henrique	Handling Aspects of Complexity in Conceptual Ship Design, IMT
IMT-18-2013	Thys, Maxime	Theoretical and Experimental Investigation of a Free Running Fishing Vessel at Small Frequency of Encounter, CeSOS
IMT-19-2013	Aglen, Ida	VIV in Free Spanning Pipelines, CeSOS

IMT-1-2014	Song, An	Theoretical and experimental studies of wave diffraction and radiation loads on a horizontally submerged perforated plate, CeSOS
IMT-2-2014	Rogne, Øyvind Ygre	Numerical and Experimental Investigation of a Hinged 5-body Wave Energy Converter, CeSOS
IMT-3-2014	Dai, Lijuan	Safe and efficient operation and maintenance of offshore wind farms ,IMT
IMT-4-2014	Bachynski, Erin Elizabeth	Design and Dynamic Analysis of Tension Leg Platform Wind Turbines, CeSOS
IMT-5-2014	Wang, Jingbo	Water Entry of Freefall Wedged – Wedge motions and Cavity Dynamics, CeSOS
IMT-6-2014	Kim, Ekaterina	Experimental and numerical studies related to the coupled behavior of ice mass and steel structures during accidental collisions, IMT
IMT-7-2014	Tan, Xiang	Numerical investigation of ship's continuous- mode icebreaking in leverl ice, CeSOS
IMT-8-2014	Muliawan, Made Jaya	Design and Analysis of Combined Floating Wave and Wind Power Facilities, with Emphasis on Extreme Load Effects of the Mooring System, CeSOS
IMT-9-2014	Jiang, Zhiyu	Long-term response analysis of wind turbines with an emphasis on fault and shutdown conditions, IMT
IMT-10-2014	Dukan, Fredrik	ROV Motion Control Systems, IMT
IMT-11-2014	Grimsmo, Nils I.	Dynamic simulations of hydraulic cylinder for heave compensation of deep water drilling risers, IMT
IMT-12-2014	Kvittem, Marit I.	Modelling and response analysis for fatigue design of a semisubmersible wind turbine, CeSOS
IMT-13-2014	Akhtar, Juned	The Effects of Human Fatigue on Risk at Sea, IMT
IMT-14-2014	Syahroni, Nur	Fatigue Assessment of Welded Joints Taking into Account Effects of Residual Stress, IMT
IMT-1-2015	Bøckmann, Eirik	Wave Propulsion of ships, IMT
IMT-2-2015	Wang, Kai	Modelling and dynamic analysis of a semi-submersible floating vertical axis wind turbine, CeSOS
IMT-3-2015	Fredriksen, Arnt Gunvald	A numerical and experimental study of a two-dimensional body with moonpool in waves and current, CeSOS
IMT-4-2015	Jose Patricio Gallardo Canabes	Numerical studies of viscous flow around bluff bodies, IMT

IMT-5-2015	Vegard Longva	Formulation and application of finite element techniques for slender marine structures subjected to contact interactions, IMT
IMT-6-2015	Jacobus De Vaal	Aerodynamic modelling of floating wind turbines, CeSOS
IMT-7-2015	Fachri Nasution	Fatigue Performance of Copper Power Conductors, IMT
IMT-8-2015	Oleh I Karpa	Development of bivariate extreme value distributions for applications in marine technology,CeSOS
IMT-9-2015	Daniel de Almeida Fernandes	An output feedback motion control system for ROVs, AMOS
IMT-10-2015	Bo Zhao	Particle Filter for Fault Diagnosis: Application to Dynamic Positioning Vessel and Underwater Robotics, CeSOS
IMT-11-2015	Wenting Zhu	Impact of emission allocation in maritime transportation, IMT
IMT-12-2015	Amir Rasekhi Nejad	Dynamic Analysis and Design of Gearboxes in Offshore Wind Turbines in a Structural Reliability Perspective, CeSOS
IMT-13-2015	Arturo Jesùs Ortega Malca	Dynamic Response of Flexibles Risers due to Unsteady Slug Flow, CeSOS
IMT-14-2015	Dagfinn Husjord	Guidance and decision-support system for safe navigation of ships operating in close proximity, IMT
IMT-15-2015	Anirban Bhattacharyya	Ducted Propellers: Behaviour in Waves and Scale Effects, IMT
IMT-16-2015	Qin Zhang	Image Processing for Ice Parameter Identification in Ice Management, IMT
IMT-1-2016	Vincentius Rumawas	Human Factors in Ship Design and Operation: An Experiential Learning, IMT
IMT-2-2016	Martin Storheim	Structural response in ship-platform and ship-ice collisions, IMT
IMT-3-2016	Mia Abrahamsen Prsic	Numerical Simulations of the Flow around single and Tandem Circular Cylinders Close to a Plane Wall, IMT
IMT-4-2016	Tufan Arslan	Large-eddy simulations of cross-flow around ship sections, IMT

IMT-5-2016	Pierre Yves-Henry	Parametrisation of aquatic vegetation in hydraulic and coastal research,IMT
IMT-6-2016	Lin Li	Dynamic Analysis of the Instalation of Monopiles for Offshore Wind Turbines, CeSOS
IMT-7-2016	Øivind Kåre Kjerstad	Dynamic Positioning of Marine Vessels in Ice, IMT
IMT-8-2016	Xiaopeng Wu	Numerical Analysis of Anchor Handling and Fish Trawling Operations in a Safety Perspective, CeSOS
IMT-9-2016	Zhengshun Cheng	Integrated Dynamic Analysis of Floating Vertical Axis Wind Turbines, CeSOS
IMT-10-2016	Ling Wan	Experimental and Numerical Study of a Combined Offshore Wind and Wave Energy Converter Concept
IMT-11-2016	Wei Chai	Stochastic dynamic analysis and reliability evaluation of the roll motion for ships in random seas, CeSOS
IMT-12-2016	Øyvind Selnes Patricksson	Decision support for conceptual ship design with focus on a changing life cycle and future uncertainty, IMT
IMT-13-2016	Mats Jørgen Thorsen	Time domain analysis of vortex-induced vibrations, IMT
IMT-14-2016	Edgar McGuinness	Safety in the Norwegian Fishing Fleet – Analysis and measures for improvement, IMT
IMT-15-2016	Sepideh Jafarzadeh	Energy effiency and emission abatement in the fishing fleet, IMT
IMT-16-2016	Wilson Ivan Guachamin Acero	Assessment of marine operations for offshore wind turbine installation with emphasis on response-based operational limits, IMT
IMT-17-2016	Mauro Candeloro	Tools and Methods for Autonomous Operations on Seabed and Water Coumn using Underwater Vehicles, IMT
IMT-18-2016	Valentin Chabaud	Real-Time Hybrid Model Testing of Floating Wind Tubines, IMT
IMT-1-2017	Mohammad Saud Afzal	Three-dimensional streaming in a sea bed boundary layer
IMT-2-2017	Peng Li	A Theoretical and Experimental Study of Wave-induced Hydroelastic Response of a Circular Floating Collar
IMT-3-2017	Martin Bergström	A simulation-based design method for arctic maritime transport systems

IMT-4-2017	Bhushan Taskar	The effect of waves on marine propellers and propulsion
IMT-5-2017	Mohsen Bardestani	A two-dimensional numerical and experimental study of a floater with net and sinker tube in waves and current
IMT-6-2017	Fatemeh Hoseini Dadmarzi	Direct Numerical Simualtion of turbulent wakes behind different plate configurations
IMT-7-2017	Michel R. Miyazaki	Modeling and control of hybrid marine power plants
IMT-8-2017	Giri Rajasekhar Gunnu	Safety and effiency enhancement of anchor handling operations with particular emphasis on the stability of anchor handling vessels
IMT-9-2017	Kevin Koosup Yum	Transient Performance and Emissions of a Turbocharged Diesel Engine for Marine Power Plants
IMT-10-2017	Zhaolong Yu	Hydrodynamic and structural aspects of ship collisions
IMT-11-2017	Martin Hassel	Risk Analysis and Modelling of Allisions between Passing Vessels and Offshore Installations
IMT-12-2017	Astrid H. Brodtkorb	Hybrid Control of Marine Vessels – Dynamic Positioning in Varying Conditions
IMT-13-2017	Kjersti Bruserud	Simultaneous stochastic model of waves and current for prediction of structural design loads
IMT-14-2017	Finn-Idar Grøtta Giske	Long-Term Extreme Response Analysis of Marine Structures Using Inverse Reliability Methods
IMT-15-2017	Stian Skjong	Modeling and Simulation of Maritime Systems and Operations for Virtual Prototyping using co-Simulations
IMT-1-2018	Yingguang Chu	Virtual Prototyping for Marine Crane Design and Operations
IMT-2-2018	Sergey Gavrilin	Validation of ship manoeuvring simulation models
IMT-3-2018	Jeevith Hegde	Tools and methods to manage risk in autonomous subsea inspection,maintenance and repair operations
IMT-4-2018	Ida M. Strand	Sea Loads on Closed Flexible Fish Cages
IMT-5-2018	Erlend Kvinge Jørgensen	Navigation and Control of Underwater Robotic Vehicles

IMT-6-2018	Bård Stovner	Aided Intertial Navigation of Underwater Vehicles
IMT-7-2018	Erlend Liavåg Grotle	Thermodynamic Response Enhanced by Sloshing in Marine LNG Fuel Tanks
IMT-8-2018	Børge Rokseth	Safety and Verification of Advanced Maritime Vessels
IMT-9-2018	Jan Vidar Ulveseter	Advances in Semi-Empirical Time Domain Modelling of Vortex-Induced Vibrations
IMT-10-2018	Chenyu Luan	Design and analysis for a steel braceless semi-submersible hull for supporting a 5-MW horizontal axis wind turbine
IMT-11-2018	Carl Fredrik Rehn	Ship Design under Uncertainty
IMT-12-2018	Øyvind Ødegård	Towards Autonomous Operations and Systems in Marine Archaeology
IMT-13-2018	Stein Melvær Nornes	Guidance and Control of Marine Robotics for Ocean Mapping and Monitoring
IMT-14-2018	Petter Norgren	Autonomous Underwater Vehicles in Arctic Marine Operations: Arctic marine research and ice monitoring
IMT-15-2018	Minjoo Choi	Modular Adaptable Ship Design for Handling Uncertainty in the Future Operating Context
MT-16-2018	Ole Alexander Eidsvik	Dynamics of Remotely Operated Underwater Vehicle Systems
IMT-17-2018	Mahdi Ghane	Fault Diagnosis of Floating Wind Turbine Drivetrain- Methodologies and Applications
IMT-18-2018	Christoph Alexander Thieme	Risk Analysis and Modelling of Autonomous Marine Systems
IMT-19-2018	Yugao Shen	Operational limits for floating-collar fish farms in waves and current, without and with well-boat presence
IMT-20-2018	Tianjiao Dai	Investigations of Shear Interaction and Stresses in Flexible Pipes and Umbilicals
IMT-21-2018	Sigurd Solheim Pettersen	Resilience by Latent Capabilities in Marine Systems
IMT-22-2018	Thomas Sauder	Fidelity of Cyber-physical Empirical Methods. Application to the Active Truncation of Slender Marine Structures
IMT-23-2018	Jan-Tore Horn	Statistical and Modelling Uncertainties in the Design of Offshore Wind Turbines

IMT-24-2018	Anna Swider	Data Mining Methods for the Analysis of Power Systems of Vessels
IMT-1-2019	Zhao He	Hydrodynamic study of a moored fish farming cage with fish influence
IMT-2-2019	Isar Ghamari	Numerical and Experimental Study on the Ship Parametric Roll Resonance and the Effect of Anti-Roll Tank
IMT-3-2019	Håkon Strandenes	Turbulent Flow Simulations at Higher Reynolds Numbers
IMT-4-2019	Siri Mariane Holen	Safety in Norwegian Fish Farming – Concepts and Methods for Improvement
IMT-5-2019	Ping Fu	Reliability Analysis of Wake-Induced Riser Collision
IMT-6-2019	Vladimir Krivopolianskii	Experimental Investigation of Injection and Combustion Processes in Marine Gas Engines using Constant Volume Rig
IMT-7-2019	Anna Maria Kozlowska	Hydrodynamic Loads on Marine Propellers Subject to Ventilation and out of Water Condition.
IMT-8-2019	Hans-Martin Heyn	Motion Sensing on Vessels Operating in Sea Ice: A Local Ice Monitoring System for Transit and Stationkeeping Operations under the Influence of Sea Ice
IMT-9-2019	Stefan Vilsen	Method for Real-Time Hybrid Model Testing of Ocean Structures – Case on Slender Marine Systems
IMT-10-2019	Finn-Christian W. Hanssen	Non-Linear Wave-Body Interaction in Severe Waves
IMT-11-2019	Trygve Olav Fossum	Adaptive Sampling for Marine Robotics
IMT-12-2019	Jørgen Bremnes Nielsen	Modeling and Simulation for Design Evaluation
IMT-13-2019	Yuna Zhao	Numerical modelling and dyncamic analysis of offshore wind turbine blade installation
IMT-14-2019	Daniela Myland	Experimental and Theoretical Investigations on the Ship Resistance in Level Ice
IMT-15-2019	Zhengru Ren	Advanced control algorithms to support automated offshore wind turbine installation
IMT-16-2019	Drazen Polic	Ice-propeller impact analysis using an inverse propulsion machinery simulation approach
IMT-17-2019	Endre Sandvik	Sea passage scenario simulation for ship system performance evaluation

IMT-18-2019	Loup Suja-Thauvin	Response of Monopile Wind Turbines to Higher Order Wave Loads
IMT-19-2019	Emil Smilden	Structural control of offshore wind turbines – Increasing the role of control design in offshore wind farm development
IMT-20-2019	Aleksandar-Sasa Milakovic	On equivalent ice thickness and machine learning in ship ice transit simulations
IMT-1-2020	Amrit Shankar Verma	Modelling, Analysis and Response-based Operability Assessment of Offshore Wind Turbine Blade Installation with Emphasis on Impact Damages
IMT-2-2020	Bent Oddvar Arnesen Haugaløkken	Autonomous Technology for Inspection, Maintenance and Repair Operations in the Norwegian Aquaculture
IMT-3-2020	Seongpil Cho	Model-based fault detection and diagnosis of a blade pitch system in floating wind turbines
IMT-4-2020	Jose Jorge Garcia Agis	Effectiveness in Decision-Making in Ship Design under Uncertainty
IMT-5-2020	Thomas H. Viuff	Uncertainty Assessment of Wave-and Current-induced Global Response of Floating Bridges
IMT-6-2020	Fredrik Mentzoni	Hydrodynamic Loads on Complex Structures in the Wave Zone
IMT-7-2020	Senthuran Ravinthrakumar	Numerical and Experimental Studies of Resonant Flow in Moonpools in Operational Conditions
IMT-8-2020	Stian Skaalvik Sandøy	Acoustic-based Probabilistic Localization and Mapping using Unmanned Underwater Vehicles for Aquaculture Operations
IMT-9-2020	Kun Xu	Design and Analysis of Mooring System for Semi-submersible Floating Wind Turbine in Shallow Water
IMT-10-2020	Jianxun Zhu	Cavity Flows and Wake Behind an Elliptic Cylinder Translating Above the Wall
IMT-11-2020	Sandra Hogenboom	Decision-making within Dynamic Positioning Operations in the Offshore Industry – A Human Factors based Approach
IMT-12-2020	Woongshik Nam	Structural Resistance of Ship and Offshore Structures Exposed to the Risk of Brittle Failure
IMT-13-2020	Svenn Are Tutturen Værnø	Transient Performance in Dynamic Positioning of Ships: Investigation of Residual Load Models and Control Methods for Effective Compensation
IMT-14-2020	Mohd Atif Siddiqui	Experimental and Numerical Hydrodynamic Analysis of a Damaged Ship Section in Waves